SEARCH FOR NEW PHYSICS IN THE EXCLUSIVE $\gamma_{DELAYED}$ + MISSING TRANSVERSE ENERGY CHANNEL IN $P\bar{P}$ COLLISIONS AT $\sqrt{S} = 1.96$ TEV

A Dissertation

by

JONATHAN ABRAHAM ASAADI

Submitted to the Office of Graduate Studies of
Texas A&M University
in partial fulfillment of the requirements for the degree of

DOCTOR OF PHILOSOPHY

Approved by:

Chair of Committee,	David Toback
Committee Members,	Guy Almes
	Bhaskar Dutta
	Ricardo Eusebi
Department Head,	George Welch

December 2012

Major Subject: Physics

ABSTRACT

This dissertation presents the results of a search in the exclusive photon plus missing transverse energy ($\gamma+ \not{E}_T$) final state in proton antiproton collisions at a center of mass energy of 1.96 TeV using the Collider Detector at Fermilab experiment. The strategy used here is to search for delayed photons coming from gauge mediated supersymmetric events with the exclusive production of $\tilde{\chi}_1^0 \to \gamma\tilde{G}$. In these models the $\tilde{\chi}_1^0$ is the lightest neutralino and has nanosecond lifetime before decaying to a photon (γ) and gravitino ($\tilde{G}$) which exits the detector unrecorded. In order to search for this process we select collisions that have a single photon plus missing transverse energy and little other activity in the detector and examine the arrival time of the photon. This arrival time is then compared against expectations from a data driven background of the standard model sources. In the data collected from the Fermilab Tevatron collider from December 2004 to June 2010, representing 6.3 fb^{-1} of data, we observe 322 events in the photon arrival timing region from 2 nanoseconds to 7 nanoseconds with a data driven background prediction of 257 ± 35. An excess of 65 events is observed, equivalent to a standard deviation (N_σ) of 1.65 from the null hypothesis.

ACKNOWLEDGEMENTS

There are a great many people to whom I owe an enormous debt of gratitude when it comes to the completion of this body of work. As in most science, and most especially High Energy Physics, no one accomplishment can happen without the endless support and work of countless people who came before me. To their effort in the building, operation, and maintenance of the Fermilab Tevatron collider and the CDF detector, without which no part of this dissertation would have been possible, I offer my deepest thanks and appreciation. As it is impossible to mention each person and their work that ultimately went into the making of this dissertation, I would like to thank a few select people who have supported me directly during my time working on this analysis.

Dave Toback, my advisor for nearly eight years, has been a mentor, leader, and friend at a level that is rarely found anywhere in this world. I am forever in debt to this man who has helped shape me as a scientist and helped lead me throughout my formative years of my twenties. He has always made time to listen to my thoughts and concerns, both professional and personal, and has offered advice that is been both profound and timely. Dave has kept me on track to becoming a scientist and has always been there to give me a friendly nudge or a hard kick in the pants when I started to stray too far. I am very proud to have my training under such a great scientist and human being and hope that one day I will be able to make him even one-tenth as proud of me and my career.

There are a number of people at Texas A&M University to whom I would like to offer special thanks. I am grateful to Bhaskar Dutta, Ricardo Eusebi, and Guy Almes for serving on my committee and their work in contributing to my research, course work, and time at Texas A&M. I also want to thank Teruki Kamon for all his time, guidance, and support and Sherry Yennello for serving on my masters committee and contributing to my research. A special thanks needs to be made to Peter McIntyre with whom I did a summer research program with as an undergraduate and without whom I would have never attended Texas A&M, would not have made it through my first year of graduate school, and would have never met my advisor. Additionally, a large sentiment of gratitude is owed to the staff in the physics department who offer their support to all students who pass through their doors. Specifically I would like to thank Sandi Smith, Minnette Bilbo, Scharlotte Jones, Cheryl Picone, and Heather Walker who at various times during my graduate student career have been of enormous help.

There are also a long list of graduate students and post-docs throughout my time at Texas A&M and Fermilab who have been of the highest support and to which I owe a great deal. Firstly, I must express recognition to Adam Aurisano a fellow graduate student and friend who has worked on this project with me throughout my entire time. Joining A&M in the same year, Adam has been an inspiration of brilliance and hard work as well as a great friend and co-worker. His work is found throughout these pages and any credit that is gained through this work is as much his as my own. Additionally I need to thank Dr. Daniel Goldin and Dr. Jason Nett for their work and time on this dissertation subject and helping propel me to finish this very difficult analysis.

My friends Dr. Alfredo Gurrola, Dr. Andrey Elagin, Dr. Eunsin Lee, Dr. Vadim Khotilovich, Dr. Peter Wagner, Lucas Naveria, and Michael Cone as well as many others in the physics department helped to make my life full and rewarding during these last eight years and I thank you all. While at Fermilab I have also had the good fortune to meet and work with Dr. Ron Moore and Dr. Homer Wolfe both of whom have become good friends and serve as mentors and models of great scientists that I strive to become.

Finally I need to thank my family for their unending support and love throughout my life. To my mother Jane Asaadi who instilled in me a great curiosity at a young age and always took time to listen to me I owe my life and undying love. To my father Mohammad Asaadi who taught me to aim high, sacrifice, and work hard; I would be nothing of the man I have become without his life long support and I will never be able to repay that debt. My brother Robert Asaadi who has been an inspiration to me in his own academic endeavors as well as a friend unlike any other. My sister Sheila Asaadi who has shown me love and unwaivering support I am very grateful. Lastly, but not leastly, my wife Heather Asaadi who has driven me to become the man I have wanted to be. Thank you for supporting me despite this taking much longer then I would have ever guessed and being an amazing wife and friend. I love you Heather more then you will ever know.

TABLE OF CONTENTS

LIST OF FIGURES

LIST OF TABLES

1. INTRODUCTION

1.1 Overview

Since time immemorial, mankind has struggled to discover deeper and more fundamental laws associated with the natural phenomena that is observed in nature. In the 20th century this struggle turned to the science of particle physics as the focus of the search for a Grand Unified Theory of all the constituents of matter and their associated forces [1]. More so, the task of testing theories against experimental data and picking the ones that are the most consistent with what is observed, and rejecting those that fail such tests, has lead to the formation of what is known as the Standard Model, here after denoted by SM, of particle physics [2].

Much as Dmitri Mendeleev's table of periodic elements allowed us to understand and predict an enormous amount of phenomena in chemistry, the SM has proven to be overwhelmingly successful for phyics. However, just as we now know that Mendeleev's table was not the fundamental theory of atoms, we believe the SM is not the fundamental theory of particles and their forces and thus must be modified or extended in some way.

Any new theory of particle physics must be capable of making predictions about observable new phenomena, and it is these predictions that we turn our attention to in this dissertation. Many contending theories predict that there should exist, as yet undiscovered, new particles and/or interactions. They also predict that in experiments where we collide high energy particles one could produce one or more collisions (or events) that "differs" from expectations of the SM.

While scientists have been performing such experiments for many years [3], history suggests that many discoveries come from the application of a new tool which allows scientists to consider information previously unavailable. In our case, we have collisions of high energy particles, at the time the highest available to man, and a detector surrounding the collision that is able to measure the time of arrival of photon (the particles of light) to a precision of just over a half a nanosecond. This tool provides a new window of opportunity to search for compelling extensions of the SM, for example theories of the Higgs boson and Supersymmetry (SUSY), that predict new particles that have a significantly long lifetime (many nanoseconds) and produce photons in such a way that they arrive at the detector a few nanoseconds later than expectations. In other words the photons would appear to arrive at the detector "delayed". The details of example theories that might produce such a set of events, how they will decay and interact with our detector, as well as our methods and results of searching for such events in this unique signature, constitutes the majority of the remaining pages of this dissertation.

While there are compelling theoretical reasons to look for this experimental signature, in point of fact, the model we are testing is the SM. In order to do this we must first understand the predictions of the SM and thereby understand the model itself in some more detail. In the next section we will present a discussion of the SM of particle physics and some of its known limitations, specifically with an eye towards potential solutions and extensions as well as ways of testing these extensions. Said colloquially, "Once you know the 'rules' of the game we can see if nature has 'changed' any of them."

1.2 Outline of the Dissertation

Before we go further, it is useful to give a more complete description about the full path laid out in this dissertation. Once we are done with our description of the SM, detailed in Section 1.3.1, we will describe more about some of the models of new physics of most interest to us from both a theoretical and experimental point of view. These models include both the Higgs mechanism and SUSY, both of which will be described in Section 1.3.2. With these ideas, in Section 1.4, we look at previous searches for evidence for specific SUSY models as well as places which are not yet covered by previous experiments. Of particular interest will be a preliminary search from the Fermilab Tevatron in 2008, the worlds highest energy proton antiproton particle accelerator, that produced what could be naively interpreted as evidence for new physics. We will discuss this original observation, and in the bulk of the this dissertation, do a thorough and systematic study to see if this potential hint is really evidence for new physics.

In Section 2 we present the experimental tools used in this analysis, including the Fermilab Tevatron collider as well as the Collider Detector at Fermilab (CDF) which surrounds the collision point and records the activities of the resulting interactions. In particular we describe the relevant subsystems used at CDF in the timing measurement. Section 2 also describes the various object identification that is performed from the information read out from the CDF detector as well as laying out many of the various useful data samples used in this analysis. In Section 3 the new calibration procedure is detailed in order to ensure that we have accurate and reliable timing information associated with photons in this analysis. Section 4 details non-collision backgrounds and new selection requriements used to minimize their presence in our final sample of events. In Section 5 we turn our attention to the various SM backgrounds and the pathological event reconstruction which results in both an underestimation of the backgrounds to the search described in Section 1.6 as well as the methods we use to mitigate many of these effects. Section 6 focuses on the development and validation of a new data-driven background estimation from SM sources. Finally, Section 7 presents the results of the search and compares them directly to the 2008 result. Section 8 ultimately summarizes these results as well as proposing possible extensions to the search which could be performed in the future. With this path in mind we begin our description of the SM of Particle Physics.

1.3 Theory

In this section we provide an overview of the prevailing theory of particle physics known as the SM. With this basis we next draw attention to known experimental and theoretical shortcomings of the SM, in particular, the Higgs mechanism of electroweak symmetry breaking, with an eye towards potential extensions to the SM. In Section 1.3.2 we put forward one potential extension to the SM known as SUSY. We provide a general overview of this theory with attention drawn toward the potential experimental ramifications of such an extension. SUSY is posited as a real symmetry in nature, and while there is clear evidence that this would have to be a broken symmetry, what is not clear is what mechanism breaks this symmetry. In order to make predictions about what we will see in experiments we need to select one of many mechanisms of SUSY breaking that are favored for one reason or another. To allow us to make specific predicitions we detail the aspects of one particular 'flavor' of symmetry breaking known as Gauge Mediated Supersymmetry Breaking (GMSB) in Section 1.3.3. Finally, since there are many versions of GMSB, we detail many of the important parameters of this model. This allows to understand both the basic theoretical underpinnings of collider based searches that have already been performed, presented in Section 1.4, as well as what areas are not yet covered. Said in a slightly different way, if the Higgs mechanism and SUSY (or theories like them) were true in nature, what type of collisions might we expect to see in high energy experiments that we would not otherwise observe? With a clear vision of what our models predict would show up in experiments, we have a clear motivation of what types of events to look for.

1.3.1 The Standard Model of Particle Physics

The SM of particle physics is a theory that describes the known elementary particles and their interactions [1]. The SM asserts that the material which makes up the observable universe is made of elementary particles interacting through fields as well as the particles associated with those interaction fields. This theory successfully describes three of the fundamental forces: the strong nuclear force, the weak nuclear force, and the electromagnetic force; the three of which are responsible for the vast majority of interactions (gravity is excluded) between elementary particles[2].

As shown in Figure 1.1 the SM contains three generations of spin $\frac{1}{2}$ (e.g. $\frac{1}{2}$,$\frac{3}{2}$,$\frac{5}{2}$...) particles called fermions that make-up the basic constituents of atomic matter. For every fermion there is an associated, so called, “anti-fermion” that possesses the same mass but opposite quantum numbers. All fermions interact with each other via the exchange of the gauge bosons representing the fundamental forces listed on the right hand side of Figure 1.1. The fundamental forces are mediated by four integer spin (e.g. 1,2,3..) vector gauge bosons particles which act as the carriers of the various interactions between the particles. These bosons are the photon (electromagnetic force), the gluon (strong force), and the W and Z bosons (weak force). The last particle of the SM is the Higgs boson, which as of this writing was just reported as potentially being observed [4].

In mathematical terms, the SM interactions can be described by a local symmetry group of $SU(3)_C \times SU(2)_L \times U(1)_Y$, where $SU(3)_C$ describes the strong force interaction through the coupling of the quarks to the $SU(3)$ gluon particles that carry “color charge” (hence the subscript C) in a theoretical framework known as Quantum Chromodynamics (QCD)[5, 6]. The $SU(2)_L \times U(1)_Y$ terms correspond to the

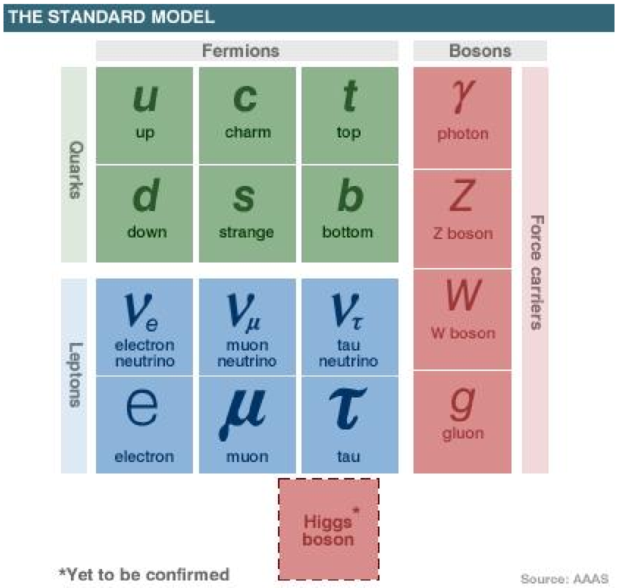

Figure 1.1: The particles that comprise the Standard Model are arranged into three generations and the interactions between them are communicated by the exchange of the force carrying particles.

electromagnetic and weak interaction, or electroweak (EWK) theory [7, 8, 9] and the couplings to the photon and the W and Z boson with the subscript L denoting the weak current and Y denoting "weak hypercharge". However, we observe the weak force and the electromagnetic force as separate; thus the $SU(2)_L \times U(1)_Y$ symmetry is observed to be broken [9]. The most common thought is that this symmetry is spontaneously broken by a fundamental scalar field, the Higgs field[10]. This symmetry breaking mechanism, while not verified in experiment yet, gives rise to the familiar mass eigenstates for the gauge bosons, such as the W and Z, and establishes the correlation between charge as we conventionally know it (Q) and "weak hypercharge". These quantities are thus what we measure experimentally[3] and summary of their names, symbols, and masses is given in Table 1.1.

The mechanism by which EWK symmetry breaking occurs will be discussed further in the next section, but has long been thought to be by the Higgs mechanism

Particle	**Symbol**	**Mass** (MeV/c^2)
Quarks		
Up	u	1.5 - 5
Down	d	3 - 9
Charm	c	1100 - 1400
Strange	s	60 - 170
Top	t	172000
Bottom	b	4100 - 4400
Leptons		
Electron	e	0.511
Electron neutrino	ν_e	∼0 (but not identically 0)
Muon	μ	105.7
Muon neutrino	ν_μ	∼0 (but not identically 0)
Tau	τ	1777.1
Tau neutrino	ν_τ	∼0 (but not identically 0)
Bosons		
Photon	γ	0
W	W	80400
Z	Z	91200
Gluon	g	0

Table 1.1: Table of the Standard Model particles, their symbols, and their measured mass.

[10]. While the effects of a Higgs mechanism have been verified to a high degree of measurements [3], and there is some evidence that the particle corresponding to fundamental scalar field (namely, the Higgs boson itself), has been observed [4], the mechanism of EWK symmetry breaking has not be verified. For now it is sufficient to remark that the Higgs field can be thought of as a sort-of viscous fluid that all particles have to constantly travel through and the resulting *drag* is what can be thought of as the particle's mass. This field gives rise to a Higgs boson whose couplings to the particles is proportional to their mass [11].

While the SM is seen as a very successful theory in both precision measurement as well as predicting new particles [12], there are several theoretical and experimental shortcomings that suggest that it is simply a low-energy approximation to a more fundamental theory. Examples of experimental results that do not immediately fall into the SM come from a variety of measurements. One such example is the observation of neutrino oscillations [13] suggesting that the neutrinos are not in fact massless as predicted by the SM. Another such measurement is the $\sim 3.4\sigma$ deviation from SM prediction of the muon magnetic moment, $g-2$, observed in experiment [14]. Perhaps the most astounding is that current cosmological observations imply that the visible matter in the universe that is described by the content of the SM only constituents $\sim 5\%$ of the known universe [15, 16].

In addition to these experimental results, an important potential theoretical shortcoming of the SM lies with the Higgs mechanism itself. For instance, the calculation of the Higgs mass in the theory leads to radiative corrections that cause the mass to diverge and is known as the "hierarchy" or "naturalness" problem [17]. These problems are so named because the values computed for the Higgs mass are wildly larger ($\sim 10^{14}$ GeV) then what is observed for the electroweak scale breaking ($\sim 10^{2}$ GeV) thus putting a large "hierarchy" into the theory and making the predicitions lack "naturalness". Without some sort of "ultra-violet cutoff" to the diverging mass calculation this will cause the theory to become not self-consistent. This problem is discussed further in the following section.

1.3.2 Higgs / Supersymmetry Theory

1.3.2.1 Higgs

To understand this Higgs problem, and a potential solution, we next describe the EWK theory. The EWK theory requires four gauge bosons (W^{+}, W^{-}, Z, γ) all of which would have to be massless in order that the SM be invariant under gauge transformations [7, 8, 9]. However, it is experimentally known that while this is true for the photon, the W and Z bosons are massive [3] and any straightforward attempt to simply add a mass term breaks the gauge symmetry and is thus not allowed. As mentioned before, there is an elegant solution known as spontaneous symmetry breaking known or the Higgs mechanism [10]. Put simply, the Higgs mechanism allows one to introduce massive gauge bosons for the weak interaction without breaking the $SU(2)_L \times U(1)_Y$ invariance.

The Higgs mechanism is the ansatz that there is a fundamental scalar field, known as the Higgs field, which makes the gauge invariant theory undergo a spontaneous symmetry breaking as the Higgs potential reaches a non-zero value for the introduced scalar field. Figure 1.2 is a schematic drawing of what the Higgs potential looks like (colloquially referred to as the "mexican hat" potential) and thus provides a sense why the non-zero value for the potential spontaneously breaks the symmetry. Namely, since the minimum of the potential is no longer located at the center of this representation for the potential, the symmetry is broken when the particles go to the low-energy state. In the SM this spontaneous symmetry breaking generates the mass terms for all the particles including the gauge bosons.

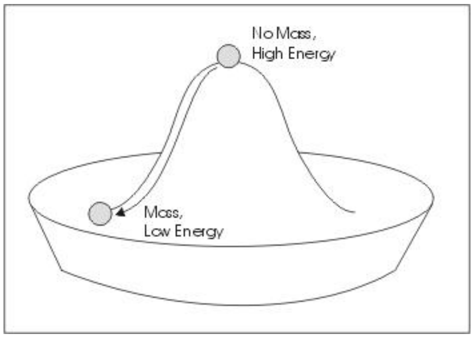

Figure 1.2: Schematic of the Higgs potential energy demonstrating how the particles of the SM obtain their mass.

In addition to giving mass to the gauge bosons, the Higgs mechanism also predicts a fundamental spin-0 particle known as the Higgs boson [10] with an unspecified mass.

It is in the calculation of this particles mass where aforementioned hierarchy problem arises. Specifically, the hierarchy problem can be seen when radiative corrections to the Higgs mass are calculated and have the basic form shown in Equation 1.1. Here, m^2_{Bare} is known as the "bare" Higgs mass and δm^2_H is the sum of the corrections due to such radiative corrections shown in Figure 1.3. We find

$$m^2_H = m^2_{Bare} + \delta m^2_H \tag{1.1}$$

where δm^2_H can be written for a fermion of mass m_f as

$$\delta m^2_H \approx \frac{\lambda^2_f}{4\pi^2}(\Lambda^2 + m^2_f) + ... \tag{1.2}$$

and λ_f is the coupling constant of the Higgs boson and Λ is the cut-off energy of the theory [1]. Unlike the fields describing all the other known particles, whose masses are protected by symmetry principles [1] that ensure the radiative corrections are only logarithmically divergent, the Higgs mass diverges quadratically when taking diagrams like Figure 1.3 into account [17]. In order to yield a Higgs mass of the order of 100 GeV, which is favored by the SM [18, 19] to preserve EWK symmetry breaking, the bare Higgs mass is forced to be the same order of magnitude as the corrections, thus forcing the theory to be "fine-tuned" to an uncomfortable number of digits to keep the Higgs mass from becoming non-physical.

Since it seems unlikely that the theory of EWK symmetry breaking requires this remarkable fine-tuning of one of its physical parameters, physicists have sought other solutions which might reveal a more fundamental understanding. One particularly elegant solution comes by extending the symmetry of the theory further to a symmetry that relates the gauge particles (bosons) and the matter particles (fermions).

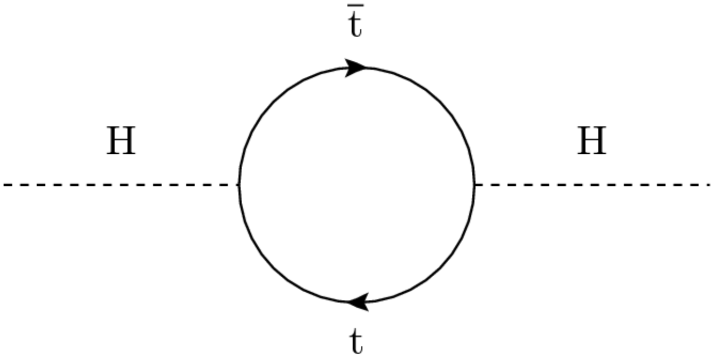

Figure 1.3: An example of the one-loop quantum corrections from fermion loops (top quark shown here) to the Higgs mass leads that lead to a divergent Higgs boson mass without “fine tuning” in the theory. This is known as the “hierarchy” problem and presents a compelling reason to believe that the SM Higgs may not be the complete theory of EWK symmetry breaking.

This theory is known as SUSY and offers a solution to the hierarchy problem as well as having many other advantages. In particular, SUSY offers intriguing solutions to other shortcomings of the SM such as an explanation of the previously mentioned anomalous muon magnetic moment and the “dark matter” question [14, 15, 16]. While a complete discussion is beyond the scope of this dissertation, it is worthwhile to note that SUSY (or something like it) is required for most grand unified models such as String Theory [20].

On the flip side, it is important to note that the SUSY solution to the hierarchy problem is not without its potential downside. For example, it more than doubles the number of particles; as such it can hardly be said to be an âelegant solution” just on the surface. Furthermore, none of these new particles have been observed, although this makes this theory wonderfully testable at high energy experiments. With this in mind we move towards a description of SUSY, eventually coming back to how it helps solve the Higgs problem.

1.3.2.2 Supersymmetry

Since SUSY is a compelling theory for many reasons, many independent of the Higgs mechanism, we describe it in some detail here. As we will see, SUSY is not just a single theory but a set of theories each of which have different advantages and disadvantages. We will focus on ones that help the Higgs mechanism, have the potential to solve other problems, and give experimental predictions that can be tested in high energy collisions.

The basic proposal of SUSY [21] is that nature posseses a symmetry law that relates elementary particles of integer spin to particles of half integer spin. Said differently, SUSY implies that for every type of boson there exists a corresponding fermion partner and vice versa. Mathematically, this transformation can be achieved by having an operator Q that is an anti-commuting spinor [21, 22, 23] such that

$$Q\left|Boson\right\rangle = \left|Fermion\right\rangle, Q\left|Fermion\right\rangle = \left|Boson\right\rangle \tag{1.3}$$

where the theory is invariant under Q transformations. This requirement is satisfied by introducing additional supersymmetric fields which correspond to the supersymmetric partners of the SM particles and thus preserve the symmetries of the SM. The consequence of this is that the number of elementary particles is essentially (at least) doubled for the Minimal Supersymmetric Standard Model (MSSM).

To simplify our description, we adopt the standard naming convention for the supersymmetric partners of the SM particles. For the partners of the fermions (leptons and quarks), we keep the same name but add an “s” to the front; they are thus referred to as “squarks” and “sleptons”. The partners of the bosons (gauge bosons) receive an “ino” as a suffix and thus become “gauginos”. Additionally, as can be seen in Figure 1.4, the symbols for the squarks, sleptons, and gauginos are the same as the corresponding fermion and boson with the addition of a “∼” denoting the supersymmetric version of the particle with a few special cases described below.

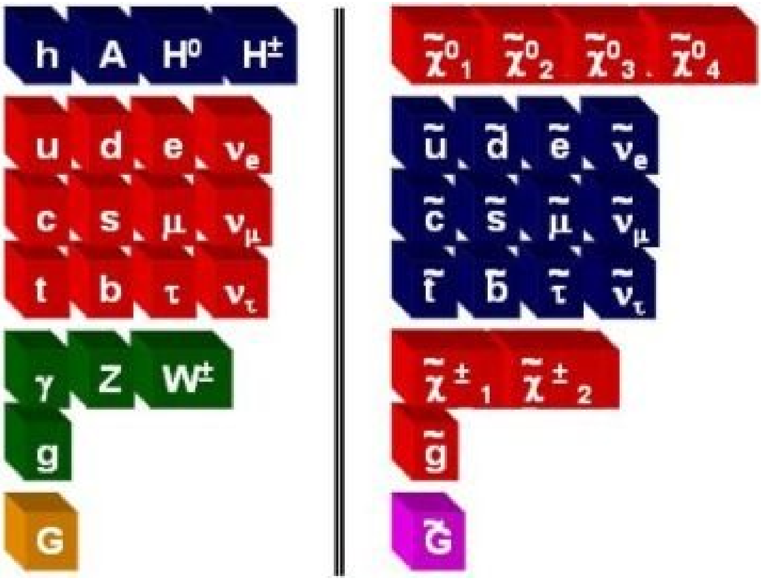

Figure 1.4: The particles of the Minimal Supersymmtric Standard Model (MSSM) extension to the SM of particle physics.

The representation of the SUSY algebra that produces the particle content of MSSM are the so called ‘supermultiplets’ which effect the mixing between the EWK and mass eigenstates of the gauginos. The supermultiplets also contain both fermion and boson states for SM and SUSY particles in such a way that the number of degrees of freedom for fermions is the same as for bosons. As shown in Figure 1.4, SUSY theories require a minimum of two complex Higgs doublets rather than just one ordinary SM Higgs [22, 23]. The supersymmetric partner to these Higgs doublets (higgsinos) mix with the supersymmetric EWK gauge particles (gauginos) because of the effects of the EWK symmetry breaking, [21, 22, 23], such that the neutral ones combine to form four mass eigenstates called the “neutralinos” ($\tilde{\chi}_i^0, i = 1, 2, 3, 4$) and the charged ones combine to form the “charginos” ($\tilde{\chi}_i^\pm, i = 1, 2$) shown in Figure 1.4 where the numbering i corresponds to the ordering of the mass eigenstates. Additionally SUSY also postulates the Gravitino, $\tilde{G}$, the SUSY partner to the as-yet-undiscovered spin 2 Graviton [21].

With a basic understanding of SUSY we can now come back to how SUSY can help solve the hierarchy problem before moving on to how SUSY and the Higgs can potentially be observed in high energy collider experiments. SUSY can solve the hierarchy problem because the SUSY particles must be included in the loop diagram corrections to the Higgs mas as shown in Figure 1.5. Each gives corrections similar to those in Equation 1.2 but with opposite sign since they are now scalar and fermion loops, such as

$$\delta m_H^2 \approx -\frac{\lambda_{\tilde{f}}^2}{4\pi^2}(\Lambda^2 + m_{\tilde{f}}^2) + ... \tag{1.4}$$

These correction terms thus are enticingly close to being exactly what is needed to cancel out the quadratic divergences from δm_H^2 and thus elegantly solves the hierarchy problem [24].

However, this solution comes at a cost; namely this theory introduces a large number of new fundamental particles, none of which have been discovered as of the writing of this dissertation [3]. Furthermore, if SUSY was a perfect symmetry the SUSY particles would have the exact same masses as their SM counterparts and thus would have been detected long ago [3]. Since SUSY provides a compelling solution to the hierarchy problem, and there are other reasons to think SUSY might still be correct in nature, a great deal of effort has gone into consider more sophisticated versions of SUSY. In particular the resonable assumption that SUSY is a broken symmetry like EWK theory. If this is the case, then our next task is to understand the mechanism of SUSY breaking. We start by considering that a spontaneous SUSY breaking takes place via some other field, since none of the fields in MSSM can develop a non-zero vacuum expectation without spoiling the gauge invariance of the theory.

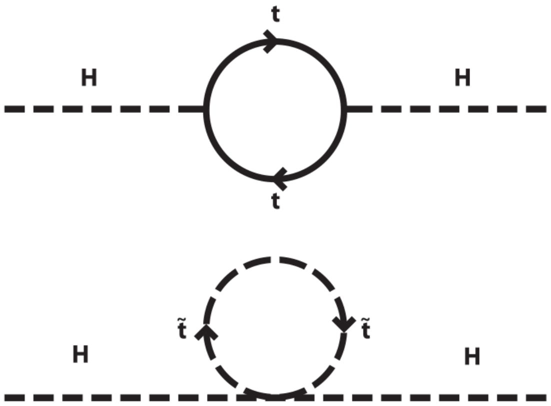

Figure 1.5: One-loop quantum corrections to the Higgs mass leads to a divergent mass in the theory known as the “hierarchy” problem. In SUSY extensions to the SM the quantum corrections for fermions and their bosonic “SUSY-partners” have opposite signs and thus can lead to a cancellation that prevents the Higgs mass from becoming divergent.

While the exact mechanism of SUSY breaking is not yet understood, a common and well motivated method of SUSY breaking is known as “hidden sector” symmetry breaking[25]. Hidden sector symmetry breaking is the idea that there is an ensemble of, as-yet-unobserved, quantum fields and particles that cause the breaking of SUSY. These quantum fields and particles would exist at much higher energies, would not directly interact with the known lower energy SM fields, and thus remain “hidden”. Only through a weak coupling of this “hidden sector” to the MSSM particles are the SUSY breaking terms introduced.

This description of SUSY breaking thus has two sectors, known as the “visible” sector (to which all the ordinary matter belongs) and the “hidden” sector (containing new fields and particles). The two sectors interact through the exchange of some “messenger” field that mediate the information about how the SUSY breaking occurs.

While there are many hidden sector variations of SUSY [21, 24], historically there have been two main competing theories for what the mediating interaction between the "hidden" sector and the "visible" sector may be. The first one of these approaches assumes that the mediation is due to gravitational interactions and is commonly referred to as minimal Supergravity (mSUGRA) symmetry breaking [26, 27]. The second possibility assumes that the mediation is due to the gauge interactions and is referred to as Gauge Mediated Supersymmetry Breaking (GMSB) [28, 29, 30].

While many searches for both types of models (and many other variations) have been performed [3], and yielded null results up to the time of the writing of this dissertation, the majority of collider searches have focused on mSUGRA type models owing to the prediction of a heavy dark matter candidate [31]. GMSB models provide a compelling alternative to mSUGRA models as well as having advantages such as natural suppression of "flavor" violating interactions [28, 29, 30]. "Flavor" is a common term to explain the assigning of quantum numbers to the various particles in the SM such as lepton number, baryon number, isospin, etc. Simple flavor conservations have been observed in SM interactions [3], such as lepton number conservation, and thus any theory that can avoid "flavor" violation that has not been previously observed is seen as favorable.

1.3.3 Gauge Mediated Symmetry Breaking

We begin with a more detailed description of GMSB. However, berfore proceeding to a discussion of its implication on observable at collider experiments we remark that even with the specification of the hidden sector breaking mechanism we are left with a huge number of free parameters in the model and we will have to further reduce them with either theoreical ideas or experimental constriants. One such example is a new conservation law postulated (and typically assumed) known as "R-parity" which simply states the number of SUSY particles in an interaction is conserved for reasons we will describe in a moment.

In GMSB models SUSY breaking originates in a “hidden sector”, which is not further specified, and “mediates” the breaking through “messenger fields” to the “visible” sector. This type of breaking mechanism causes the fields that couple to the messenger field to acquire a vacuum expectation value, denoted as <F>, and thus give the masses to the MSSM fields dynamically via loop corrections [24]. A schematic view of this SUSY breaking mechanism, commonly referred to as “soft” SUSY breaking, is shown in Figure 1.6. An appealing consequence of this solution to SUSY breaking is that since it is spontaneously broken in the hidden sector, with no direct coupling to the SM particles, one can avoid quadratic divergences of the SUSY breaking terms [25] which plagued the Higgs mechanism of EWK symmetry breaking.

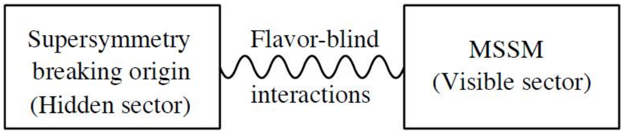

Figure 1.6: Schematic of Gauge Mediated Supersymmetry Breaking (GMSB).

With all these new particles and couplings one would naively expect a host of new interactions that would allows for the known SM particles to decay away. Since we do not observe this in nature, in addition to the known conservation laws, there must be additional mechanisms to prevent the known stable particles from decaying away. For this reason, it is typically assumed that there is a new conservation law in SUSY. In particular a value known as “R-parity” is introduced where R is a quantum multiplicative number and defined as

$$R = (-1)^{3(B-L)+2s} \tag{1.5}$$

where B, L, and s represent the baryon, lepton, and spin of the particle respectively [32]. The reason for the introduction of this conservation principal is that in the most general MSSM models there are terms introduced into the theory that allows the violation of baryon and lepton number. Interestingly, if R-Parity is violated in the most general of ways such that all B and L violating terms are allowed this would imply that the proton would become unstable and decay in a very short period of time [33]. While this phenomenological consequence of proton decay can be avoided by introducing additional terms into the SM, it is generally thought to be more theoretically appealing to simply posit R-Parity conservation [34] since both baryon and lepton number conservation have been tested to a high degree of precision [3]. This quantity is designed to be $R = +1$ for SM particles and $R = -1$ for their SUSY counterparts. R-Parity being postulated to be conserved implies a number of important phenomenological consequences for searches for sparticles at high energy colliders:

1. Any initial state created in laboratories using pairs of SM particles (such as colliders) has $R = +1$ and thus any SUSY particles created must be created in pairs.

2. All individual SUSY particles, which have $R = -1$, will decay (except the lightest supersymmetric particle) into a state that contains an odd number of SUSY particles.

3. The lightest supersymmetric particle (LSP) must be stable and cannot decay

further into SM particles, thus making it a candidate for dark matter if it is also electrically neutral [16].

GMSB models also offer distinctive phenomenological features that make them appealing for searches at particle colliders. One of these features is that the weakly interacting Gravitino ($\tilde{G}$) has a mass range of ∼eV/c^2 to ∼GeV/c^2 [28] and thus becomes the LSP. Another feature is the next-to-lightest SUSY particle (NLSP) is often the neutralino ($\tilde{\chi}_1^0$) which can decay almost exclusively to via $\tilde{\chi}_1^0 \to \gamma\tilde{G}$ making for a very distinctive signature in high energy collider experiments. While not all versions of GMSB models have this distinctive signature, in this dissertation we have chosen to focus on variations which do.

We start by listing some of the parameters of GMSB to aid in understanding quantitative predictions of the model and comment on the constraints that help us choose these parameters as well as bound their values. This will aid in our understanding of previous searches performed at collider experiments which assume certain constraints based on these model parameters. Furthermore, since a great deal of data has been gathered on the masses and other characteristics of the SM particles, we list some of the current experimental constraints that help us choose these parameters as well as bound their values. It is worth noting that we will limit ourselves to models that have predictions that can be tested at our experiment and denote which parameters this places limits on.

For GMSB models the hidden sector particles are assumed to be at a mass scale denoted as $\sqrt{F}$ and the messenger sector mass scale is given as M_{mess}. To avoid flavor breaking we require $M_{mess} > \sqrt{F}$, meanwhile M_{mess} is bounded on the other side as being below the Plank scale in order to realize SUSY breaking and help solve the hierarchy problem [35]. Thus, these values must be of the order of $\sqrt{F} \approx$10 TeV/c^2

and M_{mess} $\approx$100 TeV/c^2 [35]. With this the number of free parameters in the minimal GMSB model are reduced from over one hundred free parameters of the MSSM to 6 free parameters which are:

1. **N_{mess}:**

   The number of messenger fields. We note that while this can have any value in principle, phenomenologically low values ($\leq$ 2) of N_m lead to the next-to lightest stable particle (NLSP) being the neutralino $\tilde{\chi}_1^0$.

2. **$\Lambda = \frac{F}{M_{mess}}$:**

   The mass scale of the visible sector of SUSY breaking. For sparticles with masses on the order of the EWK scale Λ is on the order of $\frac{100 \text{ TeV}}{\sqrt{N_{mess}}}$.

3. **M_{mess}:**

   The overall messenger scale of the messenger sector. All the masses of the SUSY particles depend on M_{mess} logarithmically while the lifetime of the NLSP, which is important in this analysis, depends quadratically on M_{mess}.

4. **tan β:**

   The ratio of the vacuum expectation values of the Higgs. Large values of tanβ remove the $\tilde{\chi}_1^0$ from being the NLSP and thus remove the final state $\tilde{\chi}_1^0 \rightarrow \gamma\tilde{G}$ so we don't explore those scenarios any further.

5. **sgn(μ):**

   This is the sign of the Higgs and Higgsino supersymmetric mass parameter μ. The absolute value of μ is determined by the EWK breaking condition. Sgn(μ) is correlated with the sign of the MSSM correction to the anomalous magnetic moment of the muon, $g-2$, which is thus favored to be positive to account for this discrepancy [35].

6. C_{grav}**:**

   Represents the ratio between the scale of SUSY breaking (F_0), a generic term true in all SUSY models, and the scale of the intrinsic SUSY breaking parameter ($\frac{F_0}{F}$). This parameter contributes to the tuning of the Gravitino mass and the NLSP lifetime.

Even though this parametrization of MSSM adopted within GMSB considerably simplifies the possible phenomenological scenarios, even a six-dimensional space is too broad to be covered by any single study at a high energy experiment. For this reason, great effort has been made to create sets of combinations of the parameters that all have similar "types" of final states and phenomenologies at colliders. At this point we will shift our focus away from general and minimal GMSB theory and focus more on collider phenomenology of two different GMSB model types that have been previously searched for, as well as collider signatures which we are sensitive to but have yet to be studied. This will help provide the final pieces of focus for where we will concentrate our effort, in particular in high energy collision events that produce a photon and a Gravitino in the final state.

1.3.4 GMSB Collider Phenomenology

In order to help simplify the GMSB parameter space we will refer to two types of models each of which have a unique collider phenomenology. Both models have $\tilde{\chi}_1^0 \to \gamma\tilde{G}$ in their final state and their production and decay can be characterized as:

$$p\bar{p} \to \tilde{\chi}_1^0\tilde{\chi}_1^0 + X \to \gamma\tilde{G}\gamma\tilde{G} + X \tag{1.6}$$

where X is any other particles produced in the original interaction (if any). For now we have not specified the production mechanism of the $\tilde{\chi}_1^0$ pairs, but note that they can be directly produced or produced the the decay of other, heavier particles and this divides the various ways they produce this final state. Equally important, from the perspective of the detection of these final states, is a second bifurcation of the types into two subtypes which affect how they will detected, in particular the lifetime of the $\tilde{\chi}_1^0$ before it decays via $\tilde{\chi}_1^0 \rightarrow \gamma\tilde{G}$. We will discuss both separately. The goal of understanding these differences in the phenomenology is to aid us in understanding the previous search results presented in the next section as well as our future search strategy.

Before proceeding to the phenomenology of GMSB models, it is useful to introduce the notion of how measurements are made in high energy experiments. These ideas will be explained in much greater detail in Sections 2.1 and 2.2. The basic idea of how we produce high energy collisions comes from when two beams of energetic particles (e.g. protons and antiprotons) are made to intersect each other at a large center of mass energy. We surround the points where the beams are made to collide with large multi-purpose detectors (such as the CDF detector) that are capable of recording information relevant to the subsequent particles produced in the collisions. This information includes such quantities as collision location and collision time, as well as the 4-momentum, particle type and arrival time of the produced particles in the detector. Since the collision occurs with approximately no momentum in the plane transverse to the collision we can infer, by conservation of momentum, that the vector sum of the transverse momenta of the inital and final state particles should be approximately zero. Particles that do not interact with the calorimeter, such as neutrinos and Gravitinos (if they exist), will not deposit energy in the calorimeter so they can be inferred from the transverse energy imbalance of the detected particles in the collision. The measured missing transverse energy ($\not\!\!E_T$) is defined as the negative of the vector sum of the transverse energy measured in the detector. From this information it is possible, in principle, to reconstruct and identify the particles produced in the collision as a way to search for new particles such as those predicted in SUSY models. From this perspective, the production of spartices in Equation 1.6 gives the $\gamma\gamma+\not\!\!E_T+X$ final state, in principle, in a detector.

An important caveat to this description is the finite size of the detector which makes the lifetime of the $\tilde{\chi}_1^0$ particularly important as it affects when and how the photon is produced. The $\tilde{\chi}_1^0$ lifetime ($\tau_{\tilde{\chi}_1^0}$) given by [36]:

$$c\tau_{\tilde{\chi}_1^0} = 48\pi \frac{m_{3/2}^2 M_{Pl}^2}{m_{\tilde{\chi}_1^0}|P_{1\gamma}|^2} \tag{1.7}$$

where $m_{3/2} = \frac{|F|}{\sqrt{3}M_{Pl}}$, F is related to the value of the superpaticle masses and M_{Pl} is the Plank mass [21]. For theoretically reasonable squark masses, such that SUSY may still contribute to solving the hierarchy problem, between 2 TeV and 10 TeV [21] bounds the typical lifetime ranges to be 0.4 ns $< \tau_{\tilde{\chi}_1^0} <$ 180 ns for the $\tilde{\chi}_1^0$. This allows us to divide the possible production of $\tilde{\chi}_1^0\tilde{\chi}_1^0 \rightarrow \gamma\gamma\tilde{G}\tilde{G}$ into three possible search prospects [37]. Namely:

1. $\tau_{\tilde{\chi}_1^0} < 1$ ns:

   In this case the photons from the decay of the $\tilde{\chi}_1^0$ are produced so close to the original collision position that we are not able to distinguish them from photons directly produced in the collision.

2. 1 ns $< \tau_{\tilde{\chi}_1^0} <$ 50 ns:

   In this case the final state $\tilde{\chi}_1^0 \rightarrow \gamma\tilde{G}$ occurs at a displaced spatial location from the collision which produced the $\tilde{\chi}_1^0$ and causes the arrival time of the photon to frequently be delayed relative to expectations from promptly produced photons. This scenario will be discussed in greater detail in the following section.

3. $\tau_{\tilde{\chi}_1^0} > 50$ ns:

   In this scenario both $\tilde{\chi}_1^0$ pairs can travel a large enough distance before decaying that they typically leave the detector entirely. SUSY in this channel would not produce photons in a detector surrounding the collision point. Thus this scenerio be indistinguishable in typical collider experiments from other versions of SUSY (e.g. mSUGRA) and thus we don't consider it further.

These possibilities are what determine the last important part of the GMSB phenomenology in a detector. If GMSB models are correct, then a small fraction of high energy collisions should produce sparticles which will decay down to photons and $\not\!\!E_T$ in the final state. The question then becomes whether the neutralinos will, typically, produce two promptly produced photons, one delayed photon, or no photons in the detector. As there have been many searches for the first scenerio as well as searches for other models of SUSY, and there are compelling reasons to believe the second scenario is most likely, it is the second scenario that is the focus of this dissertation where the $\tilde{\chi}_1^0$ has a long enough lifetime to produce a photon whose reconstructed time of flight will arrive later ("delayed") than a photon promtly produced by the collision.

To quantify what is meant by "prompt" and "delayed" we consider the production and decay of a $\tilde{\chi}_1^0$ in a detector, see Figure 1.7, and write down a standard photon timing variable used known as corrected time of arrival [38], defined as:

$$t_{corr} \equiv (t_f - t_i) - \frac{|\vec{x_f} - \vec{x_i}|}{c} \tag{1.8}$$

where t_f is the arrival time of the photon at the calorimeter, t_i is the time of the collision, and $|\vec{x_f} - \vec{x_i}|$ is the distance between the collision point and the position where the photon his observed. In a perfect detector, for a promptly produced photon t_{corr}=0 ns. For a $\tilde{\chi}_1^0$ with a finite lifetime we would have t_{corr} >0 ns and we would describe this photon as being "delayed" and use the notation $\gamma_{delayed}$.

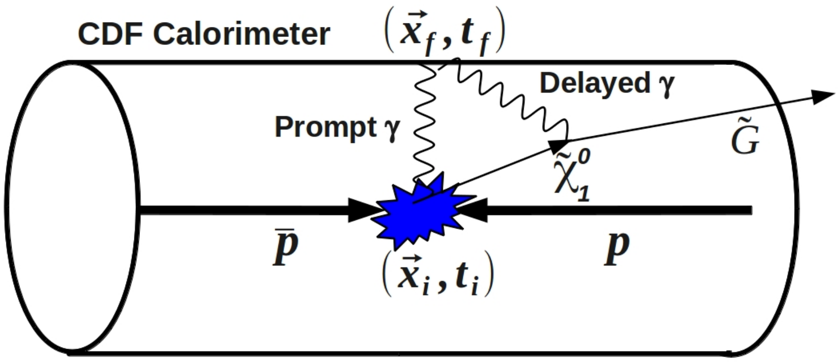

Figure 1.7: A schematic of production of long-lived $\tilde{\chi}_1^0$ at the Tevatron decaying to a Gravitino ($\tilde{G}$) and a photon (γ) inside the CDF detector with the photon arriving with a delayed time.

Coming back to the GMSB phenomenology, we can now understand our two production mechanisms in Equation 1.6 and our two decay mechanisms which give us four different final states with photons. A summary of the various scenarios described above and their resulting final states is given in Table 1.2[37]. We next describe more details about each of these four scenarios.

	$\tau_{\tilde{\chi}_1^0} < 1$ ns	$\tau_{\tilde{\chi}_1^0} \sim 5$ ns
$\tilde{\chi}_1^0\tilde{\chi}_1^0 + X$ Production	$\gamma\gamma + \not{E}_T + X$	$\gamma_{delayed} + \not{E}_T + X$
Exclusive $\tilde{\chi}_1^0\tilde{\chi}_1^0$ Production	Exclusive $\gamma\gamma + \not{E}_T$	Exclusive $\gamma_{delayed} + \not{E}_T$

Table 1.2: Table of various final states for $\tilde{\chi}_1^0$ lifetimes of interest in this analysis where X is any other particles produced in the original interaction (if any).

The most commonly discussed production models in the literature are ones where

$\tilde{\chi}_1^0 \rightarrow \gamma\tilde{G}$ is produced at the end of a long decay chain, represented by the top row of Table 1.2. An agreed upon convention was arrived at during the 2001 Snowmass Workshop on the Future of Particle Physics and is known as the Snowmass Points and Slopes (SPS) convention [39]. These are a set of benchmark points and parameters in which the MSSM parameters correspond to different general types of scenarios in SUSY for use in experimental searches. Of particular importance to us is parameter set eight, known as SPS-8, which describes benchmark set of relationships that have fixed mass relationships between the sparticles. This further simplifies the models and we are left with two free parameters: (1) The mass of one of the particles (all others are derived relative to it) and (2) the lifetime of the NLSP. Since the masses of the sparticles and their couplings are well specified, this uniquely determines their production cross sections in different types of high energy collisions, as well as their branching fractions and final state topologies.

A typical example of the production and resulting decay chain from an SPS-8 scenario for proton antiproton collisions at a center of mass energy of ~2 TeV is shown in Figure 1.8 on the left hand side where the dominant production mode is chargino pair production [37]. This diagram was chosen as it is at the limits of the sensitivity of what could be produced at the Tevatron. Similar production and decay diagrams occur at LEP and the LHC (each with slightly different diagrams) and searches for these final states have been performed at LEP [40], the Tevatron [41], and the LHC [42] for various mass and lifetime combinations which would produce the $\gamma\gamma+\not\!\!E_T$ final state as well as other ways of searching for long-lived neutralinos. All have shown no evidence for GMSB SUSY in this scenario. However, these all assume SPS-8 type relations which keep the production cross-section high but also place constraints on the possible masses of the sparticles. These limits will be described in the next section.

While the SPS-8 relations are most frequently used, a second and equally important type of production mechanism comes from models where only the $\tilde{\chi}_1^0$ and the $\tilde{G}$ have masses low enough to be produced in collider experiments [43] represented by the bottom row of Table 1.2. This scenario is referred to as the Light Neutralino and Gravitino (LNG) scenario in the literature and is important because it releases these SPS-8 type relations that are only there to help restrict the number of different search strategies for experimentalists. In these models the large direct sparticle production rates, which originally made them appealing from an experimental perspective, vanish. Said differently, the previous limits from LEP, the Tevatron, and the LHC are not applicable to these scenarios because the production mechanisms which were favored in SPS-8 models no longer produce events, thus the limits are no longer relevant. An exciting production mechanism of SUSY particles in LNG scenarios is shown on the right hand side of Figure 1.8 [43]. It shows sparticles produced in collisions is through the production of the lightest Higgs (h^0) which then decays to $\tilde{\chi}_1^0$ pairs if the masses are in a favorable configuration. The phenomenology of $h^0 \rightarrow \tilde{\chi}_1^0\tilde{\chi}_1^0$ in LGN models, where sparticle production is dominated by (h^0) events decaying to $\tilde{\chi}_1^0$ pairs, is significantly different from those seen in SPS-8 models which produce $\tilde{\chi}_1^0$ pairs at the end of long decay chains; the final state is $\gamma\gamma\tilde{G}\tilde{G}$ plus little else giving $\gamma\gamma+\not{E}_T$ if the lifetime is short and a $\gamma_{delayed}+\not{E}_T$ if the lifetime is $\sim$5 ns. It is topologies like this will be the focus for this dissertation as they are not excluded in any substantive way.

1.4 Previous Collider Searches and Model Constraints

Now that we have finished describing the basic properties of GMSB SUSY phenomenology, detailed four different phenomenological scenarios, and alluded to some previous results, we now highlight a few of the searches previously performed for each

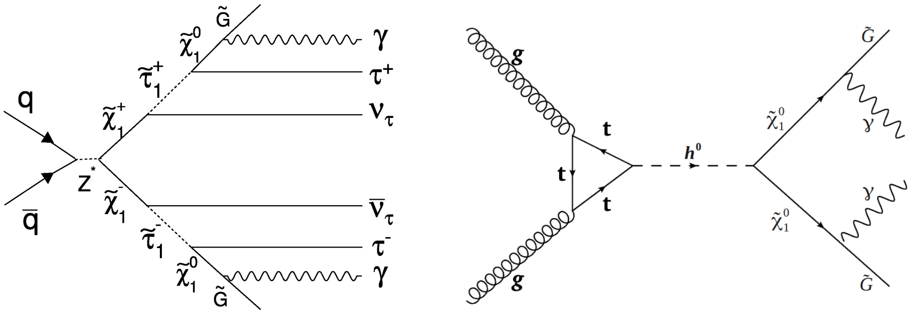

Figure 1.8: Two example Feynmann diagrams illustrating SUSY $\tilde{\chi}_1^0$ pair production event that, in the simplest GMSB models, can produce one or more photons + $\not\!\!E_T$ in high energy particle collisions.

in a little more detail. After we have completed this description and have a better understanding of which regions are most advantageous to study, we will highlight an unpublished preliminary result that was performed in 2008 and a very intriguing excess that was found in the exclusive $\gamma_{delayed}$+$\not\!\!E_T$ final state. The bulk of this dissertation is dedicated to following up on this result.

The results of various searches from LEP and the Tevatron are shown in Figure 1.9 for SPS-8 type scenarios. This figure demonstrates the parameter space that has been constrained as a function of neutralino lifetime versus mass. A few words are in order about the searches that produced these results. We begin with the e^+e^- results from the Apparatus for Large Electron Positron PHysics (ALEPH) which are a combination of direct searches for $\tilde{\chi}_1^0$'s as well as indirect searches for sleptons and charginos. In the direct searches for low lifetime $\tilde{\chi}_1^0$'s at ALEPH the channel $e^+e^- \rightarrow \tilde{\chi}_1^0\tilde{\chi}_1^0 \rightarrow \gamma\tilde{G}\gamma\tilde{G} \rightarrow \gamma\gamma+ \not\!\!E_T$ was used where the neutralino lifetime was assumed to be less than 1 ns. This implies that the photons were required to originate directly from the beam line. In the case where the lifetime was assumed larger (1 ns< $\tau_{\tilde{\chi}_1^0}$ < 10 ns) the direct searchs at ALEPH used photon "pointing" methods [40] which are complementary to the delayed photon methods previous described. In this method, photon pointing measures the way the photon interacts with the detector and searches photon candidates for evidence that they come directly from the beam line ("points" to the beam line). No evidence for SUSY was observed in these searches. These searches were only sensitive up to neutralino masses less than 100 GeV, the limiting factor being the center-of-mass energy of LEP which was only 205 GeV. We also note that while these scenarios were based on an SPS-8 like production, only the gauginos and sleptons were assumed to be light here.

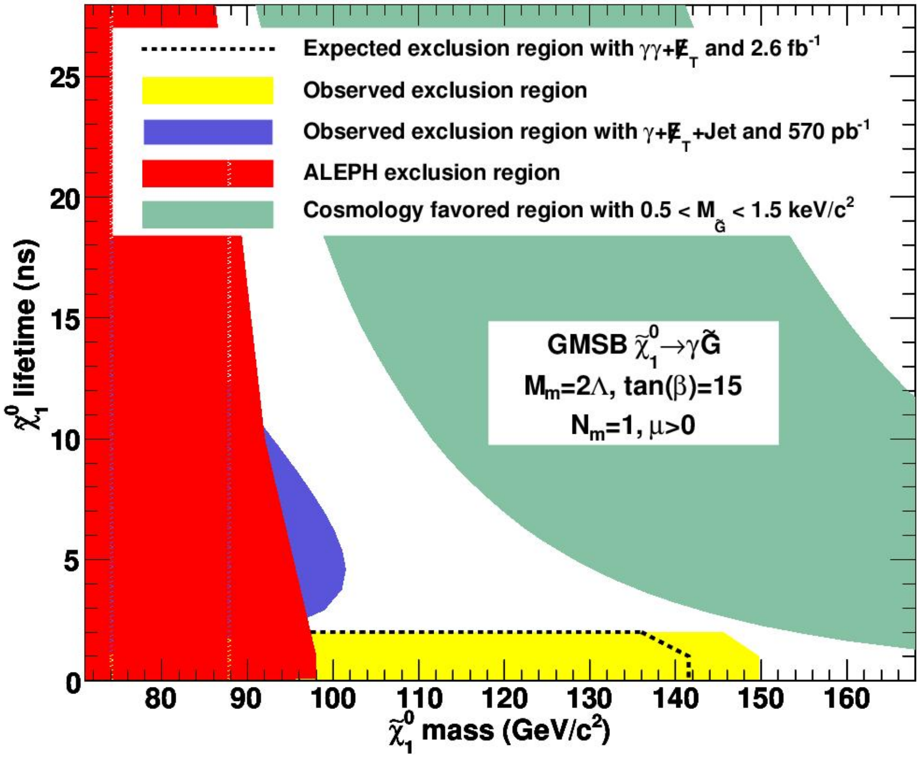

Figure 1.9: The predicted and observed exclusion regions from the ALEPH detector at LEP as well as the previous GMSB photon searches at CDF. The green shaded bands shows the cosmologically favored region where $0.5 < m_{\tilde{G}} < 1.5$ keV/c^2 [41].

A complementary set of searches were performed at the Fermilab Tevatron which focus on SPS-8 models where diagrams like the LHS of Figure 1.8 dominate. The low lifetime search was published in 2010 and assumed both $\tilde{\chi}_1^0$'s would decay inside the detector and the final state would appear as $\gamma\gamma+\not\!\!E_T+X$ where the X was required in the form of significant extra energy. The long lifetime search was performed in 2007 in the $\gamma_{delayed}$+$\not\!\!E_T$+jet final state [41]. The low lifetime result ($\tau_{\tilde{\chi}_1^0}$ <1 ns), shown in yellow, as well as a long lifetime search (1 ns < $\tau_{\tilde{\chi}_1^0}$ <20 ns), shown in blue using the delayed photon methods, are the result searches performed at CDF [41]. Figure 1.10 shows the results of a search for GMSB SUSY that was performed at the Tevatron's DØ experiment in the $\gamma\gamma$+$\not\!\!E_T$ using more luminosity, but who's final state is only sensitive for lifetimes less than ∼1 ns [44].

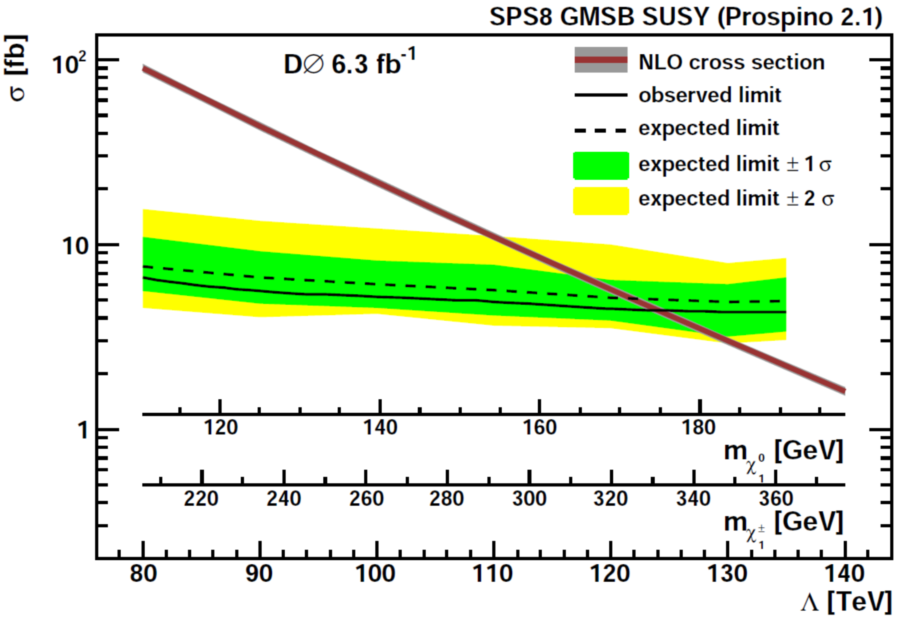

Figure 1.10: The predicted cross section and the 95% confidence limit expected and observed exclusion limit as a function of Λ from a search in $\gamma\gamma + \not\!\!E_T$ performed at the DØ experiment in 2010. This search assumes SPS-8 model parameters and thus makes the dominant production of SUSY particles gaugino pair production. The corresponding masses are shown for the lightest chargino $\chi_1^\pm$ and neutralino χ_1^0 [44].

A similar result at 3.5 times higher collision energies but with proton proton collisions and focusing on SPS-8 scenarios was done at the LHC in 2011 [42] as shown in Figure 1.11. These searches are different in that the sparticles are most often produced through strong production of squarks and gluinos. This search looked for the $\gamma\gamma$+$\not\!\!E_T + X$ in final state produced from squarks and gluinos, which decay down and eventually produce the photons, $\not\!\!E_T$ and other final state particles and these other high energy particles are required as part of the search. No evidence for SUSY is observed and limits are set in this scenario for $\tilde{\chi}_1^0$ lifetimes up to 3 ns for a neutralino mass $>$ 200 GeV/c^2 with 200 pb^{-1} of data as shown in Figure 1.11. While this search is directly comparable to the LEP and Tevatron results in that it assumes SPS-8 relationships, it is very different in that it presumes a squark-gluino production unlike the searches at the Tevatron which assume gaugino pair production. The comparison between the limited value as we move even slightly outside the SPS-8 assumptions as SPS-8 is only designed to simplify the displaying of results in terms of a model that is well specified. There is no compelling reason to believe that this particular set of choices is more likely to be observed in nature. Thus, while the parameter spaces shown for the searches are the same, the production mechanism assumptions for the LHC searches are different. We can think of them as being two different types of searches: ones where squarks/gluinos are too heavy to be produced (Tevatron and LEP are applicable only) and ones where squarks/gluinos are accessible (LHC, Tevatron and LEP are all applicable, but the LHC results are most sensitive).

While the searches described above exclude a great deal of minimal GMSB model scenarios, many of these limits may not apply if the assumptions made in the SPS mass hierarchies are relaxed. Thus, as we move out of the narrow SPS-8 interpretation these results can be considered to be covering different regions, or in some sense are complementary. However, we are left with the inescapable fact that no evidence for GMSB SUSY has been observed in any of these three searches. That being said, we also notice that these searches cover models in only the top half of Table 1.2 where the masses of all but the $\tilde{\chi}_1^0$ and Gravitino are out of reach of the collider

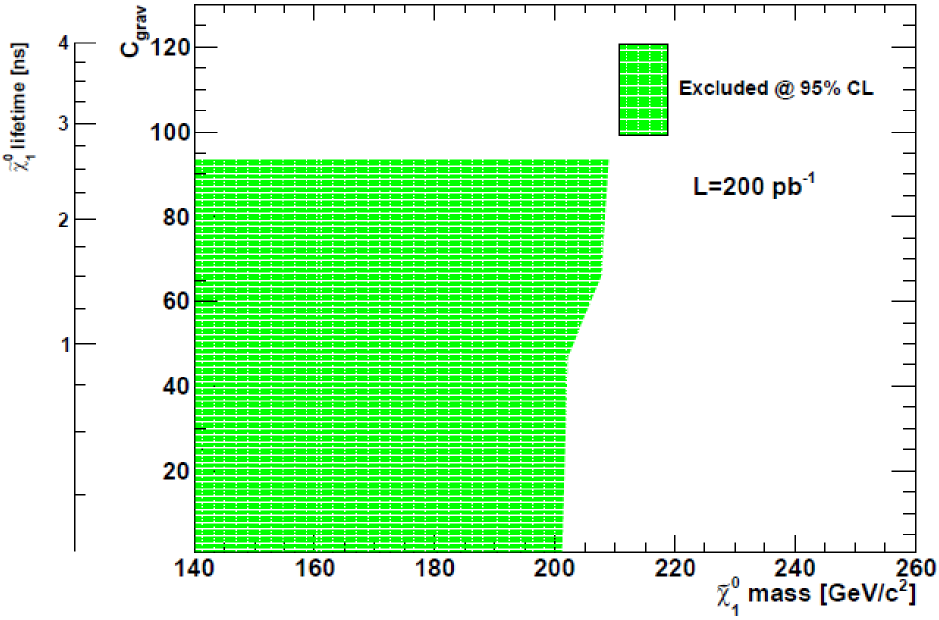

Figure 1.11: The observed exclusion regions from a GMSB search performed at the LHC in 2011 for lifetimes up to ∼3 ns for neutalino mass > 200 GeV/c^2 with 200 pb^{-1} of data. This $\gamma\gamma + \not{E}_T + X$ results are interpreted using SPS-8 model parameters which are dominated by squark-gluino production. This result is complementary to the searches performed at the Tevatron and LEP for low lifetime neutralinos in this scenario.

production energies. Before continuing, it is important note that there has been a search for exclusive $\gamma\gamma+\not{E}_T$ at CDF which did not uncover evidence for anomalous production [45].

With these results in mind, we note that there have been no published results on LNG searches for long-lived neutralinos making this a new and important window of opportunity. This provides a clear motivation to do a first search in the exclusive $\gamma_{delayed}+\not{E}_T$ final state as was first recommended in References [37] and [43]. With clear vision of what types of models to focus on, we will go into more detail about a preliminary search in this final state.

1.5 Overview of Searches for Long Lived Neutral Particles that Decay to Photons

Having motivated our search in the exclusive $\gamma_{delayed}+\not{E}_T$ final state, we turn to the details of how the search is done. We come back to the variable used to calculate t_{corr}, as defined in Equation 1.8 and consider what it will look like in a real detector. We then do a cursory summary of the typical backgrounds and their corrected time distributions as well as methods we will use in the exclusive $\gamma_{delayed}+\not{E}_T$ to measure and/or reject these backgrounds. This discussion will be especially useful as we look at some preliminary results in the next section. Note that this discussion follows the work done in [38] which was the first search for delayed photons by CDF in the $\gamma_{delayed}+\not{E}_T + Jet$ analysis.

For a promptly produced photon, with perfect measurements, $t_{corr} = 0$ ns. Since our detector is not in fact perfect this measurement has an intrinsic resolution which we have measured to be ∼0.65 ns and is thus well described by a Gaussian centered at $t_{corr} = 0$ as shown in Figure 1.12 (LHS). We refer to this distribution as the "right vertex" corrected time because it represents the timing distribution when we have correctly identified the origin of the collision which we measure experimentally as a "vertex". Photons from the decay of a long-lived $\tilde{\chi}_1^0$ would have $t_{corr} > 0$ and thus arrive at a time that is "delayed" relative to expectations from the SM as shown in Figure 1.12 (RHS). The t_{corr} variable allows for good separation between nanosecond-lifetime $\tilde{\chi}_1^0$'s and promptly produced SM photons[38]. This will be described in more detail in Section 2.2.3.

Unfortunately, there are other sources of events with large t_{corr} events which make our search more complicated. Specifically, the presence of other collisions occurring in the data-taking window that do not have anything to do with the produced photon, as seen in Figure 1.13, can lead to ambiguity in the selection of x_0 and t_0. When

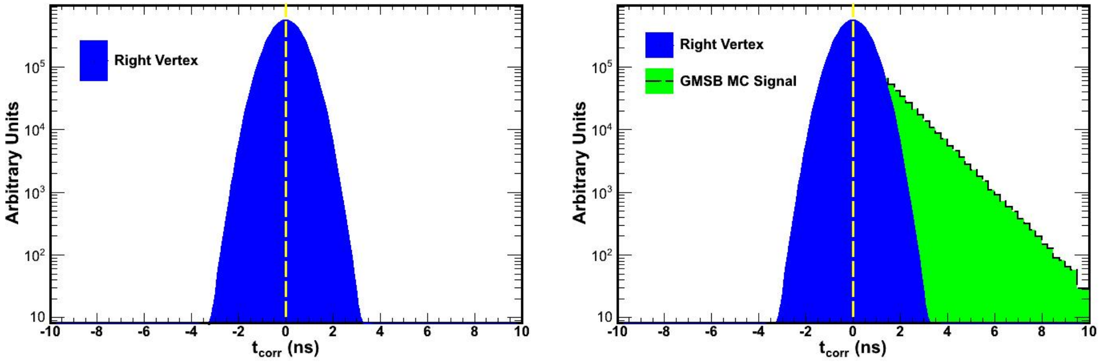

Figure 1.12: Monte Carlo example of the corrected time variable, t_{corr}, for both promptly produced photons (LHS) as well as photons from a simulated long-lived $\tilde{\chi}_1^0$ (RHS).

the incorrect initial interaction point (vertex) is selected in an event we call this a "wrong vertex" event. As will be discussed in Section 5.1, this results in the "smearing" out of the Gaussian distribution of the t_{corr} variable. The resulting RMS of the t_{corr} distribution becomes $\sim$2.0 ns where this number comes mostly from the variation in the time of collision between the protons and antiprotons, as well as timing resolution of the systems involved in measuring the initial and final positions. With this understanding of right and wrong vertices, we can see that when we select a single vertex for use in an event we will have some chance of having correctly assigned the t_0 and x_0 and some chance of having selected incorrectly. Thus the resulting corrected timing distribution will be the combination of the right and wrong vertex Gaussians as shown in Figure 1.14 where we include what a signal from $\tilde{\chi}_1^0 \rightarrow \gamma\tilde{G}$ would look like as well with a long lived $\tilde{\chi}_1^0$.

The second major background to our signal is from photon candidates that have nothing to do with the collision and originates from sources external to the detector, typically from 'cosmic rays'. These events are discussed in more detail in Section 4.2. For now it is sufficient to remark that since these events have nothing to do with the collision they effectively show up randomly in time and thus present a

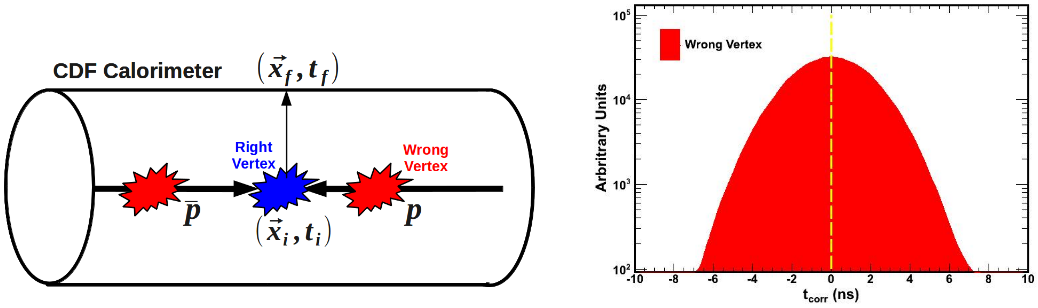

Figure 1.13: (LHS) Schematic showing how selecting a incorrect collision (i.e. wrong vertex) can cause an errant calculation of the time-of-flight ($\frac{|\vec{x_f}-\vec{x_i}|}{c}$) thus leading to a t_{corr} described by a (RHS) Gaussian with an RMS ∼2 ns for wrong vertices.

'flat' background signature in the t_{corr} distribution, as shown in Figure 1.14. A signal region, where we have the potential for separation between new physics and background sources, is readily seen between about 2 ns and 7 ns. Other regions are dominated by right vertex, wrong vertex, or cosmic rays. Each of which can be used to estimate the background rate in the signal region using data.

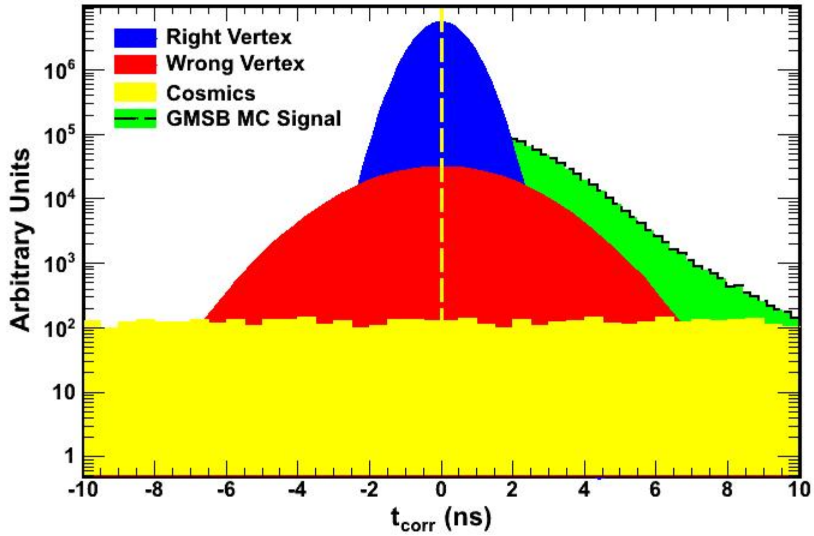

Figure 1.14: A toy simulation of t_{corr} including GMSB signal events along with a set of collision and non-collision background events. Here the right vertex (blue), wrong vertex (red), and cosmic ray (yellow) distributions are shown.

In the next section we present an overview of a preliminary search in the exclusive

γ+$\not\!\!E_T$ final state, but using simple background estimation technique and no rejection against subtle, yet insidious, backgrounds with large times.

1.6 2008 Preliminary Result

In 2008 a preliminary search looking for events that contain a single photon (identified using criteria described in Section 2.4.3) and $\not\!\!E_T$ (defined in Section 2.4.6) and little other activity in the detector was performed. This previous analysis focued on a search for new phenomena know as Large Extra Dimension [46] as it can have the γ+$\not\!\!E_T$ final state. No evidence for new physics was observed and the result was published in reference [47]. This search differed from the exclusive $\gamma_{delayed}$+$\not\!\!E_T$ final state in that the arrival time of the photon was not considered as a way to discriminate between SM and new phenomenon.

Following the publication of this result, even though this search was not optimized for a search for GMSB, the corrected time distribution for the sample of events was examined using the simple prescription assuming the symmetry in the t_{corr} distribution around t_{corr} = 0 ns, shown in Figure 1.14 for both the right and wrong vertex distributions. By exploiting the seemingly benign fact that only GMSB MC signal events were asymmetrically distributed about t_{corr}= 0 ns it seemed very straightforward to predict the number of events expected between 2 ns $< t_{corr} <$ 7 ns (signal region) by using the number of events from -7 ns $< t_{corr} <$ -2 ns. In fact this had been done in the first delayed photon search for $\gamma_{delayed}$+$\not\!\!E_T$ + Jet with the data being consistent with background expectations alone [41]. It was expected that this should have sensitivity based on a simplified, although independent, estimate of the sensitivity in the region 120 GeV/c^2 $< m_{h^0} <$ 160 GeV/c^2, 30 GeV/c^2 $< m_{\tilde{\chi}_1^0} <$ 80 GeV/c^2, and 1 ns $< \tau_{\tilde{\chi}_1^0} <$ 20 ns [43].

The results of this prelimnary search are shown in Figure 1.15. What can be seen

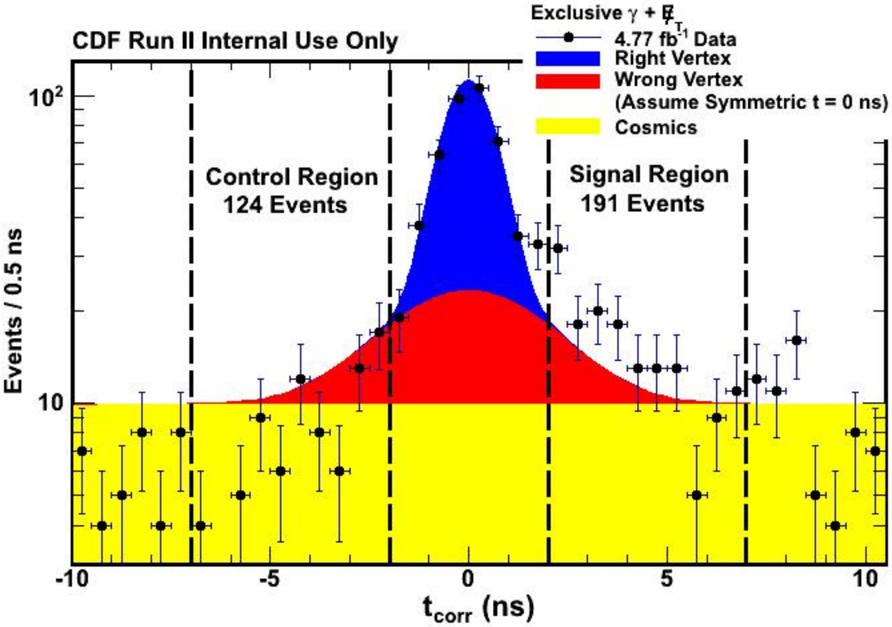

Figure 1.15: The result of a preliminary search for delayed photons performed in 2008 in the exclusive γ+$\not\!\!E_T$ final state showing an excess of events in the region 2 ns< t_{corr} < 7 ns above simple background estimation techniques.

in the corrected time distribution is a statistically significant excess of events in the region 2 ns< t_{corr} <7 ns relative to expectations. There are 191 events are observed in the signal region with a background prediction of only 124 events. Clearly, this is a very interesting result and demands a follow up with more data as well as cross-checks to the underlying assumptions of the analysis.

In many ways, this dissertation is the follow up to this reported excess. As discussed before it is possible that this result hints at the discovery of SUSY and possibly even the Higgs boson. However, extraordinary claims require extraordinary evidence. In particular we will describe the results of a thorough and systematic search for other sources of events which might produce large time photons in the exclusive γ+$\not\!\!E_T$ final state, as well as a study of the the validity of the background estimation techniques assumptions. In the next section we will lay out the outline for this analysis as we follow up on the intriguing excess observed and describe the new methods we developed for rejecting biased sources of SM events as well as for predicting the number of events from SM sources in the signal region.

1.7 Outline of the Search

This analysis is constructed to follow up on the intriguing excess that was observed in the exclusive $\gamma_{delayed}+\not\!\!E_T$ final state. We focus on doing a search in as model-independent a method as possible. For this reason, we do not focus on GMSB or Higgs specifically, rather we focus on the model of the production of a heavy neutral object that decays, after a few nanoseconds, to a photon plus something that leaves the detector without depositing any energy. While this signature is embodied in $h^0 \rightarrow \tilde{\chi}_1^0\tilde{\chi}_1^0 \rightarrow \gamma\tilde{G}\gamma\tilde{G}$, we use nothing about this decay except that the $\gamma_{delayed}+\not\!\!E_T$ final state should not be accompanied by any other high energy final state particle.

That being said, this interpretation is amenable to GMSB SUSY scenarios where the $\tilde{\chi}_1^0$ has long enough lifetime to produce a delayed photon and assume that only $\tilde{\chi}_1^0$ pairs are produced in the final state thus making the most sensitive channel the exclusive $\gamma_{delayed}+\not\!\!E_T$ [37]. Due to the length requirements (of the time spent as a Ph.D. student, not dissertation page length), we have focused on a full follow-up of the preliminary result rather than the interpretation of any final result in terms of a new physics prediction. Our analysis strategy is to study a large number of high energy proton antiproton collisions and to select interactions where the collisions produced $\gamma+\not\!\!E_T$ and little other activity in the detector. We next examine the corrected time distribution of those photons in order to look for evidence that the photons' source is non-SM in origin. As previously mentioned, the dominant backgrounds for the exclusive $\gamma_{delayed}+\not\!\!E_T$ final state comes from cosmic rays that interact with the detector producing a fake photon signal in coincidence with a collision as well as wrong vertex events where we incorrectly assign the initial time and time of flight for the photon found in the detector.

One of the most important facts uncovered during the study of the SM backgrounds using Monte Carlo techniques is that the wrong vertex timing distribution is not symmetric about $t_{corr} = 0$ ns. This makes the analysis far more complicated because this leads to the necessity to develop a new method for estimating the mean of the wrong vertex of our final sample of exclusive $\gamma + \not\!\!E_T$ events. A significant portion of this analysis is dedicated to understanding the causes of bias in wrong vertex events, and with that understanding now fully in hand it is not hard to create biased samples. For example, the top part of Figure 1.16 shows the corrected timing distribution for a very pure sample of events of known SM origin, $W \rightarrow e\nu \rightarrow e + \not\!\!E_T$, using the assumption of a symmetric background timing distribution and the identical selection criteria as the 2008 preliminary result but choosing electrons instead of photons. Clearly the assumption that the wrong vertex timing distribution is symmetric about $t_{corr} = 0$ ns does not accurately model the data. SM backgrounds do not necessarily have the same number of events in the control region as the signal region. The bottom of Figure 1.16 shows the timing distribution if we release the assumption that wrong vertex distribution is symmetric about 0.0 ns, but keep the Gaussian description of the data and allow the fit to find a value of the mean that best matches the data. What we can see here is the double Gaussian assumption of the corrected time distribution does accurately model the SM background and in this case has a wrong vertex mean ($< t^{WV}_{corr} >$) of 0.45 ns. While we now understand why the mean does not have to be zero, the distribution should be well approximated by a Gaussian with an RMS of 2 ns. The observed fact that $< t^{WV}_{coor} >$ is not zero complicates the analysis. We need new ways of predicting the number of events from SM sources in the signal region.

With the knowledge that SM collisions can have biased times, it is important to do a systematic study of all types of events that have such a bias. With this in mind, a major focus of this dissertation revolves around two important and related tasks. The first of these tasks is to understand and mitigate the contributing factors that cause SM backgrounds to give large times. As we will see, we have uncovered a good understanding of the effects that both produce large values of $< t_{corr}^{WV} >$ as well as effects that can cause t_{coor}^{WV} distribution to be asymmetric around zero. We will describe the methods to mitigate these factors and leave our data with only sources which are symmetric and have small mean values. The second task is to develop a method to predict the number of events in the signal region from SM sources now that the simple background method doesn't work. Specifically, to measure $< t_{corr}^{WV} >$ from data in a reliable way.

New features to this analysis since the preliminary result in 2008 are as follow:

1. **Adding Additional Data**:

   We have added 25% more data than was used in the initial 2008 result giving us 6.3 fb^{-1} of data analized. The data sample is described in Section 2.3.

2. **Robust Timing Calibrations**:

   A new and more robust set of timing calibration procedure has been developed that does not suffer from the wrong assumptions of previous methods. This procedure is described in detail in Section 3.

3. **Additional Cosmic Ray Rejection**:

   Two new rejection parameters are implemented in order to help reject the dominant background from cosmic rays that interact with the detector producing a fake photon candidate in coincidence with a collision. This is described in Section 4.

4. **Identification and Minimization of Pathological Event Reconstruction**:

   A systematic set of studies have been done to identify and minimize many pathological reconstruction problems in SM events that lead to a positively biased event times when a wrong vertex is selected. As a result, a suite of new rejection methods have been implemented. These studies and rejection methods are detailed in Section 5.

5. **New Data-Driven Background Estimation**:

   Finally, a new background estimation method is developed and presented which shows that it is possible to derive the underlying wrong vertex mean and thus make a proper prediction of the number of events we expect in the signal region from SM sources. The details, validation, and results of this background estimation method is shown in Section 6.

With all these new tools will will have a robust and reliable search that will be able to answer many of the questions about the search results from 2008. These results will be presented in Section 7 along with a comparison to the 2008 preliminary result.

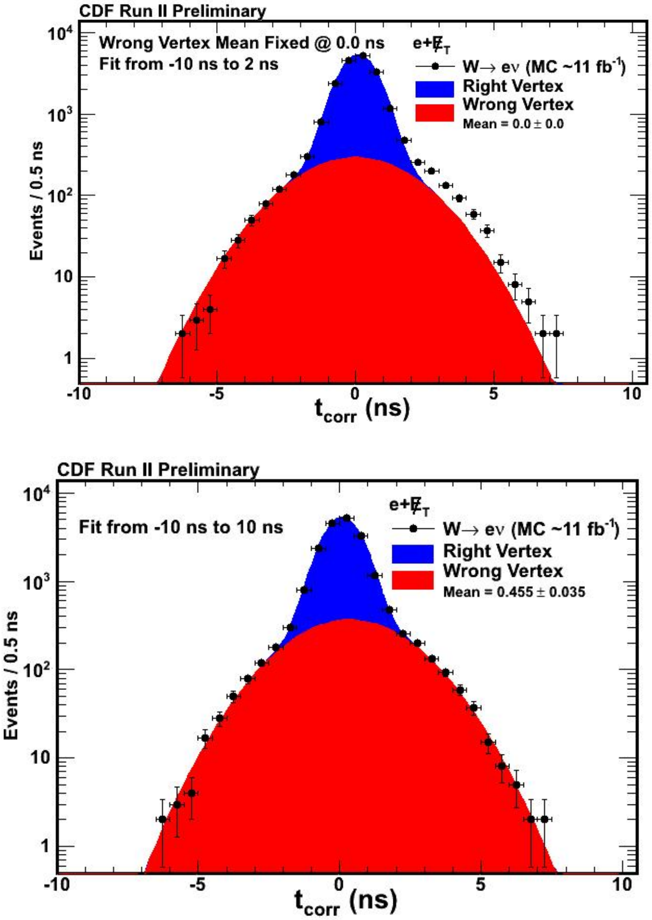

Figure 1.16: The t_{corr} distribution for a pure sample of SM W$\rightarrow e\nu \rightarrow e+\not\!\!E_T$ events in data where we ignore the electron track and allow the algorithms to pick the highest ΣP_T vertex. In this case, the wrong vertex is often selected and we see the timing distribution as being the sum of right vertex and wrong vertex events. In the top plot we show a fit to the data in the region -7 ns $< t_{corr} <$ 2 ns where we assume $< t_{corr}^{WV} >= 0$ ns. We can see that this is clearly not a good description of the data. The bottom plot shows the fit when we fit over the entire timing distribution and allow $< t_{corr}^{WV} >$ to float in the fit. The agreement between the data and the double Gaussian prediction is excellent.

2. EXPERIMENTAL TOOLS

This section describes the experimental apparatus used for this analysis. This includes the Fermilab accelerator complex, a description of the detector that surrounds the collision point and many of the algorithms used to identify our $\gamma+\not{E}_T$ events. We begin with a description of the Fermilab accelerator complex, most importantly the Tevatron circular particle accelerator [48]. The Tevatron collided proton-antiproton beams at energies which were, until 2008, the most energetic collisions in the world and continued data taking in collider mode until September 2011. Surrounding one of the collision points is the experiment known as the Collider Detector at Fermilab (hereafter referred to as CDF) which recorded the energy and trajectory as well as identified the various particles produced by the proton-antiproton collisions. The various subsystems most relevant to this analysis will be described in greater detail along with details about the information they report. The readouts of these various subsystems allow us to filter out, in real time, candidate photons from the millions of collisions every second that are being produced. From this subset of events we then search for evidence of new physics by selecting candidate collisions with the signature of $\gamma+\not{E}_T$. We then use information about the arrival time of the photon and the collision time to see if any arrive delayed relative to expectations and thus possess a signature of coming from new physics. With this in mind, we turn our discussion to the Tevatron, the CDF detector, and the process by which collisions are read out of the detector in general and reconstructed in particular.

2.1 The Fermilab Tevatron

We begin by summarizing Fermilab's accelerator chain that produces a beam of protons (p) and antiprotons ($\bar{p}$) suitable for collisions in the Tevatron. The accelerator chain is described in great detail in Reference [48, 49], but we give a brief overview here. Fermilab's accelerator chain is shown schematically and in aerial view in Figure 2.1. The particles begin as a hydrogen gas that is processed to make negatively ionized hydrogen with a small energy spread (keep them together in space and time) in a Cockcroft-Walton accelerator [48]. The ions are then passed to a linear accelerator (Linac) that accelerates the ions to 400 MeV and then passes them through a carbon foil in order to strip off the electrons. The protons are then passed to the next part of the accelerator known as the "booster". The booster consists of 18 Radio Frequency (RF) ferrite-tuned resonators, commonly referred to as "cavities" which accelerates the protons to 8 GeV as well as brings them closer together, commonly referred to as "bunching". During the bunching process the particles are captured into 37.7 MHz "buckets" before being passed to the next part of the accelerator known as the "Main-Injector". The Main-Injector accumulates, accelerates, and stores protons, taking them to energies of 150 GeV and combines the bunches from the booster into a single bunch. This process of bunching the protons is then repeated until a total of 36 bunches of protons have been produced. Taken together this set of 36 bunches is commonly referred to as a "train". These protons can now be passed to the final part of the accelerator chain, namely the Tevatron. In addition to providing protons to the Tevatron, the Main-Injector provides a source of protons that can be used in order to produce antiprotons. The antiprotons are created by accelerating the protons in the Main-Injector to 120 GeV and then colliding them into a target of nickel alloy. The byproduct of the collisions with the nickel target is a varied array of particles, from which antiprotons are selected and decelerated (reducing their momentum spread) in a part of the accelerator known as the "debuncher". From the debuncher the antiprotons are then passed to another accelerator system known as the "Accumulator". The Accumulator is located in the same tunnel and, as the name suggests, is where the antiprotons are accumulated and where they undergo stochastic cooling before being passed to another system known as the “Recycler”. The Recycler is located in the same tunnel as the Main-Injector and uses permanent magnets to store high intensity beams of 8 GeV antiprotons. It is in the Recycler where “electron cooling” is used to allow a more intense source of antiprotons to be produced. Electron cooling introduces a low emittance electron beam collinear to the antiproton beam and through momentum transfer the antiprotons are “cooled”. The antiprotons are then bunched into 36 bunches and accelerated to 150 GeV. When this process is complete, there are 36 bunches of protons and 36 bunches of antiprotons ready to be transferred (“injected”) into the Tevatron main ring to be used for high energy physics collisions[48, 49]. Within the main ring (typically just referred to as the Tevatron), which is a superconducting circular accelerator, the proton and antiproton beams are accelerated from 150 GeV to 980 GeV. The Tevatron consists of 774 superconducting dipole magnets and 240 quadrupole magnets. The former are used to bend the beam around the 3.9 mile circumference ring and the latter are used to focus the beams while electrostatic potentials accelerate the particles. The beams typically consist of $\sim 3 \times 10^{11}$ protons/bunch and $\sim 7 \times 10^{10}$ anti-protons/bunch during typical operations. These beams couter rotate in the Tevatron during data taking and are made to collide at two points along the ring, at the center of the CDF and DØ detectors as illustrated in the top of Figure 2.1. The beams remain for several hours during collisions (often referred to as a “store”). The smallest unit of data taking, referred to as a “run”, is some interval of uninterrupted time during a store (or stores) where no change in detector setup or data-acquisition system has occurred. The beams collide at a center of mass energy of 1.98 TeV every 396 ns with a typical RMS in z of $\sim$28 cm, where $+z$ is defined along the direction of the proton beam, and an RMS in collision time of $\sim$1.28 ns. A basic summary of the various Tevatron parameters that existed during the data taking for this dissertation, colloquially referred to as "Run II", is presented in Table 2.1. With a good understanding of the collisions, we move to the detector that surrounds the collision point, and eventually on to the algorithms that help us identify $\gamma+\not\!\!E_T$ events.

Parameter (Units)	**Value**
Energy per Beam	980 GeV
Number of Bunches	36
Bunch Spacing	396 ns
Protons per Bunch (N_p)	$\sim 3\times 10^{11}$
Antiprotons per Bunch ($N_{\bar{p}}$)	$\sim 7\times 10^{10}$
Collision Point RMS in z	$\sim$28 cm
Collision Point RMS in time	$\sim$1.28 ns

Table 2.1: Summary of the Tevatron accelerator parameters during "Run II" data taking.

2.2 The Collider Detection at Fermilab

The CDF detector is described in detail in Reference [50] and shown in Figure 2.2. We summarize here portions of the detector most relevant to this analysis. CDF is a forward-backward and cylindricaly symmetric multi-purpose detector that surrounds the collision point and is designed to identify and measure the 4-momentum of the particles produced in a $p\bar{p}$ collision. CDF makes use of a cylindrical coordinate system where the positive z axis is defined along the direction of the incoming proton beam with the origin at the center of the detector, ϕ is the azimuthal angle, and θ_0 is the polar angle relative to the z axis and defined with respect to $z = 0$ cm. Additionally, a useful angular variable, $\eta_{detector}$, known as detector pseudorapidity, that is used throughout the remainder of the dissertation is defined as

$$\eta_{detector} = -ln(tan(\frac{\theta_0}{2})). \tag{2.1}$$

This variable is useful in collider physics because it describes the particles angle relative to the beam axis and the differences between two particles pseudorapidity is invariant under Lorentz boosts along the z axis. Additionally, event pseudorapidity is defined relative to the collision interaction point (event) as

$$\eta_{event} = -ln(tan(\frac{\theta_{event}}{2})). \tag{2.2}$$

where the positive z axis is defined along the direction of the incoming proton beam and θ_{event} is the polar angle is calculated from our best measured position of the collision z. Within the central part of the CDF detector, ($|\eta_{detector}| < 1.1$), lies the main subdetectors used in this analysis. In the central region a 1.4 T magnetic field along the z direction is generated by a superconducting solenoid 1.5 meters in radius and 4.8 meters long. Within this magnetic field various tracking detectors are used to measure the trajectory of the charged particles produced during collisions. The magnetic field allows for a measurment of the sign of the charged particles, as well as their momentum as they traverse the tracking chamber. Surrounding the tracking chambers in concentric sub-detector systems are the various energy measuring detectors, (calorimeters), and chambers used to measure and identify muons which are located outside of the solenoid and provide further particle identification and energy measurements. The combinations of the various detector components allow for the identification of particles such as photons, electrons, muons, and objects known as “jets” originating from quarks and gluons. These detectors also allow us to measure the energy and momentum of the particles and the overall imbalance of energy in the event, $\not{E}_T$ which is used to identify particles that leave the detector after only minimal interactions, such as neutrinos. The various identification criteria used in this analysis are described later in Section 2.4. In the following sections we characterize in greater detail the subdetectors having the most impact on this analysis. We begin with the inner most tracking detectors and work our way out radially to the calorimeters and eventually the muon chambers. After this description we will discuss how each is used as part of the reconstruction of a collision and identification of our final state particles.

2.2.1 The Tracking Systems

The part of the CDF detector closest to the beam line, as shown in Figure 2.2, is made up of a set of tracking detectors used to determine the 4-momentum and charge of charged particles passing through the various subsystems by using their measured paths and curvatures in the magnetic field. This allows us to measure the origin of the tracks in both space and time (z_0 and t_0) which are expected to come from the primary collision. Groupings of the particles' trajectories are projected back to the beam line and allow reconstruction of both the position and time of the interaction in what we refer to as the event vertex. The tracking system includes two detectors: an inner Silicon VerteX detector (SVX) and a Central Outer Tracker (COT) which surrounds it. The SVX detector is described in greater detail in Reference [51], but we summarize the important features here. The SVX spans radially from the beam pipe from 2.5 cm$< r <$10.6 cm and covers a distance in the z-direction of 175 cm centered at the middle of the detector. The SVX consists of a silicon microstrip system used for precision position measurements which allow for 3D tracking reconstruction of trajectories. The SVX provides precision position location information for where the particles interact in the detector ("hits") that can be used in conjunction with the COT for high quality tracking as well as standalone tracking for charged particles independent of the COT at high values of $|\eta_{detector}|$. While the SVX provides a better spatial resolution on individual tracks (which is also used for vertexing), there is no timing information from the SVX system and thus it does not provide a t_0 measurement or improve upon the measurement of t_0 when it is used in conjunction with COT tracks.

The COT chamber is described in Reference [50], but we highlight the important features here. The COT surrounds the SVX system and is a cylindrical open-cell drift chamber that spans a radius of 44 cm $< r <$ 132 cm and covers a distace in z of 310 cm extending to $|\eta_{detector}|$ ≈1.0. The COT is filled with a 50:50 mix of argon and ethane gas along with a small admixture of isopropyl alcohol and oxygen. This provides the COT with a maximum drift time of 100 ns (small compared to the 396 ns bunch spacing in the Tevatron). Within the COT the wires are grouped into sections of 96 layers of sense wires which are grouped into eight âsuperlayersâ consisting of 12 wires each. As shown in Figure 2.3 the superlayers alternate between axial wires (running parallel to the beam line) and stereo wires that are tilted by 3 degrees with respect to the beam line. This allows for a high quality measurement of the kinematics of the track in the magnetic field, it's charge, as well as its initial position and time at the beam line. As charged particles pass through the chamber they ionize the gas leaving a trail of electrons which are attracted to the sensor wires by the electric field generated by the potential wires and cathodes. This allows for a determination of the time that the charged particle passed near the wire in three dimensions with a hit resolution of 140 μm and 0.27 ns. Combining hits along the trajectory allows for the reconstruction of charged particle trajectories with a momentum resolution of $\sigma(P_T)/P_T^2 \approx 0.3\%$ (GeV/c)$^{-1}$ and a track z position at the beam line of ∼0.22 cm. The time information associated with each hit allows for a timing measurement of the track along the trajectory and can also be used to derive the initial time (t_0) that the particle was produced. The COT is found to have a t_0 resolution for well measured tracks to be ∼0.5 ns [50].

As will be discussed further in Section 2.4, the z_0 and t_0 information obtained from the combined SVX/COT is used to create verticies that are produced along the beam line indicating where the primary collision of the proton and antiproton was likely to have occurred.

2.2.2 Electromagnetic Calorimeter

The calorimeter system at CDF is used to measure the energy and position of particles at large radii from the beam line as well as provide particle identification and a full measurement of the $\not\!\!E_T$. This becomes of particular significance when deciding which events to record from the detector based on energy measurements such as is done in this analysis. The system itself is is described in detail in Reference [50], and we provide an overview here. The calorimeters are housed just outside the solenoid and spans a radius of approximately 150 cm $< r <$ 180 cm. The calorimeter is used to measure the energy deposited by particles out to $|\eta_{detector}| < 3.64$. Since we want high quality measurements and identification of the photons in this analysis, this analysis restricts itself to only considering photons that come from the "central" ($|\eta_{detector}| < 1.0$) region. Restricting ourselves to photons in this region allows us to take advantage of the tracking having full coverage of the calorimeter and thus is the best for photon identification. The central calorimeter is constructed using a tower structure projected to the most probable collision point at the center of the detector. Each tower spans 15° in ϕ and $\sim$0.10 in $\eta_{detector}$, as shown in Figures 2.2 and 2.4 where all towers at the same ϕ on one side of the detector are physically grouped into what is referred to as a "wedge". Within each calorimeter tower there are two components, known as the ElectroMagnetic (EM) and the hadronic (HAD) components. During normal beam operations both the electromagnetic and hadronic calorimeter systems integrate the energy deposited in each tower of 132 ns time intervals that contain the collision time. The EM portion of a central EM calorimeter tower is known as the CEM and it lies closest to the beam line. In the CEM any interaction of an electromagnetic particle (like from a photon or electron) will deposit the overwhelming majority of its energy in this compartment. The CEM uses 23 lead and polystyrene scintillator layers alternating in the radial direction with ∼5 mm thickness and providing 21 radiation lengths (X_0) that almost fully contain the energy cascade showers of most electromagnetic particles such as photons and electrons. Light deposited in the scintillators strips is directed out in wavelength shifting fibers to two photo multiplier tubes (PMTs) located on opposite sides of each tower which provide an energy and a timing measurement. A deposition of a large amount of energy in one or more towers of the calorimeter is commonly referred to as a "cluster". For clusters which deposit most of their energy in the EM we find a resoltuion in the CEM of $\frac{\sigma(E)}{\sqrt{E_T}} = 0.135$. At this point it is useful to define the transverse energy (E_T) as it is used throughout this dissertation in different, and non-standard, ways.

- **E_T^0: Transverse Energy Relative to $z = 0$**

  The variable E_T^0 is defined as $E \cdot sin\theta_0$ where E is the energy deposited in the calorimeter and θ_0 is calculated from $z = 0$ cm at the beamline to the z position of the centroid of the energy location in the calorimeter.

- **E_T^{vtx}: Transverse Energy Relative the Highest $\Sigma \mathrm{P}_T$ Vertex**

  The variable E_T^{vtx} is defined as $E \cdot sin\theta_{vertex}$ where E is the energy deposited in the calorimeter and θ_{vertex} is calculated from z position of the highest $\Sigma \mathrm{P}_T$ vertex to the z position of the centroid of the energy location in the calorimeter. We note that the highest $\Sigma \mathrm{P}_T$ vertex is typically due to the collision that produced the energy in the detector, but this is not always the case.

A proportional strip and wire chamber, known as the Central Electron Strips (CES), is located at a depth of $\sim 6X_0$ in the CEM corresponding to the "shower maximum" for electrons and photons and is described in detail in [50]. Within each tower the CES consists of 256 cathode strips running in the ϕ direction and measure the position and profile in z with a resolution of $\sim$ 2 mm as well as 128 anode wires running in the z direction that measure the position and profile in the ϕ with a resolution of $\sim$ 2 mm in the local X coordinate. The CES is located at a radius of $\sim$ 184 cm from the beam line. The CES also provides an energy measurement with a resolution of $\frac{\sigma(E)=0.74}{\sqrt{E_T}} + 4\%$ that will be used later as well. Radially just outside the EM is the HAD calorimeter, which has the same tower-wedge geometry as the EM but instead uses iron sampling in order to measure the energy and shower of hadronic particles. Using both the EM and Had we can identify and measure the energy of jets with an energy resolution of $\frac{\sigma(E)}{E} = 0.1E_T + 1.0$ GeV. Considering the entire calorimeter, a full measurement of the $\not{E}_T$ can be typically measured to a few GeV.

2.2.3 EMTiming System

One system that plays a central role in this analysis is the ElectroMagnetic calorimeter Timing system (EMTiming system) which records the time of arrival of the high energy particles particles, with $|\eta_{detector}| < 2.1$. This system is described in more detail in Reference [52] and we provide a summary of this system here. In particular it provides a measurement of t_f from Equation 1.8 and can help us separate new physics signals from SM and non-collision backgrounds. Additionally, this same handle allows us to estimate the rate at which these backgrounds contaminate our searches. This will be described in greater detail in Section 4, 5, and 6. Figure 2.5 shows a schematic of the signal processing that measures the arrival time using the signal from the energy in the electromagnetic shower. The EMTiming system is attached to the outputs of the PMT's which collect the scintillated light from the interaction in the calorimeter on opposite sides of each tower in the CEM and convert this energy into an analog signal. This signal is then sent to a transition board and an Amplifier-Shaper-Discriminator which converts the analog signal into a digital signal using fixed-height discriminators. This digital signal is the sent to time-to-digital converters (TDCs) for a time measurement that is then read out by the CDF data acquisition system described in Section 2.4. The EMTiming system is observed to be 100% efficient for energies above 3 GeV in the CEM with a system resolution of ∼0.5 ns [52]. The calibration and overall uniform performance of the EMTiming system is discussed in greater length in Section 3, but is worth noting that the system has performed with nearly 100% efficiency and negligible downtime since its installation and commissioning in the fall of 2004. This translates to ∼6,600 hours of of live time or over 13 million PMT-hours of successful running.

2.2.4 Muon System

Located radially behind the calorimeter is the muon identification system. The muon system is a series of 4 layer, single-wire proportional drift chambers descirbed in greater detail in Reference [53]. The muon chambers are filled with a 50-50 mix of Agron-Ethane gas at atmospheric pressure and have a drift time of $\sim 1\mu s$. The system provides a resolution of ∼0.6 mm in the $r - \phi$ direction and about 10 cm in the z direction with nearly 100% hit efficiency[53]. In the region $|\eta_{detector}| < 0.6$, planar drift chambers inside (CMU) and outside (CMP) the magnets return yoke are used to detect muons with $P_T >$1.4 GeV. Drift chambers between $0.6 < |\eta_{detector}| < 1.0$ with a conical geometry (CMX) and "Intermediate Muon Detectors" cover the region $1.0 < |\eta_{detector}| < 1.5$ for detection of muons.

When a muon passes through each layer in this system it creates a series of "hits" which can be combined using an algorithm that searches for evidence of minimum ionizing particles that travel directly through the muon chambers. Combinations of hits that are consistent with this signature are identified as a "muon-stub". For collision based-muons, if there is a track pointing to a muon-stub this is identified as a collision muon. As will be discussed later, particles coming outside the detector, such as from cosmic rays, can produce a muon stub as they traverse the muon chamber on their way to deposit energy in the EM calorimeter and be identified as a photon candidate. In this case we will find a muon-stub (with no associated track) near a photon candidate. Since the muon chambers cover most of the detector this system provides an important tool in rejecting our cosmic ray backgrounds. This special case is descibed in detail in Appendix A.

2.3 The Data Acquisition, Trigger Systems, and Good Run List

Collisions occur at the center of the CDF detector every 396 ns making the selection and storage of useful physics events while rejecting uninteresting collisions a formidable task . The Data AcQuisition system (DAQ) at CDF, shown in Figure 2.6 and described in greater detail in Reference [54], performes this task with the necessary rejection rate of approximately 10^6:1 as only about 100 events per second can be written to record at the average logging rate of $\sim$23 MB/s.

To this end the CDF DAQ was built as a three-level trigger system to successively reduce the event logging rate. Each level is creatively referred to as Level 1 (L1), Level 2 (L2), and Level 3 (L3). The first two levels consist of custom built hardware which allowes a gradual reduction of the event rate to <50 kHz at L1 and to 300 Hz at L2. Level 1 makes decisions based on simple physics quantities using a subset of information from the detector. Level 2 uses a combination of hardware and software to perform a limited event reconstruction and chooses whether or not to accept events based on calorimeter algorithms, shower information, and combined tracking information. For each event accepted by L2, the data from all the various subdetectors is combined into a single event by the Event Builder [55] and passed to L3. Level 3 consists of a farm of computers that does a full event reconstruction and selects events based on a full (albeit preliminary) set of information. L3 filters the data coming from the event builder to 100 events per second and then sends that data to be stored on computer disks. The DAQ system is designed such that there is no or minimal loss of data (no dead time). While there are many different types of events selected for readout, the events selected for this analysis are selected by a set of 3-level trigger requirements summarized in Table 2.2, and referred to as the "WNOTRACK" trigger (pronounced W no track). This selection requires a deposition of energy in the EM calorimeter (which can be seen as a very loose selection criteria for a photon candidate) and $\not{E}_T$ to be present in the event. As the name suggests, this trigger was originally used as a backup trigger for selecting $W \rightarrow e\nu$ events without relying on tracking measurements. We use this trigger in this analysis primarily because it is one of the only triggers available for a photon selection without the CES-χ^2 requirements. The CES-χ^2 measures the lateral shape of the energy deposition at shower maximum as measured in the CES strips and wires and compares this to test beam data using a χ^2 test. Originally designed to help reject photon pairs from π^0 decays, this requirement has been found to be inefficient for photons from long-lived particles [38]. Events passing the full set of WNOTRACK requirements are then written to permanent storage to be analyzed in greater detail later. This trigger has been found to be nearly 100% efficient [56] for electrons and photons passing our final event selection requirements.

The L1 requires to have greater than 8 GeV of energy deposited in the EM-

Object Type	**Trigger**		
	Level 1	**Level 2**	**Level 3**
Electromagnetic Cluster	≥ 1 Central EM Cluster $E_T^0 > 8$ GeV $\frac{HAD(E)}{EM(E)} < 0.125$	$\lvert\eta_{detector}\rvert < 1.1$ $E_T^0 > 20$ GeV $E_T^{SeedTower} > 8$ GeV	≥ 1 EM Cluster $E_T^0 > 25$ GeV $\frac{HAD(E)}{EM(E)} < 0.125$
$\not\!\!E_T$	$\not\!\!E_T > 15$ GeV $\Sigma E_T > 1$ GeV		$\not\!\!E_T > 25$ GeV

Table 2.2: Online event selection for the WNOTRACK trigger. The variables found in this table are described in greater detail in Appendix B.

calorimeter tower used in the trigger and to have $\frac{E_{Had}}{E_{EM}} < 0.125$, in order to reject hadronic jets, as well as $\not\!\!E_T \geq 15$ GeV. L2 requires that the calorimeter clustering be central ($\eta < 1.1$) and the transverse energy $E_T > 20$ GeV. Finally, the L3 requirement for E_T and $\not\!\!E_T$ become ≥ 25 GeV.

In addition to this primary trigger, we also allow the logical *or* of a number of other associated photon triggers which all overlap with the requirements of the WNOTRACK trigger. We use these additional triggers to help ensure that we come as close as possible to 100% efficiency for selecting $\gamma+\not\!\!E_T$ candidate events. The summary of these other triggers can be found in Table 2.3.

Events constituting the data sample analyzed for this dissertation represent data taken from approximately December 2004, when the EMTiming system was fully commissioned, to June 2010 which is about 60% of the full data taking period. In conjunction with the triggering system, a list of data taking periods for which all the necessary subsystems are functioning properly is established in what is known as a “Good Run List”. In the this analysis we use a “Good Photon Run List” [57] which requires that the CEM, CES, COT, SVX, and Muon subsytems were all operational during data taking. Moreover, we apply a unique GoodEMTiming Run List that disregards runs where the EMTiming system was not functioning

Object Type	**Trigger**		
	Level 1	**Level 2**	**Level 3**
ZNOTRACK			
Electromagnetic Cluster	$\geq$ 1 Central EM Cluster $E_T^0 > 8$ GeV $\frac{HAD(E)}{EM(E)} < 0.125$	$\geq$ 2 EM Cluster $\lvert\eta_{detector}\rvert < 1.1$ Both w/ $E_T^0 > 16$ GeV Both w/ $E^0_{T SeedTower} > 8$ GeV	$\geq$ 2 EM Cluster Both w/ $E_T^0 > 16$ GeV $\frac{HAD(E)}{EM(E)} < 0.125$
SUPERPHOTON70			
Electromagnetic Cluster	$\geq$ 1 Central EM Cluster $E_T^0 > 10$ GeV	$\lvert\eta_{detector}\rvert < 1.1$ $E_T^0 > 70$ GeV $E^0_{T SeedTower} > 8$ GeV	$\geq$ 1 EM Cluster $E_T^0 > 70$ GeV $\frac{HAD(E)}{EM(E)} < 0.2$
PHOTON25ISO			
Electromagnetic Cluster	$\geq$ 1 Central EM Cluster $E_T^0 > 8$ GeV $\frac{HAD(E)}{EM(E)} < 0.125$	$\lvert\eta_{detector}\rvert < 1.1$ $E_T^0 > 21$ GeV $E^0_{T SeedTower} > 8$ GeV $E_T^{ISO} < 3$ GeV $\frac{HAD(E)}{EM(E)} < 0.125$	$\geq$ 1 EM Cluster $E_T^0 > 25$ GeV $\text{Iso}^{Total} < 2.0$ $\chi^2 < 20$ $\frac{HAD(E)}{EM(E)} < 0.055$

Table 2.3: List of additional triggers accepted on the logical *or* of the WNOTRACK trigger. The variables found in this table are described in greater detail in Appendix B.

properly (this accounts for <0.1 fb^{-1} reduction in luminosity). We furthermore require that all the runs within the good run lists must have an integrated luminosity $\geq 100\ \text{nb}^{-1}$ to ensure there are sufficient statistics to calibrate over that given run period (again resulting in only a $< 0.1\ \text{fb}^{-1}$ reduction in luminosity). After these various requirements the data analyzed corresponds to an integrated luminosity of $6.3 \pm 0.4\ \text{fb}^{-1}$ as shown in Table 2.4, using the standard CDF luminosity uncertainty [58].

Period	Run Range	SAM #	$\approx$ Luminosity (pb^{-1})
1-4	190851-203799	bhelbh	460
5-10	203819-233111	bhelbi	1020
11-13	233133-246231	bhelbj	660
14-17	252836-261005	bhelbk	410
18-28	261119-289197	bhelbm	3030
29-30	289273-293800	bhelap	720
Totals	190851 - 293800		6300

Table 2.4: Table summarizing the data set used in this analysis and luminosity over the various run ranges. The SAM # is used to label the subdivision of data from the various periods. The uncertainty on the luminosity is ~6% [58].

2.4 Object and Event Reconstruction

Once the events are selected from the DAQ system and written to disk they are processed "offline" where event reconstruction occurs. Offline processing consists of a series of steps to ensure the events are classified by their identified objects such as photons, electrons and $\not\!\!E_T$. The goal of this framework is to use various detectors in combination in order to reconstruct high level objects such as tracks, vertices, electrons, muons, and clusters of energy (jets). The details of how each of these objects is reconstructed is summarized in the following sections and with additional detail on some of the important identification variables given in Appendix B. From this data we select a subset of events that contain a γ+$\not\!\!E_T$.

We next describe how events are selected offline. It is useful to note that the way objects are identified in the detector will be used in many ways, for example to identify candidate events online, as well as for crude offline preselection and then later precise final selection. Indeed, many of the most sophisticated algorithms build on the simpler algorithms as their basis for selection. For example, electrons, photons and jet candidates all start by looking for clusters of energy in the calorimeter.

Photons and electrons are the subset of those clusters that are mostly in the EM calorimeter. Of the EM clusters, electrons are identified as EM clusters with a high P_T track associated with it, and photons are selected by virtue of the absense of such a track. Meanwhile the term "jet" is the catch all for clusters of energy which are neither of these, and can be due to a tau lepton, a poorly identified photon or electron, or radiation from a quark or gluon.

We begin with a general description of clusters of energy found in the calorimeter known as "jets". From this generic definition we will lay out the object identification for tracks, photons, and electrons in the CDF calorimeter and tracking chamber. Then we describe the technique to cluster together tracks at the beam line in order to identify the origin of the collision, known as the event vertex. Finally we describe the definition of $\not\!\!E_T$ by looking for imbalance of energy throughout the event in the CDF calorimeter.

2.4.1 Jets

The term "jet" in particle physics is typically used to refer to the hadronization of a high energy quark or gluon that is produced in the collision [3]. A "jet", as defined at CDF, is identified as a cluster of energy in the calorimeter. Thus, in addition to including energy deposited from quarks and gluons the term "jet" generically also includes energy deposited from the hadronic decays of taus, electrons, and photons. The algorithm to identify jets is a standard procedure used at CDF for many years and more information can be found in Reference [59]. This algorithm starts by looking at all calorimeter towers in the detector for the presence of a single tower with a large amount of energy, known as a "seed". Any single tower in the calorimeter with E_T >1 GeV may be used as a "seed" tower for looking for the presence of a jet. If there is a neighboring tower with significant energy, known as a shoulder tower, in an angular radius defined in $\eta - \phi$ space as $\Delta R = \sqrt{(\Delta\eta)^2 + (\Delta\phi)^2}$, we refer to this pair as a cluster and add up all towers within this radius; in this dissertation we use a cone of 0.4 although other analyses use 0.7 or 1.0 [59]. From this, a new energy-weighted centroid is determined and the center of the cone is re-centered there. This process is then repeated until the jet no longer changes; if two jets overlap by >50% they are merged into a single jet. Functionally, this process's primary goal is to determine the 4-momentum of the particle that produced the jet. A detailed explanation of the CDF jet calibration is beyond the scope of this dissertation and can be found in reference [60]. In Table 2.5 we define the variables used to identify high E_T jets in the CDF detector using the standard jet-cone algorithm in the analysis.

Variable	Selection Requirement
E_T^0	> 15.0 GeV
$\lvert\eta_{detector}\rvert$	< 3.4

Table 2.5: Table for the standard CDF jet identifcation variables. We use a jet-cone of 0.4.

2.4.2 Tracks

As previously described, the trajectory of charged particles through the SVX and COT can be reconstructed as tracks with high quality charge, 4-momentum, and z_0 and t_0 information about when they originated at the beam line. It is this path of the charged particle that we refer to as a track. We will use tracks in three different ways in this analysis:

- **For electron and photon identification:**

  We use tracks in defining whether or not an EM cluster is from an electron or a photon. We select electron candiates if there is a high P_T track associated to an EM cluster. We select photon candidates if there is no track, or a single low

P_T track, from either the SVX and COT tracking system that points to the EM cluster. These tracks and their requirements will be described later and the variables used for selection are described in more detail in Appendix B.

- **For vertex information:**

  Tracks are used in the vertexing algorithm when attempting to reconstruct the initial time (t_0) and position (z_0) of all collisions within the event. The variables used to describe these tracks are standardized within CDF and are described in more detail in Appendix B. The requirements used to select tracks for use in the vertexing are given in Table 2.6. A detailed description of the calibration procedure for track timing is given in Section 3.

- **For our high P_T track veto:**

  In the final event selection, we will reject events that have a high probability of being from background events that produce a photon and $\not\!\!E_T$ in the final state, but also typically produce a high P_T track as well (e.g. $W\gamma \rightarrow l\gamma + \not\!\!E_T$ where l is a charged lepton). For this reason we will reject events with a high momentum track as part of requiring that our γ+$\not\!\!E_T$ events be exclusive. Events with tracks we veto have a less strict definition than ones used for timing measurement. This is because we are only looking for evidence that the final state is not exclusive γ+$\not\!\!E_T$ and instead contains evidence for other activity in the detector. The veto track requirements are summarized in Table 2.7.

2.4.3 Photons

Each cluster (or "jet" using the previous definition) is studied in order to determine if it is likely to have originated from a photon. The CDF detector has been used to accurately identify and measure high energy photons for over 25 years using

Variable	**Selection Requirement**
P_T	≥ 0.3 GeV
$\lvert\eta_{event}\rvert$	< 1.6
$COTStereoSeg(5)$	≥ 2
$COTAxialSeg(5)$	≥ 2
$\lvert z\rvert$	≤ 70 cm
$\lvert d_0\rvert$	≤ 1.0 cm
$T_0\sigma$	$0.2 < T_0\sigma < 0.8$ ns

Table 2.6: The track identification requirements used to select tracks with a good timing measurement in addition to a good position measurement for use in the Space-Time vertexing. These variables are described in more detail in Appendix B.

Variable	**Selection Requirement**
P_T	≥ 10 GeV
$COTAxialSeg(5)$	≥ 2
$\frac{nCOTHits}{(LastLayerCOT+1)}$	$> 60\%$

Table 2.7: Table outlining the definition of tracks that we veto against in the exclusive $\gamma + \not\!\!E_T$ final state. These variables are described in more detail in Appendix B.

well established identification requirements [61]. For this analysis we only consider photons found in the central part of the detector ($\lvert\eta_{detector}\rvert < 1.0$) owing to the fact that the central region is not only better instrumented in the calorimeter and tracking chambers, but the EMTiming system has been fully calibrated and validated in this region.

The full list of photon identification requirements is given in Table 2.8 and allows us to select photons in the fiducial region of the CEM as well as being able to distinguish them from decays of $\pi^0 \rightarrow \gamma\gamma$, hadronic jets, electrons, and photon candidates from cosmic ray sources. The full description of the standard photon identification variables is given in Appendix B, but we draw attention to the fact that the list here differs slightly from the standard photon ID in five ways.

- **Eliminate CES χ^2 Variable:**

  As described before, the lateral shower shape of the photon at shower maximum as measured by the CES is normally compared to that resulting from test beam and a χ^2 fit < 20 is usually required. However, it has been shown that this is a poor selection requirement to use in searches for delayed photons which come from the decay of some long-lived heavy object [38]. This is mainly due to the fact that qualitative predictions show that the χ^2 measurement gets worse at large incident angle, but no reliable simulation is available to quantify this degradation. Thus, as was done in previous delayed photon searches, we exclude this cut.

- **PMT Aysmmetry Cut:**

  In the CEM, an energy deposit is identified from the output of the two PMTs that collect the light from the scintillator in the CEM [52], as shown in Figure 2.4. A high voltage breakdown in the PMT unrelated to an energy deposit in the CEM can create a photon candidate if this happens to occur in coincidence with a deposit of energy from a particle from a collision. We define the PMT asymmetry for a photons as:

  $$PMT_{Asymmetry} = \frac{|PMT_1 - PMT_2|}{PMT_1 + PMT_2} \tag{2.3}$$

  where PMT_1 and PMT_2 are the energy measurements as determined from each PMT individually. The total energy is determined using $\sqrt{PMT_1 \cdot PMT_2}$. As the rate of this potential background is small and the rejection power offered by the introduction of this selection requirement is nearly 100%, we simply cut away any spurious deviation from the symmetric PMT distribution expected from photons and ignore backgrounds from this source further.

- **EMTiming Requirement:**

  Requiring that the EMTiming system have a reasonable readout associated with the arrival of the photon (electron) is necessary since we will use this information for calibrations. The default value in the analysis code for the EMTiming variable is set to be -999 ns and by selecting times that are less than $|900|$ ns we ensure there was a timing measurement made.

- **Additional Hadronic Energy Requriement:**

  In addition to the standard hadronic energy fraction selection requirement ($\frac{\mathrm{HAD(E)}}{\mathrm{EM(E)}}$) we have added a sliding hadronic energy selection requirement (Had(E) $\geq -0.30 + 0.008 \cdot E_T$) in order to reject against cosmic ray events. This requirement is described in more detail in Section 4.2 and Appendix B.

- **CES Energy:**

  Since we have removed the CES χ^2 requirement, we have added back a set of requirements to ensure our photon candidates are well described by a shower using the CES detector. For this reasons we use a new selection requirement of CES energy to help distinguish from high energy collision photons and photons coming from cosmic rays (CES(E)). This variable is described in greater detail in Appendix B. By requiring CES(E) $>$10 GeV and $\frac{\mathrm{CES(E)}}{\mathrm{TotalE}} > 0.2$ we add to our ability to reject events originating from cosmic ray events. Both these selection requirements are described in greater detail in Section 4.2 as well as Appendix B.

Variable	Selection Requirement
$\vert\eta_{detector}\vert$	< 1.0 (Central)
Photon E_T^0 *(Measured from Z = 0)*	≥ 30 GeV
Fiducial (CES $\vert X\vert$ <21 cm, 9< CES $\vert Z\vert$ <230 cm)	$= 1$
$\frac{\text{HAD(E)}}{\text{EM(E)}}$	< 0.125
Energy Isolation	$E_{cal}^{iso} < 2.0 + (0.02 \cdot (E_T^0\text{-}20))$
Track Isolation	$\leq 2.0 + (0.005 \cdot E_T^0)$
N3D Track Rejection If N3D Track = 1	≤ 1 Track $P_T \leq 1.0 + (0.005 \cdot E_T^0)$
2^{nd} CES Cluster Energy	CES $E^{2nd} \leq 2.4 + (0.01 \cdot E_T^0)$
$\vert PMTAysmmetry\vert$	< 0.6
$\vert EMTime\vert$	< 900
Had (E) *Hadronic Energy deposited*	$\geq$ -0.30 + 0.008$\cdot E_T$
CES(E) *Total Energy in the CES*	$\geq$10 GeV $\frac{\text{CES(E)}}{\text{TotalE}} \geq 0.2$

Table 2.8: The identification requirements used to identify photon candidates in the $\gamma + \not\!\!E_T$ analysis. Note, these cuts are the standard CDF definition for photons in addition to requiring PMT Aysmmetry, EMTiming variables, total CES Energy, a sliding CES Energy fraction and additional hadronic energy requirement as well as removing CES χ^2. These variables are defined in more detail in Appendix B.

2.4.4 Electrons

Since electrons shower in the calorimeter in basically the same way as photons, we will use electrons throughout this dissertation. We identify electron candidates as clusters of energy in the CEM in the same way as photon candidates, but with a high quality track in the COT [62]. In general we use the standard electron identification variables which have been used successfully at CDF for 25 years, see Reference [62], described in Table 2.9, with greater detail on electron-only variables in Appendix B, and where we have included a PMT asymmetry selection requirement and a EMTiming time requirement to make our electron and photon requirements more consistent.

The similarity between the electron clusters and the photon cluster allow us to use the electron sample as a testing place for much of our photon analysis. For example, electron candidates are used in Section 3 to allow us to calibrate the timing of the tracking and calorimeter systems. This is possible if we simply ignore the information gained from the electron track and thus essentially treat the electron candidate as a photon. However, we can recover information about the origin of the electron, unlike a photon which has no track, and thus help refine various initial time and position assumptions on an event-by-event basis.

Variable	**Selection Requirement**
Electron E_T^0 *(Measured from Z = 0)*	>30 GeV
$\frac{\text{HAD(E)}}{\text{EM(E)}}$	$< 0.055 + 0.00045 \cdot \text{E}$
P_T	> 10 GeV
$\lvert\Delta Z\rvert$ CES	<5 cm
$\lvert\Delta X\rvert$ CES	<3 cm
Isolation	$< 0.1 \cdot E_T$
E/P	< 2 *(For $P_T < 50$ GeV)*
L_{shr}	< 2
Fiducial (CES $\lvert X\rvert$ <21 cm, 9< CES $\lvert Z\rvert$ <230 cm)	$= 1$
$\lvert Z\rvert$	< 60 cm
$\lvert PMTAysmmetry\rvert$	< 0.6
$\lvert EMTime\rvert$	< 900

Table 2.9: The identification requirements used to identify electron candidates used throughout this dissertation. Note, in addition to the standard CDF variables PMT Aysmmetry and EMTiming requirements have been added to ensure a good timing measurement is made. These variables are defined in more detail in Appendix B.

2.4.5 Verticies

A typical high energy collision produces a set of tracks that all originate at the same position and time. We reconstruct a "vertex" as a grouping of tracks that originate from the beamline and collectively indicate that a paticular point in space was the origin of the tracks. In this dissertation we use two different algorithms, but begin with the main one used. The algorithm known as the SpaceTime vertexing is described in more detail in Reference [63] and this algorithm is similar to the calorimeter clustering methods. Instead of using energies in η and ϕ, it uses track P_T in, t_0 and z_0 to determine the position and time of the collision. This algorithm starts by taking the highest P_T track which becomes a "seed" of a "cluster" of tracks. Lower P_T tracks are assigned to if they lie within three standard deviations in both t_0 and z_0, where the RMS for a cluster is taken to be 0.6 ns for t_0 and 1.0 cm for z. From the remaining set of tracks, the next highest P_T track is then picked as the next seed and tracks are assigned to it, and so forth until no tracks are left. An iterative procedure does a fit of the parameters of the vertex to determine the best value of the mean and RMS of z and t_0, as well as the number of tracks in the vertex (N_{track}) and the total scalar sum of the P_T of the tracks (ΣP_T) which is a good measure of whether this vertex is due to a high q^2 collision. It then varies these parameters of all clusters simultaneously at each iteration step n, such that it maximizes the probability that all tracks belong to a set of clusters with parameters, equivalent to a likelihood fit. If, during this process, two clusters are within both 3 cm in z and 1.8 ns in t_0 the two clusters are merged. All these procedures are iterated until the variation becomes less then one percent. After the algorithm is run, we select "good" SpaceTime vertices using the requirements in Table 2.10. We note that the typical variation in z for the SpaceTime vertices is ∼25 cm and the variation in t_0 is

$\sim$1.25 ns as discussed in more detail in Section 3.1.1.

Quantity	**Selection Requirement**
$\Sigma \mathrm{P}_T$	$\geq$ 5 GeV
N_{track}	$\geq$ 3
$\lvert z \rvert$	$\leq$ 60 cm

Table 2.10: Table of requirements to identify good SpaceTime vertices. Tracks are required to pass the selection cuts in Table 2.6

A second vertexing algorithm which only looks for clusters of tracks in the z direction is more common at CDF and is typically referred to as the "standard vertex" algorithm. More details about it are given in Reference [64], and it has been shown to reconstruct the vertex position z with a high degree of accuracy with much better efficiency and much larger values of z along the beam line. The reason we do not use this algorithm in the main part of our analysis is that it does not separate two collisions which lie close in z but happen at a different initial times (t_0). This is a trade-off in efficiency and large z coverage for finding a vertex with a high quality measurement of the reconstructed collision time central in the calculation of t_{corr}. However, we do use this vertex algorithm to determine if events have evidence of a collision at large z since this algorithm searches for vertices out to $|z|$ = 150 cm. As will be discussed in greater detail in Section 5.5.3, this becomes particularly important for minimizing highly biased events from SM sources. As summarized in Table 2.11, we search for a standard vertex with three or more tracks at $|z|$ >60 cm and use this to veto events as likely having a collision at large z position, summarized in Table 2.11.

2.4.6 Missing Transverse Energy

At collider experiments, including CDF, since collisions occur with nearly no momentum in the plane transverse to the collision, we can use conservation of mo-

Quantity	**Selection Requirement**
N_{track}	≥ 3
$\vert z\vert$	> 60 cm

Table 2.11: Table of requirements to identify standard vertices which we use to veto events with evidence of activity at large collision z. This is discussed in greater detail in Section 5.5.3.

mentum to determine if high P_T particles left the detector. Using the fact that the vector sum of all the momenta in the final state particles should be zero in the transverse plane, particles that do not interact with the calorimeter, like the SM neutrino or the SUSY gravitino ($\tilde{G}$) will cause a momentum imbalance in the detected particles. To measure this imbalance we calculate the negative of the vector sum of all the transverse energy in the calorimeter towers with $|\eta_{detector}|$ <3.6 and refer to this as $\not\!\!E_T$. While at CDF many analyses calculate the $\not\!\!E_T$ relative to the primary collision [50], in this analysis the total deposited energy in the calorimeter is calculated relative to $z = 0$ [50]. We make this choice for reasons that will be discussed in more detail in Section 5.4, but can be understood from the fact that our dominant background is wrong vertex photons. Thus, selecting the primary vertex is not useful as it is known to be a wrong calculation. But by choosing z=0 cm we pick something equally reasonable for all events, including those with no reconstructed vertex, thus treating all events on an equal footing and using the same algorithms. Studies of minimum bias events give an estimate of the $\not\!\!E_T$ resolution of $\sim 0.4\times\sqrt{\Sigma E_T}$, where ΣE_T is the scalar sum of the transverse energy of the towers in the calorimeter. This is typically a few GeV for the events in our final samples.

It is important to note that there are both non-collision and collision sources of $\not\!\!E_T$. As will be explored in the next sections, transverse energy will not be conserved if particles come from outside the beam or result from instrumental failure. Said differently, a photon deposited from a cosmic ray muon will create additional $\not\!\!E_T$ to the vector sum that is exactly equal and opposite to the photon candidate.

2.5 Monte Carlo Methods and Samples

Owing to the complexity of the interactions that take place in the detector during collisions, Monte Carlo (MC) simulation often provides the only way to accurately model both the background and signal processes. A complete and standardized physics process generation, detector simulation, and offline reconstruction package is available for use with CDF analyses [66]. While these tools are expected to do a good job of reproducing many of the interactions in the detector, we do not expect them to be sophisticated enough for us to trust the true event rates of the production of the various backgrounds as a way to estimate our backgrounds. However, since they are expected to do an excellent job of reproducing the important features of interactions with the detector in general, we use these MC samples in Section 5 when studying the nature of the various backgrounds in the γ+$\not\!\!E_T$ final state.

The simulation begins by running an event generator, such as the PYTHIA [67] or the BAUR [68] event generators, to simulate $p\bar{p}$ collisions and then uses various theoretical cross-sections, initial and final state radiation, as well as hadronization mechanisms to simulate the decay and possible outcomes of various physics processes. The standard software package known as GEANT3 [69] is then used to simulate the interaction of these particles with the detector simulation, thus giving us detector level hit information [65]. Effects such as the additional collisions during various data taking conditions (referred to as Min-Bias events) are accounted for and added to the simulation. The output of this simulation has been shown to be an excellent approximation of the production and reconstruction of the physical processes that occur in our detector. Thus, we will be able to use this simulation as a guide for understanding possible biases which could be present in our data and potentially causing an artifical excess above background predictions. A listing of the MC samples used in this analysis is given in Table 2.12.

Process	**MC Stntuple**	**MC Generator**	**Luminosity** (fb^{-1})
$W \rightarrow e\nu$	`we0she, we0sge, we0sie, we0seh, we0sej`	PYTHIA	~ 11
$\gamma + jets$	`gx0s0j`	PYTHIA	~ 24
$W\gamma \rightarrow l\nu\gamma$	`re0s68` ($e\nu\gamma$) , `re0s69` ($\mu\nu\gamma$) , `re0s6a` ($\tau\nu\gamma$)	BAUR	~ 500
$W \rightarrow \mu\nu$	`we0s8m, we0s9m, we0sam, we0sbm, we0sgm`	PYTHIA	~ 7
$W \rightarrow \tau\nu$	`we0sat, we0sbt`	PYTHIA	~ 11
$Z\gamma \rightarrow \nu\nu\gamma$	`zx0s0n`	PYTHIA	$\sim 25,000$

Table 2.12: MC samples used in this analysis [65].

As the EMTiming system is not part of the standard calorimeter simulation, the arrival time for any final state particle that hits the detector is obtained using information already available in the MC simulation. Namely:

$$t_{arrival} = t_{produced} + \frac{|\vec{x}_f - \vec{x}_{produced}|}{|\vec{v}_{part}|} \tag{2.4}$$

where $\vec{v}_{part}$ is the velocity of the particle and $\vec{x}_{produced}$ is the initial position and $t_{produced}$ is the initial time [65]. The true vertex time, $t_{produced}$, takes into account the simulation of the primary vertex position and time as well as the decay parent time needed to propagate through the detector volume. For photons from long-lived particles this is the neutralino decay point, for promptly produced photons, such as in Z$\gamma \rightarrow \nu\nu\gamma$, this is essentially the collision time. Since the actual data is calibrated such that the mean time of collision at the center of the detector (z= 0 cm) is set to t_0= 0 ns, the arrival time is corrected for the time of flight assuming the particle trajectory is approximately a straight line. Finally, the simulation checks to see if the particle actually interacts with the EMTiming detector and then applies a Gaussian smearing of the $t_{arrival}$ of 0.5 ns in order to model the intrinsic EMTiming resolution.

This information is then recorded in the event and thus allows us to simulate the EMTiming time of MC events to compare to the data. This process has been shown to accurately reproduce the EMTiming system response and resolution to a high degree of accuracy [70].

Having firmly established the tools needed to perform the search for new physics in the exclusive $\gamma_{delayed}+\not{E}_T$ final state, we now turn our attention to the calibration and validation of the various timing systems used in this analysis.

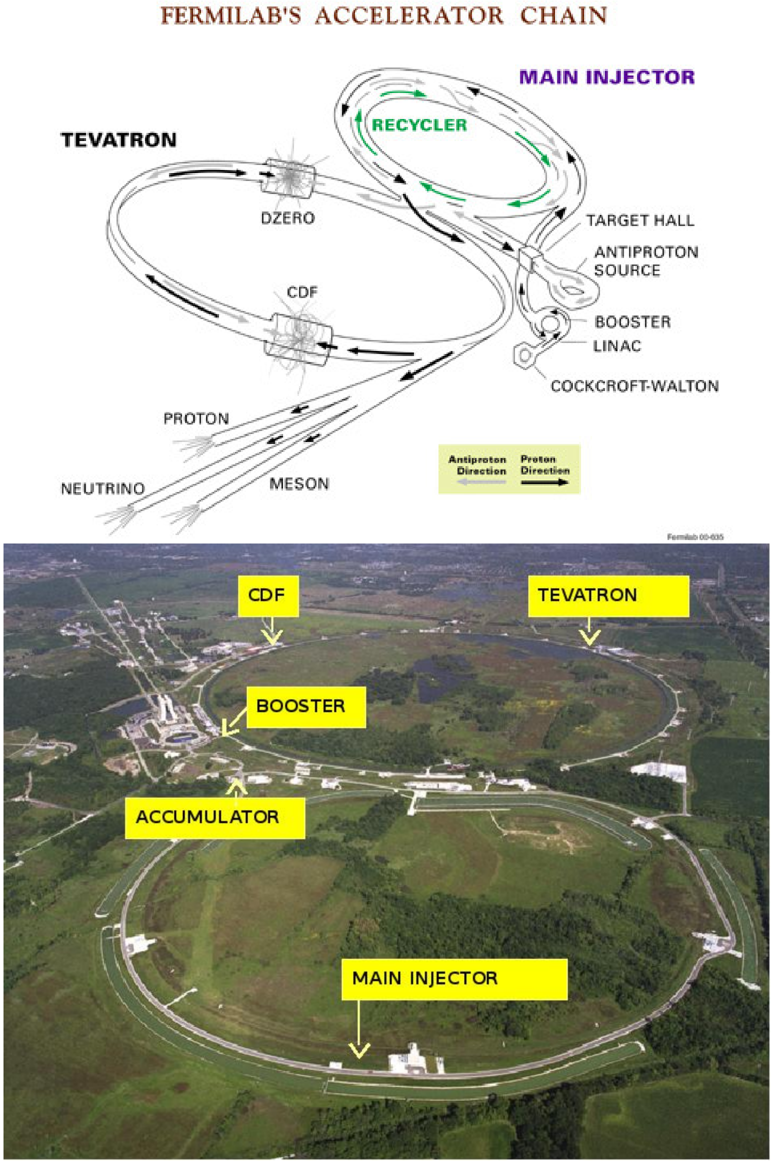

Figure 2.1: Overview of the Tevatron accelerator complex.

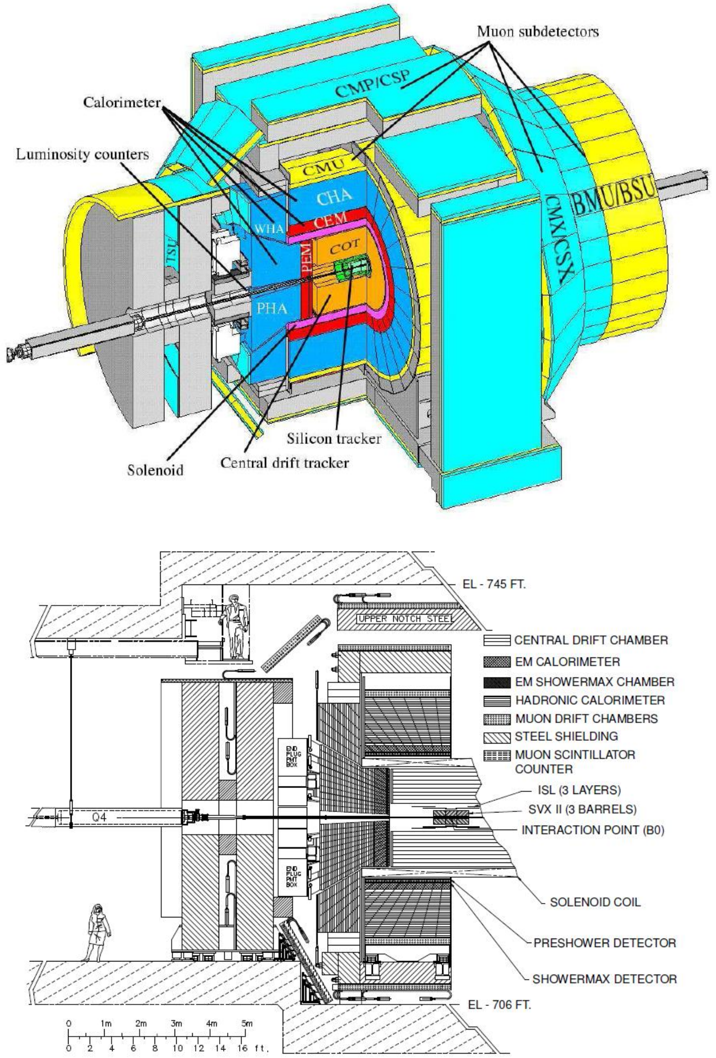

Figure 2.2: Isometric (top) view and elevation (bottom) view of the CDF detector.

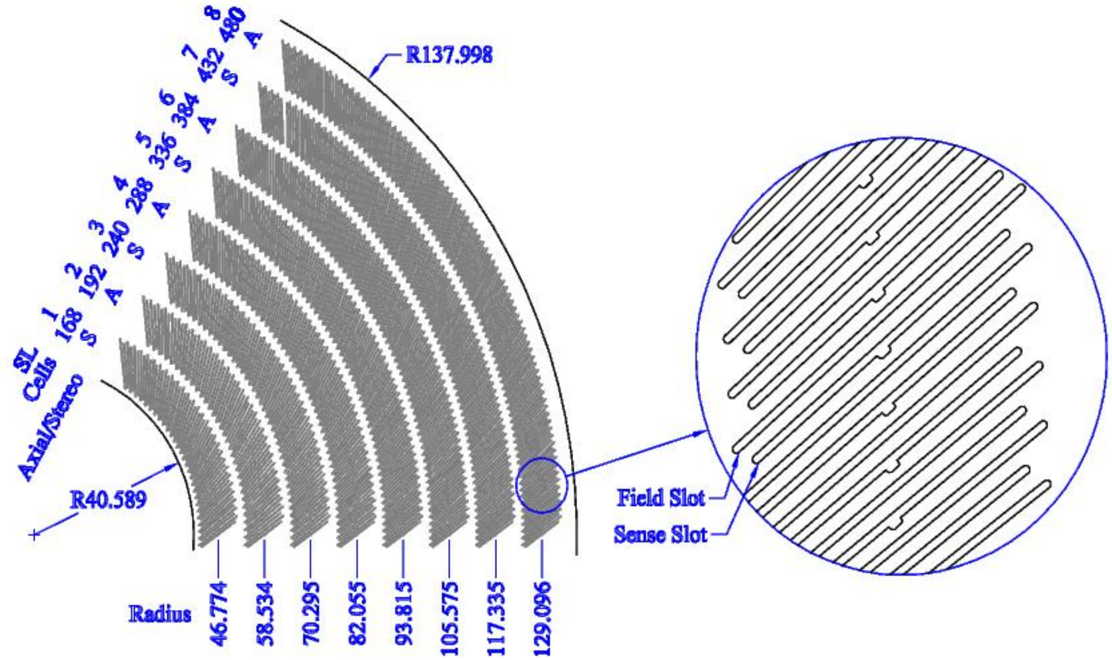

Figure 2.3: A 1/6 section of the Central Outer Tracker (COT). The COT has eight conentric "superlayers" seperated in ϕ into "supercells", with each containing 12 sense wires between field sheets. For each "superlayer" the total number of "supercells", the wire orientation (axial or stereo), as well as the average radius is given in centimeters.

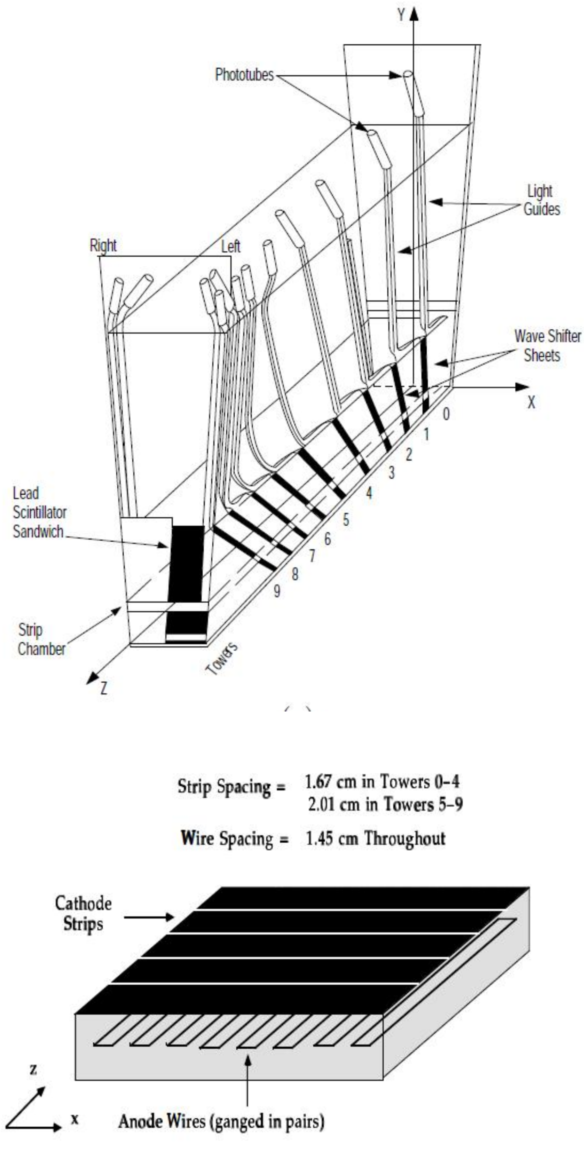

Figure 2.4: (Top) A schematic drawing of the Central ElectroMagnetic calorimeter (CEM) including the (Bottom) Central Electron Strips (CES) sub-detector showing the strips and wires.

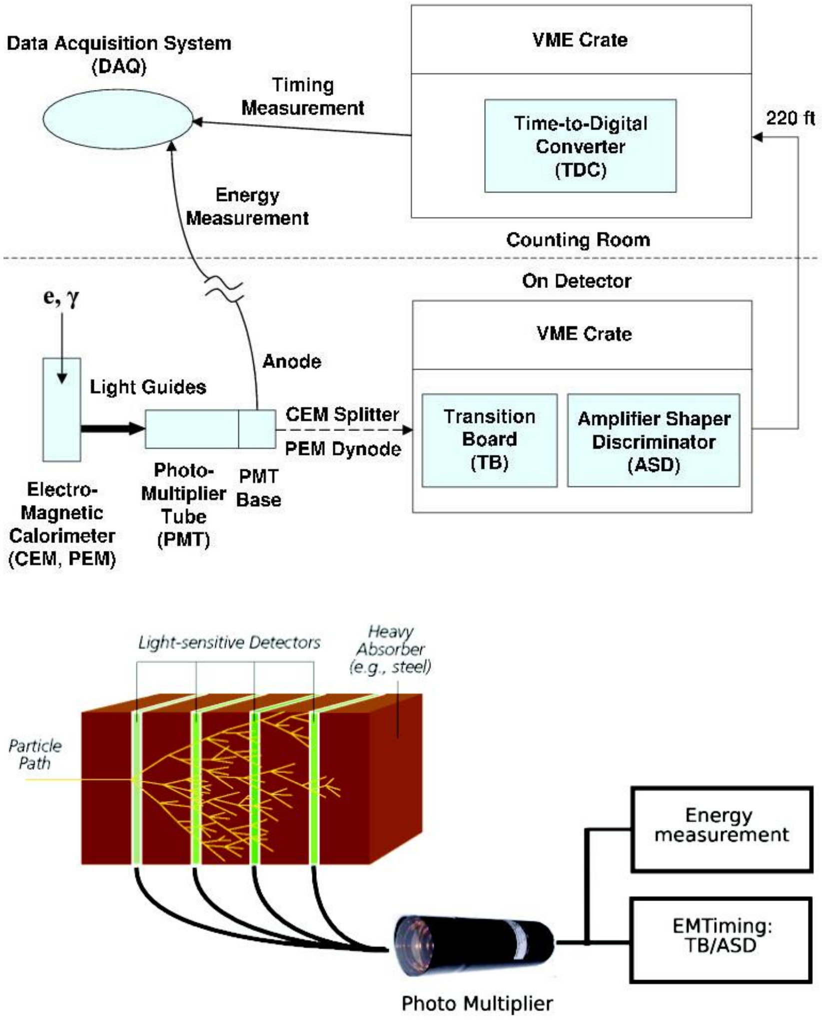

Figure 2.5: (Top) A schematic view of the signal processing in the EMTiming system. (Bottom) A diagram demonstrating how the energy and timing measurement of a particle that showers in the calorimeter is made using the light obtained from the PMT.

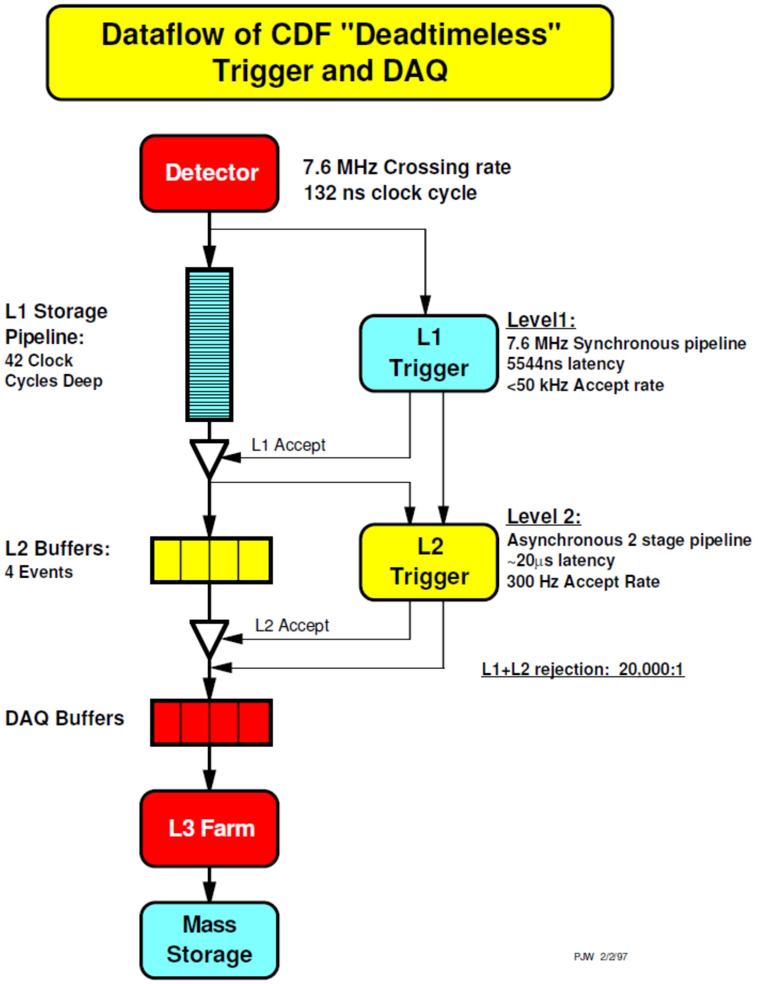

Figure 2.6: (Top) Data flow diagram of the deadtimeless trigger and Data AcQuisition (DAQ) system at CDF [54].

3. TIMING CALIBRATION METHODS AND VALIDATION

In this section we go into detail about the calibration procedure and the performance of the Electromagnetic Calorimeter Timing System (EMTiming) and the Central Outer Tracker (COT) systems for use in the final photon timing measurement, t_{corr}. We use W$\rightarrow$eν $\rightarrow$ e+ $\not\!\!E_T$ events corresponding to the same data taking period as the exclusive γ+$\not\!\!E_T$ data set. These e+$\not\!\!E_T$ events have the particular advantage of mimicking the γ+$\not\!\!E_T$ final state if we simply ignore the track from the electron when performing the vertexing but use it to help identify the correct vertex location. As we will see, the combination of timing systems have a combined resolution of 0.65 ns for events well matched to the vertex and that after calibrations the EMTiming and COT systems show no systematic variations as a function of all the important event observables to less than <100 ps.

We begin by laying out the tolerances needed for the timing calibrations as well as the procedure that will be followed in order to achieve those tolerances. From there we describe the data selection requirements as well as give more detail on the reasoning behind selecting this subset of events. Next we go into detail about the various calibration distributions and procedures for the tracks from the COT, for vertices constructed using tracks from the COT, and finally for the EMTiming system used in combination with the tracking. Lastly, we present results that demonstrate that the system is well calibrated and has systematic variations that are small compared to the needed tolerances.

Before proceeding, we note that the set of precision calibrations described below are performed after a preliminary calibration has already been done on both the COT and EMTiming systems. These calilbrations on the COT and EMTiming data are discussed in detail in Reference [71], of which we give two examples here. Specifically, for the EMTiming system, a preliminary calibration takes into account the time required for the PMT signal to travel to the TDC, an energy-dependent (slewing) correction due to the use of fixed-height discriminators, and a correction that takes into account the energy difference deposited in the two PMTs. This set of calibrations to the EMTiming system is described in greater detail in Reference [52] and is determined from fits for each channel using high statistics jet data samples. This calibration is done tower-by-tower and combined for various run sections, but only is done relative to the mean time and collision position of the sample used to select events. Since the mean time and position can vary from tower to tower this means that the calibrations can be off by almost a nanosecond which is outside our tolerance window. Additionally, run-by-run variations within a run section can vary by a full nanosecond.

Similarly, for the COT, a preliminary timing calibration is done between runs and is described in more detail in Reference [72]. In this procedure an injected calibration pulse sends a signal to each TDC similar to how real data is read out from the detector. The start time for each channel is read out and the channel-to-channel offsets are calculated and averaged before being subtracted off. These offsets are used to correct the raw hit times that come from the COT. This calibration removes channel-to-channel differences in the readout time of the COT that may arise because of variance among the electronics associated with the readout or because of differences in the cable lengths from the COT. We next move to our procedure which has a more rigorous methodology and uses improved resolutions and multiple iterations to finely tune the calibrations.

3.1 Calibration Tolerances Determination

Accurate measurement and understanding of the performance of the various timing systems used in the delayed photon analysis is of the utmost importance in identifying any evidence for new physics using the variable t_{corr} as defined in Equation 1.8. Figure 3.1 shows an example of how a systematic bias in the measurement of the wrong vertex events could result in a shift of the mean of the wrong vertex distribution. This bias could lead to an "artificial excess" of events in the signal region and may be misidentified as evidence for new physics. Such an excess could appear if there is a systematic shift present in one system but not present in the other that would get subtracted off if the right vertex were selected, but not if a wrong vertex is selected. For example, an artificial shift in the arrival time (t_f as measured using the EMTiming time) that is not corrected for when selecting an incorrect initial time (vertex time) can lead to a bias in the resulting corrected time (t_{corr}). This bias would tend to show up in the wrong vertex distribution since any artificial shift in the timing systems would be exasperated by the fact that a random inital time was chosen from the wrong vertex.

Figure 3.2 quantifies how a large timing shift in the measurement of t^{WV}_{corr} translates into a potential excess in the number of large time events using a straightforward calculation. To understand the calculation quantitatively, we start with the assumption that the wrong vertex timing distribution is given by a Gaussian with a mean of μ and an RMS of 2.0 ns and we can integrate the probability for a sample of events to show up in the control region (-7 ns $< t_{corr} <$ -2 ns) and in the signal region (2 ns $< t_{corr} <$ 7 ns).

Spelling it out in more detail, we can describe the number of events in any region, illustrated in Figure 3.1, as having two components. Namely, the number of events

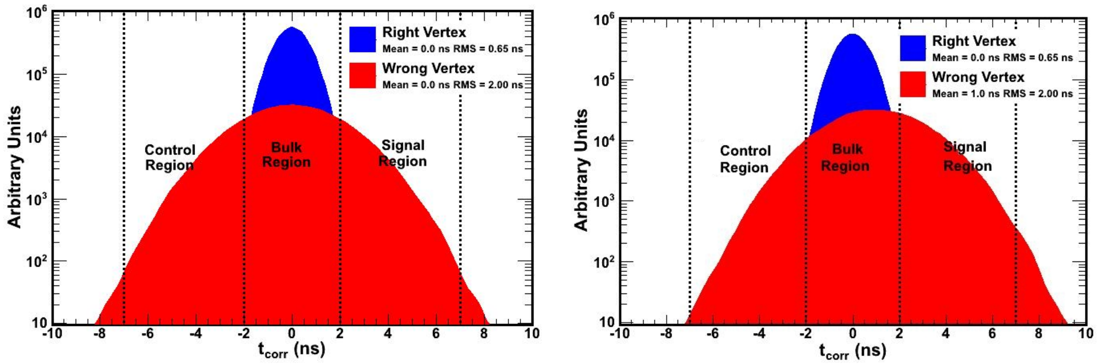

Figure 3.1: Monte Carlo simulation of a shift in the mean of our wrong vertex timing distribution that can cause an excess in the ratio of the number of events in the signal region (2 ns $< t_{corr} <$ 7 ns) to number of events in the control region (-7 ns $< t_{corr} <$ -2 ns).

coming from the right vertex (N_{RV}) and the number of events coming from the wrong vertex (N_{WV}). For clarity we take the number of events in the control region (ignoring the cosmics background for the moment), ($N_{Control}$) and write:

$$N_{Control} = \beta_{RV}^{[-7,-2]ns} \cdot N_{RV} + \beta_{WV}^{[-7,-2]ns} \cdot N_{WV} \tag{3.1}$$

where $\beta_{RV}^{[-7,-2]ns}$ and $\beta_{WV}^{[-7,-2]ns}$ can be thought of the fraction of right vertex and wrong vertex events in this region. Because the distributions are well described by Gaussians, shown in more detail in Section 5, $\beta_{RV}^{[-7,-2]ns}$ and $\beta_{WV}^{[-7,-2]ns}$ are given by the error function (Erf, [73]) of the right vertex and wrong vertex Gaussians and are hence a function of the mean and RMS of those Gaussians. The error function gives the integrated probability, assuming normally distributed errors with standard deviation σ, having a distance less then some value from the mean of the distribution [73]. The error function is generically defined as

$$Erf(x) = \frac{2}{\pi}\int_0^x e^{-t^2}\mathrm{dt}. \tag{3.2}$$

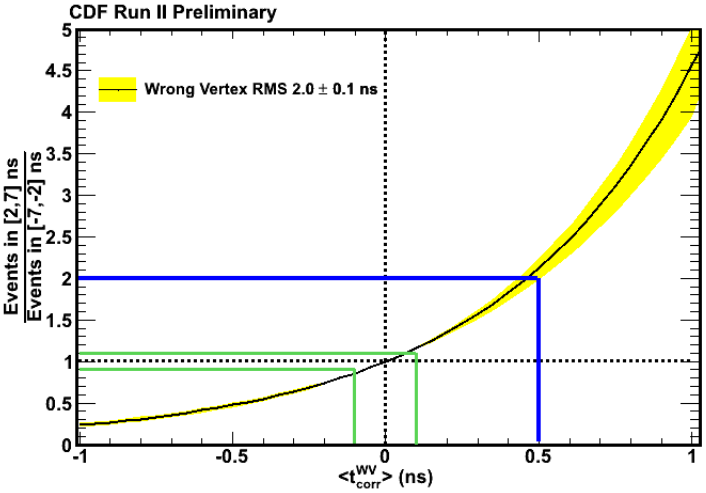

Figure 3.2: A calculation of how a shift in the mean of the wrong vertex timing distribution, $< t^{WV}_{corr} >$, can change the ratio of the number of events in the timing region 2 ns $< t_{corr} <$ 7 ns (Signal Region) to number of events in the timing region -7 ns $< t_{corr} <$ -2 ns (Control Region) for a sample of SM collision events. The nominal ratio of one for a wrong vertex mean of 0.0 ns shown by the dashed black line. The blue line demonstrates that a value of $< t^{WV}_{corr} >= 0.5$ gives you twice as many events in the signal region from SM sources than in the control region. The solid green lines indicate the desired tolerance, 100 ps, on systematic variations in $< t^{WV}_{corr} >$. This tolerance was chosen because a shift of 100 ps $< t^{WV}_{corr} >$ has less than a 10% effect in terms of an artificial "excess" or "deficit" of events expected in the signal region.

Thus for $\beta^{[-7,-2]ns}_{RV}$, since we know the mean and RMS of the right vertex Gaussian distribution we can write:

$$\beta^{[-7,-2]ns}_{RV} = Erf(\frac{\sigma^{RV}_{[0,-2]ns}}{2}) - Erf(\frac{\sigma^{RV}_{[0,-7]ns}}{2}) \tag{3.3}$$

where $\sigma^{RV}_{[x,y]ns}$ describes the distance from the mean value in terms of multipiles of the RMS where the factor of $\frac{1}{2}$ in Equation 3.3 comes from the fact we are only integrating one side of the Gaussian. For example, $\sigma^{RV}_{[0,-2]ns}$ is the distance from 0 ns to -2 ns in multiples of the right vertex RMS. Namely, $\frac{2\text{ns}}{0.65\text{ns}} = 3.08$ which is then put into Equation 3.3 where we are evaluating this error function for the right vertex at two points (-2 ns and -7 ns) assuming the mean of the distribution is at 0 ns. Specifically this implies:

$$\begin{aligned} \sigma^{RV}_{[\mu,x]ns} &= \tfrac{x-\mu}{\sigma^{RV}\sqrt{2}} \\ \sigma^{RV}_{[0,-2]ns} &= \tfrac{2}{0.65\sqrt{2}} \end{aligned} \tag{3.4}$$

where σ^{RV} is the RMS of the right vertex (0.65 ns) and we have taken μ =0. Analogously we evaluate the second error function $Erf(\frac{\sigma^{RV}_{[0,-7]ns}}{2})$ in the same way thus giving us the fraction of events we expect from the right vertex in the control region.

Similarly we evaluate $\beta^{[-7,-2]ns}_{WV}$ which is the fraction of events from the wrong vertex Gaussian in the control region.

$$\begin{gathered} \beta^{[-7,-2]ns}_{WV}(\mu) = Erf(\tfrac{\sigma^{WV}_{[\mu,-2]ns}}{2}) - Erf(\tfrac{\sigma^{WV}_{[\mu,-7]ns}}{2}) \\ \text{where} \end{gathered} \tag{3.5}$$

$$\begin{aligned} \sigma^{WV}_{[\mu,x]ns} &= \tfrac{x-\mu}{\sigma^{WV}\sqrt{2}} \\ \sigma^{WV}_{[\mu,-2]ns} &= \tfrac{2-\mu}{2.0\sqrt{2}} \\ \sigma^{WV}_{[\mu,-7]ns} &= \tfrac{7-\mu}{2.0\sqrt{2}} \end{aligned} \tag{3.6}$$

where in Equations 3.6 we explicitly leave the mean of the wrong vertex as a variable allowing us to evaluate this for a range of different wrong vertex means with an RMS = 2.0 ns. Thus, we have reduced Equation 3.1 to having only three unknowns, namely N_{RV}, N_{WV}, and μ. We now note that we can write a very similar equation for the number of events in the bulk region (-2 ns to 2 ns):

$$N_{Bulk} = \beta^{[-2,2]ns}_{RV} \cdot N_{RV} + \beta^{[-2,2]ns}_{WV} \cdot N_{WV} \tag{3.7}$$

where $\beta^{[-2,2]ns}_{RV}$ and $\beta^{[-2,2]ns}_{WV}$ are the fraction of right vertex and wrong vertex in the bulk region. Again, we write the error functions of the right vertex and wrong vertex Gaussians in this region as:

$$
\begin{aligned}
\beta_{RV}^{[-2,2]ns} &= Erf(\tfrac{\sigma^{RV}_{[0,-2]ns}}{2}) - Erf(\tfrac{\sigma^{RV}_{[2,0]ns}}{2}) \\
\beta_{WV}^{[-2,2]ns} &= Erf(\tfrac{\sigma^{WV}_{[\mu,-2]ns}}{2}) - Erf(\tfrac{\sigma^{WV}_{[2,\mu]ns}}{2}).
\end{aligned}
\tag{3.8}
$$

The evaluation of the error functions in Equation 3.8 follows exactly as before. Since we can count the number of events in both regions straightforwardly, after subtracting off cosmics in the data, we are left with Equations 3.1 and 3.7 giving two equations and three unknowns. Said differently, we can exactly solve for the number of events in any timing region, in particular the signal region, in terms of the number of events from the right vertex and wrong vertex Gaussians if we can measure, or assume μ. Moreover, we can solve this for a range of wrong vertex means as well as allowing the wrong vertex RMS to vary within known systematics.

Looking at the ratio of the $\frac{N_{SR}}{N_{CR}}$ has the advantage of the normalization of the Gaussians dropping out of the prediction in the limit that the contribution from $\beta_{RV} \cdot N_{RV}$ is small. Doing all the steps we find that the only important variable is the mean of the wrong vertex distribution using

$$
Ratio(\mu) = \frac{N_{Signal}}{N_{Control}}(\mu) = \frac{\beta_{RV}^{[2,7]ns} \cdot N_{RV} + \beta_{WV}^{[2,7]ns} \cdot N_{WV}}{\beta_{RV}^{[-7,-2]ns} \cdot N_{RV} + \beta_{WV}^{[-7,-2]ns} \cdot N_{WV}}
\tag{3.9}
$$

where, if we assume the contribution from β_{RV} is small we find

$$
\begin{aligned}
Ratio(\mu) &\sim \tfrac{\beta_{WV}^{[2,7]ns} \cdot N_{WV}}{\beta_{WV}^{[-7,-2]ns} \cdot N_{WV}} \\
Ratio(\mu) &\sim \tfrac{\beta_{WV}^{[2,7]ns}}{\beta_{WV}^{[-7,-2]ns}}
\end{aligned}
\tag{3.10}
$$

Thus, to a good degree of approximation, we can estimate the ratio as a function of the wrong vertex mean, $Ratio(\mu)$ which is the black curve in Figure 3.2 (the yellow band corresponds to an uncertainty on the RMS of the wrong vertex mean of 5%, where this uncertainty is determined using the methods in Section 5). Said differently, given a number of events in the control region and the mean of the wrong vertex we can predict the number of events in the signal region coming from wrong vertex sources using the relationship

$$N_{Signal} = R(\mu) \cdot N_{Control} \tag{3.11}$$

Coming back to Figure 3.2, we see that a timing shift of ≈500 ps in the wrong vertex distribution (dashed blue line) can lead to twice as many events in the signal region than would be found in the control region from SM sources. Previous versions of this analysis assumed $\mu =< t_{corr}^{WV} >= 0$ ns which gives us back the original assumption of $N_{Signal} = N_{Control}$. More so, Figure 3.2 allows us to understand what the tolerance for calibrations on the t_{corr} variable should be, specifically as shown by the solid green lines which indicate that variations of less than 100 ps (0.1 ns) have a negligible effect (<10%) in terms of creating an artificial "excess" or "deficit" of events expected in the signal region. With this knowledge, we are able to lay out a general procedure for calibrating the various timing subsystems that go into the t_{corr} variable.

In the next section we describe the selection of electron events from $W \rightarrow e\nu$ data as well as the broad overall calibration procedure. This procedure includes the calibration of COT tracks, SpaceTime vertices, and the EMTiming system. It is worthwhile to mention that a well "calibrated" system is one where the mean of the t_{corr} distribution for right vertex events is centered at t_{corr} =0 ns, and that this distribution does not show any systematic variation as a function of any important variables in the analysis. To "calibrate" the system is to add corrections to t_0 for the tracking and t_f for the EMTiming system such that each system does not have systematic variations as a function of any important measurement variable. Often this is an offset. For example, if we note that all the events from a certain run have a mean track t_0 = -1 ns, then we add 1 ns to all events in that run. Since there are correlations between variables we will also have correlated corrections we often need to iterate the calibration procedure until the samples stabilize in terms of the magnitude of the corrections being generated. We stop when all the means and variations are small compared to our tolerances. Additionally, we check to be sure that the distributions are well centered and symmetric.

3.1.1 Outline of the Calibration Procedure

We begin this section by selecting a set of events in data which pass the W$\rightarrow e\nu \rightarrow e+\not\!\!E_T$ requirements described below and summarized in Table 3.1. We next describe the matching criteria and how they were selected.

A sample of electrons from W$\rightarrow$ eν events are chosen to calibrate the detector systems as they do an excellent job providing a pure sample of electrons. These events mimick the way a photon interacts with the calorimeter as well as directly identifying the origin of the event in both space and time. This allows us to correctly calibrate the timing systems to this origin event-by-event. To ensure that the electron comes from the vertex we are considering, we require that the electron track has the same value of z_0 and t_0 as the primary vertex within some reasonable tolerances. Figure 3.3 shows the typical matching quality variables by which we match the electron track to the vertex as they appear before our precision timing calibrations. Here, ΔT is the difference between the reported track time and the vertex time ($|t_{electron} - t_0|$) and ΔZ is the absolute value of the difference between the reported track initial z

Event Selection	**Number of Events**
Pass Trigger and Good Run List requriments *See Table 2.2 and 2.3 and Section 2.4*	4,858,466
$\not{E}_T^0 > 30$ GeV	3,893,252
Identified Electron w/ $E_T^0 > 30$ GeV *(See Table 2.9)*	3,221,638
Passing Beam Halo Rejection *(Discussed in detail later)*	3,184,983
Good Space Time Vertex *Note: Electron Track is removed from the Vertexing* *See Table 2.10*	2,605,338
Only one SpaceTime Vertex is matched to the electron track $\lvert\Delta T\rvert = \lvert t_{electron} - t_0\rvert <$ *1.8 ns* and $\lvert\Delta Z\rvert = \lvert z_{electron} - z_0\rvert <$ *3.0 cm*	2,010,699

Table 3.1: Event reduction table summarizing the requirements used to generate the $e+\not{E}_T$ timing calibration sample. Note that the final number of events reported here is after all calibrations have been applied.

position and the vertex z position ($|z_{electron} - z_0|$). A cursory glance at these variables shows evidence for the need of more detailed timing calibrations but that a reasonable match requirement of $|\Delta T|$ <1.8 ns and $|\Delta Z|$ <3.0 cm will be almost fully efficient and produce a small amount of bias. Since there are skews and non-centered mean time effects, we will calibrate and then reselect to minimize this bias. We note that the z distribution looks well matched so we do not consider it further.

The first place to begin when calibrating the detector is with the calibration of COT tracks. These tracks acquire their timing information based on reconstructed hit times in the COT. The initial calibration of the COT times is described in Reference [71]. Our final calibratinon, described in Section 3.2, is designed to calibrate the t_0 of the tracks so that their timing variation as a function of any important variables is small compared to the individual track resolution which is ~ 0.4 ns.

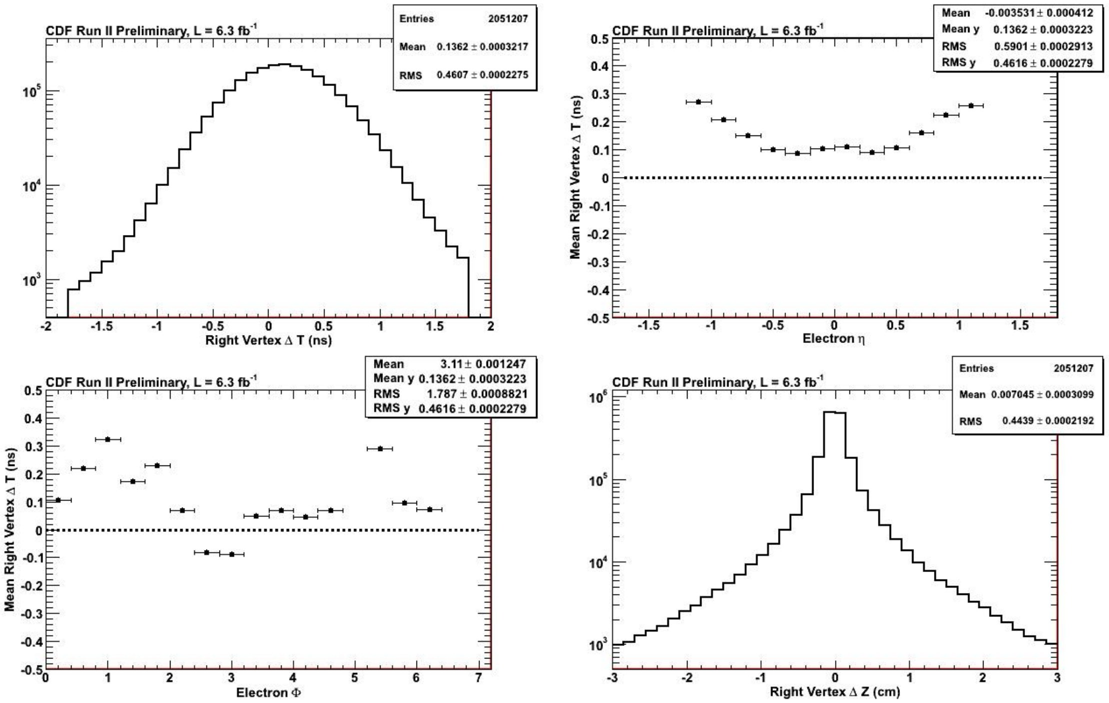

Figure 3.3: The ΔT between the electron track and the vertex, ΔT vs. electron η, ΔT vs. electron ϕ, and the ΔZ between the electron track and the vertex before calibrations. Note that they are not centered at zero, demonstrating the need for further timing calibrations. Note that despite the timing bias, these figures show that the required matching requirements, listed in Table 3.1, are very efficient.

Before describing the calibration it is worth describing the limiting terms in the track timing uncertainty as well as its overall resolution. For each track the tracking algorithms determines t_0 along with an uncertainty on the measurement of t_0. This value, which we call $\mathrm{T}_0\sigma$, is shown in Figure 3.4 for the good tracks in our sample that pass the requirements in Table 2.6. It is dominated by the ability to reconstruct tracks in a complicated environment where each hit is measured with a 1 ns TDC. This reported uncertainty is compared with a second measure that comes from vertices reconstructed from tracks. On the RHS of Figure 3.4 we see the RMS of the t_0 of the tracks fit to determine the mean time and z of the SpaceTime vertices matched to electrons. Both results are around $\sim$0.5 ns, indicating that the $\mathrm{T}_0\sigma$ of the tracks is likely a low end approximation. This implies that any systematic variations which are under the uncertainty of the measurement of the track itself will not significantly contribute to the systematic variation in t_{corr} which uses the vertices which combine the results from multiple tracks. Since we will get multiple measurements of approximately 0.5 ns resolution tracks, and the final t_{corr} resolution is dominated by the single 0.5 ns EMTiming measurement of t_f there is no significant value to improving the resolution of the tracks. Thus we begin the calibration procedure described in Section 3.2 by focusing on the variations in t_0 as a function of a number of important variables and calibrate these variations in each to make sure the biases are small compared to the resolution.

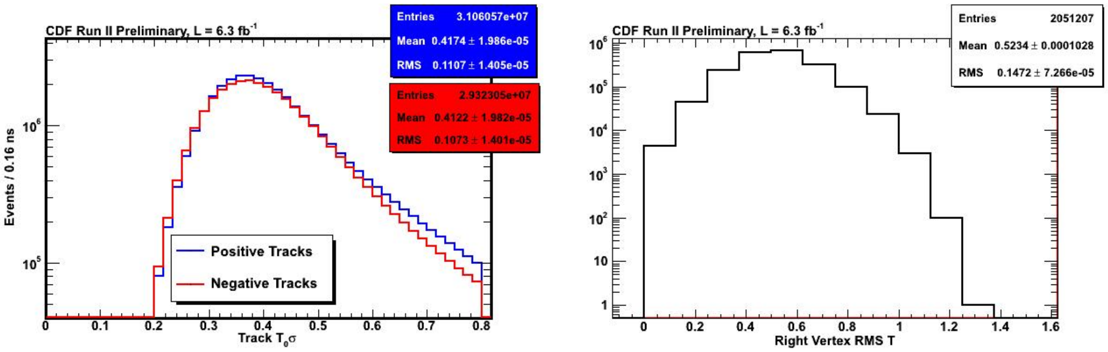

Figure 3.4: (LHS) The reported $\mathrm{T}_0\sigma$ for COT tracks (Blue = positively charged tracks and Red = negatively charged tracks) and (RHS) RMS of the t_0 of the tracks used in the vertex distributions. The track $\mathrm{T}_0\sigma$ as well as the RMS of the tracks around the mean of the best fit vertex allow us to infer the intrinsic uncertainty of the timing measurement associated with the tracks and allow us to infer the necessary sensitivity of the calibrations of the track times.

While this will make better measurements, we note that as the track time changes and the vertex time changes after calibrations, this has the possibility of making individual events just pass or fail the selection requirements of the matching. To keep the timing distributions fully symmetric, and allows us to calculate the mean of the distribution rather than do a full fit, we reselect our data sample. As such, we proceed with a consistent set of events and then check for any remaining variations after corrections and proceed to remove any systematic variation. Once the tracks t_0 has been calibrated, we move to the calibration of the vertices. This begins by reselecting the $e+\not\!\!E_T$ sample using calibrated tracks in the SpaceTime vertex algorithm [63], as detailed in Section 3.3. After calibration of the tracks the vertexing can do a better job of combining tracks and give a better overall measurement of the collision position and time.

After calibrating the tracks and the vertices we reselect the $e+\not\!\!E_T$ sample again and turn to calibrating the arrival time as recorded by the EMTiming system. A proper calibration of the EMTiming system ensures accurate measurement of the arrival time of objects in the calorimeter while avoiding artificial biases due to event topology. The details of calibration of the EMTiming system is given in Section 3.4. We note that the RMS of the EMTiming measurement is approximately 0.5 ns, but what we are interested in is whether there is a bias in the mean of the distribution as a function of any important variable, any of which can be calibrated out.

The summary of the full calibration procedure used to calibrate the COT, vertexing, and EMTiming systems for this analysis is summarized in Table 3.2 and briefly goes as:

- **Select a sample of W→eν events:**

  Here we use the selection requirements outlined in Table 3.1 to select a sample of W→eν events corresponding to 6.3 fb^{-1} of data. Note that after each step in which the timing information is calibrated we will reselect our sample using all selection and matching criteria.

- **Select and calibrate a set of "good" COT tracks:**

Calibration Procedure Summary
Select a sample of W→eν events with a well-matched electron to a vertex
Select and calibrate a set of "good" COT tracks. If the calibration change is significant compared to the tolerances defined, reselect W→eν events and repeat this step
(Re)Select and calibrate a set of "good" SpaceTime vertices. If the calibration change is significant compared to the tolerances defined, reselect W→eν events and repeat this step
(Re)Select and calibrate the EMTiming system for well matched electron candidates in the calorimeter. If the calibration change is significant compared to the tolerances defined, repeat this step

Table 3.2: Table summarizing the calibration procedure for tracks, SpaceTime vertices, and EMTiming times. Each step in this procedure is iterated until the samples stabilize in terms of the magnitude of the corrections being generated and the track t_0, vertex t_0, and t_{corr} timing distributions fall within the tolerances defined for each.

For each event we select a set of tracks from our events using the track requirement in Table 2.6 in order to insure that we have good t_0 and z_0 measurements associated with each track. We then use a set of variables that have a strong impact on the track t_0 and fit the data using polynomials as well as cross terms in order to create track-by-track corrections which are then applied run-by-run. The variables and procedure is described in more detail in the Section 3.2. Using these corrected tracks we re-run the vertexing and reselect our e+$\not\!\!E_T$ sample using the calibrated track times. We iterate on this step until we find that the track corrections are less than 0.4 ns.

- **Calibrate "good" SpaceTime vertices:**

  After the vertexing has been performed we select "good" SpaceTime vertices as defined in Table 2.10 and re-select events that have a well matched electron to the vertex. We next study these vertices to see if there is any variation as a function of any important variables. We note a bias in the overall vertexing measurement and, at this stage, calibrate this out (described in Section 3.3) on a run-by-run basis. Using these corrected vertices we reselect our $e+\not\!\!E_T$ sample. We iterate on this step until we find that the vertex timing corrections are less than 0.01 ns.

- **Calibrate the EMTiming System:**

  After vertexing calibrations are done we reselect events and calculate t_{corr} for each electron so that we can calibrate the EMTiming system. In a manner similar to that of tracks, we find that the mean of the t_{corr} varies significantly as a function of many variables (described further in Section 3.4). We iterate on this step until we find that the EMTiming time corrections are less than 0.1 ns.

In the next sections give more detail about the individual procedures for COT Tracks, SpaceTime Vertices, and the EMTiming system. Finally, we present the results of all these individual calibrations on the t_{corr} variable and demonstrate that we have removed systematic variations as a function of all the important event observables to less than <100 ps.

3.2 Calibrating COT Tracks

In this section we detail the procedure for calibrating "good" COT tracks for use in the SpaceTime vertexing. Figure 3.5 shows the 1-dimensional timing distribution of t_0 of the tracks, after first event selection but before calibrations, as well as $< t_0 >$ as a function of the various tracking variables. The five tracking parameters ($T_0\sigma$, ϕ, η, d_0, and q) are chosen here because they uniquely describe the 3-dimensional track trajectory with the exception of Z along the beamline (this is expected to not have a mean of zero for reasons described in References [38, 63, 74] resulting from the structure of the beam and thus should not be calibrated against). Additionally, "Run Number" is used to account for any variation over time and data taking configuration. Clearly, positive and negative charge appear very different and there is significant variation in the mean time as a function of many of the variables. Not only is $< t_0 >$ not centered at 0 ns, but there are systematic variations on the order of 1 ns. Additionally, these variations change independently over time (as a function of run number) as well as becoming increasingly worse for low p_T tracks. This is especially troublesome for the exclusive $\gamma + \not\!\!E_T$ analysis since we explicitly veto any event that has large p_T tracks, thus most of our vertices are made up of these poorly calibrated tracks.

Figure 3.6 shows how these poorly calibrated tracks effect even our selection of $e + \not\!\!E_T$ events by looking at the individual electron track time variables before calibrations. We draw attention to the fact that the electron track mean time is not well centered at $t_0 = 0$ and there is a large systematic variation in $< t_0 >$ as a function of η, ϕ, and run number.

As described previously, we begin the calibration procedure with the goal to calibrate the t_0 of the tracks such that the systematic variation small compared to the intrinsic resolution of the track itself of 0.4 ns. Table 3.3 gives the summary of the track calibration procedure, a more detailed description follows:

- **Select W→eν candidate events:**

  Select W→eν candidate events where the electron track is well matched to any good SpaceTime vertex (see Table 3.1).

- **Calibrate the timing versus variables that have an impact on the track time:**

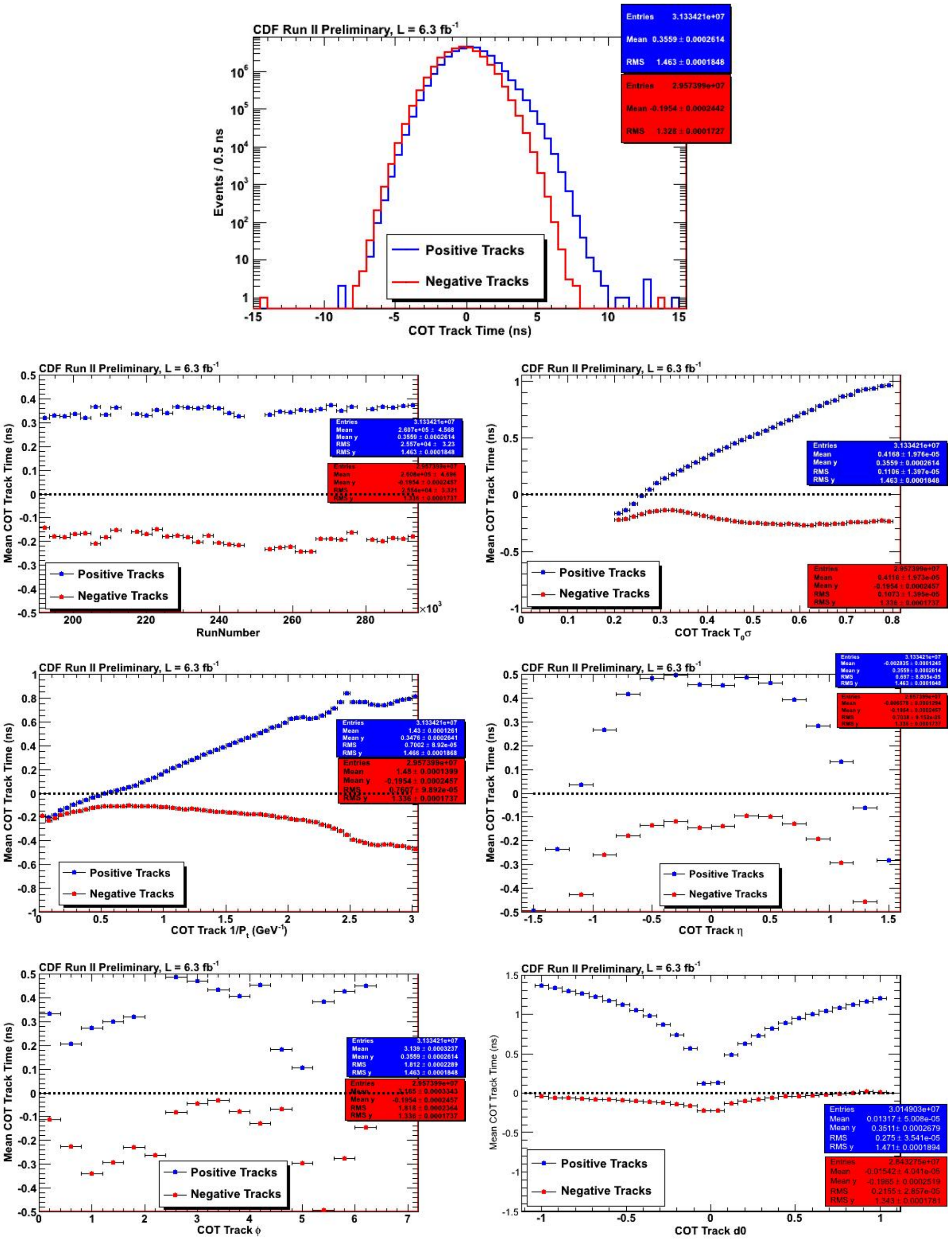

Figure 3.5: The COT track t_0 for positive (blue) and negative charges (red) in the top row and the mean time of the COT tracks, $< t_0 >$, plotted as a function of various variables before calibrations. Note the scale on the y-axis in some of the plots is much larger than others.

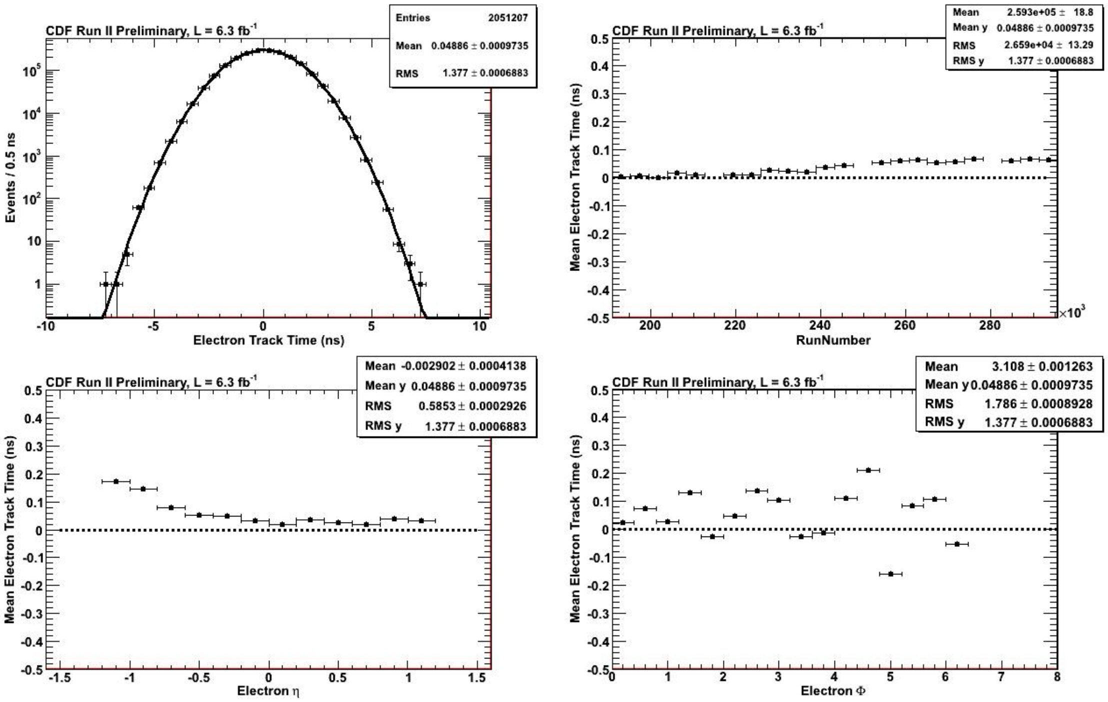

Figure 3.6: The electron track t_0, and mean t_0 as a function of RunNumber η and ϕ variables before calibrations.

Determine the $< t_0 >$ as a function of Run Number, $T_0\sigma$, Φ, η, Impact Parameter (d_0), and q, where each variable is described in Appendix B.1. The calibration procedure is to perform a polynomial fit of the timing distribution as a function of these variables, taking into account correlations from their cross-terms as many variables are highly correlated in the original tracking fit procedure. We then take these fits as corrections to the track times to center each at $< t_0 > =0$ ns.

- **Reselect W→eν candidate events:**

  Re-select W→eν candidate events using the generated calibrations including re-running the vertexing. We continue to iterate this procedure until the largest deviation in the fit as a function of any variable is less than 0.4 ns.

COT Track Calibration Procedure Summary
Select W→eν candidate events
Determine the mean track time, $< t_0 >$, as a function of important variables and use this as a timing correction to make the $< t_0 >= 0$ ns as a function of all variables. (Run Number, $T_0\sigma$, ϕ, η, d_0, and q)
Reselect W→eν candidate events and iterate until the corrections converge

Table 3.3: Table outlining the COT track calibration procedure.

Figure 3.7 shows $< t_0 >$ as a function of the 1-d variables after applying the calibrations and iterating multiple times. We note that for the calibrated COT tracks there is no longer any significant difference between positive and negative tracks as was seen before the calibrations. Additional studies show that the tracks are well calibrated in two dimensional profile plots as well [75]. Furthermore, the systematic variations of the track t_0 are all well within the 0.4 ns tolerances versus the dominant variables. It is important to draw attention to the fact that the range of the y-axis in the plots before calibrations (Figure 3.5) was large, ranging from -1.5 ns to 1.5 ns while the range shown after calibration (Figure 3.7) is now -0.5 ns to 0.5 ns. Thus, the structure that is visually present in Figure 3.7 is significantly exaggerated when compared to the plots before calibrations.

A second check, shown in Figure 3.8, shows the effect these track calibrations have on the electron track time showing that much of the variation is now gone, despite the fact that some residual variation in ϕ remains. This variation in ϕ is well within the individual track resolution and is thus not considered a problem for vertexing.

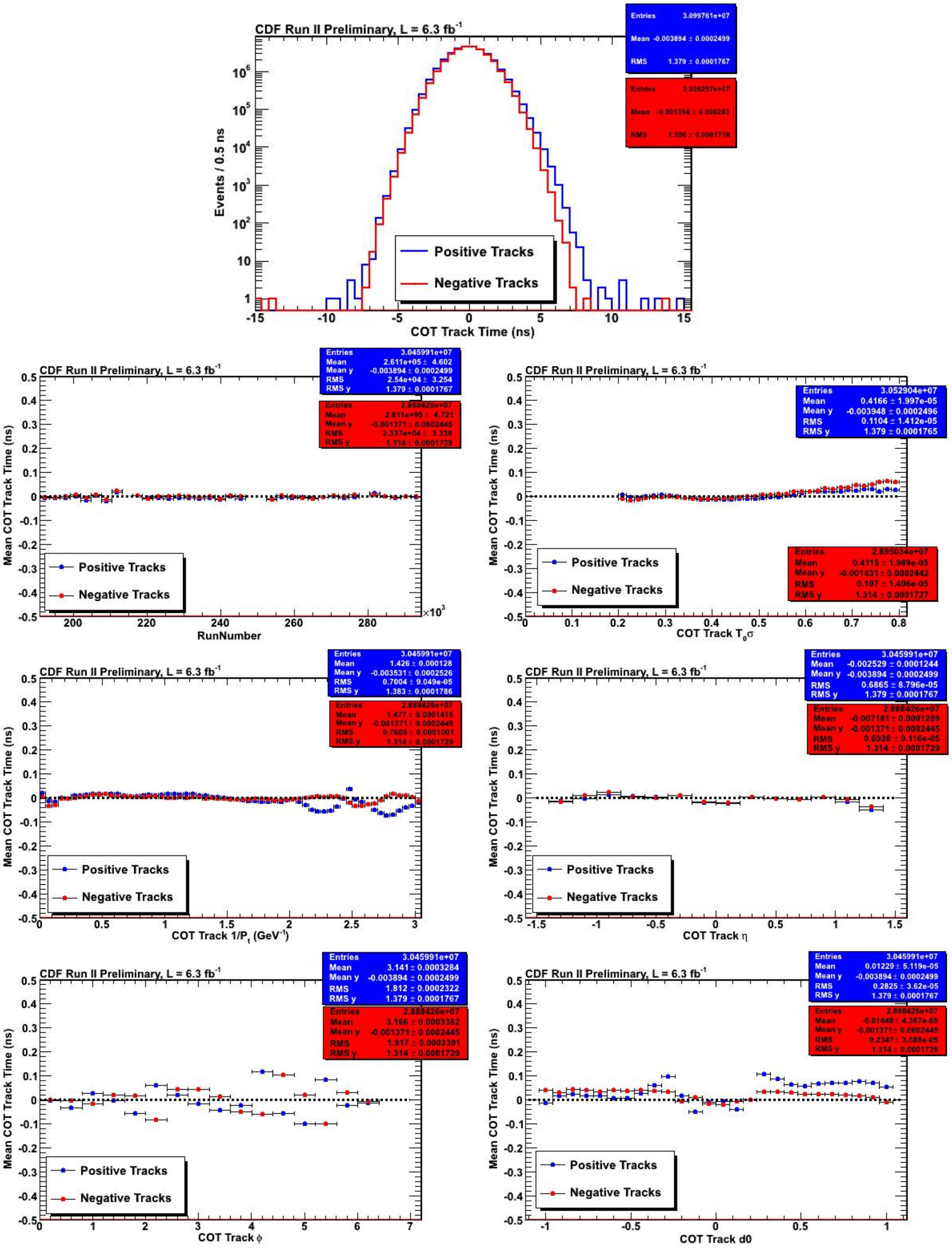

Figure 3.7: The COT track t_0 after calibrations for positive (blue) and negative charges (red) in the top row and the mean time of the COT tracks, $< t_0 >$, plotted as a function of various variables. Note the scale on the y-axis is now ±500 ps.

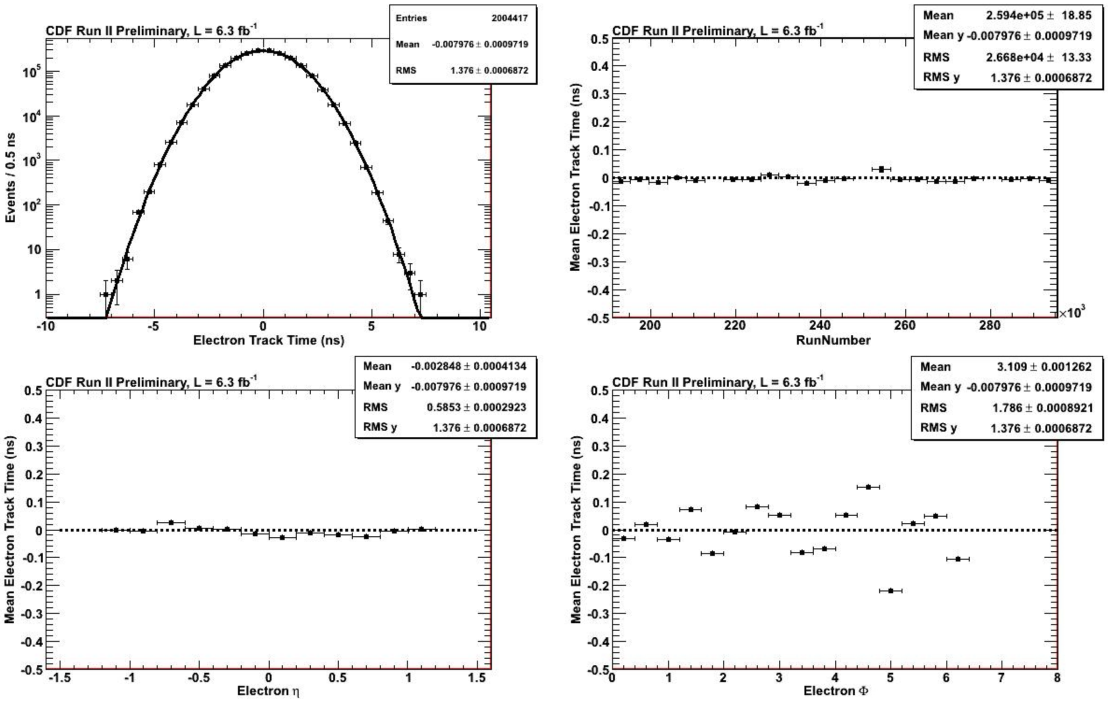

Figure 3.8: The electron track t_0, and $< t_0 >$ as a function of RunNumber η and ϕ variables after calibrations. Note the variations are small here compared to the variations in Figure 3.6.

3.3 Verticies

Once the tracks t_0 have been calibrated using the procedure described in the previous section, we move to the calibration of the vertexing. Since the measurement of the initial time of the event, t_0 in Equation 1.8, is directly extracted from the vertex time information, this is a particularly important quantity to have calibrated as accurately as possible. Thus, we define our tolerance for systematic variation in the vertex calibration to be <0.1 ns.

We begin the calibration of the SpaceTime vertices by re-selecting our sample of W→eν candidate events using the calibrated tracks and re-running the SpaceTime vertexing algorithms. The vertex timing distribution after track calibrations, but before any additional vertex calibrations, can be seen in Figure 3.9. We see that there is still a systematic shift in the vertex mean time. This likely results from the fact that the SpaceTime vertex algorithm only selects a subsample of all the tracks in the event; the remaining tracks are unrelated and can cause biases in the overall tracking calibration that is fixed by the vertexing procedure of combining multiple tracks to eliminate bias. As a result any bias in the selection of tracks used in the tracking calibrations algorithm may introduce a slight offset in the mean time and thus need to be corrected for. We note that this effect is small, only has a shift of ∼55 ps. However, we have more than enough statistics to determine this mean to high precision and thus can remove this offset. This time we show that the $< t_0 >$ versus z position in Figure 3.9 and again note that has a prevalant slope. The plot of the mean vertex time versus ΣP_T in Figure 3.9 is believed to have an offset reflecting the offset in Run Number. As we will see this variation vanishes after calibrations are applied. We describe the vertex timing calibration procedure, which is summarized in Table 3.4, below.

Vertex Calibration Procedure Summary
Reselect W→eν candidate events
Determine the mean vertex time, $< t_0 >$, as a function of important variables and use this as a timing correction to make the average $< t_0 > = 0$ as a function of all variables. (Run Number)
Reselect W→eν candidate events and iterate until the corrections converge

Table 3.4: Table outlining the SpaceTime vertex calibration procedure.

- **Reselect W→eν candidate events:**

  Reselect W→eν candidate events, using calibrated tracks, where the electron track is well matched to a good SpaceTime Vertex (See Table 3.1).

- **Calibrate the vertex time versus variables that have an impact on the vertex time:**

  Determine $< t_0 >$ of the vertex as a function of Run Number since this variable has the overall systematic shift in the mean time. Average all the times within the same run number and subtract off the difference from $< t_0 > = 0$ in the average. Apply this generated correction to each vertex event-by-event.

- **Reselect W→eν candidate events and iterate:**

  Reselect W→eν candidate events, using the vertex calibrations. We continue to iterate this procedure until the largest deviation in the mean is less than <0.01 ns per run.

The results of this calibration can be seen in Figure 3.10. Clearly, these corrections maintain the vertex time distribution to be Gaussian to many sigma and well centered at $t_0 = 0$. Figure 3.10 also shows the $< t_0 >$ versus other variables (vertex ΣP_T, number of vertices present in the event, vertex z position) in order to demonstrate that none of the calibrations have introduced any unforeseen biases. We have included the z distribution here for completeness. Specifically, the variation in $\Sigma \mathrm{P}_T$ has disappeared and the expected slope in $< t_0 >$ vs. z plot remains. Finally, coming back to the issue raised at the beginning of this section, Figure 3.11 also shows that the COT track calibrations and the vertex calibration maintain their balance between the track times and the vertex times by plotting the ΔT and ΔZ between the vertex and the electron track versus Run Number and showing them to be both well centered and flat over time.

With the vertexing well calibrated, we can move to calibrate the EMTiming system. In the next section we outline the procedure for calibrating the corrected time which takes into account the calibration of the EMTiming system as well as correlations between the EMTiming system and the COT, as well as event-by-event corrections that occur because of different time-of-flight from the vertex to the CEM tower location.

3.4 EMTiming

In order to calibrate the EMTiming time associated with the well matched electrons one must take special care not to artificially calibrate against any real effects due to the underlying topology of the events selected and instead only calibrate out real systematics in the system. To do this we follow a calibration procedure that differs slightly from the methods used for tracks and vertices as well as by previous versions of this analysis. Previous calibrations (Reference [38]) simply calibrated against the average EMTiming time or time corrected for the average time of flight. We now call this t^0_{corr} and it is defined as

$$t^0_{corr} = t_f - t_0 - \frac{|\vec{x_f} - \vec{x_0}|}{c} \tag{3.12}$$

where t_0 is equal to zero (the average time of collision in teh cneter of the detector) and x_0 =0 cm, which is the center of the detector. We will show why this is the wrong procedure and outline a more proper procedure that takes into account the best estimate of the vertex time and time-of-flight of the electron event-by-event.

To calibrate the EMTiming system we calibrate against the mean t_{corr}, $< t_{corr} >$, as a function of variables that the EMTiming time should not have systematic variation with respect to. This is because the EMTiming system measures the time of arrival, not the time of collision. Thus, we want to make sure we are not biased by time-of-flight systematics from the sample we have chosen. . For example, if most of the electrons that hit a tower at high $|\eta|$ are from a different average collision z_0 or t_0 then from low $|\eta|$, then they will be calibrated to different expected arrival times rather than to their true time-of-origin and time-of-flight. Said differently, we want to calibrate on the actual time-of-flight, not to average t_0 and z_0 positions that produce hits in this tower. We find that there are three variables of interest to calibrate in which the corrected time distribution shows significant variation. They are run number, energy, and tower number. These distributions are shown in Figure 3.12 and were chosen because they correspond to the physical location in the detector and exhibited the need for additional calibrations. While there are other interesting variables, such as z of the vertex, we will use them as a check of our methods.

After reselecting W→eν events where we match the electron to the SpaceTime vertex, using the calibrated tracks and vertices, we use the calibrations derived from the 'uncalibrated' t_{corr} distributions obtained from as the parent distributions for the EMTiming calibrations. The calibration procedure is outlined in Table 3.5 and described in more detail below.

EMTiming Calibration Procedure Summary
Reselect W→eν candidate events
Determine the mean t_{corr}, $< t_{corr} >$, as a function of important variables and use this as a timing correction to make the average $< t_{corr} >= 0$ ns as a function of all variables (Run number, Tower, Energy)
Iterate until the corrections converge

Table 3.5: Table outlining the EMTiming time calibration procedure.

- **Reselect W→eν candidate events:**

  Reselect the subset of W→eν candidate events where the electron track is well matched to a good SpaceTime Vertex (See Table 3.1). Note this step uses the previous track and vertex calibrations already performed.

- **Calibrate variables that have an impact on the corrected time:**

Determine $< t_{corr} >$ as a function of: Run Number, tower, and energy. There should be no systematic dependencies on $< t_{corr} >$ as a function of these variables. Create a set of corrections that make $< t_{corr} >= 0$ ns as a function of Run Number, for each tower independently, and energy. We then apply this set of corrections to the EMTiming time.

- **Iterate this procedure until the calibrations reach convergence:**

  We continue to iterate this procedure until the resulting variation in the calibration becomes less then 0.1 ns. Note, unlike before, it is unnecessary to reselect our sample. This is because the arrival time of the electrons that is being calibrated during this procedure does not effect the content of our sample.

Finally we present the result of the full set of timing calibrations, including the EMTiming calibrations described here.

3.5 Summary and Validation Results

The results for the entire calibration procedure are shown in Figure 3.13 using t_{corr} for electrons that are well-matched to a vertex. The resulting t_{corr} distribution has a mean of 0.002 ns and and RMS of 0.69 ns, which is well within the nominal expectations of having a mean of 0.0 ns and an RMS of 0.65 ns. We also see in Figure 3.13 that the $< t_{corr} >$ distribution is flat and centered as a function of other variables that were not part of the calibration procedure including vertex ΣP_T, vertex z, and number of vertices in the event. The fact that the distributions are flat versus important variables that we should not calibrate on, especially the z of the collision, gives us confidence that we have taken into account all important sources of calibration bias. We also see that none of these distributions have a systematic variation >0.1 ns thus placing us well within our predefined tolerances for our timing measurement. Finally, we note that the timing distribution is Gaussian out to many sigma. It is possible that the events on the tail are due no non-collision events such as cosmic rays, but this has not been studied in further detail as it has no impact on our conclusions about how well the detector is calibrated.

Before we conclude this section we make a few comments about the differences between calibrating on t_{corr} verses the old method of calibrating on t^0_{corr}. We show the EMTiming time (t^0_{corr}) distributions after all calibrations in Figure 3.13. It is evident that this calibration did have the desired effect for most, but not all variables. For the t^0_{corr} for well-matched electrons we observe that the distribution is Gaussian out to many sigma and has a mean of 0.05 ns. The t^0_{corr} distribution is also very flat with little variation over the entire run range as well as having no geometric variation by tower (η), ϕ, or z position (z CES position). However, the last plot in Figure 3.14 shows a timing shift of $\sim$200 ps starting at 50 GeV for t^0_{corr} which is not seen Figure 3.13. This shift can be understood as being a real effect due to detector and reconstruction properties of the sample of events being examined and thus does not offer concern to the calibration of the final sample using our method. This becomes evident when we look at the time-of-flight (TOF) from the right vertex as a function of energy and tower shown in Figure 3.15.

Now that we have confirmed that our detector is well calibrated and free of timing biases, we turn our attention to the sources of background in the exclusive $\gamma_{delayed}+ \not\!\!E_T$ final state. In the next section we address non-collision sources of backgrounds and lay out a series of selection requirements to reduce their present in our final state.

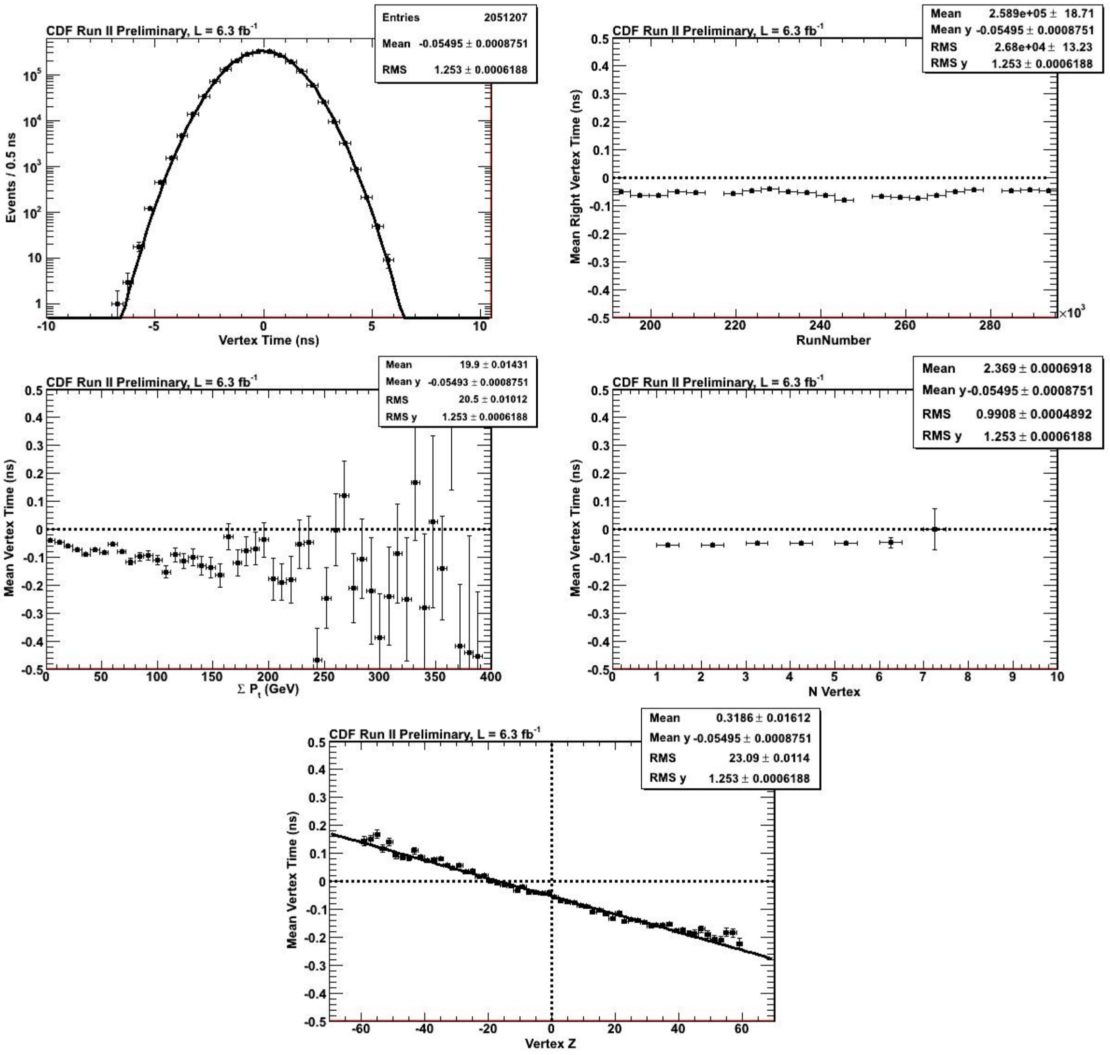

Figure 3.9: The SpaceTime vertex t_0 as well as $< t_0 >$ plotted versus various variables after track calibrations, but before vertex calibrations. This demonstrates that even following the COT track calibrations there is still a systematic offset of the mean time on the order of 55 ps, thus necessitating a simple calibration subtraction. The slope in the bottom figure of $< t_0 >$ vs. z is expected and described in detail in Reference [74].

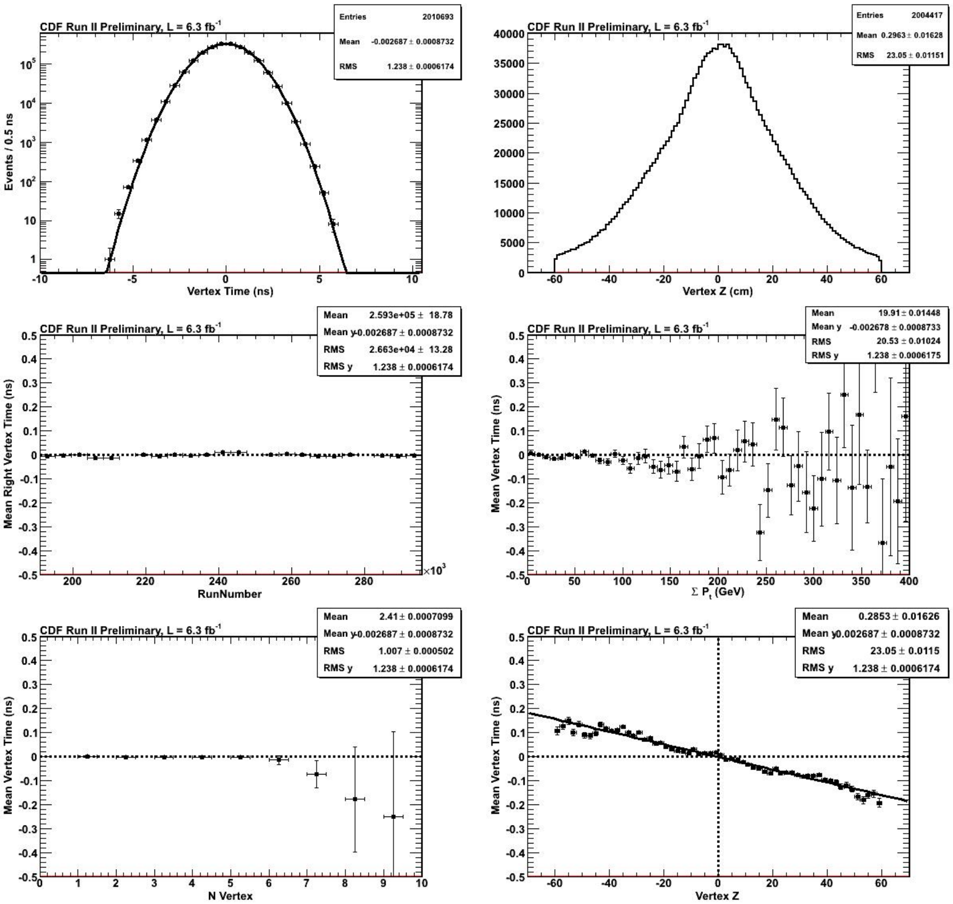

Figure 3.10: The SpaceTime variables after calibrations showing that the vertexing is well calibrated. The slope in the bottom figure of mean $< t_0 >$ vs. z is expected and described in detail in Reference [74].

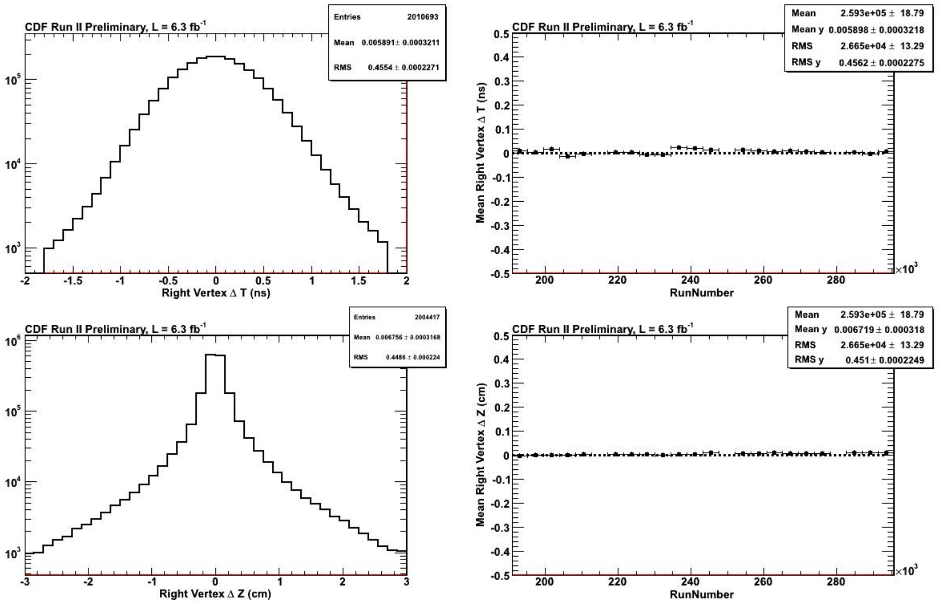

Figure 3.11: (Top) The ΔT and (Bottom) ΔZ and $< \Delta T >$ and $< \Delta Z >$ vs Run Number between the electron track and the SpaceTime vertex demonstrating that the track and vertex calibrations have removed any bias between the electron track and the SpaceTime vertex.

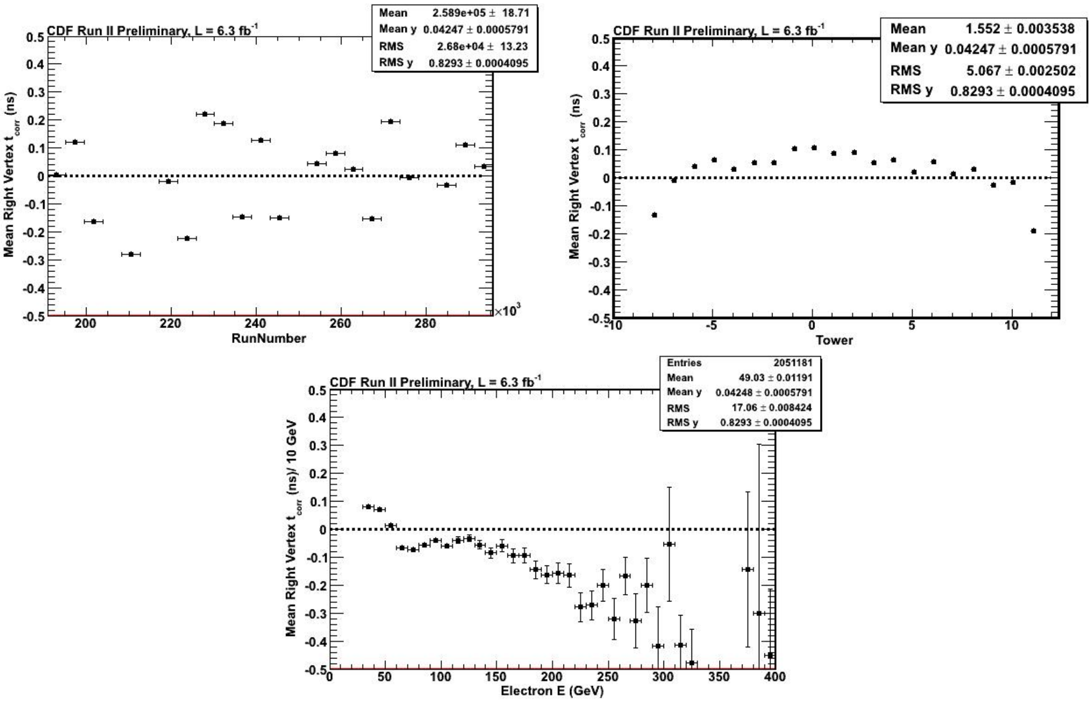

Figure 3.12: The $< t_{corr} >$ distributions before EMTiming calibrations used to generate the run-by-run, tower, and energy calibrations.

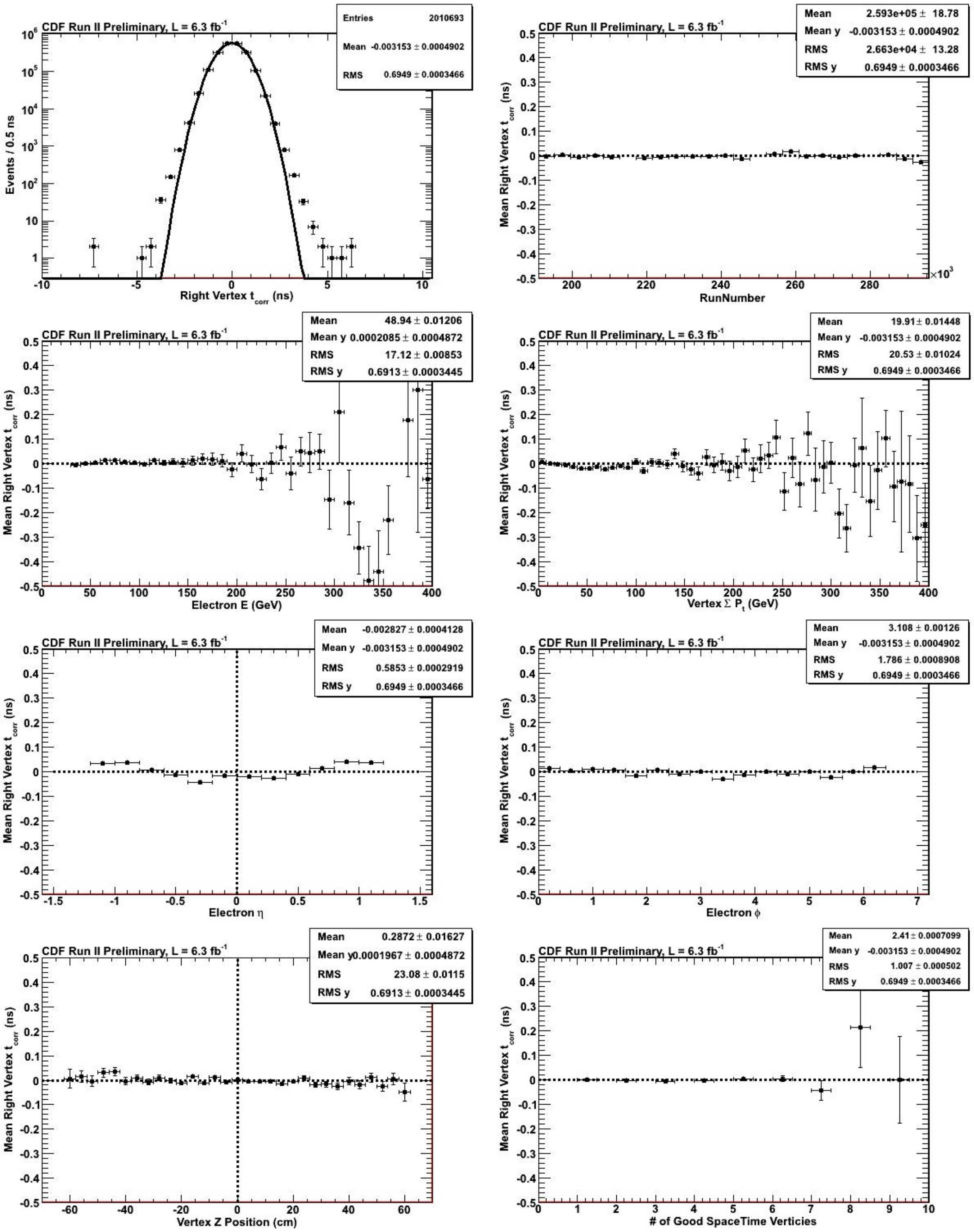

Figure 3.13: The distribution of t$_{corr}$ after the full set of calibrations for the $W \rightarrow e\nu$ sample. We note that the distributions have a mean of 0.002 ns and and RMS of 0.69 ns, which is well within the nominal expectations of having a mean of 0.0 ns and an RMS of 0.65 ns. We also see that distribution of $< t_{corr} >$ is flat and centered as a function of run number, energy, vertex ΣP_T, η, ϕ, vertex z, and number of vertices in the event.

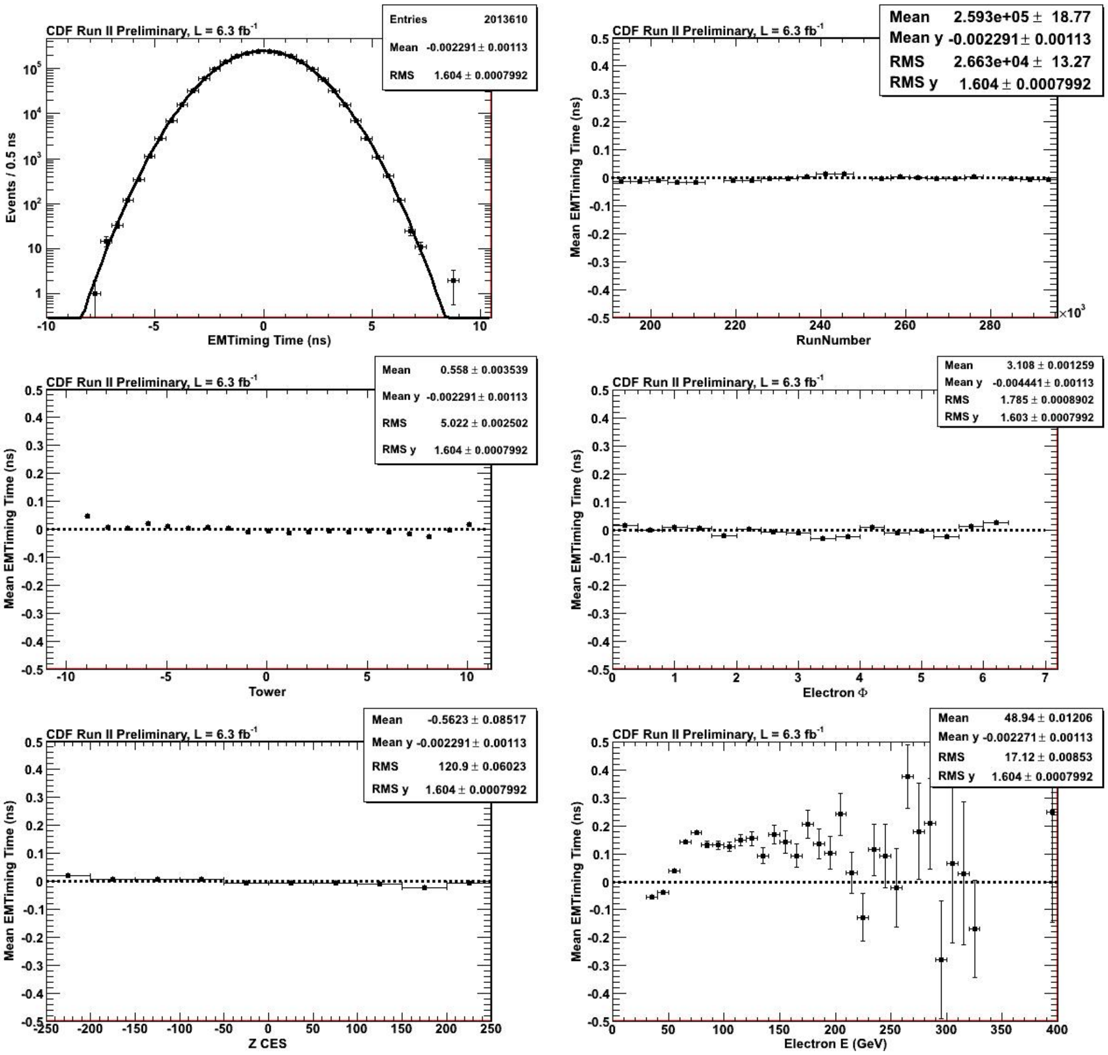

Figure 3.14: EMTiming variables, t^0_{corr}, after calibrations. Note that this variable is not flat as a function E.

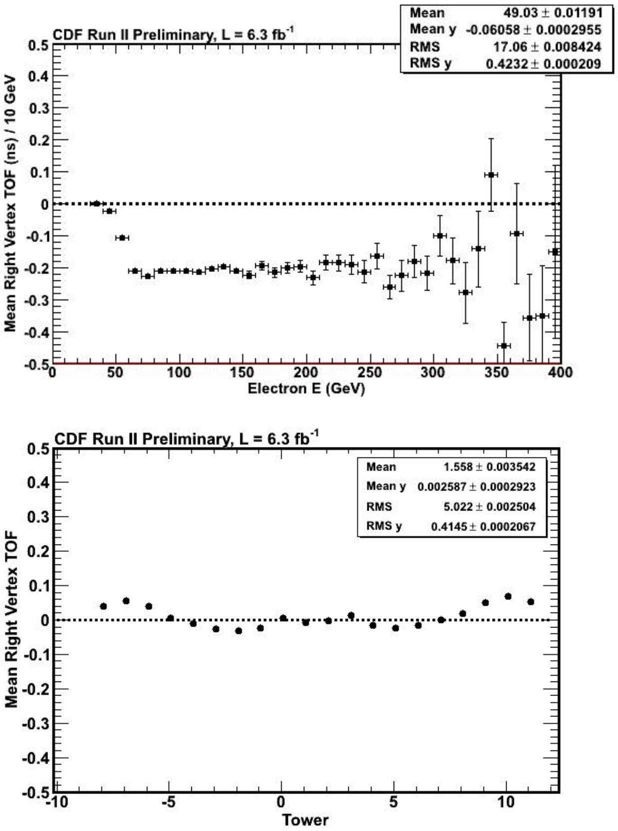

Figure 3.15: The mean time-of-flight correction from the right vertex, instead of $z =$ 0 cm, as a function of energy and tower after calibrations for the W→ $e\nu$ sample. The evidence of variation in this variable gives us an understanding of why calibrating versus t^0_{corr} does not take into account the effect due to detector and reconstruction properties of the sample of events.

4. NON-COLLISION BACKGROUNDS

4.1 Overview

Non-collision based sources can produce objects that look like photons and can fake the exclusive $\gamma_{delayed}+\not\!\!E_T$ final state [76]. The most common sources of these non-collision backgrounds include cosmic ray muons which interact with the detector (discussed in Section 4.2), beam interactions with the beam pipe, commonly referred to as "beam halo" (discussed in Section 4.3), and satellite bunch interactions resulting from unexpected collisions between stray proton and antiproton bunches that did not form with the main bunches (discussed in Section 4.4). Each of these sources has a different rate of production that passes all the final selection requirements, has a different t_{corr} distribution and thus affect the search differently. In this section we will describe these backgrounds individually and detail the rejection and estimation methods used for each.

In Table 4.1 we lay out the selection criteria we use to create a presample of events likely originating from non-collision sources. We will use this sample to study the effects of the various selection criteria applied in order to reject non-collision backgrounds. Depending on the particular non-collision background being studied, additional cuts will be added to produce a pure sample of cosmic rays, beam halo, and satellite events.

4.2 Cosmic Rays

Cosmic rays are charged particles that originate in outer space and then interact with the Earth's atmosphere producing secondary charged particles that then shower down to the Earth's surface, as shown schematically in the top of Figure 4.1. If these particles have an energy of ∼GeV they can reach the surface of the Earth and interact

Event Selection
Pass Trigger and Good Run List *(See Table 2.2 and 2.3 and Section 2.4)*
Pass Tight Photon requirements w/ $E_T^0 > 30$ GeV and $\not\!\!E_T^0 > 30$ GeV *(See Table 2.8 and Section 2.4.6)*
No SpaceTime Vertex Reconstructed *(See Table 2.10)*

Table 4.1: List of cuts summarizing the non-collision background presample.

with our detectors [77]. The bottom of Figure 4.1 shows a cartoon representation of a cosmic ray that interacts with the detector in such a way that produces a signal which mimics a photon. If this happens in coincidence with an unrelated collision in the detector this may lead to both incorrectly assigning the "photon" to a vertex that had nothing to do with its production as well as leaving an imbalance of energy in the detector which is misidentified as $\not\!\!E_T$.

The mis-identification of a photon can occur if the cosmic ray produces an electromagnetic cluster via a bremsstrahlung interaction or a high q^2 interaction showering within the EM calorimeter [76]. This "outside-in" topology of a cosmic ray event allows us to develop a series of selection requirements to help veto against misidentifying an EM cluster from a cosmic ray event versus a real photon coming from a collision.

There are three main selection criteria used in this analysis to veto events which are likely to have originated from cosmic rays, summarized in Table 4.2. We note for completeness that many of these requirements are what we would call photon ID requirements and were included for completeness in Table 2.8. All of these selection criteria ("cuts") take advantage of the fact that a cosmic ray will come from the outside of the detector and propagate inside (the reverse of how a collision created photon will go). The first of these utilizes the muon subdetector located on the outer radius of the CDF detector, the second examines the energy found in the hadronic calorimeter, and the third considers the energy as measured by the CES. All are discussed in more detail in Appendix A and summarized here.

The first of these cuts, known as a "muon-stub" veto, has been used at CDF for many years and in previous delayed photon searches with great success [38, 76]. This cut is discussed in more detail in Appendix A.1. To quickly summarize, the algorithm uses the muon detection system, described in Section 2.2.4, located on the outer radius of the CDF detector, and looks for activity in this outer detector within a close angle ($|\Delta\phi| < 30°$) to the electromagnetic cluster giving an indication that the "photon" may have originated from a cosmic ray source. As reported in Reference [76], using the sample in Table 4.1, but requiring 20 ns $< t_{corr} <$ 80 ns to create a pure sample cosmics. We find that the muon-stub veto rejects $\sim$80% of all events in our sample. To measure the efficiency of this requirement we consider our electron control sample, selected using the requirements in Table 3.1. We find that $\sim$95% of real electrons would pass this requirement.

The second cosmics rejection requirement is based on the fact that we expect high-energy photons from collisions to shower mostly in the EM calorimeter (located closer to the collision point) but leave some energy in the HAD calorimeter (located further out from the collision point, directly behind the EM calorimeter). However cosmic ray photon candidates typically leave very little energy in the HAD calorimeter, and do so in a way that is largely independent of the energy deposited in the EM. Therefore we require a small amount of energy in the HAD, but require that amount to go up as a function of the photon E_T. The details of this cut can be found in Appendix A.2. Using the same samples as above, but with the addition of the muon-stub requirement, we find that a selection criteria of the HAD(E) $\geq$ -0.30+0.008$\cdot E_T$ is 95% efficient for electron data with a 66% rejection power for cosmic ray photons.

The third of the cosmic ray veto selection requirements we use takes advantage of the fact that comic rays photons do not typically shower in the CEM in the same was as photons from a collision. Specifically, cosmic rays will deposit a very small fraction of their total energy in the CES detector (CES(E)) when compared to the total energy in the rest of the calorimeter tower. As detailed in Appendix A.3, we use a selection $\frac{\text{CES(E)}}{\text{TotalE}}$ >0.2 as well as requring a minimum CES(E)>10 GeV of energy to be present in the CES. Using the same samples as described above, but after the HAD energy criteria, we measure the CES energy cuts to be 92% efficient for collision electrons. Since there is a correlation between the way cosmic rays and real photons interact with the detector, we consider the combined effectiveness of the requirements and have a 76% rejection of cosmic ray photons.

Variable	**Selection Criteria**
μ-Stub $\|\Delta\phi\| <$ 30°	< 1
Had(E) *Hadronic Energy deposited*	$\geq$ -0.30 + 0.008$\cdot E_T$
CES(E) *Total Energy in the CES*	$\geq$10 GeV $\frac{CES(E)}{TotalE} \geq 0.2$

Table 4.2: Summary of requirements used to veto photon candidates as originating from cosmic rays. Note, the hadronic energy cut Had(E), CES(E), and the fraction of energy deposited in the CES (CES(E)/Total E) are included in the photon ID variable listed in Table 2.8. We include them here in order to explain why these non-standard cuts are present in the photon ID used in this analysis.

Now that we have finished our description of the cosmic ray rejection requirements, we turn to methods of how these backgrounds contribute to the signal region. It is straight forward to determine the rate of cosmic rays per ns in $\gamma+\not\!\!E_T$ events from the cosmics region and extrapolate to the number of events expected in the signal region. To create a pure cosmics sample from the non-collision presample, defined in Table 4.1, we add requirements to ensure these events are not beam halo and requirements to help ensure they are from cosmics. Specifically, we require ≥ 1 μ-Stub with a $|\Delta\phi| < 30°$, Had(E)<-0.30 + 0.008$\cdot E_T$, CES(E) $\leq$ 10 GeV, and $\frac{\text{CES(E)}}{\text{TotalE}}$ <0.2 to all be true. We also require the event not be identified as beam halo using the requirements in Table 4.3. As shown in Figure 4.2, the timing distribution does in fact appear flat with respect to time for most of the timing region. Furthermore, we can validate that the rate at which cosmic rays occur in the cosmics region (20 ns $< t^0_{corr} <$ 80 ns) is roughly the same as the rate in the signal region (2 ns $< t^0_{corr} <$ 7 ns) in data. It is worth noting that the gradual rise and fall of the number of events from -60 ns $< t^0_{corr} <$ -20 ns and 100 ns $< t^0_{corr} <$ 120 ns is the beginning and end of the energy integration window for the calorimeter as described in Section 2.2 and is thus a well understood phenomenon.

Having established the basic event selection criteria used to veto against cosmic ray events, summarized in Table 4.2, we now turn to detailing the method by which we estimate the rate at which cosmic rays pass the final $\gamma+\not\!\!E_T$ requirements using the data. Since the event rate is a flat as a function of t_{corr} we can estimate the cosmic ray rate in the signal region (2 ns $< t_{corr} <$ 7 ns), $N^{cosmics}_{\text{SignalRegion}}$, using a sideband timing region where we do not expect to see any collision sources. One such timing region, as seen in Figure 4.2 (selected using the requirements in Table 4.1, Table 4.2 and Table 4.3) is given by 20 ns $< t_{corr} <$ 80 ns and we call this the "cosmics region". The number of events measured in this region, after all the final cuts, is $N^{cosmics}_{\text{SignalRegion}}$. Specifically, we can estimate the number of events in the signal from the number of events in the cosmics region using

$$N^{cosmics}_{\text{SignalRegion}} = \Delta T_{\text{SignalRegion}} \cdot \frac{N^{cosmics}_{\text{CosmicsRegion}}}{\Delta T_{\text{CosmicsRegion}}} \tag{4.1}$$

$$= 5\,\text{ns} \cdot \frac{\text{N}^{\text{cosmics}}_{\text{CosmicsRegion}}}{60\,\text{ns}} \tag{4.2}$$

$$= \frac{1}{12} N^{cosmics}_{\text{CosmicsRegion}} \tag{4.3}$$

4.3 Beam Halo

Beam Halo related backgrounds arise from particles created in interactions between the beam and material near the beam pipe upstream of the CDF detector. This background has been studied at CDF for many years, as described in greater detail in Reference [76]. We quickly describe this background and the standard methods for rejecting it. As shown in Figure 4.3, these particles travel parallel to the beam and thus form a "halo" around it and gives this background its name. By and large, the particles that interact with the detector are muons (typically from the decay of $\pi^+ \to \nu\mu$) that can travel through the calorimeter, not entirely unlike a cosmic ray particle. This beam halo can traverse the HAD and/or EM calorimeters where, if they interact, they can deposit energy in the detector. While these particles typically have a minimum ionizing interaction, and leave a small amount of energy in multiple towers, they can deposit significant energy in a single EM tower and thus mimic a photon candidate in the detector. Since the photon candidate is uncorrelated with the collision this produces an equal and opposite amount of $\not\!\!E_T$ in the detector. An unrelated collision that creates a vertex could otherwise put these events into our final γ+$\not\!\!E_T$ final sample.

The timing of beam halo photons is very different from cosmic ray backgrounds and collision backgrounds. These beam halo "photons" typically arrive a few nanoseconds earlier than prompt photons from collisions owing to the nature of the beam structure which was outlined in Section 2.1; this makes them potentially a large source of γ+ $\not\!\!E_T$ events, but small source in the signal region. Similarly, while the rate is lower, these beam halo "photons" also arrive at $\sim$18 ns intervals following the primary collision and can be observed with the EMTiming system. Therefore, for these events to appear in the signal region we need events from beam halo interactions to occur early or for resolution issues to push them into the signal region.

Before showing the timing distribution of beam halo candidates, we describe more how to identify them. Like the cosmic ray photons, the unique topology of beam halo events lends itself to developing a set of selection criteria to veto "photons" coming from beam halo sources. The first of the beam halo selection criteria looks for activity in the same wedge as the "photon" candidate coming from when the minimum ionizing particle was traversing the wedge parallel to the beam. If we find 8 or more hits, each of which have E_T^0 >0.1 GeV, in adjacent towers in the same wedge as the photon candidate we veto this event as likely having come from a beam halo interaction. This number of hits is referred to as 'seedWedge' in Table 4.3.

The second of these selection criteria looks at hadronic towers located at $|\eta_{detector}| > 1.0$ portion of the detector in the same wedge and we count the number of hits with E_T^0 >0.1 GeV. If we find 2 or more hits at $|\eta_{detector}| > 1.0$ then we veto this photon candidate as likely coming from a beam halo source which traversed the entire detector. This the number of hits is labeled as 'NHadPlug' in Table 4.3 because the calorimeter with $|\eta_{detector}| > 1.0$ is known as the "plug" calorimeter.

These selection criteria are summarized in Table 4.3 and have been well vetted and used in previous delayed photon searches at CDF with great success as shown in References [41, 38, 76]. It should be noted that these cuts are used on the "logical or", such that if the event fails either one it is discarded as likely coming from a beam halo source. These beam halo vetos have been shown to be $> 98\%$ efficient for real photons and electrons while vetoing almost all the associated beam halo events [76].

seedWedge *Number of Hits with* E_T^0 *>0.1 GeV in the same wedge as the photon*	≥ 8
NHadPlug *Number of plug HAD tower hits with* E_T^0 *>0.1 GeV*	≥ 2

Table 4.3: Summary of requirements used to identify and veto photon candidates as originating from beam halo sources.

To study the timing of beam halo candidates we create a pure sample of beam halo events in data by selecting events which pass the requirements in Table 4.1, as well as applying the cosmic ray vetos, defined in Table 4.2, and inverting the beam halo veto, defined in Table 4.3. We note that when we invert the vetos defined in Table 4.3 we explicitly require the candidate photon to have seedWedge >8 and NHadPlug > 2. The timing distribution in Figure 4.4. Immediately it can be seen that the structure of the timing events is exactly what we expect from the beam structure with the majority of events coming slightly before $t^0_{corr} = 0$ ns with peaks at ~18 ns and 36 ns corresponding to the radio frequency bucket length of the beam.

To estimate the amount of beam halo present in the final γ+$\not\!\!E_T$ selection we look at the timing region -10 ns $< t^0_{corr} <$ -5 ns in Figure 4.4. We note that this region contains ~40% of all the pure beam halo data while the signal region contains ~10%. Thus, we can look to the exclusive γ+$\not\!\!E_T$ sample in the region -10 ns $< t_{corr} <$ -5 ns and estimate the amount of beam halo in our final sample. By taking the measured cosmics rate (from the cosmics region) and subtracting that from the data in the region -10 ns $< t_{corr} <$ -5 ns, we overestimate that all the remaining data from -10 ns $< t_{corr} <$ -5 ns is from beam halo we will have an upper bound on the amount of beam halo in our sample. As we will see in Section 7, the beam halo rate is measured to be <1% of the final sample and negligible in our final search.

4.4 Satellite Bunches

The last non-collision source we will consider originates from collisions that are not part of the primary beam-beam interactions. As described in Section 2.1, during the process of forming the proton and antiproton bunches, in the RF cavities in the Main-Injector, some of these bunches can form outside of their prescribed location in z and t. In particular this can create bunches that fall out of the main bunch "bucket" with half RF cavity timing at $\sim$1% the main bunch intensity [79] as estimated using the resistive wall detector in the Main-Injector, decribed in greater detail in Reference [48]. When these stray bunches are then carried along in the beam we call them "satellite bunches" and they present a unique background to the delayed photon search. These satellite bunches are observed to proceed and lag the main bunches used for collisions as shown in Figure 4.5 which is the same structure as seen in the beam halo timing distribution.

The resulting timing distribution from interactions of these satellite bunches with the main bunches, as well as with their counterparts, could potentially produce events with photons that arrive later than we expect or with very large z with respect to the center of the detector. Particularly, we simulate what the t_{corr} distribution would look like in Figure 4.6 using MC methods if the satellite bunch interactions produced photons from their collision (but arriving in the detector evenly distributed in z CES) and we incorrectly assigned a vertex that occurred at $t = 0$ and $z = 0$ (this being the most likely place for a collision to occur). We can see from Figure 4.6 that we would expect to see an excess of events at ±5 ns and ±10 ns coming from main bunch - satellite bunch interactions and satellite bunch - satellite bunch interactions respectively. However, it is not possible to know directly how big of an effect this potentially is in the exclusive $\gamma+\not{E}_T$ final state from simulations.

To study the timing of satellite bunch candidates we create a pure sample of non-collision events in data using the non-collision presample, defined in Table 4.1, as well as applying the cosmic ray vetos, defined in Table 4.2, and the beam halo veto, defined in Table 4.3. This study was performed on a portion of the total data ($\sim$5 fb^{-1}) used in the final sample, but the results are believed to scale directly with luminosity. We construct the t^0_{corr} distribution for the remaining events since there is no vertex in the event. We then estimate the cosmics rate by estimating the number of cosmics from the cosmics region (20 ns $< t^0_{corr} <$ 80 ns) and subtract this off. We plot the result in Figure 4.7. Clearly there is very little activity observed at ±5 and ±10 ns where we would expect to see evidence from satellite bunch interactions. The central peak is believed to be from main bunch interactions that simply did not reconstruct a SpaceTime Vertex.

Using the scale of the main peak to the event rates observed at 5 and 10 nanoseconds we are able to conclude that the satellite bunch interaction rate is <1% when compared to our collision backgrounds. Moreover, we can see leakage from beam halo in Figure 4.7 at the peak near 18 ns, leading us to believe that beam halo (already established as a small background for the exclusive $\gamma_{delayed}$+$\not\!\!E_T$ final state) is a much larger background then satellite bunches. Using these results as a guide, we do not add any additional cuts to reject against satellite bunch interactions concluding that this produces a negligible number of events in the signal region for this analysis.

Having finished a discussion of non-collision based backgrounds for the exclusive $\gamma_{delayed}$+$\not\!\!E_T$ final state we now return to the SM backgrounds and sources of timing biases. We note that the only background we will consider further in our final study is from cosmic ray sources, and that will be the dominant background. We will make additional comments about beam halo as well for our final data sample once we have finished the full set of requiremnts for the γ+$\not\!\!E_T$ dataset.

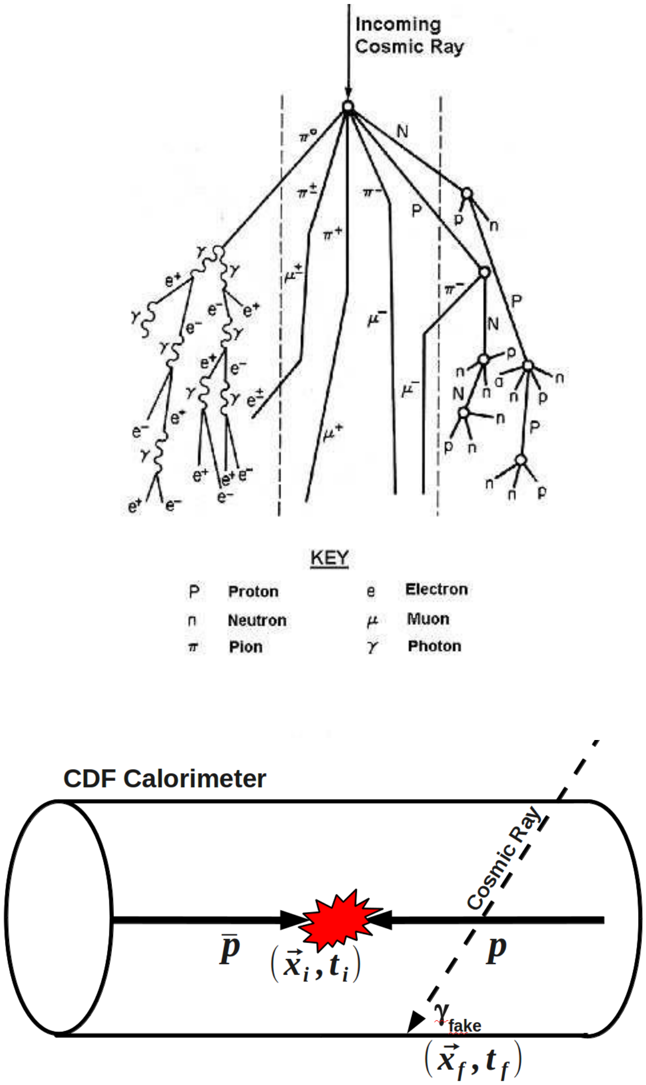

Figure 4.1: (Top) Cartoon schematic of how an incoming cosmic ray can interact with the atmosphere and create a cascade of particles which, if they originate with enough energy, can reach the surface of the Earth and appear in our detector. Taken from Reference [78]. (Bottom) Schematic view of how a cosmic ray can create a $\gamma+\not\!\!E_T$ candidate event if it produces a fake photon in the detector that arrives in coincidence with a collision.

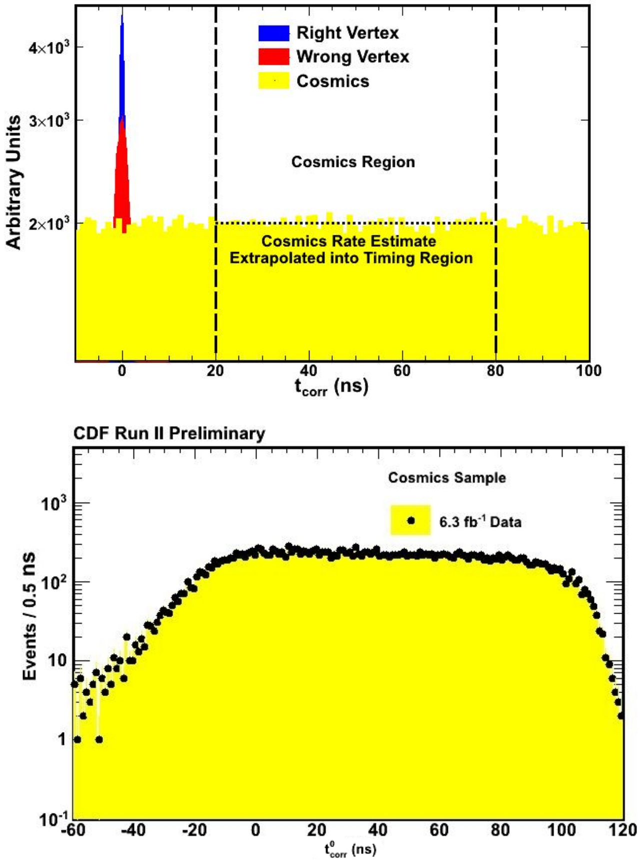

Figure 4.2: (Top) Schematic of the timing distribution of cosmic ray events present in photon data. The timing distribution is roughly flat over time allowing us to estimate the rate of cosmics in the signal region by measuring it in the region 20 ns $< t_{corr} <$ 80 ns. (Bottom) Timing distribution of of our cosmic ray presample selected from photon data, using Table 4.1 and the inversion of the cuts in Table 4.2 and 4.3. The timing distribution is roughly flat over time allowing us to estimate the rate of cosmics in the signal region from data.

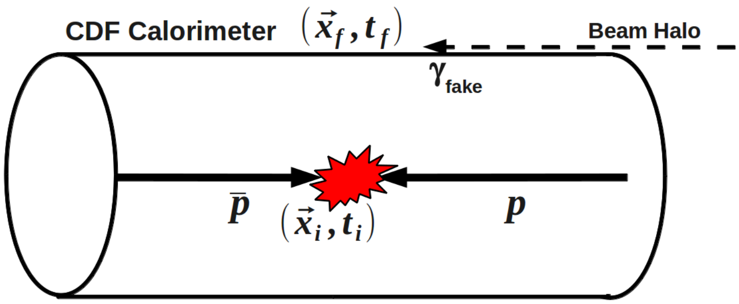

Figure 4.3: Schematic view of how beam halo can create fake photons in the detector if they happen to arrive in coincidence with a collision.

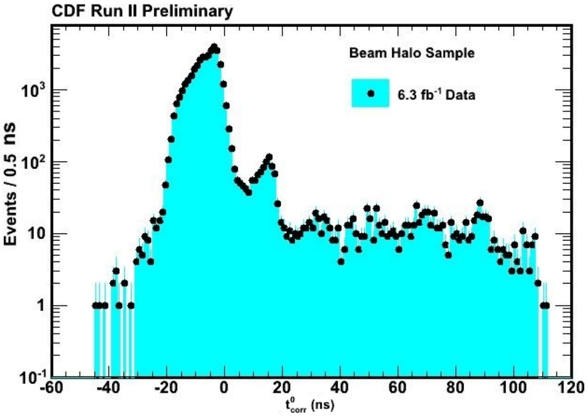

Figure 4.4: Timing distribution of beam halo events selected from photon data by applying the non-collision presample, defined in Table 4.1, as well as applying the cosmic ray vetos, defined in Table 4.2, and inverting the beam halo veto, defined in Table 4.3. We note that when we invert the vetos defined in Table 4.3 we explicitly require the candidate photon to have seedWedge >8 and NHadPlug > 2. Here you can see the structure in the timing distribution created during the coalescing of the proton-antiproton bunches.

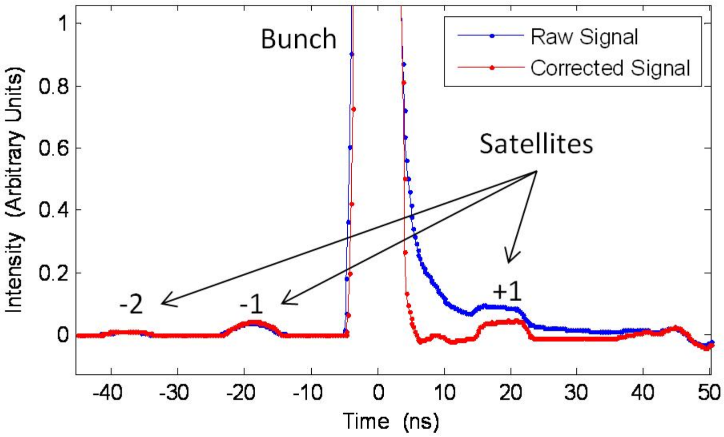

Figure 4.5: Plot of beam intensity output as measured by the Main Injector resistive wall detector (as described in Reference [48]) for the Tevatron proton and satellite bunches, taken from [79]. This shows that the satellite bunches both proceed and follow the main bunch by tens of nanoseconds with approximately one percent the intensity of the main bunch.

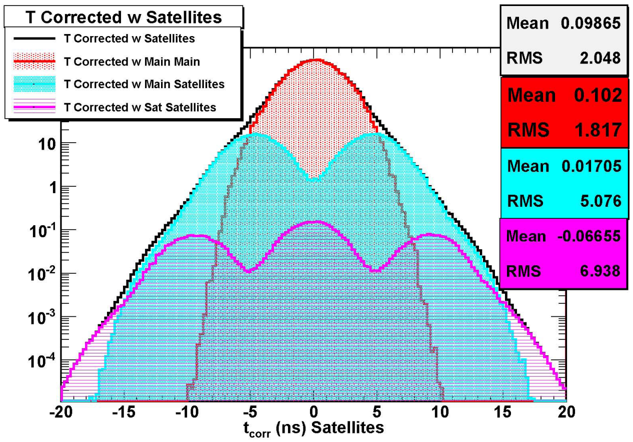

Figure 4.6: Monte Carlo simulation of the t^0_{corr} distribution for beam-beam, beam-satellite, and satellite-satellite bunch collisions.

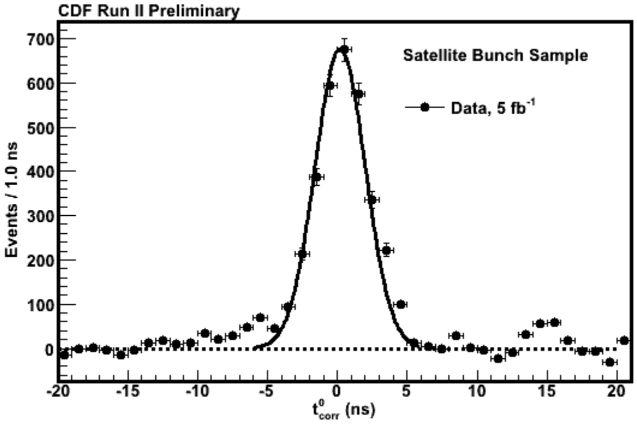

Figure 4.7: Timing distribution of events selected to look for the presence of satellite bunches in data. We construct the t^0_{corr} distribution since there is no vertex reconstructed in the event. We estimate the cosmics rate from the cosmics region (20 ns $< t_{corr} <$ 80 ns) and subtract this off. We note that there is no evidence for satellite bunch interactions being a significant source of backgrounds and thus we do not apply any specific method to reject against them. Note, there is some evidence for beam halo sources with events below -5 ns and a peak at 15 ns.

5. STANDARD MODEL BACKGROUNDS AND TIMING BIASES IN THE EXCLUSIVE γ+$\not\!\!E_T$ FINAL STATE

In this section we describe the SM backgrounds that are present in the exclusive $\gamma_{delayed}$+$\not\!\!E_T$ final state. We first establish what the backgrounds are to the γ+$\not\!\!E_T$ final state and their relative importance to the final search region used in this dissertation. As we will see, various SM backgrounds have timing distributions, after the preliminary cuts, that can be very biased toward large values of t_{corr} when the wrong vertex is selected. Moreover, in the exclusive $\gamma_{delayed}$+$\not\!\!E_T$ final state there is explicitly a lack of other final state particles, thus there are fewer tracks present in the event to produce a vertex. This means that for the SM backgrounds the collision which produced the photon is both less likely to have its vertex reconstructed and less likely to be selected as the highest ΣP_T vertex used in the timing measurement and photon identification.

After a description of the timing distribution for wrong vertex events and detailing the SM backgrounds, we present a study of SM events that give large times and find, in general, three types of events that give large times. These large times are produced two ways, when a background source: 1) produces a small number of individual events with anomalously large times and/or 2) passes the final γ+$\not\!\!E_T$ requirements in a way this is biased, on average, towards positive t_{corr} when a wrong vertex is selected. After describing each of these ways that events can have large times, we discuss how to remove/mitigate each problem. Once these steps are taken to reduce the amount of bias present in the wrong vertex distribution we then look at the timing distribution of the known SM backgrounds. In the next section we describe how to measure the remaining amount of bias present in the sample.

5.1 Overview of the double Gaussian description of the timing

As described in Section 1, the timing distribution for SM events is well described by a combination of events with a right vertex and events where the a wrong vertex is selected. We next detail more about why our events have these Gaussian shapes. The origin of the Gaussian timing distribution for right vertex events can be understood from the fact that all the measurements of the four quantities for t_{corr} in Equation 1.8 are simple, but dominated by the EMTiming measurement which is a Gaussian measurement (when a discriminator fires a TDC) which has a resolution of 0.5 ns. Taken in quadrature with the other terms (resolution of the vertex time and the time of flight) we get a Gaussian with an RMS of 0.65 ns, as shown in Section 3. More details about the resolution of the measurement are given in Reference [52].

The timing distribution for wrong vertex events is more subtle, but still readily described by a Gaussian with an RMS of $\sim$2 ns but a mean that is not zero, as shown in Figure 1.16. To understand this we describe the calculation of the timing distribution for wrong vertex (WV) events. Specifically,

$$t_{corr}^{WV} = t_f - t_0^{WV} - \frac{|\vec{x_f} - \vec{x_0}^{WV}|}{c} = t_f - t_0^{WV} - TOF_{WV} \tag{5.1}$$

where t_0^{WV} and x_0^{WV} are the time and collision z position of the wrong vertex, and where we have relabeled the last term as the time-of-flight from the wrong vertex to the position of the photon in the calorimeter, TOF_{WV}. However, we note that $t_f = t_0^{RV} + TOF_{RV}$ where TOF_{RV} is the time-of-flight from the true collision point to calorimeter location. Plugging into the equation above we find:

$$t_{corr}^{WV} = (t_0^{RV} + TOF_{RV}) - t_0^{WV} - TOF_{WV} \tag{5.2}$$

and re-writing in a suggestive form we find

$$t_{corr}^{WV} = (t_0^{RV} - t_0^{WV}) + (TOF_{RV} - TOF_{WV}) \tag{5.3}$$

The first term in Equation 5.3 is made up of two parts, both given by the Tevatron beam timing structure as described in Section 2.4.5. Both are independent of each other and well described by a Gaussian with a mean of zero and an RMS of 1.28 ns as shown in Figure 3.10. Thus, we expect them to give a contribution to the final value of $< t_{corr}^{WV} >$ of 0 ns with an RMS of $\sqrt{2} \cdot 1.28 = 1.8$ ns and a shape that is roughly Gaussian. The second term is pure geometry and can have a mean value that can be many hundreds of ps, but an RMS that, except for the most mis-measured events, is typically small compared to the 1.8 ns of the first term. We will often refer to this term as the bias and it is what produces the events with a large time as well as an overall mean in the wrong vertex distribution. Thus, we see that the wrong vertex timing distribution is expected to not be centered at zero, but will be, to a high degree of approximation, well described by a Gaussian with an RMS slightly above 1.8 ns because of the resolutions of the EMTiming system and the COT vertex time; as we will see in Section 5.6 the RMS will be measured measured with MC and data to be 2.0 ± 0.1 ns taking into account all known effects, such as the 0.5 ns resolution on the EMTiming. As was shown in Figure 3.2, a $< t_{corr}^{WV} > \sim 0.5$ ns can cause there to be twice as many events in the signal region as in the control region for SM backgrounds.

This description of the t_{corr} distribution as a double Gaussian with right and wrong vertex is confirmed when we look at data from $e + \not{E}_T$ calibration events in the top of Figure 5.1 (data selection described in Table 3.1). Here we pick the highest ΣP_T vertex as the inital collision position (t_0 and z) to calculate the corrected time.

Using the matching of the electron track to the vertex we can further divide this distribution into the right and wrong vertex samples individually. This is done in order to verify the Gaussian nature of both distributions. This description clearly models the data very well and thus gives us confidence in the use of a double Gaussian function to describe the corrected time of collision events.

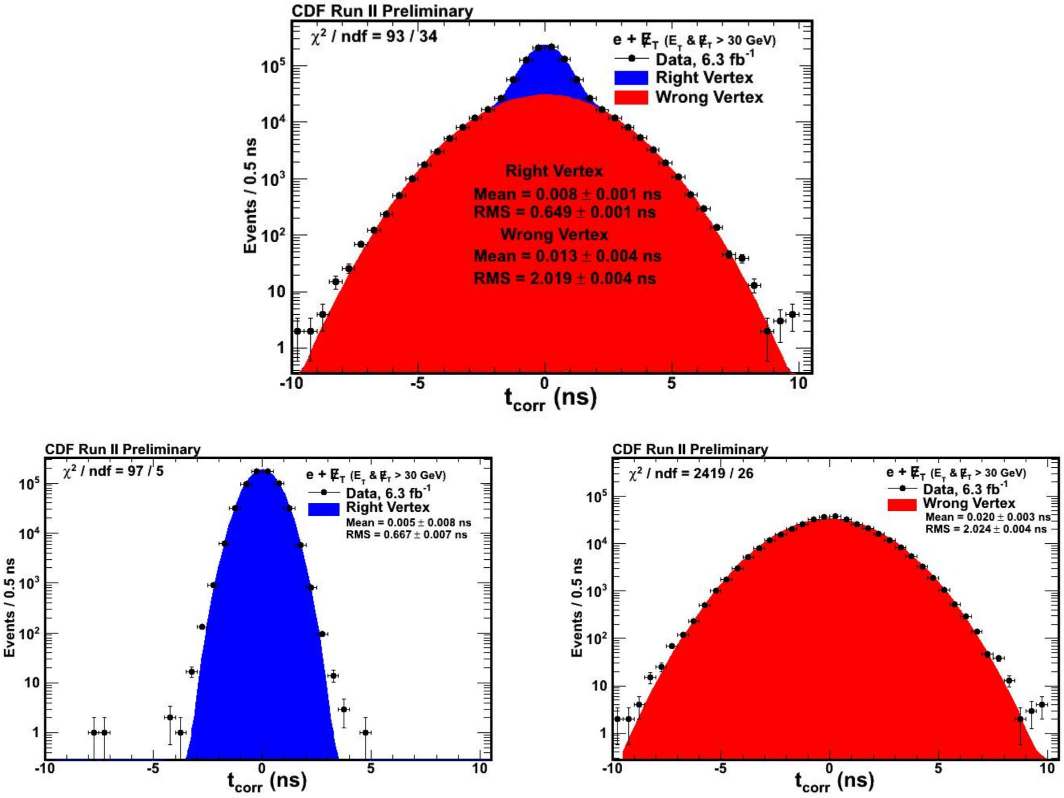

Figure 5.1: The t_{corr} distribution using the $e+\not\!\!E_T$ calibration data (defined in Table 3.1) using the highest ΣP_T vertex (top) as well as the right and wrong vertex Gaussians using the matching of the electron track to the vertex (bottom) verifying the description of the timing distribution as being well described by a double Gaussian distribution of two well understood and seperate contributions.

5.2 Standard Model Backgrounds

We now turn to the various SM processes that can produce the exclusive $\gamma+\not\!\!E_T$ final state with an eye towards the biases each might bring to the wrong vertex timing distributions. Since the appearance of a single photon plus missing energy with little other activity present in the detector is a very unlikely thing to have coming directly from SM processes, the presence of these backgrounds normally results from a coincidence of various processes taking place in the detector which is likely to have a bias. For example, a W$\rightarrow e\nu$ event will usually produce significant $\not\!\!E_T$ from the neutrino, but will only have the electron mis-reconstructed as a photon a tiny fraction of the time, but in a way that produces a biased time. This is because electrons that have longer path lengths are more likely to produce a fake photon as well as have a large value of t^{WV}_{corr} since TOF_{RV} will be longer, on average, than TOV_{WV}. Broadly speaking this type of coincidence of unusual occurances is what occurs for all our SM processes. Almost all have a very large production cross-section while the occurrence of the detector or reconstruction failing to properly reconstruct the collisions is a small fraction. This multiplication of a large number (SM cross-section) times a small number (detector/reconstruction failure) makes a direct estimate of SM backgrounds using only MC methods difficult as elaborated upon below.

We focus on MC simulation of all known SM sources that produce γ+$\not\!\!E_T$ for any and all types of example events that could give a large time bias. Said differently, we use each observed event in the MC with a large time to try and construct an understanding of what types of events cause a bias. By studying all the sources below, we have confidence that we have considered all the important sources of large time events that can be produced.

We next describe all the SM backgrounds that produce the γ+$\not\!\!E_T$ final state, summarized in Table 5.1 using the MC samples described in Table 2.12. We note that the rates from each background is never determined individually, but are done collectively using the data-driven procedures described in Section 6.

Standard Model Process
W$\rightarrow$ e$\nu \rightarrow \gamma_{fake} + \not\!\!E_T$
γ+Jet $\rightarrow \gamma$+Jet$_{Lost} \rightarrow \gamma + \not\!\!E_T^{fake}$
Z$\gamma \rightarrow \gamma\nu\nu \rightarrow \gamma + \not\!\!E_T$
W$\rightarrow \mu\nu \rightarrow \gamma_{fake} + \not\!\!E_T$
W$\rightarrow \tau\nu \rightarrow \gamma_{fake} + \not\!\!E_T$
W$\gamma \rightarrow$ lepton$_{lost}$ $\nu\gamma \rightarrow \gamma + \not\!\!E_T$

Table 5.1: Summary of the various SM backgrounds considered for the exclusive $\gamma_{delayed}$+$\not\!\!E_T$ final state. Each sample of events is simulated with MC with more details given in Table 2.12.

- W$\rightarrow$ e$\nu \rightarrow \gamma_{fake}$+$\not\!\!E_T$:

  The first of the processes considered for the exclusive $\gamma_{delayed}$+$\not\!\!E_T$ final state comes from the SM process where a W boson is produced from the collision and the subsequently decays to an electron (e) and a neutrino (ν) but where the electron is identified as a photon (commonly referred to as a γ_{fake}) in the detector. The probability of the electron faking a photon of ~1% [80]. Of particular importance, W$\rightarrow$ e$\nu \rightarrow \gamma_{fake}$+$\not\!\!E_T$ events often have the wrong vertex selected, for reasons explained later, and do so in ways that have large values of $TOF_{RV} - TOF_{WV}$ (the second term in Equation 5.3). Specifically, the ways that electrons fake photons, and the E_T distribution of electrons from W$\rightarrow$ e$\nu \rightarrow \gamma_{fake}$+$\not\!\!E_T$ events can both bias $< t^{WV}_{corr} >$ distribution as well as significantly change which events enter and leave our sample. This is elaborated on further in Section 5.5.1. We note that W$\rightarrow$ $e\nu$ events that are produced in association with a photon, but where the electron is not reconstructed by the detector (referred to as Wγ) are included in a later background.

- γ+Jet $\rightarrow \gamma$+Jet$_{Lost} \rightarrow \gamma + \not\!\!E_T^{fake}$:

  QCD processes, such as a photon plus a jet coming from a quark or gluon

(γ+Jet), do not have any intrinsic $\not\!\!E_T$ in their production. However, a large value of $\not\!\!E_T$ can be measured in the event via mis-reconstruction or mis-measurement of the energy contained in the reconstructed jet or photon. One such example of how this can occur is when energy from the jet is produced at large $|\eta|$ and travels down the beam pipe or otherwise hits an un-instrumented region of the detector. While the fraction of QCD events with a mis-measurement of $\not\!\!E_T$ as high as 45 GeV is very small (<5%), the total QCD cross section is very large ($\mathcal{O}$(1000's pb)) [3], thus making this another potentially large background to γ+$\not\!\!E_T$ final state. In particular, it can be a significant background to exclusive $\gamma_{delayed}$ + $\not\!\!E_T$ because the topology of the events that do pass have a high correlation between large $\not\!\!E_T$ and the vertex being mis-measured or not reconstructed in a way that biases this sample towards large values of $TOF_{RV} - TOF_{WV}$. This process is presented in greater detail in Section 5.5.3.

- Z$\gamma \rightarrow \gamma\nu\nu \rightarrow \gamma + \not\!\!E_T$:

  An irreducible background in the exclusive γ+$\not\!\!E_T$ final state comes from the production of a Z boson made in association with a photon from initial state radiation. The Z subsequently decays into to a pair of neutrinos which escape the detector in the form of $\not\!\!E_T$ and we thus end up with the γ+$\not\!\!E_T$ final state. While the decay rate of the Z boson to pairs of neutrinos is much higher than to charged leptons (which we are able to veto with a high efficiency), the rate at which a 45 GeV photon is produced in the central part of the detector is small. The topology of these events causes a relatively small wrong vertex mean, as will be discussed further in Section 5.6. This further diminishes the importance of this otherwise irreducible background.

- $W \rightarrow \mu\nu, W \rightarrow \tau\nu$, and $W\gamma$ sources:

The last major sources of backgrounds in the exclusive $\gamma+\not\!\!E_T$ final state are from W$\rightarrow$ lepton + ν boson sources where the lepton may fake a photon or become lost. Two such examples of this decay are W$\rightarrow$ $\mu\nu \rightarrow \gamma_{fake} + \not\!\!E_T$ and W$\rightarrow$ $\tau\nu \rightarrow \gamma_{fake} + \not\!\!E_T$. While the production cross-section of these processes is known to be relatively large ($\sim$1000 pb[81]), the likelihood of these leptons faking a photon is much smaller than for electrons [61] in the CDF detector. Therefore we do not devote any specific cuts to rejecting these processes. The last of the W boson processes we consider comes from the production of a W boson with initial or final state radiation where the W boson decays to a lepton plus a neutrino and the lepton becomes "lost" (in contrast to "faking") in the detector giving us the $\gamma+\not\!\!E_T$ final state. This decay is dealt with in part in Section 5.5.2. In addition we note that the tracking efficiency in the CDF detector is known to be $> 95\%$ [50], thus making this a low rate background in this analysis.

5.3 Presamples and Control Samples for use in the Exclusive $\gamma_{delayed} + \not\!\!E_T$ Final State

Having finished an overview of the individual SM backgrounds that can produce the exclusive $\gamma + \not\!\!E_T$ final state, we now turn our attention to defining a number of "presamples" and "control samples" to help study them. A presample is a set of events that pass a set of selection requirements, but not all the final requirements so that we may study the effect of some of the later requirements. A control sample is a sample of events, data or MC, that is selected in a way so that it can be compared to the results expected from $\gamma+\not\!\!E_T$ events in data after all the requirements.

As previously mentioned in Table 5.1, we have six sources of SM backgrounds which are studied separately using independent MC data sets whose production were described in Table 2.12. Additionally, we have an e+$\not\!\!E_T$ data samples that will be used to generate sets of presamples and control samples. The specific set of selection requirements each presample will be given later, for now we simply summarize the two different types of presamples we will use.

- **Exclusive Electron and Missing Energy Sample:**

  This presample will mirror the γ+$\not\!\!E_T$ final state used in the final search except that instead of a photon we require an electron. Since the electron tracks in these events are excluded from use in the SpaceTime vertexing algorithm this presample provides a very good analog to the γ+$\not\!\!E_T$ sample as well as a data-based way of testing the background estimation methods described in Section 6.1. Particularly, the use of the electron track seperate from the vertex will allow us to have important information about the initial position and time of the event as well as provide a testing ground for our analysis. This presample will be used to create control samples in both our MC and data. The exclusive e+$\not\!\!E_T$ presample selection requirements is summarized in Table 5.2.

- **Exclusive Photon and Missing Energy Sample:**

  This presample is designed to mirror the selection used in the preliminary result from 2008 and allow us to study the effects of various background processes in this final state. This set of presample selection requirements will be used to create control samples from our MC datasets, help us understand the sources of biased events, and determine our background rejection requirements. The exclusive γ+$\not\!\!E_T$ presample selection requirements are summarized in Table 5.3.

We create ten control samples that will be used throughout the remainder of this dissertation. In particular, we create the six γ+$\not\!\!E_T$ samples from the MC datasets

Exclusive $e+\not\!\!E_T$ Presample Event Selection
Pass Trigger and Good Run List *(See Table 2.2 and 2.3 and Section 2.4)*
Pass Electron requirements w/ $E_T^0 > 45$ (30) GeV and $\not\!\!E_T^0 > 45$ (30) GeV *(See Table 2.9 and Section 2.4.6)*
Pass Beam Halo Rejection *(See Table 4.3)*
Pass Track Veto for Tracks with $P_T > 10$ GeV *(See Table 2.7)*
Pass Jet Veto for Jets with $E_T^0 > 15$ GeV *(See Table 2.5)*

Table 5.2: List of selection requirments summarizing the exclusive $e+\not\!\!E_T$ presample. Note, that our sample requires one with E_T^0 and $\not\!\!E_T^0$ at 30 GeV, but we will frequently make a subsample of this with requirements at E_T^0 and $\not\!\!E_T^0$ at 45 GeV. Note that the trigger, beam halo, and good run list requirements are only for data and not used on the MC.

described in Table 5.1 and require each event to pass all the preseample requirements in Table 5.3. Similarly, we create four samples of e+$\not\!\!E_T$ using real data and MC using the requirements in Table 5.2, but where we have one sample with $E_T > 45$ GeV to fully mimic the final requirements, and one with $E_T > 30$ GeV to give us better statistics. Finally, we will create a presample of $\gamma+\not\!\!E_T$ events from data that will be used to select cosmics events in Section 5.5.3. We will detail the control samples used in Section 6 after we have finished the event rejection requirements in this section.

5.4 Sources and Categorizing the Causes of Large Mean Shifts

With these samples in hand we are now ready to return to the task of showing the various pathologies and biases present in the exclusive $\gamma+\not\!\!E_T$ final state. This will show just how bad the underlying assumption that the wrong vertex mean is centered at $t_{corr} = 0.0$ ns can be and why it was particularly poor for the case in the preliminary study performed in 2008. We next provide a convenient categorization of

Exclusive $\gamma+\not{E}_T$ Presample Event Selection
Pass Trigger and Good Run List *(See Table 2.2 and 2.3 and Section 2.4)*
Pass Tight Photon requirements w/ $E_T^0 > 45$ GeV and $\not{E}_T^0 > 45$ GeV *(See Table 2.8 and Section 2.4.6)*
Pass Beam Halo Rejection *(See Table 4.3)*
Pass Cosmics Rejection *(See Table 4.2)*
Pass Track Veto for Tracks with $P_T > 10$ GeV *(See Table 2.7)*
Pass Jet Veto for Jets with $E_T^0 > 15$ GeV *(See Table 2.5)*

Table 5.3: List of selection requirments summarizing the exclusive $\gamma+\not{E}_T$ presample. Note that the trigger, good run list, beam halo, and cosmics requirements are only for data and not used on the MC.

the dominant effects that cause SM events to have large values of t_{corr}^{WV} as a prelude to a set of selection criteria to reject the most biased effects and minimize the $< t_{corr}^{WV} >$ distribution.

Rather than describe a historical summary of how we came to understand these effects, we quickly summarize the effects that cause large values of large time events and outline criteria to systematically remove or minimize their impact. In particular, the types of events that produce large values of $TOF_{RV} - TOF_{WV}$.

- **Events with Geometric and Kinematic Biases:**

  Incorrect selection of the vertex causes an incorrect $\sin\theta$ to be assigned to the measurement of the photon's E_T. This can cause events to be incorrectly included in our sample, as described in Section 5.5.1. This same effect can also cause a mis-measured/biased timing distribution because, as we will see, the E_T as mis-measured from the wrong vertex is highly correlated with $TOF_{RV} - TOF_{WV}$. This timing mismeasurement can lead to events migrating into the signal region and out of the control region and further exasperate problems in estimating the mean of the wrong vertex, thus ‘faking’ a signal.

In order to reduce the impact of this migration of events we will redefine our E_T variable. In doing so we will take advantage of the fact that on average most collisions occur at $z = 0$. This will be described in more detail in Section 5.5.1. This definition will have further advantages when we describe the background estimation techniques in Section 6.

- **Events with $e \rightarrow \gamma_{fake}$ Sources:**

  Incorrect selection of the vertex also causes the standard photon identification variables used to reject sources which “fake” a photon in the detector to become less powerful [82] because they assume the primary vertex. Specifically, identifications like track isolation currently require that the tracks being considered are within 5 cm of the primary vertex. Since selection of the correct vertex becomes a problem in the exclusive γ+$\not{E}_T$ final state, it becomes necessary to employ new ‘fake’ photon rejection. A second, and correlated, issue is that the same thing that makes an electron fake a photon, e.g. large path length, is also correlated with a large value of $TOF_{RV} - TOF_{WV}$ causing electrons that fake photons have a large value of $< t^{WV}_{corr} >$.

  Since the typical tools for $e \rightarrow \gamma_{fake}$ are found to be not as powerful in the case when the wrong vertex is selected, they are a problem for the exclusive $\gamma_{delayed}$+$\not{E}_T$ analysis. For this reason we have developed a new method whereby we can reject 67% of events coming from W$\rightarrow$ $e\nu \rightarrow \gamma_{fake}$+$\not{E}_T$ with a 95% efficiency for real photons. This removes the majority of the most biased events from the γ+$\not{E}_T$ sample. This is detailed in Section 5.5.2.

- **Events originating from Large $|z|$:**

  Finally, the last of the important reconstruction pathologies that effects the timing distribution comes from events originating from a large $|z|$ collision location. If there is a collision that occurs with $|z| >$60 cm which creates a real photon that is then observed in the central calorimeter, this vertex will not be reconstructed or reported by the SpaceTime vertexing algorithm. This is due to the fact that we explicitly require that the SpaceTime vertices used in the exclusive $\gamma+ \not\!\!E_T$ analysis to come from $|z| <$60 cm in order to have a good timing measurement associated with the vertex. If there happens to be a min-bias event near the center of the detector that creates a good SpaceTime vertex, a wrong vertex will be assigned to the event. This is most easily seen in γ + jet events where there is a high degree of correlation between the production of fake $\not\!\!E_T$ and large values of $|z|$.

  Since the timing bias from wrong vertex events can be especially large if the true collision occurred with $|z| >$60 cm, we reject events that have evidence of a collision occurring at large $|z|$ position. This will help minimize the wrong vertex mean bias as well as reduce the most pathologically mis-reconstructed events that have the largest value of $TOF_{RV} - TOF_{WV}$. This veto is detailed in Section 5.5.3.

5.5 Rejecting Backgrounds with Large Times

With this basic understanding of the types of events that have large times from wrong vertex pathologies, we next move to a description of how to reject many of these events. Since they come in three basic types, have created a set of three rejection criteria to systematically remove or minimize their impact. We will discuss in more detail how to measure the remaining amount of bias in the next section.

5.5.1 Minimizing the Correlations Between Geometric and Kinematic Biases

As seen in Figure 5.2, selection of a wrong vertex affects both the t_{corr} calculation as well as the E_T calculation. This occurs because the geometry of the events effects the kinematics, and vice versa and, for some samples of events, can cause events selected using the E_T of the photons to bias the mean time of the t_{corr}^{wv} distribution. To understand why this is particularly important for this search, we next describe the correlation between the measured E_T and t_{corr}.

Before we begin this discussion it is important to know the standard ways of measuring E_T in the detector which will illustrate why we do something a little different, as first described in Section 2. Specifically when we select the highest ΣP_T vertex we calculate $E_T^{Measured}$ and $t_{corr}^{Measured}$, but these may not be the same values as when measure them from the true vertex, E_T^{True} and t_{corr}^{True}. The same geometric effects which cause $E_T^{Measured} > E_T^{True}$ can also cause $t_{corr}^{Measured} > t_{corr}^{True}$. Before going forward it is also worth clarifying the use of the angle measured from the beamline, θ. As we can see from Figure 5.2, there are many different θ's that are possible to define. For example, there is θ_{True} which is θ measured from the true collision, and can be referred to as θ_{RV}. If we select a wrong vertex then we could refer to the $\theta_{Measured}$ as θ_{WV}. In general $\theta_{Measured}$ can be either θ_{WV} or θ_{RV}. Previously in this dissertation we have defined θ_0 as measured from the center of the detector and θ_{vertex} as measured from the vertex. In the following discussion we will use $\theta_{Measured}$ and θ_{True} as our notation to be more explicit where it is most helpful.

Consider the configuration in Figure 5.2 where the vertexing algorithm does not select the correct collision point, either because it is not reconstructed or because a higher ΣP_T vertex from a min-bias interaction happens to exist. In this case we have $\theta_{Measured} > \theta_{True}$, so that $TOF_{WV} < TOF_{RV}$ ($|\vec{x}_f - \vec{x}_{Measured}| < |\vec{x}_f - \vec{x}_{True}|$),

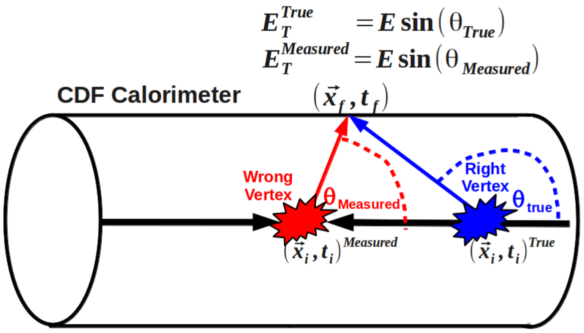

Figure 5.2: A schematic drawing of a W$\rightarrow e\nu \rightarrow \gamma_{fake}+\not\!\!E_T$ where we have selected a wrong vertex. For this example, the selection of the wrong vertex leads to an $\theta_{Measured} > \theta_{True}$ where θ_{True} is the real angle the photon/electron came from. This results in a larger measured value for E_T ($E_T^{Measured} > E_T^{True}$), thus preferentially causing us to select these events. Furthermore, the path length calculated for the wrong vertex is shorter than the true path length of the photon/electron resulting in an apparent longer time of flight and thus $t_{corr}^{Measured} > t_{corr}^{True}$ causing an overall shift in the mean.

resulting in $t_{corr}^{Measured} > t_{corr}^{True}$ (ignoring the contribution from t_i and t_{WV}), or said differnetly $(TOF_{RV} - TOF_{WV})$ >0 ns.

At the same time, since $\theta_{Measured} > \theta_{True}$, we find $E_T^{Measured} > E_T^{True}$. This implies that events that have a positively shifted $t_{corr}^{Measured}$ will also have a larger $E_T^{Measured}$. This fact has a remarkable consequence. Namely, this means that some of the events that have E_T^{True} slightly less than 45 GeV, and should not be in our sample of events, can have an $E_T^{Measured} > 45$ GeV and will enter the sample because we chose the wrong vertex. Since these events will also have a timing bias, this means that all the events that enter the sample (i.e., that pass the cuts but shouldn't have) will have $< t_{corr}^{WV} > > 0$ ns.

The converse is also true, a configuration with a mis-measured vertex, where $\theta_{Measured} < \theta_{True}$, would lead to a lower measured of $t_{corr}^{Measured}$ and lower value of $E_T^{Measured}$. Specifcally, events that have E_T^{True} slightly more than 45 GeV and should remain in our sample of events but have an $E_T^{Measured} < 45$ GeV will leave the sample because of the choice of the wrong vertex. These events have a negitive t_{corr} timing bias, but go unobserved since they leave the sample. The bottom line of all this is that misidentification of vertices leads to values of $t_{corr}^{Measured}$ and $E_T^{Measured}$ being shifted in the same positively biased direction.

Tying this all together we find that events that migrate into the sample have large times and events that leave the sample have smaller times. While this might not be a big effect in principle, the number of events entering and leaving around an E_T cut is frequently asymmetric as demonstrated in Figure 5.3 which shows our presample of W→ $e\nu$ MC events that pass the requirements in Table 5.3, but have lowered the E_T requirement, E_T^{cut} to 25 GeV so we can see the full E_T distribution. Since we are placing our E_T^{cut} just past the peak of E_T^{True}, many events make it past the value of E_T^{cut}, resulting in a higher value of $< t_{corr}^{WV} >$ and many events just fail the cut also resulting in a higher value of $< t_{corr}^{WV} >$. At 45 GeV (where our E_T selection resides) the peak of the E_T^{True} distribution makes the migration effect very significant.

In order to mitigate this effect, we exploit the fact that at CDF most collisions occur on average at $z = 0$. Thus, if we instead define E_T for the photons reconstructed in our events from $z = 0$, E_T^0, (as was used in Tables 5.2 and 5.3) instead of from the highest ΣP_T vertex, we will never be exactly right on an event-by-event basis, but be more right on average for events when we select the wrong vertex. This is particularly important as it reduces the amount of bias for the most biased events. The effect of this is that fewer events will be "promoted" into our sample by having $E_T^{Measured} > E_T^{True}$ (on average) as well as fewer events being "demoted" out of our sample with $E_T^{Measured} < E_T^{True}$. Similarly this means that fewer events with $t_{corr}^{Measured} > t_{corr}^{True}$ will be entering our sample on average as well as fewer events with

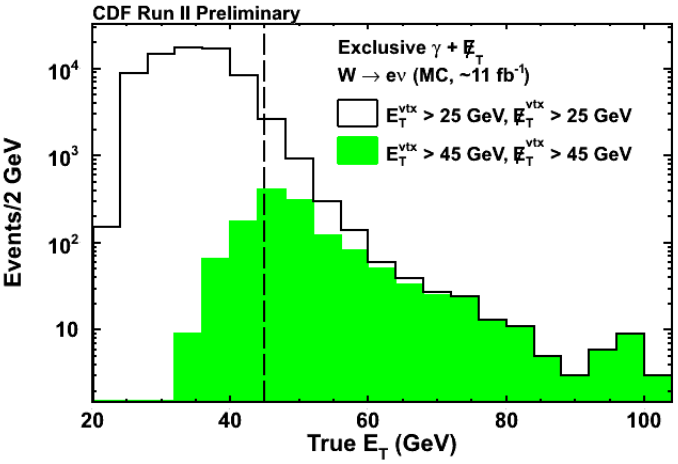

Figure 5.3: The E_T^{True} distribution for a sample of W→ $e\nu$ MC events selected with Table 5.3 that make it into the exclusive $\gamma+\not\!\!E_T$ presample but with two different E_T requirements. The unshaded histogram is the true E_T for electrons that fake photons with E_T^{True} >25 GeV while the solid histogram (shown in green) is the E_T^{True} for electrons that were identified as photons, and passed the $E_T^{Measured}$ >45 GeV cut. Events both entering the sample (green events below the dashed line) and the events leaving the sample (area under the open histogram but above the green, to the right of the dashed line) bias the measurement of t_{corr}^{WV} since large time events enter the sample and low time events leave the sample.

$t_{corr}^{Measured} < t_{corr}^{True}$ leaving our sample. Perhaps more importantly, the variation of the most extreme events in $TOF_{RV} - TOF_{WV}$ is smaller than $TOF_{WV} - TOF_0$. The net result is the kinematic bias that was present before as a result of this definition of E_T is diminished and the most biased events are removed.

To see how much this redefinition can help, we consider our presamples of $e+\not\!\!E_T$ from both data and W→ $e\nu \rightarrow e+ \not\!\!E_T$ MC selected using the cuts in Table 5.2. The results are shown in Figure 5.4 where we select events based on $E_T^{Measured}$ and E_T^0 >45 GeV. On the left hand side of Figure 5.4 we see that in both data and MC have $< t_{corr}^{WV} >$~0.4 ns when we select on $E_T^{Measured}$. On the right hand side of Figure 5.4 we find $< t_{corr}^{WV} >$ is only ~0.2 ns when select on E_T^0 and $\not\!\!E_T^0$. The remarkable agreement between data and MC gives us great confidence that the understanding of the source of this bias is well modeled and understood, and that a large portion of the bias present in the wrong vertex distribution for SM processes in the exclusive γ+$\not\!\!E_T$ final state can be reduced. It is also worth noting at this point that the timing distributions for both data and MC are well described by a double Gaussian distribution, as expected.

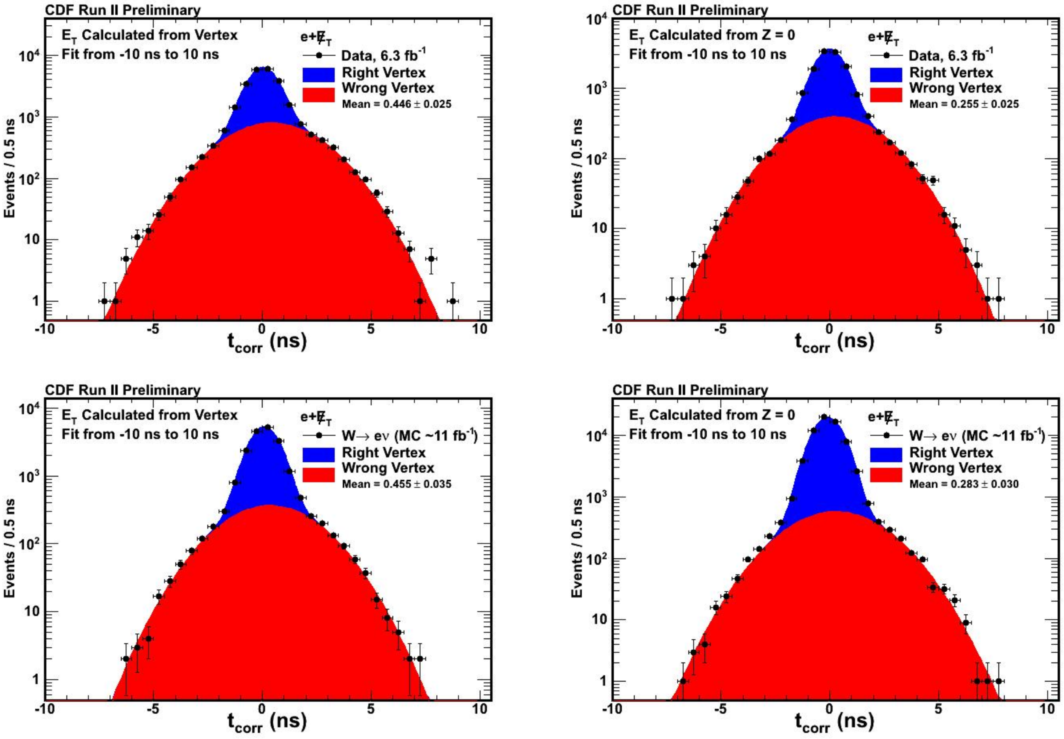

Figure 5.4: The t_{corr} timing distribution for the e+$\not\!\!E_T$ presamples described in Table 5.2 from data (Top Row) and W→ $e\nu$ MC (Bottom Row) when the events are selected using $E_T^{Measured}$ >45 GeV (LHS) and using E_T^0 >45 GeV (RHS). This showes that you can reduce the value of $< t_{corr}^{WV} >$ by simply calculating E_T and $\not\!\!E_T$ from $z = 0$. Note that data and MC give very similar results showing that this effect is well understood.

5.5.2 Rejecting Events from $e \rightarrow \gamma_{fake}$ Sources

Since the W$\rightarrow$ $e\nu$ $\rightarrow$ γ_{fake}+$\not\!\!E_T$ process is a considerable background to any search with a γ+$\not\!\!E_T$ final state it is useful to understand why this background gives a large timing bias and what causes this background to occur so we can reject it more effectively. This discussion follows the description given in Reference [83]. The first point is that, in the exclusive γ+$\not\!\!E_T$ final state, the lack of other activity in the detector required means the primary vertex is both less likely to be reconstructed and less likely to be the highest ΣP_T vertex in the event. Additionally, as discussed in Section 5.4, the same geometric effects that lead to a positive time bias are also the same issues that contribute electrons to fake photons. Namely an electron with a longer path length from the collision point to the calorimeter is more likely to 'fake' a photon. This is because as the electron traverses more material it is more likely to interact and bremsstrahlung a large energy photon that will be identified in the calorimeter as good photon. A longer path length for wrong vertex events implies $TOF_{WV} < TOF_{RV}$ ($|\vec{x}_f - \vec{x}_{Measured}| < |\vec{x}_f - \vec{x}_{True}|$), which also implies $E_T^{Measured} > E_T^{True}$ and $t_{corr}^{Measured} > t_{corr}^{True}$ and thus also is subject to the same bias arguments just given.

To reduce the fraction of the time an electron fakes a photon we first note that the dominant way that electrons fake photons is when there is a hard bremsstrahlung interaction in the detector material. A schematic drawing of this process of how these $e \rightarrow \gamma_{fake}$ events from hard bremsstrahlung interactions appear in the detector is shown in Figure 5.5. As an electron travels through the detector material, the hard interaction can cause it to lose a large fraction of its energy to a photon. The electronâs trajectory is severely affected by the energy and momentum loss; it may either leave a much lower energy deposition in a calorimeter or be swept away completely by the magnetic field of the solenoid. The bulk of the energy of the photon candidate in the calorimeter is thus due to the bremâd photon. The candidates that enter our sample are the ones where the bending is so large that the track is no longer associated with the photon candidate by the standard photon reconstruction algorithms.

To understand this process in more detail we consider our $\gamma+\not\!\!E_T$ presample created from the set of W→ $e\nu$ MC events that have a photon in them that pass all the selection requirements in Table 5.3. Looking at the generator level information we can identify the location of the largest transfer of energy to a single photon [83]. We find that 93% of the time the electron gives more than 50% of its energy to a single photon in a single interaction. The remaining 7% are most likely tracking failures. Thus, we focus on hard-brem interactions as the primary cause of the $e \rightarrow \gamma_{fake}$ candidates. A simple requirement of fraction of the energy lost to be greater than 50% allows us to map out the locations of the hard bremsstrahlung interaction inside the detector. This is shown in the top of Figure 5.6. Note that this figure shows clearly the material inside the detector, an “x-ray” of sorts; showing the bulk of the bremsstrahlung interactions occur where the SVX detector and its support structure reside. The fact that so many of the electrons undergo bremsstrahlung early allows us to understand why the conventional rejection methods fail, namely there is not much detector information available to reconstruct the track associated with the electron.

We can now also see why these photon candidates are not rejected by the N3D track requirement of the standard photon ID cuts given in Table 2.8. The post-brem electron loses its initial momentum and is left with low P_T, so the track is significantly curved away from the final location of the photon candidate in the calorimeter. Since the ϕ position of the low P_T track at the face of the calorimeter is far from the reconstructed ϕ position of the photon candidate, it is unlikely for the track to be "matched" to the photon candidate by the standard photon reconstruction algorithms [61]. We find that a low P_T bremâd track can end up at least three towers away from the EM cluster[83]. While the standard methods are effective for rejecting electrons in general, since the charged track is readily identified and rejected, we clearly can do much better.

Since the standard electron rejection methods leave a large number of fake events in our sample, and the remaining ones have a large time bias, we have developed a new method that takes advantage of the observation that the majority of the $e \rightarrow \gamma_{fake}$ candidates are due to electrons which interact with detector material and brem but still have a track that can be found. This method considers all reconstructed tracks that pass the requirements in Table 5.4 in the event and compares candidate tracks to the photon candidates in order to veto these events. We note that this track definition is a 'looser' definition then the tracks defined in Table 2.6 for 'good' timing tracks and high P_T isolated tracks in Table 5.4. The reason for this is we expect these tracks to only be present as high P_T tracks early in the detector and then undergo a hard brem changing their trajectory mid-flight, and thus be of lower quality. Therefore we use this looser definition in order to maximize the likelihood of finding this track.

COTAxialSeg(5) *Number of COT Axial Segments with hits*	≥ 2
COTStereoSeg(5) *Number of COT Stereo Segments with hits*	≥ 2
$\lvert z \rvert$ *Z Position of the track*	≤ 150 cm

Table 5.4: Track identification variables for use in $e \rightarrow \gamma_{fake}$ veto. Note, these variables are defined in Appendix B.1.

Since the amount of variation in the expected measurement of the track position in ϕ and η are different, we do matching between the location of the photon in the calorimeter and the original track direction using a normalized variable. We define the matching variable ΔR_{Pull} to determine if the track is matched to the photon candidate as:

$$\Delta R_{Pull} = \sqrt{\Delta\phi^2_{Pull} + \Delta\eta^2_{Pull}}. \tag{5.4}$$

where $\Delta\phi^2_{Pull}$ and $\Delta\eta^2_{Pull}$ are defined in order to account for the detector response as:

$$\Delta\phi_{Pull} = \frac{\Delta\phi}{\sigma_\phi} \tag{5.5}$$

where σ_ϕ is measured to be $\sigma_\phi = 8.1 \cdot 10^{-2}$ and

$$\Delta\eta_{Pull} = \frac{\Delta\eta}{\sigma_\eta} \tag{5.6}$$

and $\sigma_\eta = 6.3 \cdot 10^{-3}$ [83]. The top of Figure 5.7 shows the distribution of the closest track to the photon candidate in $\Delta\phi_{Pull}$ and $\Delta\eta_{Pull}$ as being symmetric and small for our control sample of W$\rightarrow e\nu \rightarrow \gamma_{fake}+ \not\!\!E_T$ events. This allows us to draw a circle in ΔR_{Pull} in order to veto events that are likely to have come from $e \rightarrow \gamma_{Fake}$ processes. The bottom of Figure 5.7 shows what the ΔR_{Pull} variable looks like for a presample of W$\rightarrow e\nu \rightarrow \gamma_{fake}+\not\!\!E_T$ (shown in Black) and a presample of $\gamma+\not\!\!E_T$ events from $Z\gamma \rightarrow \nu\nu\gamma$ events (shown in red) where both samples pass the requirements for the $\gamma+\not\!\!E_T$ presample requirements in Table 5.3.

We have chosen to place a cut at $\Delta R_{Pull} > 5$ in order to veto $e \rightarrow \gamma_{fake}$ events. As shown in Figure 5.8, this selection is 93% efficient for real photons with a rejection power of 75% for $e \rightarrow \gamma_{fake}$. It is important to note, as shown in Figure 5.9, that this cut does not reduce the shifted mean of the wrong vertex distribution for $e \rightarrow \gamma_{fake}$ events. However it does reduce the overall rate at which they appear in our final sample. This reduces the overall importance of this background and makes us less sensitive to the wrong vertex mean shift.

5.5.3 Rejecting Events from Large $|Z_{Collision}|$ Sources

The final source of timing biases we address here comes from events where a collision occurs at $|z| > 60$ cm and produces a photon candidate that is then found in the calorimeter. Since vertices at $|z| > 60$ cm cannot be selected as the highest ΣP_T vertex in the exclusive $\gamma+\not\!\!E_T$ analysis, if a min-bias collision happens to occur at the center of the detector the only way this event is selected is if we mis-assign the vertex and thus incorrectly calculate the corrected time. Since these events always have $TOF_{RV} > TOF_{WV}$ they can have significantly biased $< t^{WV}_{corr} >$.

This situation is most easily seen in our $\gamma+\not\!\!E_T$ presample of γ + Jet events. In order for these QCD based events to enter the exclusive $\gamma+\not\!\!E_T$ they must have a unique topology in order to produce fake $\not\!\!E_T$. In Figure 5.10 we plot the true z position of the collision for γ + Jet events simulated with MC and see that it extends far beyond $|z| = 60$ cm. Therefore we veto any event that has evidence there was a collision at >60 cm. Specifically, to be more efficient at rejecting these vertices, we use CDF's standard vertex algorithm, described in greater detail in reference [64] to search for vertices out to $|z| = 150$ cm and provide a handle on events that have evidence of activity at large collision z. If we find a standard vertex with three or more tracks at $|z| > 60$ cm we veto this event as likely having a collision at large z position, as outlined in Table 2.11.

The effect of this veto can be seen in Figure 5.11 where we show the timing distribution of our $\gamma+\not\!\!E_T$ presample from γ + Jet MC. We then apply the large $|z|$

vertex veto to the sample and show that $< t_{corr}^{WV} >$ goes from 0.38 ns to 0.18 ns, greatly reducing the timing bias present in this sample.

Before we continue, we show that the large $|z|$ veto does not effect the timing distribution for a sample of events which originate inside the $|z|$ <60 cm area, for example as would be the case with a potential signal sample. To illustrate this, we consider again our γ+$\not\!\!E_T$ presample of Z$\gamma \rightarrow \nu\nu\gamma$ MC. In Figure 5.12 we show the t_{corr} distribution for the Zγ events before and after the application the large $|z|$ veto showing very little effect to the timing distribution, as expected.

Finally, we estimate the efficiency of the large $|z|$ veto by applying it to our γ+$\not\!\!E_T$ presample, but where we select a subsample of cosmic ray events by considering events in the timing region 20 ns $< t_{corr} <$ 80 ns. The timing distribution before and after the large $|z|$ veto shown in Figure 5.13. From this sample we estimate that the large $|z|$ veto is >95% efficient for real photons and collisions coming from $|z|$ <60 cm.

5.6 Timing Distributions for the Standard Model Backgrounds

Now that we have completed our discussion of the mechanisms for the production of SM events with large times, and methods for rejecting and/or minimizing the bias, we now consider the SM backgrounds as well as our electron samples after all the cuts. The final set of requirements are shown in Table 5.5.

With the final event selection established for the exclusive γ+$\not\!\!E_T$ final state we now select our control samples as passing the subset of events in our presample that also pass all the requirements in Tables 5.5 and 5.2. With these samples we can examine their timing distributions. Figure 5.14 shows the timing distribution for six SM MC background control samples as well as our two exclusive e+$\not\!\!E_T$ control samples in data using Tables 5.2 and 5.5. We see that each is well described by a

Pass Trigger and Photon Good Run List *(See Table 2.2 and 2.3 and Section 2.4)*
Pass Tight Photon requirements w/ $E_T^0 > 45$ GeV and $\not\!\!E_T^0 > 45$ GeV *(See Table 2.8 and Section 2.4.6)*
Pass Beam Halo Rejection *(See Table 4.3)*
Pass Cosmics Rejection *(See Table 4.2)*
Pass Track Veto for Tracks with $P_T > 10$ GeV *(See Table 2.7)*
Pass Jet Veto for Jets with $E_T^0 > 15$ GeV *(See Table 2.5)*
Pass Large $\lvert Z \rvert$ Vertex Veto *(See Section 5.5.3)*
Pass $e \rightarrow \gamma_{fake}$ Veto *(See Table 5.4 and Section 5.5.2)*
Require a Good SpaceTime Vertex *(See Table 2.10)*

Table 5.5: Exclusive $\gamma + \not\!\!E_T$ complete table of event selection requirements.

double Gaussian fit where the right vertex mean and RMS are fixed to be 0.0 ns and 0.65 ns respectively and the normalization is allowed to float. Likewise the wrong vertex RMS is fixed to 2.0 ns while the mean and normalization of the distribution are allowed to float. The results are summarized in Table 5.6.

We can further examine one of the assumptions; namely the assumption that the wrong vertex distribution is described by a Gaussian with an RMS of 2.0 ± 0.1 ns. Figure 5.15 shows the results of testing this hypothesis for our six MC samples and two $e+\not\!\!E_T$ data samples but where we allow the wrong vertex mean and RMS to vary for each sample during the fitting procedure and keep the right vertex mean and RMS fixed to 0.0 and 0.65 ns respectively. The results are summarized in Table 5.7. They clearly show that the assumption that the wrong vertex distribution is given by a Gaussian with RMS 2.0 ± 0.1 ns is an accurate description over a large

Sample	**Wrong Vertex Mean (ns)**
W→ eν MC	0.73 ± 0.19 ns
γ+Jet MC	0.18 ± 0.13 ns
Zγ MC	0.12 ± 0.01 ns
W→ $\mu\nu$ MC	0.29 ± 0.26 ns
W→ $\tau\nu$ MC	0.43 ± 0.26 ns
Wγ MC	0.14 ± 0.07 ns
e+$\not\!\!E_T$ Data	0.17 ± 0.05 ns
e+$\not\!\!E_T$ Data (E_T&$\not\!\!E_T$ > 30 GeV)	0.04 ± 0.01 ns

Table 5.6: Summary of the measured mean of the wrong vertex timing distribution, $< t^{WV}_{corr} >$, from the double Gaussian fit for our six MC and two e+$\not\!\!E_T$ data control samples. Here the right vertex Gaussian is fixed with a mean =0.0 ns and a RMS =0.65 ns and the wrong vertex Gaussian RMS is fixed =2.0 ns while the mean and normalization are allowed to vary. These results are taken from Figure 5.14.

range of wrong vertex means and across a variety of background samples.

With a complete set of data selection requirements well defined to reduce the bias and systematic production of large time events, and confidence that our SM collisions are well described by a double Gaussian with well understood RMS's but a variable WV mean, we next turn to the subject of being able to predict the wrong vertex mean which is needed to estimate the number of SM events in the signal region. In the next section, we will use events similar to those in the presamples to create a data-driven estimate of the number of background events in the signal region.

Sample	**Wrong Vertex Mean (ns)**	**Wrong Vertex RMS (ns)**
W→ eν MC	0.69 ± 0.22 ns	2.18 ± 0.17 ns
γ+Jet MC	0.18 ± 0.13 ns	2.04 ± 0.16 ns
Zγ MC	0.08 ± 0.05 ns	1.97 ± 0.05 ns
W→ $\mu\nu$ MC	0.30 ± 0.23 ns	2.06 ± 0.18 ns
W→ $\tau\nu$ MC	0.48 ± 0.22 ns	1.97 ± 0.22 ns
Wγ MC	0.14 ± 0.09 ns	2.14 ± 0.08 ns
e+$\not\!\!E_T$ Data	0.16 ± 0.07 ns	2.05 ± 0.07 ns
e+$\not\!\!E_T$ Data (E_T&$\not\!\!E_T > 30$ GeV)	0.04 ± 0.05 ns	1.98 ± 0.05 ns

Table 5.7: Summary of the measured mean and RMS of the wrong vertex timing distributions, $< t^{WV}_{corr} >$ for our six MC γ+$\not\!\!E_T$ and two e+ $\not\!\!E_T$ control samples where we allow the mean and RMS of the wrong vertex Gaussian to float in the fit. These results are plotted in Figure 5.15

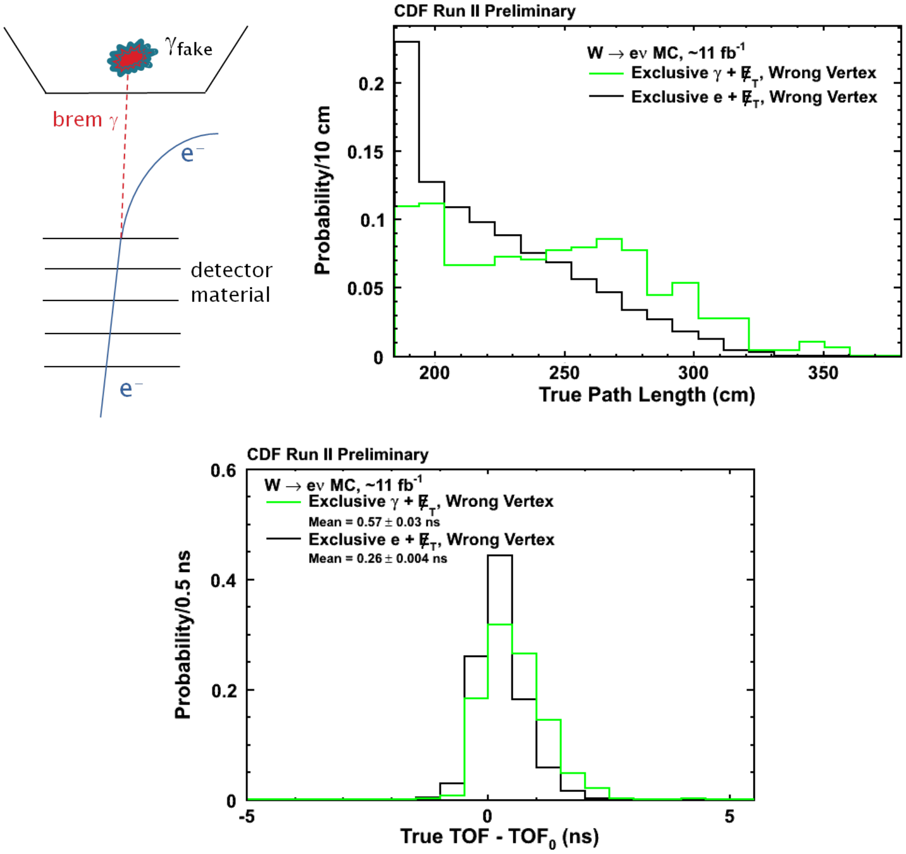

Figure 5.5: (Top-LHS)A schematic representation of an electron interacting with the detector material and having a hard bremsstrahlung interaction. After the interaction the electron curves off because of its resulting lower energy and thus its trajectory becomes highly curved in the magnetic field and is no longer associated with the photon using the standard photon identification algorithms. It is important to note that both before and after the bremsstrahlung the trajectory can be reconstructed as a single low P$_T$ track. (Top-RHS) The true path length for electrons mis-identified as photons, selected with Table 5.3 for the exclusive $\gamma+\not\!\!E_T$ presample, showing that these events tend to have larger path lengths than correctly identified electrons. (Bottom) The ΔTOF between the true vertex and z =0 cm for the same sample of events demonstrating that events from electrons mis-identified as photons will have a larger bias.

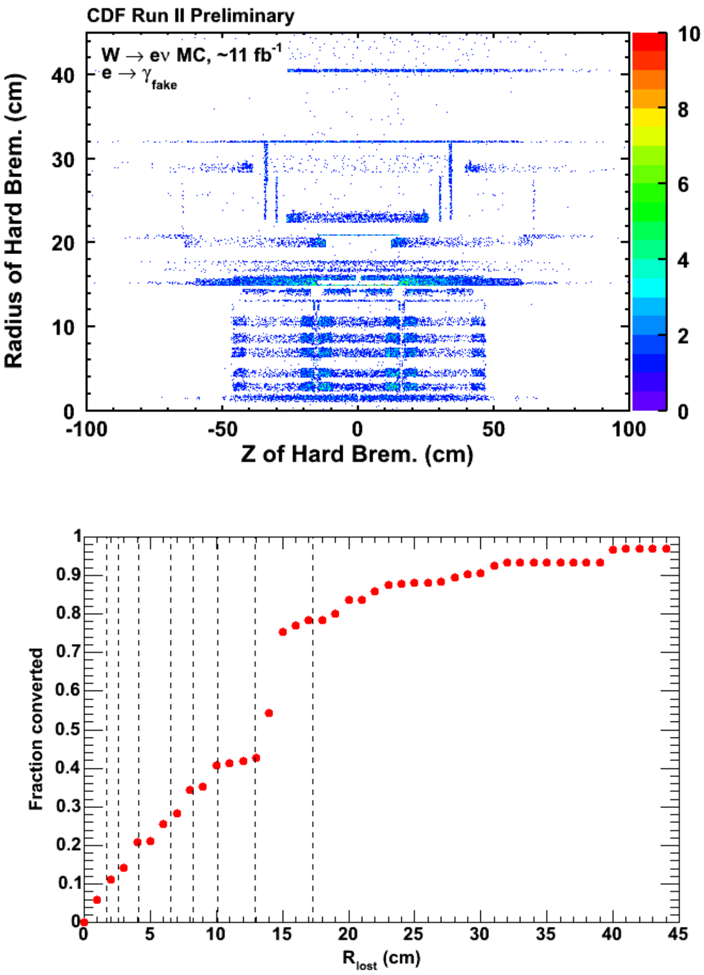

Figure 5.6: Two different plots showing where, inside the detector, an electron interacts with the detector and loses more than half of its energy to a photon that is ultimately identified as passing all the photon ID requirements in Table 2.8. In the top plot we see a 2-D histogram showing the location in the radius vs. the z position along the beamline. The bottom shows an integral plot of the fraction of events which converted within the detector. Both indicate that the majority of events are seen to brem inside the silicon detector and the port cards (denoted with the dashed lines).

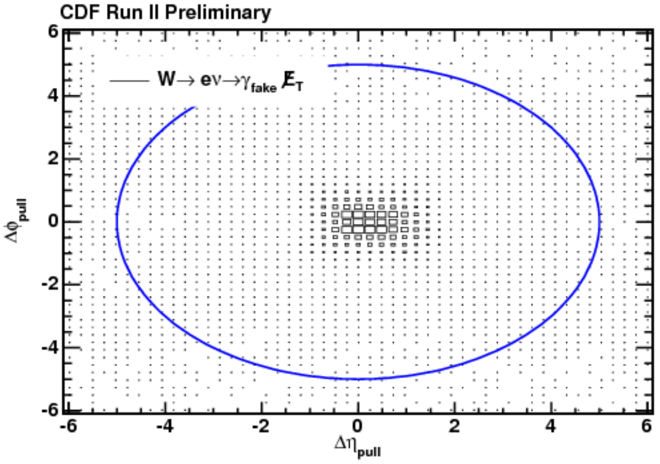

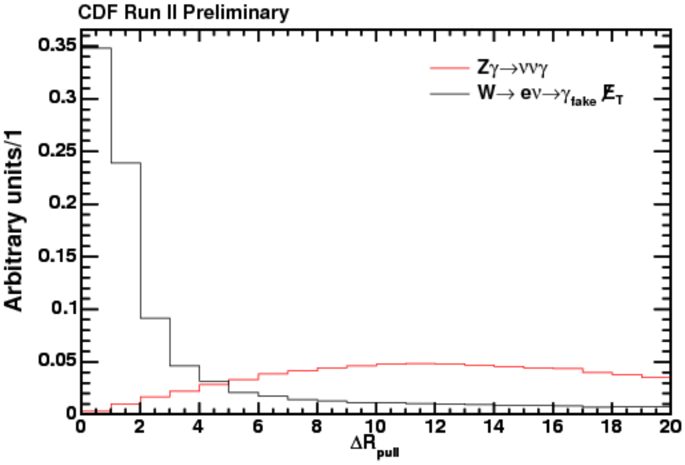

Figure 5.7: To help reject electrons that fake photons, we have measured the angular separation between the photon and the closest track direction normalized to these measurement resolutions for our control sample of $\gamma+\not{E}_T$ events from W→ $e\nu$ MC with the added requirement that the photon come directly from an electron. The top plot shows the correlation between $\Delta\eta_{Pull}$ and $\Delta\phi_{Pull}$. The bottom plot shows a comparison of the ΔR_{pull} for our presample, along with a second $\gamma+\not{E}_T$ control sample from $Z\gamma \rightarrow \nu\nu\gamma$ MC showing the rejection power of this cut. Note, both samples are normalized unit area.

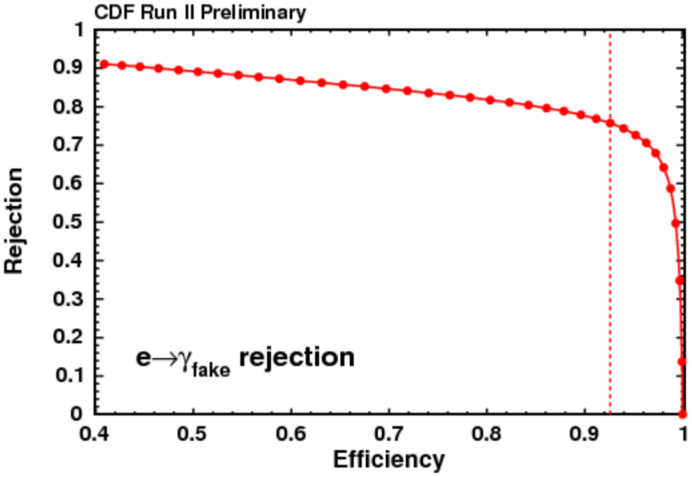

Figure 5.8: This plot show the rejection of a electron rejection cut on ΔR_{pull} as a function of the efficiency. As the cut gets tighter the rejection gets worse but the efficiency goes up. A cut at $\Delta R_{Pull} = 5$ (red dashed line) results in approximately 93% efficiency of MC $Z\gamma \to \nu\nu\gamma \to \gamma + \not{E}_T$ and 75% rejection of $e \to \gamma_{fake}$.

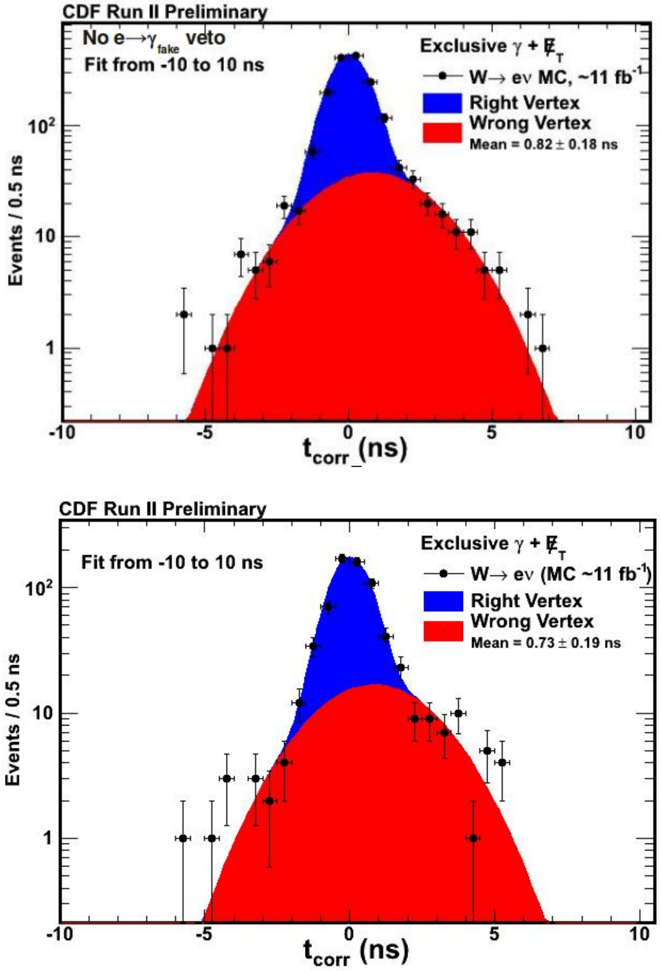

Figure 5.9: The timing distribution for the $\gamma + \not\!\!E_T$ presample from W→ $e\nu$ MC before (top) and after (bottom) the ΔR_{Pull} cut. The application of this cut does not reduce the wrong vertex timing bias but does reduce the overall rate at which this background appears in our final sample.

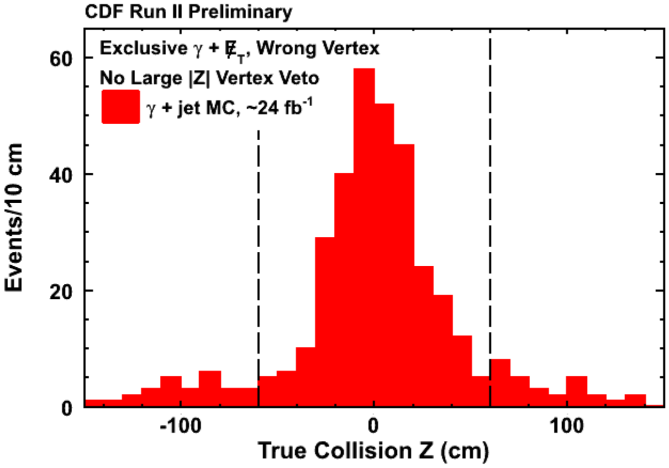

Figure 5.10: The z distribution of the true collision position for a MC sample of γ+Jet events selected using Table 5.3 which defines the $\gamma+\not{E}_T$ presample. This distribution shows many events which originate at $|z|$ >60 cm.

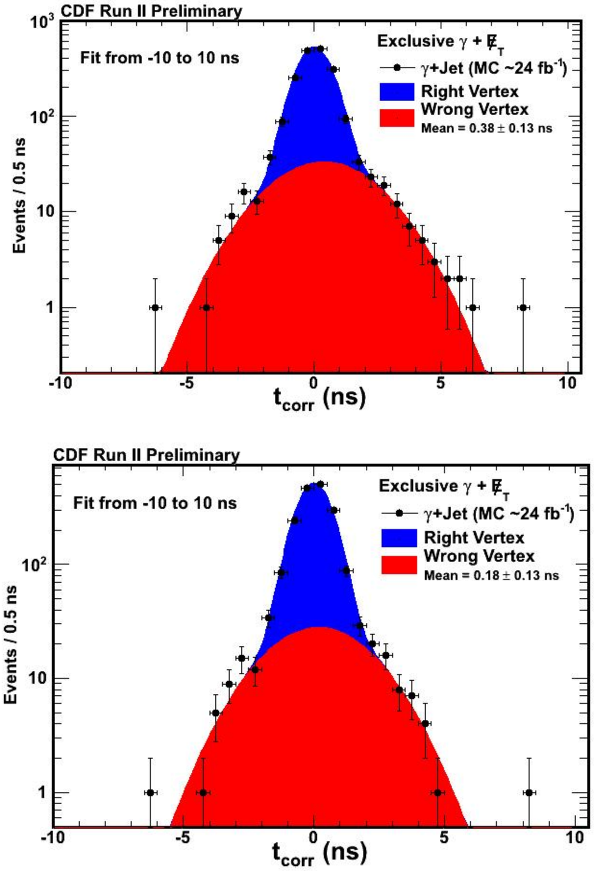

Figure 5.11: The timing distribution for the $\gamma+\not\!\!E_T$ presample from γ+Jet MC events (Top) and the same sample after applying the large z veto (Bottom) showing the wrong vertex mean becomes much less biased.

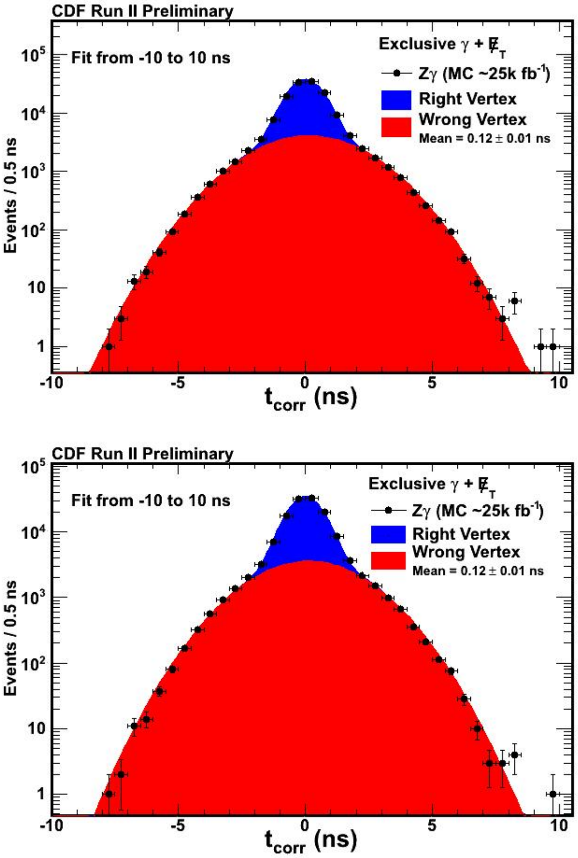

Figure 5.12: The timing distribution for the γ+$\not\!\!E_T$ presample from from Z$\gamma \rightarrow \nu\nu\gamma$ MC events (Top) and the same sample after applying the large z veto (Bottom) showing very little effect in the timing distribution for events which originate from within $|z| <$60 cm.

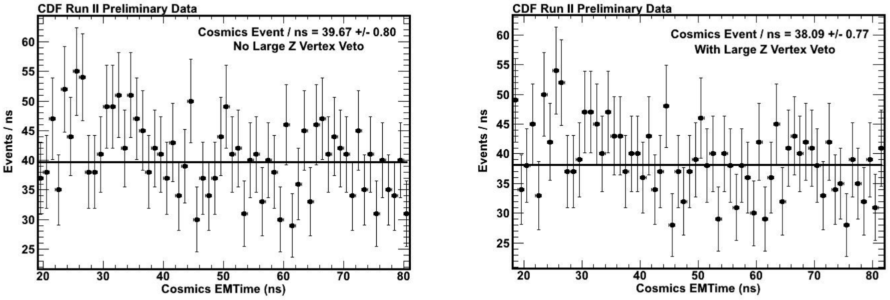

Figure 5.13: The timing distribution for cosmic ray events selected using $\gamma+\not\!\!E_T$ data presample using the requirements in Table 5.3 but adding the restriction of the timing region from 20 ns $< t_{corr} <$ 80 ns. The left and right plots show the timing distribution before and after the large z veto the rate of cosmic rays is effectively not effected, as expected, by the large z veto

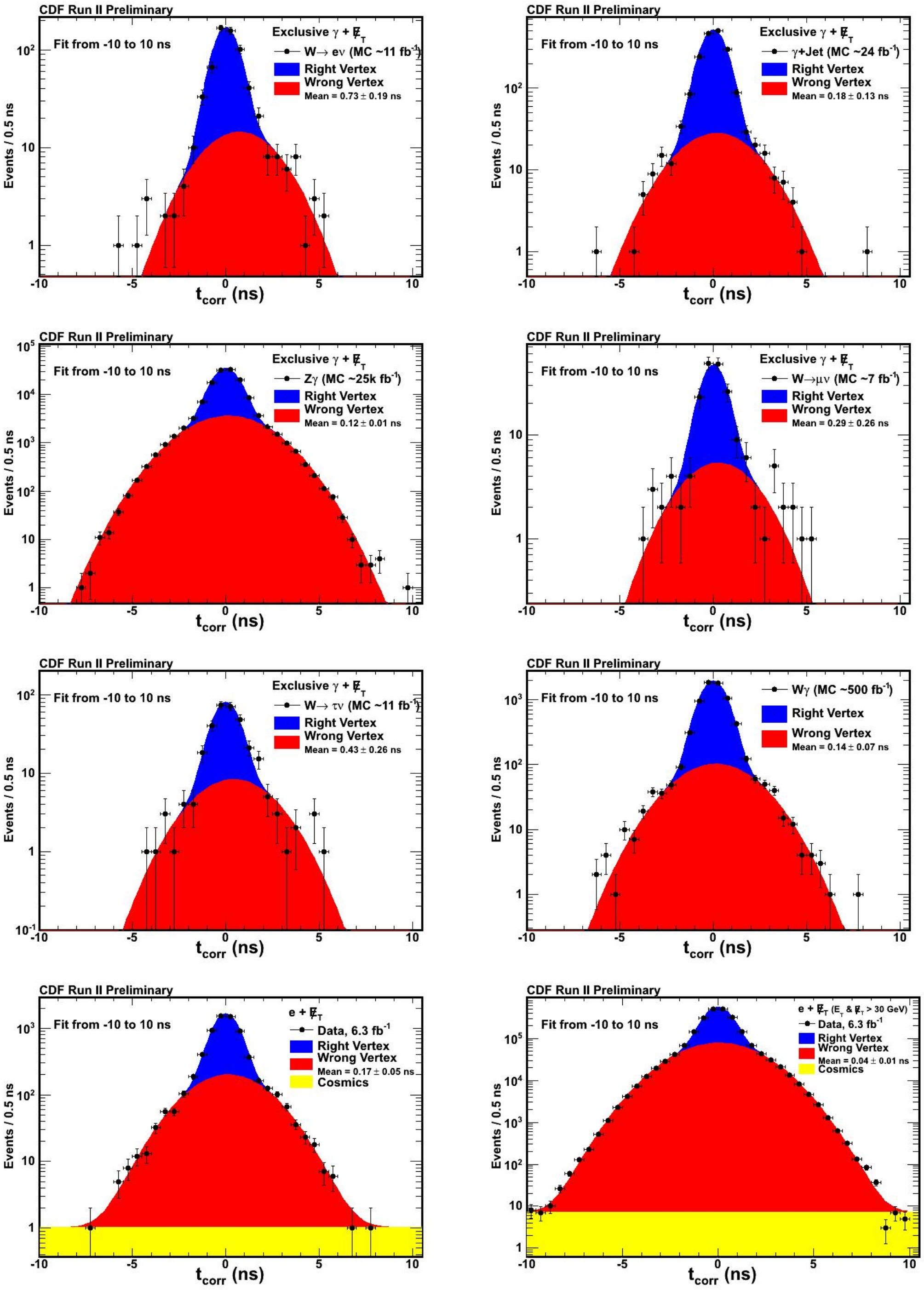

Figure 5.14: The timing distributions for the W→ eν, γ+Jet, Zγ, W→ $\mu\nu$, W→ $\tau\nu$, and Wγ MC control samples and the e+$\not\!\!E_T$ control samples. The distributions are well fit by a double Gaussian distribution. In this fit the right vertex (blue) Gaussian is fixed with a mean =0.0 ns and a RMS =0.65 ns and the wrong vertex (red) Gaussian RMS is fixed =2.0 ns while the mean and normalization are allowed to vary.

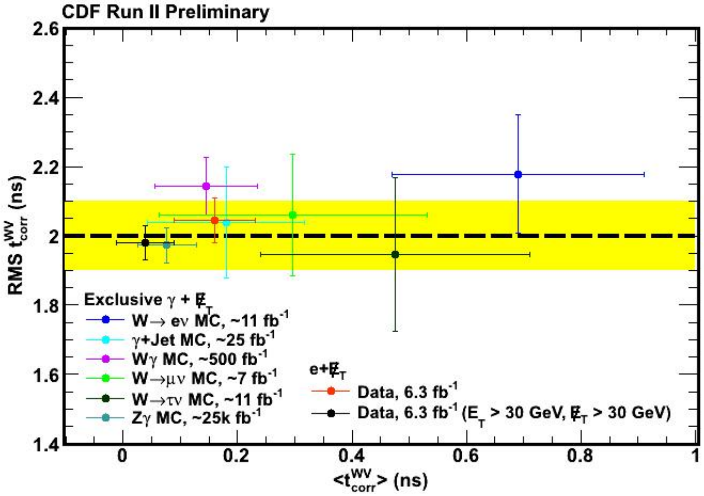

Figure 5.15: The measured mean RMS of the wrong vertex versus the mean of the wrong vertex timing distribution, $< t^{WV}_{corr} >$ where we have allowed both the mean and the RMS to vary in the fit for our six MC $\gamma+\not\!\!E_T$ and two $e+\not\!\!E_T$ data control samples. The results show that the description that the wrong vertex distribution is well modeled by a Gaussian with an RMS of 2.0 ± 0.1 ns.

6. BACKGROUND ESTIMATION METHODS

Having completed our description of the various SM and non-collision backgrounds, we now turn our attention to predicting the number of events we expect from each in the signal region for our final sample. This process is purely based on data-driven methods and is a multi-step process. We will address each step in turn.

Since the two dominant backgrounds are wrong vertex SM events with an unknown mean and cosmic ray events we describe their rates one at a time. Section 6.1 provides an overview of how we will use the double Gaussian nature of the timing distributions in order to perform a data-driven background estimation of the wrong vertex mean. Futhermore we demonstrate that if we know the mean of the wrong vertex distribution we are able to predict the number of events expected in the signal region from SM sources from data-only methods.

Since an important piece of the SM estimate is the determination of the wrong vertex mean, in Section 6.2 we detail a data-driven method to obtain a good estimate of the wrong vertex mean. This is done using a second sample of events that has identical cuts to the signal region, but with one requirement reversed. This allows the sample to be independent but have similar properties that should allow us to measure the mean of the wrong vertex distribution. In particular, we select a sample of events passing all the exclusive $\gamma+\not\!\!E_T$ events (found in Table 5.5) but failing to reconstruct a vertex. We call this sample the "no vertex sample".

This sample is particularly useful because, as we will show, the mean of the t^0_{corr} distribution, $< t^0_{corr} >$, should reproduce the mean of wrong vertex sample, $< t^{WV}_{corr} >$, within small uncertainties. Then, using our six MC control samples and two $e+\not\!\!E_T$ control samples we will show that $< t^0_{corr} >=< t^{WV}_{corr} >$ to within 80 ps. This value will serve as a systematic uncertainty which will be taken into account in the final estimation of the number of events in the signal region. Finally, in Section 6.3 we will lay out the final procedure for predicting the expected number of events in the signal region from SM sources along with the contribution from cosmic rays for a final predicited value.

6.1 Overview of Data-Driven Background Method for Collision Backgrounds

We can use the data and an understanding of the shape of the wrong vertex timing distribution to predict the number of events in the signal region from collision backgrounds. As we showed in Section 5.6, a sample of collision events can be described by a double Gaussian timing distribution. Said differently, all the collision backgrounds are well described by six parameters, namely the mean and RMS of the two Gaussians (the right and wrong vertex) as well as their normalizations.

While the mean of the wrong vertex may vary sample to sample, as we have seen in Section 5.6, three out of six of these parameters do not change from sample to sample and all that is left is to determine the wrong vertex mean and the relative normalization in order to have a full understanding of the collision backgrounds. With this in hand we can make a prediction of the number of events in the signal region.

In Section 3 we laid out this argument, with the conclusion summarized in Equation 3.11, that it is straightforward to predict the number of events in the signal region (N_{SR}) if you know $< t^{WV}_{corr} >$ distribution and the number of events in the control region (N_{CR}). This result is visualized in Figure 3.2 with the double Gaussian assumption for various wrong vertex means where we ignore the contribution from the right vertex sample and cosmics. This assumption is typically true for wrong vertex fractions of ∼10% or greater. The yellow band represents a systematic uncertainty in the RMS of the wrong vertex of ±0.1 ns which is the one of the systematic uncertainties we will take into account when predicting the expected number of events in the signal region from SM sources. It should be noted here that we are only trying to predict the number of background events from SM contributions in the signal region. At no point have we used any information about the number of events in the signal region nor anything about the shape of the timing distribution in the signal region except that SM sources will be Gaussian.

We now test the hypothesis put forward in Equation 3.11 by looking at how well the prediction between the wrong vertex mean and the ratio of events in the signal and control regions holds in our various MC and data control samples. Figure 6.1 shows the results of the counting experiment for the various MC and $e+\not\!\!E_T$ data control samples that pass all the selection requirments in Table 5.5 for photons and Table 5.2 for electrons. In this case we count the number of events in the signal and control regions and compute the ratio; note that the error is just the statistical error on the sample. We then plot this versus the fitted wrong vertex mean when we fit the various samples in the region -10 ns $< t_{corr} <$ 10 ns using the double Gaussian assumption where the mean and RMS of the right vertex are fixed to 0.0 ns and 0.65 ns respectively and the RMS of the wrong vertex is fixed to 2.0 ns as shown in Figure 5.14. The results of these fits are summarized in Table 6.1.

The various sample points clearly follow the expected relationship and demonstrate that our distributions are well modeled by our double Gaussian assumption. Note that the line in Figure 6.1 is not a fit, but is simply the prediction from Equation 3.11. This remarkable result means that for a sample of collision events in the exclusive $\gamma+\not\!\!E_T$ final state, that once we are able to determine the wrong vertex mean and we count the number of events in the control region from collision sources we can determine the number of events expected in the signal region. The task of

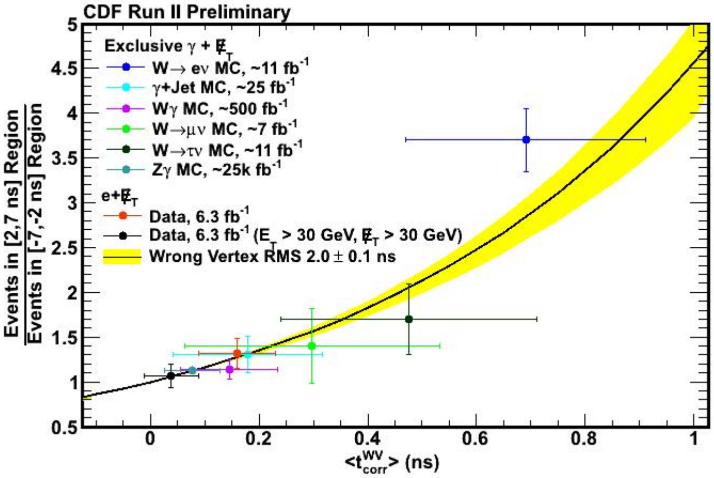

Figure 6.1: Ratio of the number of events observed in the signal region (2 ns $< t_{corr} <$ 7 ns) to the number of event observed in the control region (-7 ns $< t_{corr} <$ 2 ns) versus the measured wrong vertex mean for our eight control samples. The black line is not a fit, but rather is the prediction from the double Gaussian assumption where the right vertex distribution is fixed and the wrong vertex mean is allowed to vary. It does an excellent job of predicting the numer of events in the signal region. Note that in this figure we have measured $< t^{WV}_{corr} >$ from a full fit of the control sample (see Figure 5.14), which we cannot do directly in the real data.

finding an independent way of determining the wrong vertex mean, and thus measuring the bias present in the sample, is the subject of the next section. We note that additional studies show that this is true, to within the stated uncertainties even if the sample is made of two very different vertex means because the means are small compared to the overall 2.0 ns RMS [75].

6.2 Measuring the Wrong Vertex Mean for the Sample

The first thing that is important to note, as we now turn our attention to establishing a way to measure the wrong vertex mean, is that naively we may attempt to establish the mean of the wrong vertex by simply fitting the full data sample from -7 ns $< t_{corr} <$ +2 ns and then extrapolating this fit into the signal region. While this should work in the limit of having infinite statistics, this method does not work

Sample	**Observed Wrong Vertex Mean (ns)**	**Predicted Ratio**	**Observed Ratio**
W→ eν MC	0.73 ± 0.19 ns	2.92 ± 1.01	3.70 ± 0.36
γ+Jet MC	0.18 ± 0.13 ns	1.30 ± 0.26	1.30 ± 0.20
Wγ MC	0.14 ± 0.07 ns	1.22 ± 0.14	1.14 ± 0.11
Zγ MC	0.12 ± 0.01 ns	1.20 ± 0.01	1.12 ± 0.02
W→ $\mu\nu$ MC	0.29 ± 0.26 ns	1.50 ± 0.70	1.40 ± 0.41
W→ $\tau\nu$ MC	0.43 ± 0.26 ns	1.90 ± 0.90	1.70 ± 0.40
e+$\not\!\!E_T$ Data	0.16 ± 0.05 ns	1.26 ± 0.16	1.32 ± 0.17
e+$\not\!\!E_T$ Data ($E_T > 30$ GeV and $\not\!\!E_T > 30$ GeV)	0.04 ± 0.05 ns	1.03 ± 0.07	1.06 ± 0.13

Table 6.1: Summary of the results shown if Figure 6.1 showing the predicted and observed ratio of the number of events in the signal region (2 ns $< t_{corr} <$ 7 ns) to the number of events in the control region (-7 ns $< t_{corr} <$ -2 ns) for our six MC and two e+$\not\!\!E_T$ control samples. The observed wrong vertex mean here is measured using a double Gaussian fit to the data and assuming a right vertex mean = 0.0 ns and RMS = 0.65 ns as well as a wrong vertex RMS=2.0.

in our data for three major reasons:

1) Events from cosmics rays constitute a significant fraction of the number of events in the region from -7 ns $< t_{corr} <$ -2 ns and thus may distort the wrong vertex distribution in this area.

2) In the region from -2 ns $< t_{corr} <$ 2 ns events from the right vertex dominate thus making it difficult to measure the mean of the wrong vertex in this region.

3) All of these problems are compounded as the wrong vertex mean becomes larger. Said differently, as the wrong vertex mean gets larger the distribution in the control region (-7 ns $< t_{corr} <$ -2 ns) only gives a smaller and smaller fraction of the events from which to estimate the mean.

With these problems in mind, we consider an orthogonal set of events that allows us to measure $< t^{WV}_{corr} >$. For such a sample we look to the events that pass all of our exclusive γ+$\not\!\!E_T$ requirements (outlined in Table 5.5) but do not have a reconstructed

SpaceTime vertex. As illustrated in Figure 6.2, we refer to this sample as the "no vertex" sample. We expect this sample to be very similar to the wrong vertex events for a number of reasons. The first is that in wrong vertex events they may or may not have had their true vertex reconstructed. We note that in our MC backgrounds samples where we selected the wrong vertex, the right vertex was only available to be selected a small fraction (~50%) of the time. Furthermore, we expect the topology of the events where we select a wrong vertex to be similar to those with no vertex. We will check this assumption in more detail after we describe more about the timing we use for no vertex events.

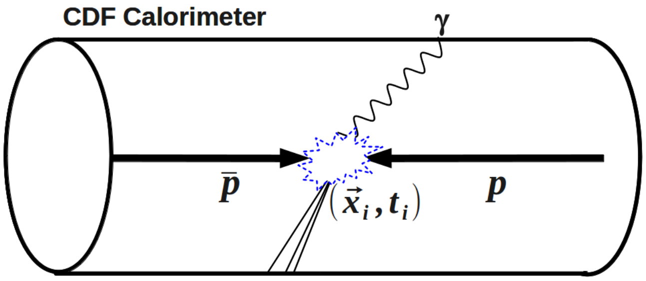

Figure 6.2: This figure shows the creation of a $\gamma+\not{E}_T$ event where the primary collision does not produce a reconstructed vertex. We use a sample of events with this topology because their timing distribution, t^0_{corr}, is dominated by the topology of the SM events where the wrong vertex is selected. If no good SpaceTime vertex is reconstructed, but the event passes all the other exclusive $\gamma+\not{E}_T$ event selection requirements there is a clear relationship between $< t^0_{corr} >$ and $< t^{WV}_{corr} >$.

If no good SpaceTime vertex is reconstructed, but the event passes all the other exclusive $\gamma+\not{E}_T$ event selection requirements we can still construct t^0_{corr} where we assume the initial time and position was $t_0 = 0$ ns and $z = 0$ cm respectively. This is a reasonable assumption on average since this is the most common place for collisions to occur. From this point, we can see why moving to E^0_T and $\not{E}^0_T$, as was described in Section 5.5.1, was doubly advantageous. In addition to reducing the bias in the t^{WV}_{corr}

distribution, we can select this sample in exactly the same way as the main sample regardless of whether there is a vertex reconstructed in the event.

While we expect this sample to be dominated by cosmic ray backgrounds, the events from a collision which had no reconstructed vertex should have the same underlying physics and topology and thus the same timing bias as the wrong vertex distribution. We can see this by rewriting Equation 1.8 for t^0_{corr}

$$t^0_{corr} = t_f - t_0 - \frac{|\vec{x_f} - \vec{x_0}|}{c} \tag{6.1}$$

where t_0 and x_0 are measured at the center of the detector. However, as we saw in Equation 5.2, we can rewrite t_f as

$$t_f = t_{RV} + TOF_{RV} \tag{6.2}$$

Plugging this in and setting $\frac{\vec{x_f} - \vec{x_0}}{c} = TOF_0$ and t_0 =0 ns we find

$$t^0_{corr} = TOF_{RV} + t_{RV} - TOF_0 \tag{6.3}$$

where TOF_0 is the predicted time of flight from z=0 cm to the calorimeter position. Since many of these terms are the same as in the t^{WV}_{corr} equation described in Equation 5.3 we can plug this relation in to find

$$t^{WV}_{corr} = t^0_{corr} - t^0_{WV} + (TOF_0 - TOF_{WV}). \tag{6.4}$$

This relationship is useful because what we are after is $< t^{WV}_{corr} >$. Since the three terms in Equation 6.4 are not correlated with one another, or are small, we can consider each term independently in terms of its contribution to $< t^{WV}_{corr} >$. We can directly measure $< t^{0}_{corr} >$ distribution from the data. The t^{0}_{WV} distribution is zero purely from beam related parameters with a mean of 0 ns and an RMS of 1.28 ns as shown in Figure 3.10. Finally, we note that $TOF_0 - TOF_{WV}$ term is fairly narrow and has a mean of ∼0 ns for geometric reasons. This is true because wrong vertices are produced independently of the physics of the right vertex, so $TOF_0 - TOF_{WV}$ is largely process independent. A representation of this can be seen on the LHS of Figure 6.3. We note that the distance from the beam line to the calorimeter is much larger (∼184 cm) than the scale of the variation in the collision distribution (RMS of ∼28 cm shown in Section 2.4.5). This fact implies that $TOF_0 - TOF_{WV}$ should be small on average. The RHS of Figure 6.3 shows this quantitatively in a series of toy pseudo-experiments where we calculate the time-of-flight of the wrong vertex, TOF_{WV}, and the time-of-flight for the no vertex, TOF_0, distributions. Here we generate verticies according to the z and t parameters of the Tevatron beam in Table 2.1 and assume sa uniform arrival in the CES z position. We see that $< TOF_0 - TOF_{WV} >$ is consistent with zero to less than 40 ps. With this understanding we see why, to a good degree of approximation, $< t^{WV}_{corr} >=< t^{0}_{corr} >$.

To test this hypothesis we use our six MC control samples as well as our two $e + \not\!\!E_T$ data control samples. We select events using Tables 5.5 for photons and 5.2 for electrons but this time require these samples to explicitly fail the good SpaceTime vertex selection in order to construct the no vertex timing distribution. We examine t^{0}_{corr} for each sample, shown in Figure 6.4, and fit a Gaussian from -5 ns $< t^{0}_{corr} <$ 3 ns allowing the mean to vary and find the best fit parameter while fixing the RMS= 1.6 ns. We pick the range for the Gaussian fit to start at -5 ns in order to avoid any potential contamination from beam halo events which we expect to begin to be present at t^{0}_{corr} <-5 ns, as described in Section 4.3. We only fit out to $t^{0}_{corr} = 3$ ns in order to avoid any potential contamination from signal like events that we expect to

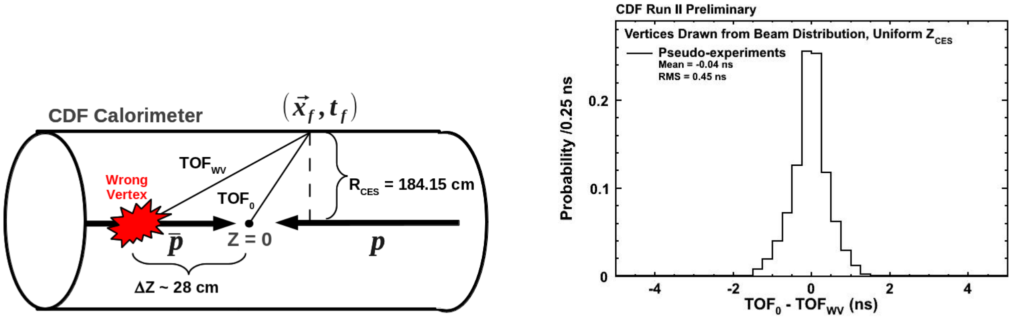

Figure 6.3: (LHS) An illustration showing the various components of the time-of-flight components of the t_{corr}^{WV} coming from the difference relative to the center of the detector (TOF_0) and the time-of-flight difference relative to a wrong vertex (TOF_{WV}). (RHS) The results of toy pseudo-experiments where verticies are generated according to the z and t parameters of the Tevatron and we calculate the time-of-flight of the wrong vertex, TOF_{WV}, and the time-of-flight for the no vertex, TOF_0 demonstrating that $< TOF_0 - TOF_{WV} >= 0$ to less than 40 ps.

see above 3 ns, as described in Section 1.5. We choose the RMS= 1.6 ns since this is the expected t_{corr}^0 timing resolution as described in Section 5.1. We also note that for the control $e+\not{E}_T$ samples from data we include a fit to the cosmics by extrapolating to the cosmics region 20 ns $< t_{corr} <$ 80 ns. The results for all eight are are shown in Figure 6.4.

To test the assumption that the t_{corr}^0 distribution is well modeled by a Gaussian with an RMS= 1.6 ns we do a second fit with a Gaussian in the range -5 ns $< t_{corr}^0 <$ 3 ns and allow both the mean and RMS to vary and find the best fit parameter for each sample. The results are summarized Table 6.2 and can be seen graphically in Figure 6.5. We find that, as expected, the mean varies but is again independent of RMS. Similarly, we note that the data points all fall within the yellow band (± 10% the nominal RMS) for a wide range of $< t_{corr}^0 >$.

Having established the assumption that the no vertex timing distribution is accurately described by a Gaussian with an RMS of 1.6 ns for our MC backgrounds

Sample	**No Vertex Mean (ns)**	**No Vertex RMS (ns)**
W→ eν MC	0.61 ± 0.20 ns	1.68 ± 0.14 ns
γ+Jet MC	0.16 ± 0.11 ns	1.58 ± 0.06 ns
Zγ MC	0.07 ± 0.05 ns	1.55 ± 0.05 ns
W→ $\mu\nu$ MC	0.27 ± 0.20 ns	1.64 ± 0.17 ns
W→ $\tau\nu$ MC	0.31 ± 0.19 ns	1.56 ± 0.19 ns
Wγ MC	0.13 ± 0.06 ns	1.50 ± 0.05 ns
e+$\not\!\!E_T$ Data	0.23 ± 0.08 ns	1.66 ± 0.09 ns
e+$\not\!\!E_T$ Data $(E_T\&\not\!\!E_T) > 30$ GeV	0.04 ± 0.05 ns	1.69 ± 0.05 ns

Table 6.2: Summary of the results in Figure 6.5 which plots the relationship between the mean and RMS of the t^0_{corr} distributions for the six MC and two e+$\not\!\!E_T$ control datasets for sets of events where we require the events to pass all the requirements in Tables 5.5 and 5.2 but have no SpaceTime vertex reconstructed. The $< t^0_{corr} >$ and RMS is found by fitting the no vertex corrected time (t^0_{corr}) distribution with a single Gaussian from -5 ns $< t^0_{corr} <$ 3 ns where the Gaussian RMS and mean are allowed to vary to find the best fit.

and e+$\not\!\!E_T$ data, we now look to the comparison of $< t^{WV}_{corr} >$ (which we can measure for our control samples since we know the true vertex, but not the real data) versus $< t^0_{corr} >$ (which we can measure with real data). In Figure 6.6, and summarized in Table 6.3, we compare the two measured timing means. We quickly notice that all of the points lie on the line at 45 degrees (where the two measured timing means equal one another). The mean of the wrong vertex and the mean of the no vertex distribution are thus shown to be nearly equivalent values for our six MC control samples as the two control e+$\not\!\!E_T$ data samples.

We note that although the two are always equal within uncertainties, the two measurements are not always identical, so for this reason we conservatively overestimate any systematic difference between the wrong vertex mean and the no vertex mean to be 100 picoseconds.

Sample	**Wrong Vertex Mean (ns)**	**No Vertex Mean (ns)**
W→ eν MC	0.73 ± 0.19 ns	0.68 ± 0.16
γ+Jet MC	0.18 ± 0.13 ns	0.16 ± 0.10
Wγ MC	0.14 ± 0.07 ns	0.14 ± 0.03
Zγ MC	0.12 ± 0.01 ns	0.06 ± 0.01
W→ $\mu\nu$ MC	0.29 ± 0.26 ns	0.25 ± 0.19
W→ $\tau\nu$ MC	0.43 ± 0.26 ns	0.38 ± 0.17
e+$\not\!\!E_T$ Data	0.16 ± 0.05 ns	0.23 ± 0.05
e+$\not\!\!E_T$ Data *($E_T > 30$ GeV and$\not\!\!E_T > 30$ GeV)*	0.04 ± 0.05 ns	0.02 ± 0.01

Table 6.3: Summary of the two different measurements of the wrong vertex mean using the six MC backgrounds control samples, selected using Table 5.5, and the two $e+\not\!\!E_T$ data control samples, selected using Table 5.2. Here we obtain the wrong vertex mean by fitting the corrected time (t_{corr}) distribution with a double Gaussian function from -10 ns $< t_{corr} <$ 10 ns where the right vertex Gaussian mean = 0.0 ns and RMS = 0.65 ns and the wrong vertex Gaussian RMS = 2.0 ns and the mean is allowed to vary to find the best fit. The no vertex mean is found by fitting the no vertex corrected time (t^0_{corr}) distribution with a single Gaussian from -5 ns $< t^0_{corr} <$ 3 ns where the Gaussian RMS = 1.6 ns and the mean is allowed to vary to find the best fit. These results are plotted in Figure 6.6.

With this assumption, we can rewrite Equation 3.11 using $\mu^{NV} =< t^0_{corr} >$ and $\mu^{WV} =< t^{WV}_{corr} >$ and determine the number of events in the signal region from collision backgrounds using the relation:

$$N^{SM}_{signal} = R(\mu^{WV} = \mu^{NV}) \cdot N^{SM}_{control} \tag{6.5}$$

and take the systematics on R due to the uncertainty between the relation $\mu^{WV} = \mu^{NV}$ and the uncertainty of the RMS of the wrong vertex Gaussian.

To test how well this relation predicts the number of events in the signal region with our eight control samples we show the results in Figure 6.7 as if they were real data. By comparing the prediction we see that the measured value of $< t^0_{corr} >$ does an excellent job of predicting the ratio of events in the sample of events with a good vertex. Again, the black line is a prediction based on the measure $< t^0_{corr} >$ and not a fit. A comparison of the the measured and observed ratio is given in Table 6.4. Thus, we have confirmed that our method that uses an independent sample, the "no vertex" sample, in conjunction with the number of events in the control region gives us a data-driven estimate of the number of events in the signal region for SM backgrounds. The uncertainty, as we will see is dominated by the statistical uncertainty of the number of events from collision in the no vertex sample to determine $< t^0_{corr} >$.

Sample	**Observed No Vertex Mean (ns)**	**Predicted Ratio**	**Observed Ratio**
W→ $e\nu$ MC	0.68 ± 0.16 ns	2.74 ± 0.76	3.70 ± 0.36
γ+Jet MC	0.16 ± 0.10 ns	1.27 ± 0.20	1.30 ± 0.20
Wγ MC	0.14 ± 0.03 ns	1.23 ± 0.05	1.14 ± 0.11
Zγ MC	0.06 ± 0.01 ns	1.09 ± 0.02	1.12 ± 0.02
W→ $\mu\nu$ MC	0.25 ± 0.19 ns	1.46 ± 0.48	1.40 ± 0.41
W→ $\tau\nu$ MC	0.38 ± 0.17 ns	1.77 ± 0.51	1.70 ± 0.40
e+$\not\!\!E_T$ Data	0.23 ± 0.05 ns	1.39 ± 0.31	1.32 ± 0.17
e+$\not\!\!E_T$ Data *($E_T > 30$ GeV and $\not\!\!E_T > 30$ GeV)*	0.02 ± 0.01 ns	1.03 ± 0.07	1.06 ± 0.13

Table 6.4: Summary of the results shown in Figure 6.7 of our method for the SM MC samples and our e+$\not\!\!E_T$ data "no vertex"control samples. We find the predicted ratio using that measured mean as well as the observed ratio of the number of events in the signal region to the control region agree to within errors.

In the next section we formalize the background estimation procedure in the exclusive $\gamma_{delayed}$+$\not\!\!E_T$ final state utilizing the fact that we can predict the wrong vertex mean from the "no vertex" sample, but at the same time take into account the contributions from cosmic ray background sources.

6.3 The Combined Background Estimation Procedure

To briefly recap, in Section 6.1 we demonstrated how the double Gaussian nature of the corrected time distribution makes it possible to predict the number of events expected in the signal region (2 ns $< t_{corr} <$ 7 ns) from SM sources if we know the mean of the wrong vertex distribution. In Section 6.2 we showed how we can estimate the wrong vertex mean using a sample of events that pass all our event selection requirements but fail to reconstruct a vertex and measure $< t^0_{corr} >$. In Section 4.2 we outlined how we estimate the cosmic ray rate in the signal region by measuring the number of events in the cosmics region (20 ns $< t_{corr} <$ 80 ns) where we do not expect to see any collision sources which we call this the "cosmics region".

We now combine these two estimate and lay out the final procedure by which we will use the information from the cosmics region, the mean of the no vertex distribution, and the number of events observed in the control region (-7 ns $< t_{corr} <$ -2 ns) to predict the number of events expected in the signal region (2 ns $< t_{corr} <$ 7 ns) from SM sources. We procedure is as follows:

- **Select events for the exclusive $\gamma + \not\!\!E_T$ final state:**

  All events are selected using the criteria in Table 5.5. We sort events into events that have a good SpaceTime vertex and events with no good SpaceTime vertex. From this bifurcation we construct the corrected time distributions for each. For the events having a good SpaceTime vertex we construct the t_{corr} variable defined in Equation 1.8. Events that do not have a good SpaceTime vertex are part of the "no vertex" sample and we construct the t^0_{corr} timing distribution defined in Equation 6.4.

- **Estimate the cosmic ray event rate:**

  Since events from cosmic rays represent a significant contribution for both the good vertex and no vertex sample, we must estimate their contamination to the regions under consideration. Thus, for both the t_{corr} and t^0_{corr} timing distributions, we look at the events in the timing region from 20 ns $< t_{corr} <$

80 ns and 20 ns < t^0_{corr} < 80 ns and fit a straight line in this region. This fitted rate gives us an estimate of the rate of cosmics per nanosecond present in both the no vertex and good vertex samples (which is expected to be different for each). This is then straightforwardly extrapolated to the number of events in the signal region using Equation 4.3 and a similar relation for the no vertex sample.

- **Measure the mean of the "no vertex" timing distribution:**

  Using the t^0_{corr} distribution, we fit a straight line fixed at the cosmics rate plus a Gaussian with an RMS = 1.6 ns from -5 ns < t^0_{corr} < 3 ns and measure the mean of this distribution and the uncertainty of the fit.

- **Predict the number of background events in the Signal Region:**

  Finally, using the mean of the no vertex distribution, the measured cosmics rate for the good vertex sample, and the number of events observed in the control regions in the good vertex sample we can uniquely calculate the number of events expected from SM sources using Equation 6.5. With this prediction we can sum the number of events from both cosmics and wrong vertex events in the signal region as well as determine the uncertainty on this estimation.

With the data-driven background procedure now laid out, we now turn to the results of the search in the exclusive $\gamma + \not\!\!E_T$ final state and the quantification of the associated errors with our prediction. Ultimately, the difference between the predicted number of events in the signal region and the observed number will indicate whether we have evidence for new physics in the exclusive $\gamma_{delayed} + \not\!\!E_T$ final state.

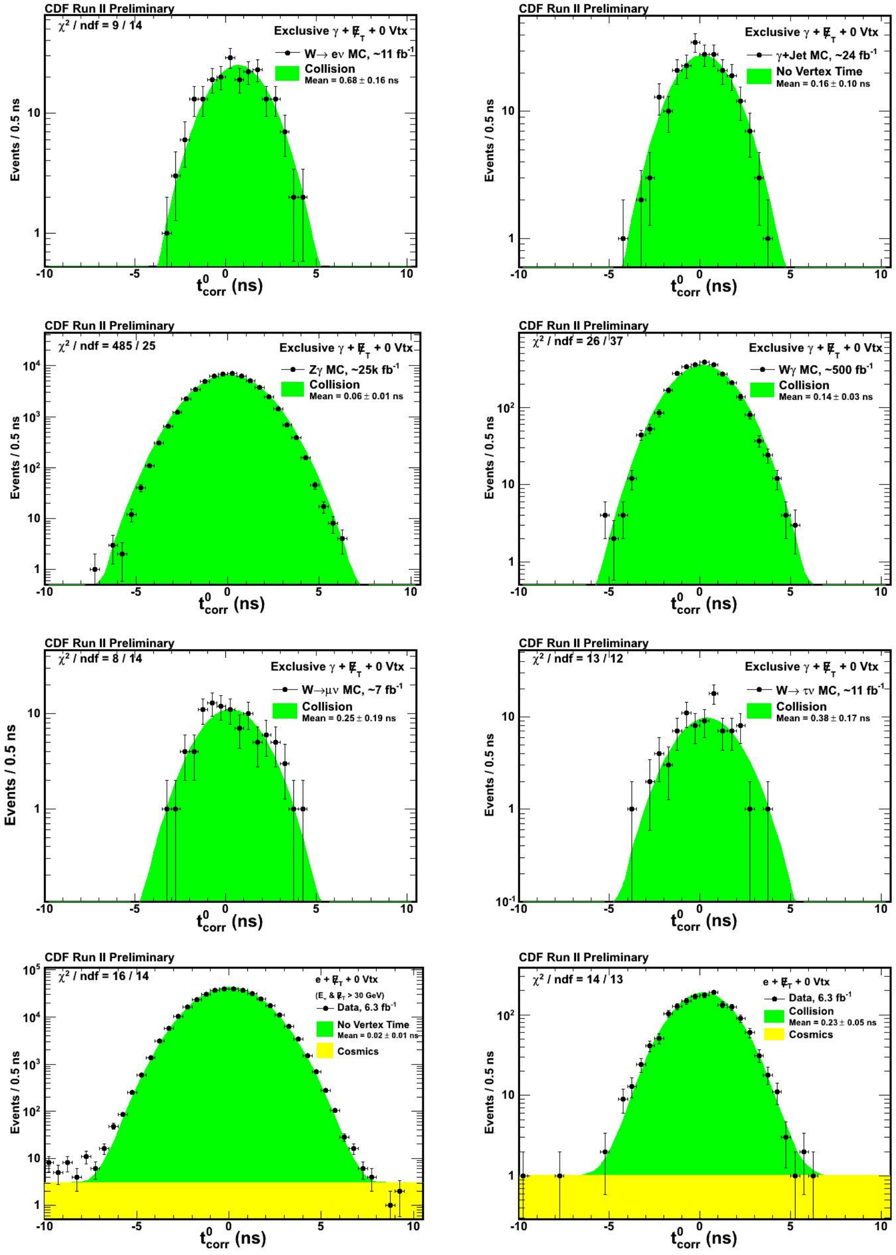

Figure 6.4: The t^0_{corr} distribution for the no vertex samples from the six MC control samples as well as the two control e+$\not\!\!E_T$ sample from data. The fit is for a Gaussian fit from -5 ns < t^0_{corr} < 3 ns with a fixed RMS = 1.6 ns in order to estimate to measure < t^0_{corr} > which is a good estimate of < t^{WV}_{corr} >.

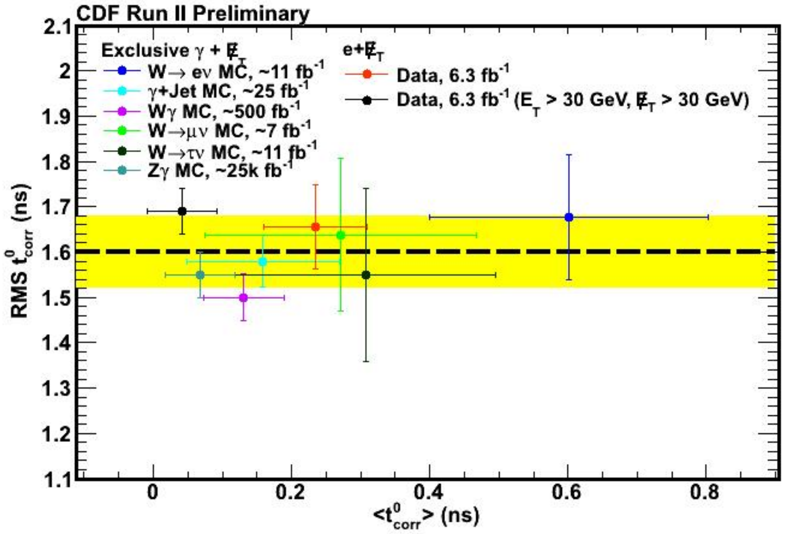

Figure 6.5: A plot showing the relationship between the RMS of the t^0_{corr} distribution for no vertex events versus $< t^0_{corr} >$ for our MC and e+Met data control samples. This demonstrates that the assumption that the no vertex corrected time distribution is well modeled by a Gaussian with an RMS of 1.6±0.08 ns for the various MC backgrounds in addition to e+$\not\!\!E_T$ data samples is a good one. The no vertex mean and RMS is found by fitting the no vertex corrected time (t^0_{corr}) distribution with a single Gaussian from -5 ns $< t^0_{corr} <$ 3 ns where the Gaussian RMS and mean are allowed to vary to find the best fit.

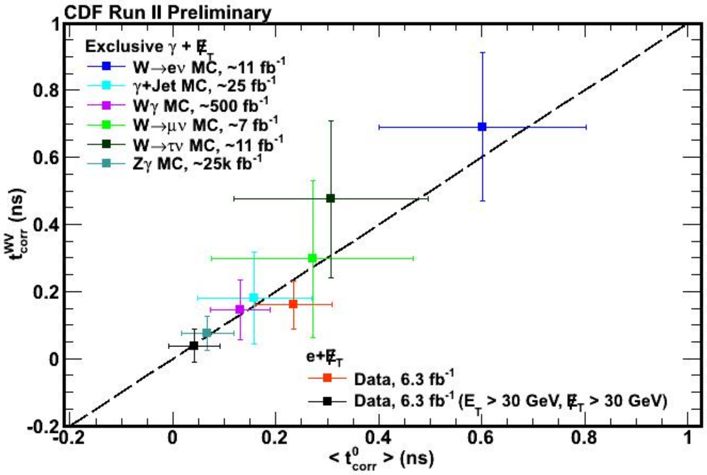

Figure 6.6: The correlation between $< t_{corr}^{WV} >$ and $< t_{corr}^{0} >$ for our MC and $e+\not\!\!E_T$ data control samples. One method is taken from Table 5.6 and is where we measure the WV directly from a full fit to the data, which is only possible in MC, and one from the no-vertex sample which is available in data. Note that the two agree to a high degree of precision. This fact allows us to predict the wrong vertex mean for a given sample by measuring a sample of events that pass all the other selection requirements but fail to reconstruct a vertex.

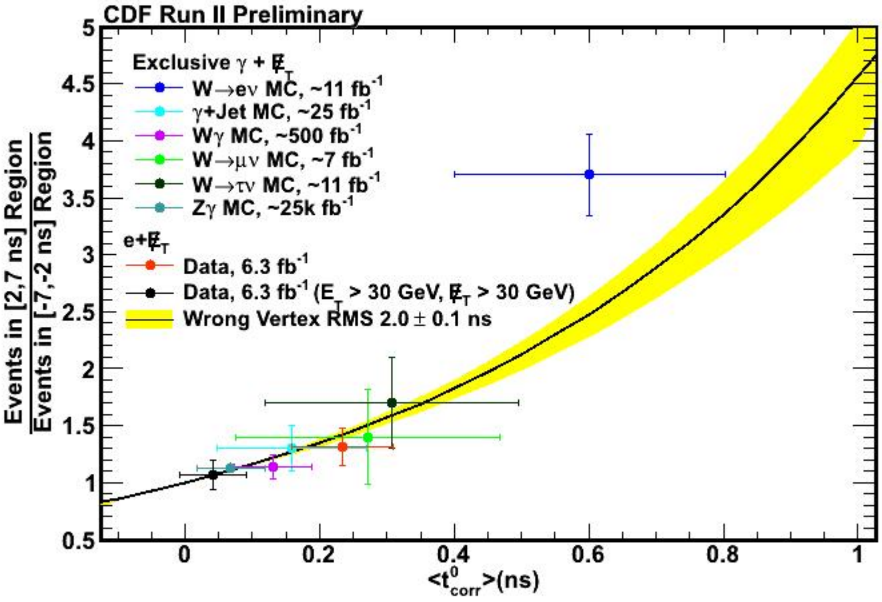

Figure 6.7: The ratio of the number of events observed in the signal region (2 ns $< t_{corr} <$ 7 ns) to the number of event observed in the control region (-7 ns $< t_{corr} <$ -2 ns) versus the observed "no vertex" mean for the eight MC and data control samples. This shows that using the double Gaussian assumption and measuring the mean of the "no vertex" distribution we can accurately predict the number of events in the signal region for all our control samples within uncertainties.

7. SEARCHING FOR NEW PHYSICS IN THE EXCLUSIVE $\gamma_{Delayed} + \not\!\!E_T$ FINAL STATE

In this section we will present the results of the search in the exclusive $\gamma_{delayed} + \not\!\!E_T$ final state. Section 7.1 presents the results of the event selection outlined in Table 5.5 when applied to the 6.3 fb^{-1} data sample. We next use the data-driven background methods, described in Section 6.3, to estimate the number of events expected in the signal region (2 ns $< t_{corr} <$ 7 ns) from SM and non-collision sources. In Section 7.2 we detail the results of the search and conclude that we find only a modest excess above background predicition. Section 7.3 compares this result to the 2008 result.

7.1 Event Selection and Background Predictions

Table 7.1 shows the event reduction from the full set of events collected by CDF to the final exclusive $\gamma + \not\!\!E_T$ event selection described in Table 5.5 before the final signal region timing requirement. We have 5,421 events passing all our event selection requirements and having a SpaceTime vertex which we will use to construct the t_{corr} timing distribution and look for evidence of $\gamma_{delayed} + \not\!\!E_T$. We also have 4,942 events which pass all the event selection requirements but have no SpaceTime vertex reconstructed ("no vertex sample") which we will use to measure $< t^0_{corr} >$ as our estimate of $< t^{WV}_{corr} >$. The timing distributions are shown in Figure 7.1 and 7.2 respectively.

As described in the background estimation procedure (Section 6.3), we begin by estimating the cosmic ray event rate for both the t_{corr} and t^0_{corr} distributions. In Figure 7.1, we take the sample of events that have a SpaceTime vertex and look in the timing region between 20 ns $< t_{corr} <$ 80 ns. We fit a straight line in this region and use this to estimate the number of events from cosmic rays per nanosecond to

Event Selection	**Number of Events**
Pass Online/Offline Trigger selection with an identified photon w/ $E_T^0 \geq 45$ GeV and $\not{E}_T^0 \geq 45$ GeV	38,291
Pass Beam Halo Veto	36,764
Pass Cosmics Veto	24,462
Pass Track Veto for Tracks with $P_T > 10$ GeV	16,831
Pass Jet Cluster Veto for Jets with $E_T^0 > 15$ GeV	12,708
Pass Large $\lvert Z \rvert$ Vertex Veto	11,702
Pass $e \rightarrow \gamma_{fake}$ Veto	10,363
Events with Good SpaceTime Vertex / No Reconstructed Vertex ***"Good Vertex Sample" / "No Vertex Sample"***	5,421 / 4,942

Table 7.1: Event reduction table for the exclusive $\gamma + \not{E}_T$ search. The last selection requirement breaks the events into two samples: 1) Events that do have a reconstructed vertex and 2) Events that do not have a good SpaceTime vertex ("no vertex sample"). The sample of events that do have a reconstructed vertex are the events in which we perform our search for $\gamma_{delayed} + \not{E}_T$ while the "no vertex sample" is used to estimate the mean of the wrong vertex as described in Section 6.2.

be 32 ± 1 events. This rate is then used to predict the number of cosmic ray events we expect in the control and signal regions. Using Equation 4.3 we find:

$$N^{cosmics}_{\text{SignalRegion}} = 5\text{ ns} \cdot \frac{32\text{ events}}{\text{ns}} = 160 \pm 5\text{ events} \tag{7.1}$$

Similarly, we perform a straight line fit from 20 ns $< t^0_{corr} <$ 80 ns for the no vertex sample to find the cosmics rate 38 ± 1 events per ns. We use a modified version of Equation 4.3 to find the cosmic rate in the region -5 ns$< t^0_{corr} <$3 ns:

$$N^{cosmics}_{\text{NV}} = \Delta T_{-5\ ns<t^0_{corr}<3\ ns} \cdot \frac{N^{cosmics}_{\text{NVCosmicsRegion}}}{\Delta T_{\text{CosmicsRegion}}} \tag{7.2}$$

$$N^{cosmics}_{\text{NV}} = 8\text{ ns} \cdot \frac{38\text{ events}}{\text{ns}} = 307 \pm 8\text{ events.} \tag{7.3}$$

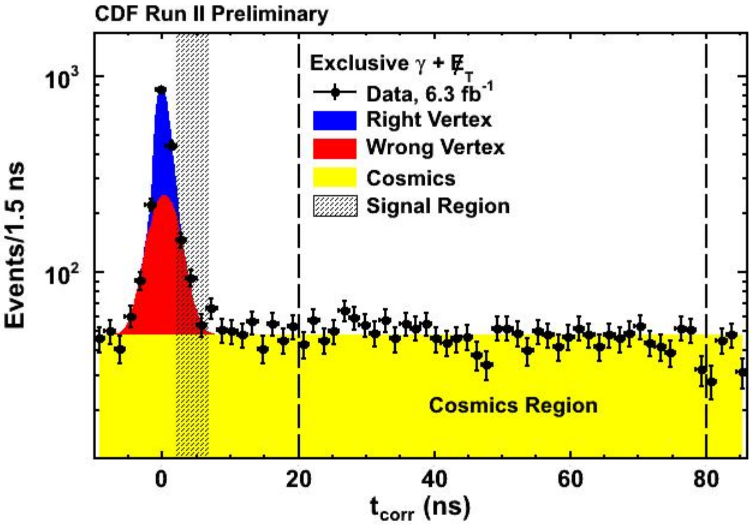

Figure 7.1: The t_{corr} distribution for the final γ+$\not\!\!E_T$ dataset. In this plot we highlight the cosmics region, 20 ns $< t_{corr} <$ 80 ns, and use this to estimate the cosmic ray rate in the signal region 2 ns $< t_{corr} <$ 7 ns as well as our control region as part of the background estimate procedure.

Using this we next perform a Gaussian plus straight line fit from -5 ns$< t^0_{corr} <$3 ns with a fixed RMS = 1.6 ns to measure $< t^0_{corr} >$ as shown in Figure 7.2. We find $< t^0_{corr} >= 0.12 \pm 0.17$ ns. The bottom of Figure 7.2 shows that the $\pm 1\sigma$ variation of the no vertex mean does describe the data well and thus gives us good confidence that this is a good measure of $< t^0_{corr} >$.

We estimate $< t^{WV}_{corr} >=< t^0_{corr} >$ and conservatively overestimate a 100 ps systematic on the error of this predicition as described in Section 6.2. Using the estimation methods described in Section 6.3 and adding the uncertainties in quadrature we find $< t^{WV}_{corr} >= 0.12 \pm 0.20$ ns.

Finally we count the number of events in the bulk (-2 ns $< t_{corr} <$ 2 ns) and control (-7 ns $< t_{corr} <$ -2 ns) timing regions for the good vertex sample. The summary of the basic background estimation values and the breakdown of the number of observed events in the cosmics, bulk, and control region is given in Table 7.2.

Quantity	**Measured Value**	**Error**
No Vertex Mean	0.12 (ns)	±0.17 (ns)
Cosmics per Nanosecond	32 (Events)	±1 (Events)
Wrong Vertex Mean	0.12 (ns)	±0.20 (ns)
Number of Events in the Cosmics Region *20 ns* $< t_{corr} <$ *80 ns*	1,919 (Events)	-
Number of Events in the Control Region *-7 ns* $< t_{corr} <$ *-2 ns*	241 (Events)	-
Number of Events in the Bulk Region *-2 ns* $< t_{corr} <$ *2 ns*	1,463 (Events)	-

Table 7.2: Summary of the data-driven background measurements used for the exclusive $\gamma + \not\!\!E_T$ sample prediction.

7.2 Results

Utilizing the estimation methods described in Section 6.3 and the results in Table 7.2 we can now predict the number of background events in the signal region. Using Equation 3.11 we can compute the ratio of the number of events in the signal region to the number of events in the control region. From the mean of 0.12 ± 0.20 ns and Equation 3.10 we find a ratio of 1.20 ± 0.44 taking into account the uncertainty on the mean as well as the RMS. We predict the number of events from cosmic rays in the control region (-7 ns $< t_{corr} <$ -2 ns) to be 160 ± 5 events using Equation 7.1. Taking the number of observed events in the control region from Table 7.2 minus the number of cosmics events we find

$$N^{WV}_{Control} = N^{Obs}_{Control} - N^{Cosmics}_{Control} = 241 - 160 = 81 \pm 17 \,\text{events} \tag{7.4}$$

where we have ignored the right vertex contribution as it is expected to be less than 1 event in the control and signal timing region, and included the statistical uncertainties on the measured values. To estimate the number of wrong vertex events in the signal region we take:

$$N^{WV}_{Signal} = R \cdot N_{Control} = 1.20 \cdot 81 = 96 \pm 35\,\text{events} \tag{7.5}$$

where we have taken into account the statistical uncertainties of the number of events observed as well as the uncertainties on R which is dominated by the uncertainty on the wrong vertex mean.

Combining the backgrounds, we find that

$$N^{Expected}_{Signal} = N^{WV}_{Signal} + N^{Cosmics}_{Signal} = 96 + 160 = 257 \pm \ 35\,\text{events.} \tag{7.6}$$

These results are summarized in Table 7.3. This procedure predicts that there are ∼2 events from right vertex in the control and signal regions, well below the uncertainty of ±35 events and thus is essentially negligible. The largest background in this final state comes from cosmics rays at almost a 2:1 ratio in the signal region. Meanwhile, our largest systematic uncertainty comes from the error on the wrong vertex mean which is dominated by the statistics of the events in the “no vertex” sample.

We now compare our background estimation to the data looking at the t_{corr} distribution shown in Figure 7.3 where we have used the 1,463 events in the bulk region and the methods in Section 3 to determine the total number of right vertex events. We observe 322 events in the signal region. To show how well the data is described, we compare the full background estimate and the data in the top of Figure 7.3 and the ±1σ variation of the wrong vertex mean in the bottom of Figure

Quantity *(Events)*	**Prediction** *(Events)*
Number of Events from Cosmic Rays expected in the Signal Region	160 ± 1
Number of Events from Wrong Vertex expected in the Signal Region	96 ± 35
Total Number of Background Events Predicted in the Signal Region	257 ± 35
Total Number of Events Observed in the Signal Region	322

Table 7.3: Summary of the data-driven background prediction and observation for the exclusive $\gamma_{delayed} + \not\!\!E_T$ sample.

7.3. Figure 7.4 shows the background subtracted results where the yellow and green bands represent the $\pm 1\sigma$ and $\pm 2\sigma$ uncertainties in the systematics and the error bars on the data points represent the statistical uncertainties. We note that all errors were symmetrized in this plot for simplicity.

A modest excess remains in the data of observed minus predicted ($N_{Observed} - N_{Predicted}$) of 65 events in the signal region. While we note that the majority of the bins are above the expectations, we calculate the significance of this excess based purely on the results of the counting experiment. By taking into account both the systematic and the statistical uncertainty expected from the number of observed events in the data as part of the overall uncertainty we find:

$$\begin{gathered} N_\sigma = \frac{N_{Observed} - N_{Predicted}}{\sqrt{\sigma^2_{N_{Pred}} + \sigma^2_{N_{Obs}}}} \\ N_\sigma = \frac{322 - 257}{\sqrt{35^2 + 322}} \\ N_\sigma = 1.65 \end{gathered} \tag{7.7}$$

An $N_\sigma = 1.65$ gives a one sided p-value (the estimated probability that this excess is inconsistent with a null hypothesis) of ~5%. Since the standard for discovery in particle physics is considered 5σ (and for evidence is typically 3σ) we clearly cannot claim any evidence for new physics in our signal region, thus leading to the conclusion that we see no evidence for new physics in the exclusive $\gamma_{delayed} + \not\!\!E_T$ final state.

7.3 Comparison of the New Results with the Preliminary 2008 Results

The first question that arises following the results presented in Section 7.2 might be, "what happened to the excess shown in the preliminary 2008 result?". As discussed in Section 1.6 an "excess" number of events above the background expectations of 67 events with a preliminary significance of $N_\sigma \sim 4$ was reported only using $\sim$4.77 fb^{-1} of data. However, as we have learned, much of this excess was due to a poor background estimation technique, as well as due to sources of biased SM backgrounds in the sample. With the addition of numerous background rejection methods (Section 5.5), a more robust set of calibrations (Section 3), and a new data-driven background estimation procedure (Section 6.3) to predict the mean of the wrong vertex we now have an excess with a much smaller significance. While this provides a qualitative description, it is useful to make quantitative the difference between the previous analysis result and our current result. Asked differently, can we tell which cuts made the difference and is there any evidence we made a real signal go away inappropriately?

We begin by listing the changes in the analysis which have taken place since the preliminary result in 2008. These changes are summarized in Table 7.4.

- **Remove photon CES χ^2 requirement:**

  Since the original analysis was done as a search for Large Extra Dimensions it included a selection on the CES χ^2 since this requirement aids in the reduction of jets that fake photons as well as cosmic ray candidates since the photon is assumed to come from the beamline. However, since it is known that this

Change in Analysis	**Impact on the Sample**
Remove photon CES χ^2 requirement *Discussed in Section 2*	Add more events to our sample
Define photon ID relative to $z = 0$	Change the events in our sample
Add new cosmics veto: CES(E) and HAD(E) *Discussed in Section 4*	Remove events from our sample
Addition of data *Expand to 6.3 fb^{-1}*	Add more events to our sample
New calibrations procedure *Discussed in Section 3*	Changes the timing of the events
Change event E_T and $\not\!\!E_T$ definition *Discussed in Section 5.5.1*	Change the events in our sample
Add large $\|z\|$ vertex veto *Discussed in Section 5.5.3*	Remove events from our sample
Add $e \rightarrow \gamma_{fake}$ veto *Discussed in Section 5.5.2*	Remove events from our sample
New $< t^{WV}_{corr} >$ estimation method	Changes the number of SM background events expected in the signal region

Table 7.4: List of changes and the impacted quantites in the analysis since the original 2008 γ+$\not\!\!E_T$ preliminary result.

cut can be inefficient for photons that do not come directly from the beam line, for example, for use in searches for delayed photons which come from the decay of some long-lived heavy object [38], we have elected to remove this requirement. The effect of this update is to allow more events into our sample some of which increase the jet background (although this is expected to be small since production rates for fake photons with more than 45 GeV is small) and some of which increases the cosmics rate. Additional cosmic ray rejection requirements are added later.

- **Define photon ID relative to $z = 0$:**

  Another change to the photon definition includes a redefinition of the photon identification variables relative to z =0 cm. Specifically, this effects the E^0_T, energy isolation, track isolation, N3D track rejection, and 2^{nd} CES cluster energy variables from Table 2.8 and discussed further in Appendix A. The overall effect of this update is to change the events that will be identified as having a "good" photon passing all our requirements. We note that despite including the E_T^0 variable in the photon identification, we still (at this point) select the events based on requiring E_T^{vtx} >45 GeV and $\not\!\!E_T^{vtx}$ >45 GeV to distinguish between photon identification changes to the analysis and the impact of changing the E_T thresholds.

- **Add new cosmics veto: CES(E) and HAD(E)**

  As discussed in Section 4, we also include the new cosmics rejection requriments into the photon identification variables. The addition of these requirements only reduce the total number of events that are present in our sample, specifically events likely to have originated from cosmic ray events.

- **Addition of data:**

  Here we are simply adding data in order to update our result from the original 4.77 fb^{-1} to 6.3 fb^{-1} of data. The overall effect of this update should be to simply add more events to our sample.

- **New calibrations procedure:**

  As discussed in Section 3, we include a new set of calibrations for the track t_0 as reported by the COT, the vertex t_0 as reported by the SpaceTime vertexing algorithm, and the photon t_f as determined by the EMTiming system. While this will change the number of events found in any one timing region, this will not effect the overall number of events in our sample.

- **Change event E_T and $\not\!\!E_T$ definition:**

As described in Section 5.4, the correlation between geometric and kinematic biases that come from the selection of an incorrect vertex leads to a migration of events into our sample with a large timing bias and out of the sample with a small timing bias. Therefore, we redefine our event selection to be $E_T^0 >$45 GeV and $\not{E}_T^0 >$45 GeV. This changes the number of events in the sample.

- **Add large $|z|$ vertex veto:**

  Some of the most biased time events come from collisions that occur with $|z| >$60 cm. As we showed in Section 5.5.3, these events have a large timing bias, and thus we veto them. The effect of this veto only reduces the number of events in our sample.

- **Add $e \rightarrow \gamma_{fake}$ veto:**

  We implement the new $e \rightarrow \gamma_{fake}$ veto (described in Section 5.5.2). This veto is introduced in order to reduce the rate of events that enter our sample where an electron fakes a photon which are expected to have a large timing bias. The effect of this veto reduces the number of events in our sample.

- **New $< t_{corr}^{WV} >$ estimation method:**

  Finally, we use the new data-driven background estimation method, detailed in Section 6, to predict $< t_{corr}^{WV} >$. While this does not change the number of events in the sample, it does change our prediction of the number of expected events from SM sources in the signal region.

Now that we have a complete list of all the changes to the analysis we look to the impact of these changes to the number of events in the control and signal regions of the t_{corr} distribution. These results are summarized in Table 7.5. Since it is useful to quantify how much of the "excess" comes or goes because of an individual cut, we define the the term "pseudo-excess" which is the number of events in the signal region minus the number of events in the control region. Said differently, it would be the excess if we used the old assumption of $< t_{corr}^{WV} >= 0.0$ ns. While this doesn't not give a proper quantification because all the changes are correlated in the final analysis, and the order in which we present the changes matters, it does give a feel for the importance of each effect.

Sample	**Number of Events in the Control Region**	**Number of Events in the Signal Region**
Original 4.77 fb^{-1} $\gamma+\not\!\!E_T$ Sample *(See Table 5.3)* *(w/ original E_T and $\not\!\!E_T$ definitions)*	124	191
Remove CES χ^2 requriment, apply new photon ID, and add cosmics veto	233	315
Add data	335	506
Apply new calibrations *(See Section 3)*	323	459
Redefine E_T^{Vtx} to E_T^0 *(See Section 5.5.1)*	315	453
Add large $\|z\|$ veto *(See Section 5.5.3)*	267	375
Add $e \rightarrow \gamma_{fake}$ veto *(See Section 5.5.2)*	241	322
New $< t_{corr}^{WV} >$ estimation method *(See Section 6)*	$241 \rightarrow 257 \pm 35$ expected	322

Table 7.5: Comparison of the new results against the original 2008 $\gamma+\not\!\!E_T$ preliminary result.

- **Updating the Photon Identification and Adding the Cosmics Rejection:**

  As part of making our search more appropriate for a long-lived particle that decays to a photon we have removed the photon CES χ^2 (described in Section 2.4.3), applied the new photon identification requirements defined relative to

$z = 0$ cm, and included of the new cosmics ray vetos (described in Section 4.2). We see an increase of 124 events in the signal region and 109 in the control region. This suggests an increase in the "pseudo-excess" from 67 to 82 events, which is reasonable since we have increased, overall, the number of events in the sample significantly. However, we must recall that at this point we have not taken into account many of the known biases (e.g. geometric biases, $e \rightarrow \gamma_{fake}$, large $|z|$ events, new calibrations, data-driven background prediction).

- **Add data:**

  We now include the data up to 6.3 fb^{-1} and observe the number of events in the control region to rise to 335 and the number of events in the signal region to be 506. This is an increase of 191 events in the signal region and 102 in the control region and is in part due to additional luminosity as well as higher instantaneous luminosity affecting the rate at which cosmics enter the sample. This translates to an increase in the "pseudo-excess" from 82 to 171 events. This is the largest value we will see.

- **Apply new calibrations:**

  The new calibration procedure calibrates using the event-by-event reconstructed time-of-flight rather than an assumed average time-of-flight. As seen in Table 7.5 this also has an effect of "reducing" the previously observed "pseudo-excess". We observe after this change that there are 459 events in the signal region and 323 events in the control region, reducing the "pseudo-excess" of from 171 events to 136 events. This result roughly implies that some 35 events of the "excess" were due to poorly calibrated vertex and/or EMTiming times.

- **Redefine E_T^{Vtx} to E_T^0:**

When we apply the redefinition of E_T^0 and $\not\!\!E_T^0$ to our event selection we observe that the number of events in the signal region is reduced from 459 to 453 events in the signal region and from 323 to 315 events in the control region. This slightly adds to our "pseudo-excess" by raising it from 136 to 138 events. This implies that only a small fraction of the events, if any, in the signal region were a result of a kinematic selection bias.

- **Add large $|z|$ veto:**

  As we can see from Table 7.5, after applying the large $|z|$ veto we are left with 375 events in the signal region and 267 events in the control region. This is a reduction of 78 and 48 events respectively, reducing the "pseudo-excess" from 138 to 108. To help further illustrate the impact of this veto we examine the events that fail the large $|z|$ veto but pass all the other requirements. Figure 7.5 shows the timing distribution for events that pass all the selection requirements in Table 5.5 up to the large $|z|$ vertex veto (i.e., without the $e \to \gamma_{fake}$ veto), but where we require the event to fail the large $|z|$ veto and have a good SpaceTime vertex. The shape of the double Gaussian suggests that the overwhelming majority of the events originate from wrong vertex events. The mean of the wrong vertex distribution is found to be shifted to 1.4 ns. While these events could have been rejected by the $e \to \gamma_{fake}$ veto, it is clear that if left in our final sample this shift in the wrong vertex distribution would introduce a large timing bias and thus contribute to events in the signal region from SM sources.

- **Add $e \to \gamma_{fake}$ veto:**

  After applying the $e \to \gamma_{fake}$ veto we arrive back at our original number of 322 events in the signal region and 241 events in the control region which is a reduction of 53 events in the signal region and 26 events in the control region; shrinking the "pseudo-excess" from 108 to 81. Figure 7.6 shows the t_{corr} timing distribution for events that pass all the selection requirements in Table 5.5 up to the $e \rightarrow \gamma_{fake}$ veto, but failing the $e \rightarrow \gamma_{fake}$ veto and then requiring these events to have a good SpaceTime vertex. These events are likely coming from $W \rightarrow e\nu \rightarrow \gamma_{fake} + \not\!\!E_T$ and have a mean time of ~0.5 ns. It is clear that the inclusion of this new veto further reduces SM events in the signal region as expected and contributed to the excess in 2008.

- **New $< t_{corr}^{WV} >$ estimation method:**

  Figure 7.7 shows the t_{corr} distribution for the final 6.3 fb^{-1} result where the background estimation method assumes $< t_{corr}^{WV} >= 0$ ns. The comparison with Figure 7.3 allows us to show how using the incorrect assumption that the $< t_{corr}^{WV} >= 0$ ns can lead to the errant conclusion of an excess number of events in the signal region (2 ns $< t_{corr} <$ 7 ns). The proper background estimate changes the 241 events in the control region to a proper background estimate of 257 events. We thus go from a "pseudo-excess" from 81 events to an excess of 65 events clearly indicating that part of the excess seen in 2008 was from mis-modeling of the background.

With all this in mind, in the next section we summarize the results of this search, describe how future versions of this analysis may gain sensitivity, and outline how to quantify our sensitivity to new physics models.

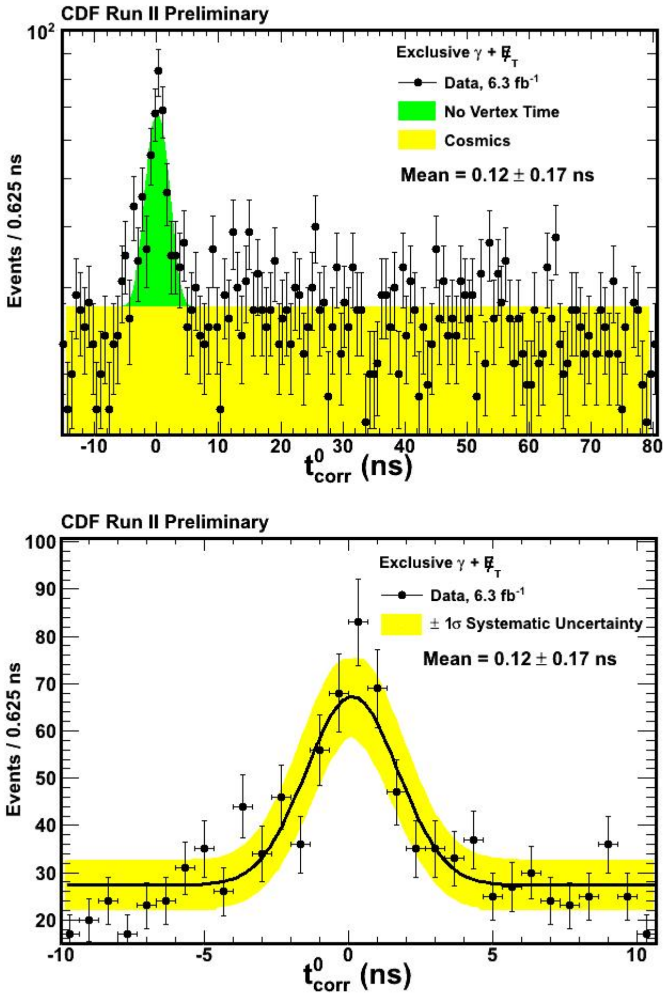

Figure 7.2: (Top) The t^0_{corr} distribution for the no vertex sample. Note that the straight line fit is performed in the cosmics region 20 ns$< t^0_{corr} <$80 ns and for the collision distribution a Gaussian is fit from -5 ns $< t^0_{corr} <$ 3 ns with the RMS fixed to 1.6 ns while the mean of the Gaussian is allowed to vary in order to determine the best fit mean. (Bottom) Taking the $\pm 1\sigma$ systematic variation of the mean from the no vertex corrected time showing that $< t^0_{corr} >= 0.12 \pm 0.17$ ns well describes the distribution.

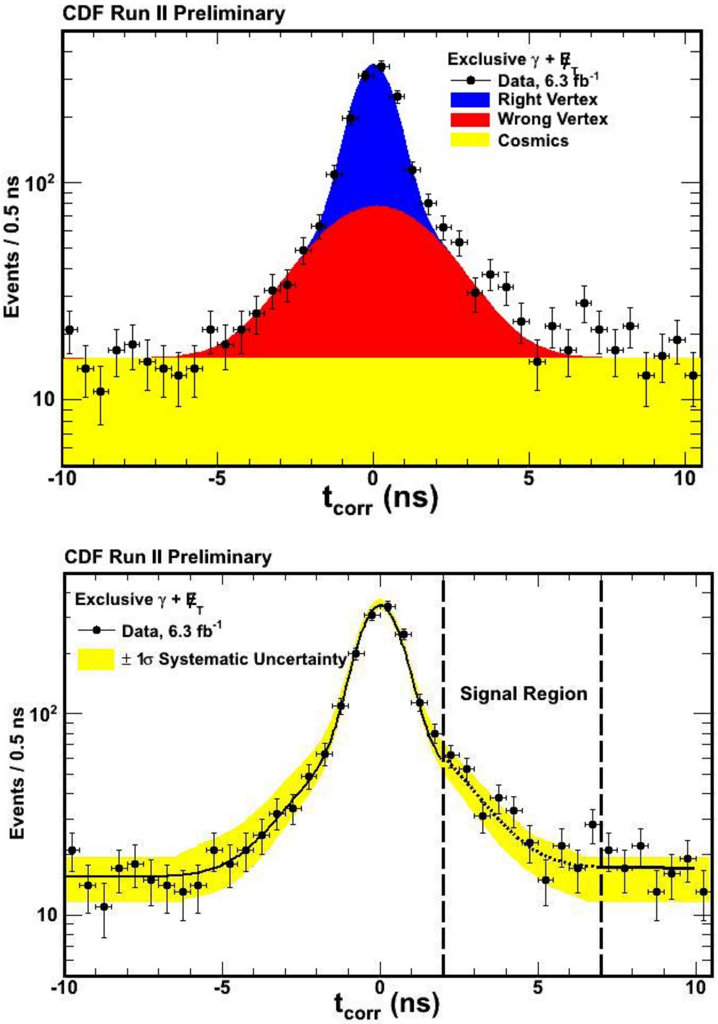

Figure 7.3: (Top) The t_{corr} distribution of the 6.3 fb^{-1} $\gamma+\not\!\!E_T$ data showing the right, wrong vertex, and cosmics prediction. (Bottom) Taking the $\pm 1\sigma$ systematic variation of the mean of the wrong vertex showing that $< t_{corr}^{WV} >= 0.12 \pm 0.20$ ns well describes the background distribution outside the signal region.

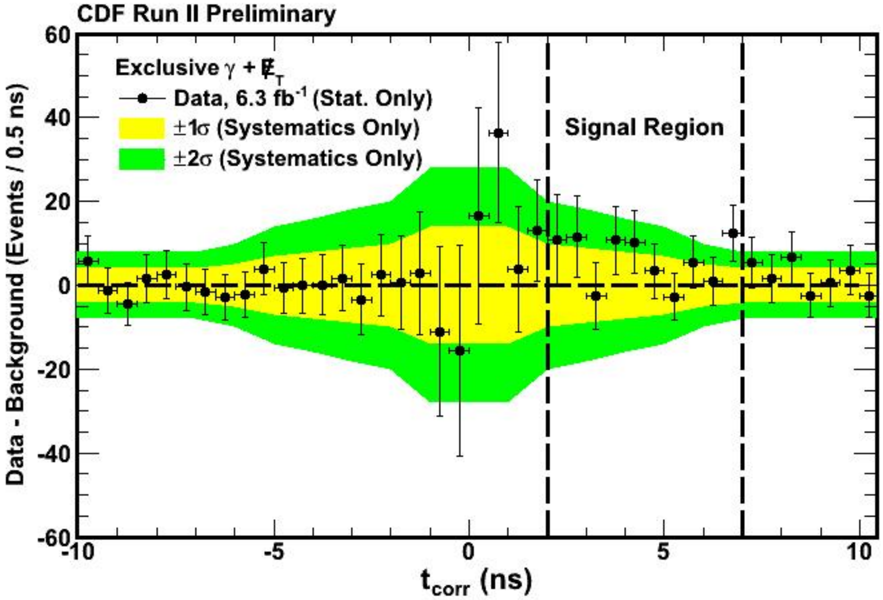

Figure 7.4: The data minus background plot for the t_{corr} distribution where the yellow and green represent the $\pm1\sigma$ and 2σ variation of the systematic and the error bars representing statistical error on the data. The events in the signal region correspond to a 1.65σ excess taking into account all the statistical and systematic uncertainties.

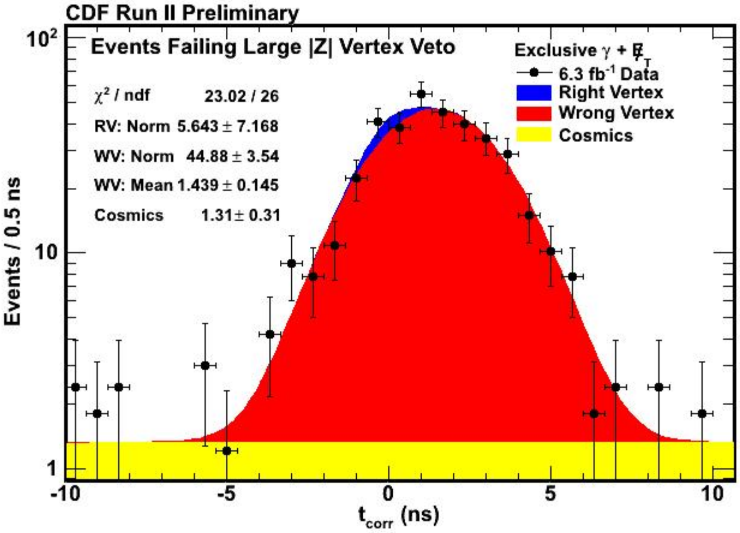

Figure 7.5: The t_{corr} distribution for the exclusive $\gamma+\not\!\!E_T$ events that pass all the selection requirements in Table 5.5 but fail the large $|z|$ veto and where no $e \rightarrow \gamma_{fake}$ veto is applied and we require a good SpaceTime vertex. These events have a clear bias to large t_{corr} times with 78 events between 2 ns $< t_{corr} <$ 7 ns and 48 events between -7 ns $< t_{corr} <$ -2 ns and thus contributed to the excess seen in the preliminary study done in 2008.

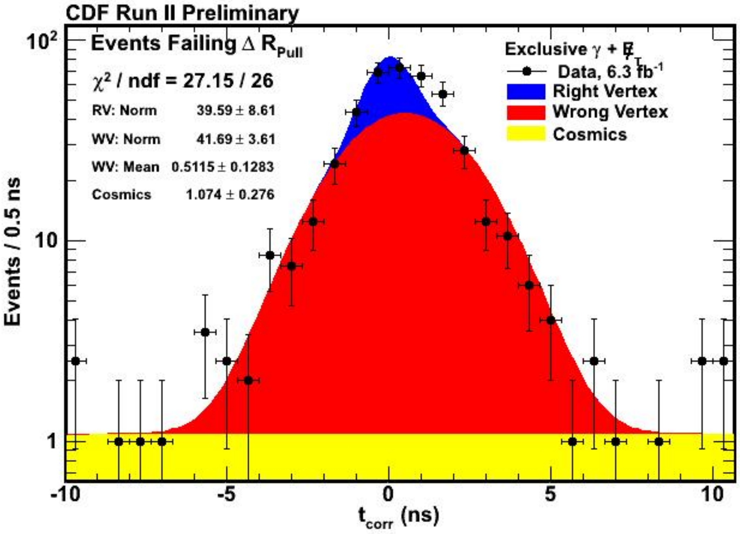

Figure 7.6: The t_{corr} distribution for the exclusive γ+$\not\!\!E_T$ events that pass all the selection requirements in Table 5.5 but fail the ΔR_{Pull} veto. These events, likely coming from W$\rightarrow$ $e\nu$ $\rightarrow$ γ_{fake}+ $\not\!\!E_T$, have a clear bias to large t_{corr} times with 53 events between 2 ns $< t_{corr} <$ 7 ns and 26 events between - 7 ns $< t_{corr} <$ -2 ns and thus contributed to the excess seen in the preliminary study done in 2008.

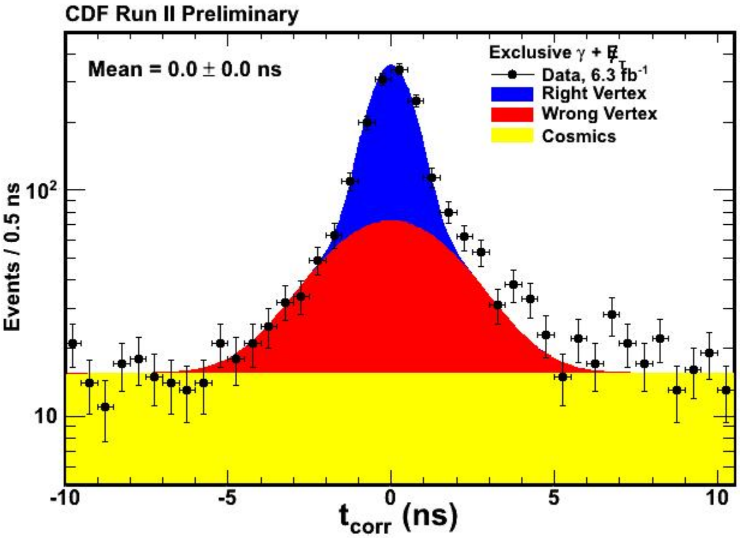

Figure 7.7: The t_{corr} distribution for the final exclusive γ+$\not\!\!E_T$ but where we assume $< t_{corr}^{WV} >= 0$ ns in the background estimate. This is to be compared to Figure 7.3 where we find $< t_{corr}^{WV} >= 0.12 \pm 0.20$ ns from our data-driven background estimation. This illustrates how this assumption can lead to the errant conclusion of an excess number of events in the signal region (2 ns $< t_{corr} <$ 7 ns).

8. CONCLUSIONS

8.1 Summary of the Search

This dissertation has presented the first systematic search for new physics in the exclusive $\gamma_{delayed}+ \not\!\!E_T$ final state which was a follow up on an intriguing excess that was observed in the same final state in early 2008. The candidate events were selected based on the corrected arrival time of the photon at the calorimeter as measured with the EMTiming system. The data sample analyzed represent data taken from December 2004 to June 2010 and correspond to an integrated luminosity of 6.3 ± 0.4 fb^{-1}. While we have endeavored to keep the same event selection, we decided to add a number of new requirements to reduce a number of newly understood backgrounds that produce biased events. We also used a new background estimate that takes into account that this final state has collision backgrounds that have a wrong vertex timing mean that is not actually zero. Using a data-driven background prediction method we predict 257 ± 35 events expected in the signal region (2 ns $< t_{corr} <$ 7 ns) and observe 322 events resulting in a modest excess remaining of observed minus predicted ($N_{Observed} - N_{Predicted}$) of 65 events. We can calculate the significance of this excess as $N_\sigma = 1.65$ which gives a one sided p-value (the estimatied probability that this excess is inconsistent with a null hypothesis) of $\sim 5\%$.

8.2 Interpretation of the Data

Our primary interpretation of the data is that we see no evidence for new physics in the exclusive $\gamma_{delayed} + \not\!\!E_T$ final state. That being said, we make note that the modest excess of $N_\sigma = 1.65$ is present without any optimization for sensitivity to GMSB models. In addition we note that the shape of the excess is just what we would expect for a signal of new physics in that it is present in almost every timing bin in roughly the shape of an exponential.

The second conclusion is our answer to the question "what should we make of the preliminary search performed in 2008?" To answer this question we have followed up by using many of the analysis identification and selection variables to be identical to the previous search. This was done to aid in the interpretation of the previous search which showed an excess of $N_\sigma \sim 4$ using the previous background estimation technique which incorrectly assumed a timing distribution centered at $t_{corr} = 0$ ns. We arrive at the conclusion that the bulk of the previously seen excess was largely due to an incorrect background estimation assumption as well copious amounts of SM backgrounds with large times and poor calibration methods.

Since this search was performed in a quasi-model independent approach, and there is a modest excess, we do not set a direct cross-section limits on any one particular model. However, we do note that we anticipate that this search is sensitive to GMSB breaking models of SUSY in Light Neutralino and Gravitino (LNG) models [43]. As discussed in Section 1, the LGN models sparticle production is dominated by $h^0 \rightarrow \tilde{\chi}_1^0\tilde{\chi}_1^0$ pairs, which is significantly different from those of the more conventional SPS-8 models which produce $\tilde{\chi}_1^0$ pairs at the end of long decay chains. It is certainly possible to do a quantitative estimate of the sensitivity to models amenable to LNG scenarios, but this will be done in the next generation of this analysis using the full Tevatron dataset of $\sim$10 fb^{-1}. For completeness we note that a phenomenology paper [43] shows that we expect to have sensitivity to the regions where the $\tilde{\chi}_1^0$ has long enough lifetime to produce a delayed photon and assume that only $\tilde{\chi}_1^0$ pairs are produced in the final state. In the next section we address future prospects that can lead to a more sensitive search to $h^0 \rightarrow \tilde{\chi}_1^0\tilde{\chi}_1^0 \rightarrow \gamma+ \not{E}_T$ as well as a further exploration of the intriguing excess that remains in the exclusive $\gamma_{delayed}+ \not{E}_T$ final state.

8.3 Future Prospects

At the end of a analysis it is always worth looking back to see what areas could be improved, and followed up on by future scientists. A few areas that remain to be explored that could result in improving upon the analysis laid forth in this dissertation include:

- **Analyze the full 10 fb^{-1} dataset:**

  The most straightforward thing to do is to add more data. Since this analysis only utilized ∼60% of the Tevatron data set, adding the additional data will enhance our sensitivity to new physics models as well as aid in clarifying if the modest excess is due to a statistical fluctuation or not.

- **Reducing the systematic error on the wrong vertex mean:**

  The largest systematic uncertainty on the number of background events in the signal region comes from the measurement of $< t^0_{corr} >$ using the "no vertex" sample. The Gaussian fit results in an uncertainty of 0.17 ns on the mean which in turn causes a ±35 event uncertainty in our prediction.

  We quickly describe a second method that has been explored [84] in order to reduce this uncertainty. This method utilizes a binned maximum likelihood fit of the data in the no vertex sample as well as in the control and bulk regions. The likelihood fit is performed over events with a vertex in the bins spanning $V \equiv t_{corr} \in$ [-7 ns, 2 ns] $\cup$ [20 ns, 80 ns], and for events without a vertex in the bins spanning $N \equiv t^0_{corr} \in$ [-3 ns, 5 ns] $\cup$ [20 ns, 80 ns]. This method of estimating the wrong vertex mean is shown to reduce the overall uncertainty and thus improves our sensitivity to new physics. We anticipate that this technique will reduce the uncertainty on the number of SM background events in the signal region by ~30%. However, we do not speculate on how it will affect the prediction of the mean value of the SM background prediction.

- **Reducing the cosmics ray background:**

  The largest background in the exclusive $\gamma_{delayed} + \not\!\!E_T$ analysis remains events coming from cosmic ray events. We estimate a cosmic ray event rate of ~32 events per nanosecond. This rate remains even after new optimized cuts outlined in Section 4.2. One additional option that takes advantage of the fact that there is no true collision for cosmic ray backgrounds is that all vertices must be produced by an unrelated min-bias collision. Thus, one way to reduce this background is to increase the ΣP_T required on reconstructed SpaceTime vertices. This has the additional advantage that it would increase the overall number of events which are classified as not reconstructing a vertex, giving more statistics to the no-vertex sample and thus reducing the uncertainty of the measurement of the wrong vertex mean.

  An important caveat comes along with increasing the ΣP_T required on the SpaceTime vertex, namely the effect this could potentially have on reducing the efficiency for a hypothetical signal. Thus a study would need to be performed on various signal models to determine what trade-off, if any, between efficiency and rejection power can be made.

- **Optimizing event level cuts:**

  As mentioned before, many of the event level selection requirements were kept the same in order to allow a comparison with the previously performed analysis. A study of optimizing the E_T and $\not\!\!E_T$ kinematic requirements as well as the optimizing of jet and track veto parameters may allow this search to extend its potential sensitivity to new phyiscs. For example, we note that the trigger we use in this analysis (see Section 2.3) allows us to move the E_T and $\not\!\!E_T$ thresholds down to 30 GeV. The previous reason for choosing an E_T cut of 45 GeV was to reduce the $W \rightarrow e\nu \rightarrow \gamma_{fake} + \not\!\!E_T$, but now that additional cuts already reduce this background we can consider lowering this cut. We expect that a Higgs of 125 GeV would produce low E_T photons and $\not\!\!E_T$, but this would require a full optimization between background and signal expectations. A second possibility is to allow the presence of a second photon in the event since there is a reasonable possibility that one might have been created in our signal production model, especially at low lifetimes.

In conclusion, we have presented a search for new physics in the exclusive $\gamma_{delayed}$ + $\not\!\!E_T$ final state. We have used more data, multiple analysis improvements, and a better understanding of the backgrounds to follow up on a interesting hint in a preliminary search. We have found that the majority of that excess was from previously unknown and poorly modeled backgrounds, but a modest excess remains. With a clear view of potential new physics models, the rest of the Fermilab Tevatron data and potential improvements and optimization to a future analysis, we will either uncover a discovery or show that this was just one of the many statistical fluctuations that occur in collider experiments. Only time will tell.

REFERENCES

[1] S. Weinberg, *The Quantum Theory of Fields* (Cambridge Univ. Pr., Cambridge, UK, 1995-2000), **Vol. 1-3**.

[2] W.N. Cottingham and D.A. Greenwood *An Introduction to the Standard Model of Particle Physics* Second Edition (Cambridge Univ. Pr., Cambridge, UK 2007)

[3] W.M. Yao, *et al.*, [Particle Data Group], Journal of Physics G **33**, 1 (2006), and partial update for 2011.

[4] The TEVNPH Working Group (CDF and D0 Collaborations), "Updated Combination of CDF and D0 Searches for Standard Model Higgs Boson Production with up to 10 fb^{-1} of Data" arXiv:1207.0449v2.

[5] H.D. Politzer, "Asymptotic Freedom: An Approach to Strong Interactions", Phys. Rept., **14** (1974), pp. 129-180.

[6] D.J. Gross and F. Wilczek, "Asymptotically Free Gauge Theories", Phys Rev., D **8** (1973), pp. 3633-3652.

[7] - S. Weinberg, "A Model of Leptons", Phys. Rev. Lett., **19** (1967), pp. 1264-1266.

[8] A. Salam and J.C. Ward, "Electromagnetic and Weak Interactions", Phys. Lett., **13** (1964).

[9] S.L. Glashow, "Partial Symmetries of Weak Interactions", Nucl. Phys., **22** (1961).

[10] P. W. Higgs, “Broken Symmetries and the Masses of Gauge Bosons”, Phys. Rev. Lett. **13**, 508 (1964), F. Englert and R. Brout, “Broken Symmetry and the Mass of Gauge Vector Mesons”, Phys. Rev. Lett. **13**, 321 (1964).

[11] International Masters Classes “Hands on Particle Physics”, https://kjende.web.cern.ch/kjende/en/wpath/higgs.htm (accessed 2012).

[12] F. Halzen and A.D. Martin, *Quarks and Leptons: An Introductory Course in Modern Particle Physics*, John Wiley and Sons, 1984.

[13] Y. Fukunda et. al. (Super-Kamiokande Collaboration), “Evidence for Oscillation of Atmospheric Neutrinos”, Phys. Rev. Lett 81 (1998) pp. 1562-1587.

[14] G.W. Bennett, et. al., “Measurement of the Negative Muon Anomalous Magnetic Moment to 0.7 ppm”, Phys. Rev. Lett. **92**, 161802 (2004)

[15] D. N. Spergel et al. (WMAP Collaboration), “Wilkinson Microwave Anisotropy Probe (WMAP) Three Year Results: Implications for Cosmology”, Astrophys. J. Suppl. **170**, 377 (2007); arXiv:astro-ph/0603449

[16] G. Bertone, D. Hooper, and J. silk, “Particle Dark Matter: Evidence, Candidates and Constraints”, Phys. Rept. **405**, 279 (2005); arXiv:hep-ph/0404175.

[17] S. Weinberg, “Implications of Dynamical Symmetry Breaking”, Phys. Rev. D **13** 974 (1976), “Implications of Dynamical Symmetry Breaking: An Addendum”, Phys. Rev. D 19, 1277 (1979); E. Glidener, “Gauge-Symmetry Hierarchies”, Phys. Rev. D **14** 1667 (1976); L. Susskind, “Dynamics of Spontaneous Symmetry Breaking in the Weinberg-Salam Theory” Phys. Rev. D **20**, 2619-2625 (1979).

[18] B. W. Lee, C. Quigg and H. B. Thacker, “Weak Interactions at Very High Energies: The Role of the Higgs-Boson Mass”, Phys. Rev. D **16**, 1519 (1977).

[19] K. Nakamura et al. (Particle Data Group), “Review of Particle Physics ” J.Phys. G **37**, 075021 (2010).

[20] M. Kaku, Introduction to Superstring and M-Theory, *Springer-Verlag* (2nd edition).

[21] Stephen P. Martin. “A Supersymmetry Primer”, 1997, hep-ph/9709356.

[22] H. P. Nilles, “Supersymmetry, Supergravity and Particle Physics”, Phys. Rept. **110**, 1 (1984).

[23] H. E. Haber and G. L. Kane, “The Search for Supersymmetry: Probing Physics Beyond the Standard Model”, Phys. Rept. **117**, 75 (1985).

[24] S. Dawson. “The MSSM and Why it Works” 1997, hep-ph/9712464.

[25] L. Hall, J. Lykken and S. Weinberg, “Supergravity as the Messenger of Supersymmetry Breaking”, Phys. Rev. D **27**, 2359 (1983).

[26] L. Alvarez-Gaume, J. Polchinski, and M. Wise, “Minimal Low-Energy Supergravity”, Nucl. Phys. **B221** (1983) 495.

[27] A. Chamseddine, R. Arnowitt, and P. Nath, “Locally Supersymmetric Grand Unification”, Phys. Rev. Lett. **49** (1982) 970.

[28] G.F. Giudice and R. Rattazzi. “Theories with Gauge-Mediated Supersymmetry Breaking”, CERN-TH-97-380, hep-ph/9801271 (1998).

[29] M. Dine and A. Nelson, “Dynamical Supersymmetry Breaking at Low-Energies”, Phys. Rev. D **48** (1993) 1277, hep-ph/9303230.

[30] M. Dine, A. Nelson, and Y. Shirman, “Low-Energy Dynamical Supersymmetry Breaking Simplfied”, Phys. Rev. **D51** (1995) 1362, hep-ph/9408384.

[31] N. Vittorio and J. Silk, Astrophys. Journal, Part 2-Letters to the Editor **285**, L39-L43 (1984).

[32] S. Dawson, "R Parity Breaking in Supersymmetric Theories", Nucl. Phys. B **261**, 297 (1985).

[33] H. K. Dreiner, "An Introduction to Explicit R-parity Violation", hep-ph/9707435.

[34] P. Fileviez Perez and S. Spinner, "Spontaneous R-Parity Breaking in SUSY Models", arXiv:0904.2213.

[35] J. L. Feng and T. Moroi, "Fermilab Tevatron Signatures of Long-Lived Charged Sleptons in Gauge-Mediated Supersymmetry Breaking Models", Phys. Rev. D **58**, 035001 (1998).

[36] S. Dimopoulos, M. Dine, S. Raby, S. D. Thomas, "Experimental Signatures of Low Energy Gauge Mediated Supersymmetry Breaking", Phys. Rev. Lett. **76**, 3494-3497 (1996).

[37] D. A. Toback and P. Wagner, "Prospects of Searches for Neutral, Long-Lived Particles that Decay to Photons Using Timing at CDF", Phys. Rev. D **70** (2004) 114032.

[38] T. Aaltonen et al. (CDF Collaboration), "Search for Heavy, Long-Lived Neutralinos that Decay to Photons at CDF II Using Photon Timing," Phys. Rev. D **78** (2008) 032015, [arXiv:0804.1043 [hep-ex]]; A. Abulencia et al. (CDF Collaboration), "Search for Heavy, Long-Lived Particles that Decay to Photons at CDF II," Phys. Rev. Lett. **99** (2007) 121801.

[39] B. C. Allanach et al., in Proc. of the APS/DPF/DPB "Summer Study on the Future of Particle Physics" (Snowmass 2001) ed. N. Graf, Eur. Phys. J. C **25** (2002) 113.

[40] LEP SUSY Working Group, ALEPH, DELPHI, L3, and OPAL Collaborations, LEPSUSYWG/04-09.1 (http://lepsusy.web.cern.ch); A. Heister et al. (ALEPH Collaboration), "Search for Gauge Mediated SUSY Breaking Topologies in e+e^- Collisions at Center-of-Mass Energies up to 209 GeV," Eur. Phys. J. C **25** (2002) 339, arXiv:hep-ex/0203024; M. Gataullin, S. Rosier, L. Xia and H. Yang, "Searches for Gauge-Mediated SUSY Breaking Topologies with the L3 Detector at LEP," AIP Conf. Proc. **903**, 217 (2007), arXiv:hep-ex/0611010; G. Pasztor, "Search for Gauginos and Gauge Mediated SUSY Breaking Scenarios at LEP," PoS 46 HEP2005, 346 (2006), arXiv:hep-ex/0512054; J. Abdallah et al. (DELPHI Collaboration), "Search for One Large Extra Dimension with the DELPHI Detector at LEP," Eur. Phys. J. C **60** (2009) 17, arXiv:0901.4486.

[41] B. Abbott et al. (D0 Collaboration), "Experimental Search for Chargino and Neutralino Production via Gauge Mediated Supersymmetry Breaking Models," Phys. Rev. Lett. **80** (1998) 442, arXiv:hep-ex/9708005; F. Abe et al. (CDF Collaboration), "Searches for New Physics in Diphoton Events in $p\bar{p}$ Collisions at $\sqrt{s} = 1.8$ TeV," Phys. Rev. Lett. **81** (1998) 1791, arXiv:hep-ex/9801019; F. Abe et al. (CDF Collaboration), "Searches for New Physics in Diphoton Events in $p\bar{p}$ Collisions at $\sqrt{s} = 1.8$ TeV," Phys. Rev. D **59** (1999) 092002, arXiv:hepex/9806034; V. M. Abazov et al. (D0 Collaboration), "Search for Supersymmetry with Gauge-Mediated Breaking in Diphoton Events at D0," Phys. Rev. Lett. **94** (2005) 041801, arXiv:hep-ex/0408146; T. Aaltonen et al. (CDF Collaboration), "Search for Supersymmetry with Gauge-Mediated Breaking in

Diphoton Events with Missing Transverse Energy at CDF II," Phys. Rev. Lett. **104** (2010) 011801, arXiv:0910.3606 ; V. M. Abazov et al. (D0 Collaboration), "Search for Dark Photons from Supersymmetric Hidden Valleys," Phys. Rev. Lett. **103** (2009) 081902, arxiv:hep-ex/0905.1478v2.

[42] G. Aad et al. (ATLAS Collaboration), "Search for Diphoton Events with Large Missing Transverse Energy in 7 TeV Proton-Proton Collisions with the ATLAS Detector," arXiv:1012.4272; S. Chatrchyan et al. (CMS Collaboration), "Search for Supersymmetry in pp Collisions at $\sqrt{s} = 7$ TeV in Events with Two Photons and Missing Transverse Energy", arXiv:hep-ex/1103.0953 submitted to Phys. Rev. Lett.

[43] J. D. Mason and D. Toback, "Prospects of Searches for Gauge Mediated Supersymmetry with $h^0 \to \tilde{\chi}_1^0 \tilde{\chi}_1^0$ production in the Time-Delayed Photon + MET Final State at the Tevatron", Phys. Lett. B **702**, 377 (2011), arXiv:1105.2194.

[44] V. M. Abazov et al. (D0 Collaboration), "Search for Diphoton Events with Large Missing Transverse Energy in 6.3 fb^{-1} of $p\bar{p}$ collisions at $\sqrt{s} = 1.96$ TeV", Phys. Rev. Lett. **105** (2010) 221802, arXiv:hep-ex/1008.2133.

[45] Ray Culbertson and Tingjun Yang, "Search for Randall-Sundrum Gravitons in the Diphoton Channel at CDF", CDF Note 10160.

[46] T. Appelquist, H. C. Cheng and B. A. Dobrescu, "Bounds on Universal Extra Dimensions" Phys. Rev. D **64** (2001) 035002, arXiv:hep-ph/0012100v2; H. C. Cheng, J. L. Feng, K. T. Matchev, "Kaluza-Klein Dark Matter" Phys. Rev. Lett. **89** (2002) 211301, arXiv:hep-ph/0207125v2; G. Servant and T. M. P. Tait, "Is the Lightest Kaluza-Klein Particle a Viable Dark Matter Candidate?," Nucl. Phys. B **650** (2003) 391, arXiv:hep-ph/0206071.

[47] T. Aaltonen et al. “Search for Large Extra Dimensions in Final States Containing on Photon or Jet and Large Missing Transverse Energy Produced in p$\bar{p}$ Collisions at $\sqrt{s} = 1.96$ TeV” Phys. Rev. Lett. **101**:181602, 2008.

[48] Tevatron Accelerator Division, “Operations Rookie Books,” http://www-bdnew.fnal.gov/operations/rookie books/rbooks.html.

[49] Fermilab Beams Division,“Run II Handbook” (1998), http://wwwbd.fnal.gov/runII/index.html.

[50] CDF Run IIb Technical Documents, http://www-cdf.fnal.gov/run2b.html (accessed 2012).

[51] C. S. Hill et al. (CDF Collaboration), “CDF Run II Silicon Tracking Projects”, Nucl. Instrum. Meth. A **530**, 1 (2004); A. Sill et al. (CDF Collaboration), Nucl. Instrum. Meth. A **447**, 1 (2000).

[52] M. Goncharov, et al. “The Timing System for the CDF Electromagnetic Calorimeters”, Nucl. Instrum. Meth. A **563**, 543 (2006).

[53] G. Ascoli et al. (CDF Collaboration), “The CDF Forward Muon System”, Nucl. Instrum. Meth. A **268**, 33 (1988).

[54] R. Blair et al: (CDF Collaboration), “The CDF-II detector: Technical Design Report”, Fermilab Report No. FERMILAB-PUB-96-390-E.

[55] G. Gomez-Ceballos et al., “Event Builder and Level 3 at the CDF Experiment”, Nucl. Instrum. Meth. A **518**, 522 (2004).

[56] P. Onyisi, “Run 2 γ+$\not\!\!E_T$ Search”, CDF Report No. CDF-NOTE-6381 (2003), unpublished.

[57] http://www-cdf.fnal.gov/internal/physics/photon/docs/goodrun_v36_pho_00.txt.

[58] J. Elias et al., Nucl. Instrum. Methods Phys. Res., Sect. A **441**, 366 (2000); D. Acosta et al., Nucl. Instrum. Methods Phys. Res., Sect. A **461**, 540 (2001).

[59] F. Abe et al. (CDF Collaboration), "Topology of Three-Jet Events in $p\bar{p}$ Collisions at $\sqrt{s} = 1.8$ TeV", Phys. Rev. D 45, 1448 (1992).

[60] A. Bhatti et al., "Determination of the Jet Energy Scale at the Collider Detector at Fermilab", Nucl. Instrum. Meth. A **566**, 375 (2006); arXiv:hep-ex/0510047.

[61] D. Toback, Ph.D. thesis, University of Chicago, "Searches for New Physics in Diphoton Event in p anti-p Collisions at $\sqrt{s} = 1.8$ TeV", FERMILAB-THESIS-1997-36 (1997); J. Berryhill, Ph.D. thesis, University of Chicago, "A Search for New Physics in Photon Lepton Events in Proton Anti-proton Collisions at $\sqrt{s} = 1.8$ TeV", FERMILAB-THESIS-2000-02 (2000); Y. Liu, Ph.D. thesis, UniversitÂŽe de Gen‘eve, "Measurement of the Cross Section for Production of Prompt Diphoton in proton anti-proton Collisions at $\sqrt{s} = 1.96$-TeV" FERMILAB-THESIS-2004-37 (2004).

[62] Sunil Somalwar Sourabh Dube, John Zhou., "Medium E_T Electron Identification Efficiency and Scale-Factors", CDF Note 8321, unpublished.

[63] M. Goncharov, V. Krutelyov, D. Toback, and P. Wagner, "Space-Time Vertex Reconstruction Using COT Tracks", CDF Note 8015, unpublished.

[64] Carsten Rott, Daniela Bortoletto, "Primary Vertex Algorithm Comparison for High P_T Physics", CDF Note 6472 (2003), unpublished.

[65] K. Bloom, "Getting Started with CDF Run 2 Offline", CDF Note 5294 unpublished.

[66] S. D'Auria et al., "Run-Dependent MC Production for Summer 2004 ", CDF Note 7055 (2004), unpublished.

[67] T. Sjostrand et al., "High-energy physics event generation with PYTHIA 6.1", Comput. Phys. Commun. **135**, 238 (2001). We use version 6.216.

[68] U. Baur, T. Han, and J. Ohnemus, "QCD Corrections to Hadronic $W\hat{I}^3$ Production with Non-standard $WW\hat{I}^3$ Couplings", Phys. Rev. D **48**, 5140 (1993); U. Baur, T. Han, and J. Ohnemus, ibid. 57, 2823 (1998).

[69] R. Brun et al. "GEANT 3 Manual", CERN Program Library Long Writeup. 1994, W5013.

[70] D. Toback and P. Wagner "Simulation of the Calorimeter Timing System for the CDF Detector", CDF-NOTE-5866 (2001), unpublished.

[71] S. Klimenko, J. Konigsberg, A. Madorsky, A. Nomerotski, A. Safonov, D. Tsybychev, S. Wang "CLC Calibrations", CDF Note 5548 (2001), unpublished. Gervasio Gomez, Matthew Jones, Jaison Lee, Youngdo Oh, Ivan Vila "Online Calibrations of the CDF-II Time-of-Flight Detector", CDF Note 6050 (2002), unpublished. Ben Cooper, Dustin McGivern, Rob Snihur "Coordination of CDF Offline Calibrations", CDF Note 6817 (2003), unpublished. Stefano Giagu "COT dE/dx Calibrations for 0d/0h datasets" CDF Note 8144 (2006).

[72] W. Orejudos "COT Calibration Software" CDF Note 5656 (2001), unpublished.

[73] Lozier, Daniel M.; Boisvert, Ronald F. et al., *NIST Handbook of Mathematical Functions*, Cambridge University Press, ISBN 978-0521192255, MR2723248.

[74] J.Asaadi, R. Moore, D. Toback. "Tevatron Timing and z Collision Distributions for use in the Delayed Photon Analysis", CDF Note 9812 (2009), unpublished.

[75] A. Aursiano "Search for Exclusive $\gamma_{Delayed}+ \not\!\!E_T$ Final State in $p\bar{p}$ Collisions at $\sqrt{s} = 1.96$ TeV", forthcoming thesis (2012).

[76] For a description of beam halo and cosmic ray backgrounds see R. Tesarek, CDF Report No. CDF Note 5873 (2002) and P. Onyisi, CDF Report No. CDF Note 6009 (2003), M. Goncharov et al., CDF Report No. CDF Note 8409 (2006), all unpublished.

[77] T. K. Gaisser, *Cosmic Rays and Particle Physics*, Cambridge University Press, 1990

[78] Bartol Research Institute, "Cosmic Rays and Earth", http://http://neutronm.bartol.udel.edu/catch/cr2.html (accessed 2012).

[79] R. Thurman-Keup, C. Bhat, W. Blokland, et. al "Longitudinal bunch monitoring at the Fermilab Tevatron and Main Injector synchrotrons", JINST 6 T10004 (2011).

[80] R. Culbertson, A. Pronko, Shin-Shan Eiko Yu, "The Probability of an Electron Faking an Isolated Prompt Photon in CEM", CDF Note 8220 (2006), unpublished.

[81] D. Stentz, "Measurement of the Cross Section for W Boson Production in Association with Jets", CDF Note 10294 (2010), unpublished.

[82] T. Nelson, R. Snider, D. Stuart, "Forward Electron Tracking with the Phoenix-Mods Package," CDF Note 6278 (2003), unpublished.

[83] Jonathan Asaadi, Adam Aurisano, Daniel Goldin, Jason Nett, David Toback, "Rejecting $e \rightarrow \gamma_{fake}$ Candidates With Loose Track Matching" CDF-NOTE-10773 (2012).

[84] Jonathan Asaadi, Adam Aurisano, Daniel Goldin, Jason Nett, David Toback, "The Search For New Physics in the $\gamma_{delayed} + \not\!\!E_T$ Signature in p-$\bar{p}$ Collisions at $\sqrt{s} = 1.96$ TeV" CDF Note 10789 (2012) (To be submitted to PRL).

APPENDIX A

ADDITIONAL MATERIAL FOR COSMIC RAY REJECTION

In this appendix we provide additional supporting material to help further explain the selection criteria used to reduce cosmic ray backgrounds which are the dominant background in this analysis. As described in Section 4, cosmic rays produce photons in the detector. As shown in Figure 4.1, cosmic rays are, in general, particles that originate in outer space and then interact with the Earth's atmosphere producing secondary particles that then shower down to the Earth's surface. The majority of particles that interact with our detector are muons as they have a long enough lifetime and small enough cross section with ordinary matter to reach the detector. If a cosmic ray happens to deposit energy in the detector, in particular the EM calorimeter, it can mimic a photon candidate signature (i.e., an energy deposit in the EM calorimeter only and no track pointing to it in from the tracking chamber). If this deposit occurs in coincidence with a collision in the detector it can lead to both an incorrectly assigned photon to a vertex that had nothing to do with its production as well as leaving an imbalance of energy in the detector which is misidentified as $\not{E}_T$. This mis-identification of a photon can occur if the cosmic ray produces an electromagnetic cluster via the the emission of a real, high-energy photon inside the detector that occurs as the cosmic ray traverses the detector or if the cosmic ray undergoes a bremsstrahlung interaction or a high q^2 interaction within the EM calorimeter. While only a small fraction of cosmic ray collisions fake the photon signature, the sheer flux of cosmic rays makes them a significant background in our search.

There are a number of features which allow us to separate photons from cosmic ray sources from physics sources. While many standard techniques have been created over the years [76], what makes this task particularly difficult in this analysis is that we are trying to identify photons emanated from a new particle that traveled for awhile before decaying to a photon (see Figure 1.7). Thus, the photon can hit the calorimeter face at an incident angle that is different from photons that come from the beam line. Unfortunately, many of the vetos for cosmic rays were developed based on just this difference requiring that the photon comes directly from the beam line. For example, the CES χ^2 selection requirement in the standard photon identification requirement. Luckily there are many other features which allow us to develop a series of cuts to help veto against mis-identifying an photon candidate from a cosmic ray event. We next describe three sets of requirements designed to remove events in our sample from cosmic ray sources.

Before we begin it is worth saying how we will estimate the rejection power and efficiency of these requirements. Since we have large number of cosmic rays in our data, we select a pure sample of cosmics using γ+$\not\!\!E_T$ data, using the sample of events that pass all the requirements in Table 4.1, but requiring 20 ns $< t_{corr} <$ 80 ns to create a pure sample cosmics. Other cuts will be added as is useful/necessary. For our efficiency measurements we a clean sample of W$\rightarrow e\nu \rightarrow e+\not\!\!E_T$ events. Recall, as discussed in Section 2.4.5, electrons do a good job of simulating photons in the calorimeter, but provide a pure sample of collision events.

A.1 Muon Stub Cosmic Ray Rejection

We begin by describing a veto used to reject photon events coming from cosmic rays that is based on the presence of activity in the muon chambers just outside the location of the photon candidate in the calorimeter. This method has been used at CDF and in previous delayed photon searches with great success [38, 76]. The veto focuses on cosmic ray that have traversed the muon chambers as it entered the detector and then deposited a significant amount of energy in a nearby EM calorimeter tower creating a photon candidate. Our rejection technique is designed to find this topology.

Since our search strategy starts by focusing on the using of the ‘outside-in’ topology of the majority cosmic ray events, we look to the muon detector, which is on the outside radius of the CDF detector, for activity which corresponds to the electromagnetic shower we see in the calorimeter. As described in Section 2, the muon system is a series of 4 layer single wire proportional drift chamber. A schematic of the CDF detector with the muon systems highlighted is shown in Figure A.1. When a muon passes through this system it creates a series of “hits” along the trajectory regardless of whether it comes from the outside in, or from the inside out. In the typical muon identification procedure, an algorithm searches for sets of hits which could be from the presence of such a muon trajectory in the muon chambers. If it finds a grouping of such hits its position is determined and the collection is labeled a “stub”. After this, a second algorithm then searches for tracks in the COT that point to this outer “stub”. For collision-based muons, if there is a track pointing to a muon-stub this combination is identified as a collision muon. A cosmic ray will often leave a muon stub, but no track in the COT (the trajectory would be moving backwards in time and so would not be reconstructed). It is these types of stubs that we search for (i.e. stubs without an associated track) which lie within a close angle to the photon candidate. The final requirement is that if we find a muon stub within a $|\Delta\phi| < 30$ degrees we veto that event as likely having come from a cosmic ray.

Using our pure cosmic ray sample the muon-stub veto is found to reject >85% of cosmic ray candidates while being >95% efficient for electron data [76]. The

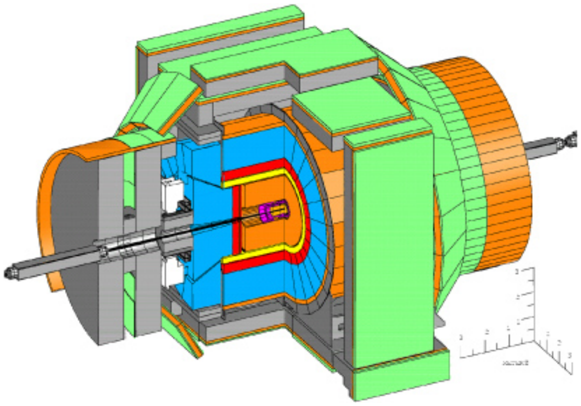

Figure A.1: Schematic view of the CDF detector where the muon detection system is highlighted in green. These muon detectors allow us to distinguish cosmic rays which originate outside the detector and pass through the muon detectors and may be incorrectly identified as a photon.

inefficiency comes from cosmics which produce a stub that occur in coincidence with the event but do not produce a photon. This veto has been used as a standard CDF cosmic veto for many years and we utilize this veto "as is" without any additional optimization.

A.2 Hadronic Energy Fraction Selection Criteria for Cosmics Rays

A second requirement considers the amount of energy deposited in the hadronic calorimeter to separate cosmic ray sources from photons that come from collisions. We expect high energy photons from collisions to end up showering mostly in the EM calorimeter but leaves some small fraction of their energy in the HAD calorimeter. In addition, we expect the amount of energy deposited in the HAD to scale with the total photon energy. However, cosmic ray photons resulting from bremsstrahlung interactions or a high q^2 collision in the EM calorimeter will leave very little energy in the hadronic calorimeter on average.

To compare the deposition of energy in the calorimeter we consider our same sample of cosmics and electrons but also require a muon stub within a $|\Delta\phi| < 30°$ help us focus on cosmics that are not already rejected. The hadronic energy distribution can be seen in Figure A.2 where we have scaled the amount of energy deposted in the HAD in conjunction with the total energy deposited. Specifically, you can see a great deal more hadronic energy is deposited by high energy electrons then cosmic ray photons. To separate photons from collision sources from photons candidates from cosmics we required each candidate to pass HAD(E) $\geq -0.30 + 0.008 \cdot E_T$. We find this cut to be 95% efficicient and reject ∼66% of cosmic candidate events.

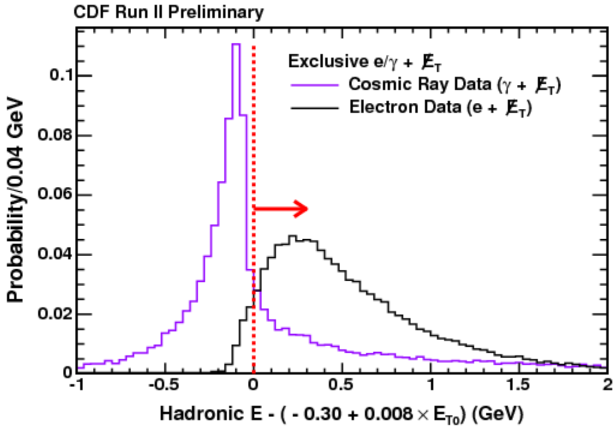

Figure A.2: The distribution of the modified version of HAD(E), taking into account the photon candidate energy, for electrons coming from collisions using selection requirements in Table 3.1 (black line) as well as the hadronic energy distribution coming from cosmic ray photons using the selection requirements in Table 4.1 (pink line) and reversing the muon-stub veto in Table 4.2. We note that high energy objects coming from the collision deposit more energy in the hadronic calorimeter then minimum ionizing events like cosmic rays. The dashed line shows our requirement.

A.3 Central Electromagnetic Shower Energy Selection Criteria for Cosmics Rays

An additional requirement to help reject cosmic ray backgrounds takes advantage of the fact that cosmic rays photons often interact with the EM calorimeter by a single high q^2 interaction in the detector. This produces a lot of light in just a few layers of the calorimeter rather than the deposition being consistent with a full shower coming from the beam line. Thus, the amount of energy deposited near shower maximum (and measured by the CES) is typically small. By way of contrast a photon that hits the calorimeter and fully showers will have its shower maximum at the CES and deposits a lot of energy there. Since a coarse measurement of the total energy can be determined using the CES alone (CES(E)), we compare its measurement to the measurement from the full tower.

Since the energy deposition in the CES is very different for cosmics and real photons we use this to reject cosmic ray sources. To do this we have two cuts, one on the total energy deposited in the CES, CES(E)>10 GeV, as well as one that considers the fraction of CES energy over the total energy to help distinguish from high energy collision photons and photons coming from cosmic rays ($\frac{\text{CES(E)}}{\text{TotalE}}$). Figure A.3 shows the ratio for identified cosmic rays versus electrons coming from a collision is shown in Figure A.3 and using the same samples as in the previous section, but after the HAD requirements as well.

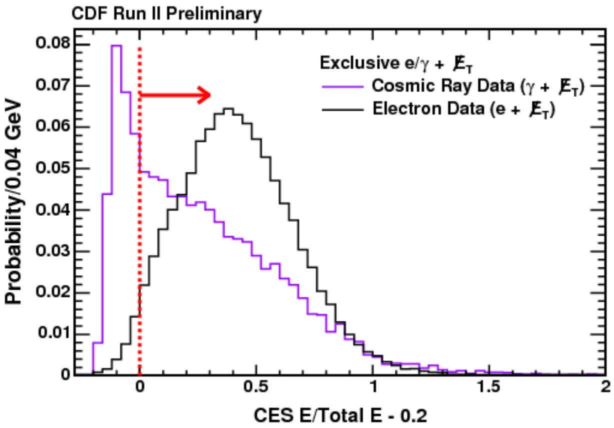

Figure A.3: This plot shows a comparison of $\frac{\text{CES(E)}}{\text{TotalE}}$ for cosmic ray photons identified (pink line) using the selection requirements in Tables 4.1 and 4.2 and (black line) electrons using Table 3.1. We note that high energy objects coming from the collision deposit a larger fraction of their energy in the CES detector then photon candidates from cosmic ray sources do.

The combination of all three cosmic ray rejection requirements are very powerful. As shown in Figure A.4, when we make a cut $\frac{\text{CES(E)}}{\text{TotalE}} > 0.2$ in addition to the Hadronic Energy sliding cut we have an overall 92% efficiency for a 76% rejection of cosmic ray photons.

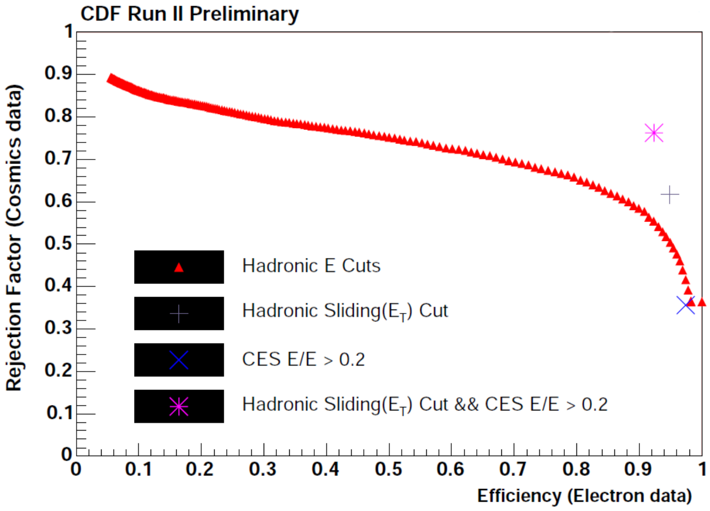

Figure A.4: Rejection versus efficiency curve for the combination of the Had(E) cut and the CES energy fraction taken together resulting in a 92% efficency for a 76% rejection of cosmic ray photons.

APPENDIX B

DEFINITIONS OF THE VARIABLES USED IN OBJECT IDENTIFICATION

In this appendix we provide a more detailed description of the various particle identification algorithms and the variables used to select reconstructed objects in this analysis that were not defined in the text. Since these are discussed in detail elsewhere, See References [50, 63, 61, 62], and have been used for years at CDF, we only provide a summary here.

In this analysis we consider jets, tracks, vertices, photons, electrons and missing energy. Recall that jets in the calorimeter, as was described in Section 2.4.1, are due to quarks and gluons, taus, photons, and electrons which deposit energy in the calorimeter in a clustered way. Since jets are simple objects and have been defined elsewhere, we begin this appendix by defining the variables used for charged particles as they pass through the various tracking subsystems known as "tracks". Since combinations of tracks are used to determine the origin of the primary collision we describe the algorithm by which we cluster together tracks to identify the origin of the collision point in space and time, known as a "SpaceTime vertex". From here we use tracks to differentiate between clusters of energy that are mostly deposited in the EM calorimeter into the electron, photon or neither category. Finally we describe the measurement of the energy imbalance in the detector known as missing transverse energy ($\not\!\!E_T$).

B.1 Tracks

As described in Section 2.4.2, a charged particle that traverses through the SVX and COT systems energy deposits energy in localized positions at specific times within these subsystems and we refer to each as “hits” in the detector [50]. Since these systems are in a magnetic field tracks are reconstructed by fitting the hit locations using helical pattern recognition algorithms. In the same way that jets are seeded with a single tower with significant energy, tracks are seeded by looking for a grouping of hits (known as “segments”) in each of the 12 sense wires in each superlayer in the COT. Then, to reduce problems from ‘fake’ hits and achieve better resolution, only segments of significant quality are linked together using a fit to a five parameter helix to form tracks. The helix terms are defined by its curvature $C = q/2R$, where R is the radius of the helix $x - y$ projection and q is the charge of the particle. The rest of the helix terms are defined below. When the SVX tracking information is available the information from the two tracking chambers can be combined which improves the overall track resolution and allows a more robust 3D pattern recognition of the trajectory [50]. Below are the various definitions for the track related parameters used in Tables 2.6 and 2.7 and calibrated against in Section 3. .

- t_0 **Track Inital Time:**

  The time information of each hit along the trajectory of the track is used as part of the overall fit of the track. When all the hits are associated with the fitted track, a best fit inital time of the track is determined.

- $T_0\sigma$ **Track Time Uncertainty:**

  This is the uncertainty associated with the track time measurement based on the spread the timing of the hits in the COT around the best fit time.

- P_T **Beam Constrained Track Momentum:**

  This is a track’s transverse momentum. While this momentum can be calculated without assuming the particle originates from the beam line, it has been shown that by assuming the track does originate from the beam line, and by correcting for the spatial location of the beam we, on average, improve the measurement of the track momentum.

- $COTStereoSeg(5)$ **Number of COT Stereo Segments with 5 or more Hits:**

  For a track to have an accurate timing measurement it must have a significant number of hits along the trajectory. This variable measures the number of segments found in the stereo superlayers that have five or more hits in that segment.

- $COTAxialSeg(5)$ **Number of COT Axial Segments with 5 or more Hits:**

  For a track to have an accurate timing measurement it must have a significant number of hits along the trajectory. This variable measures the number of segments found in the axial superlayers that have five or more hits in that segment.

- Z **Z Position:**

  This variable defines where along the direction of the beam the track originates. We typically only consider tracks that have come from a $|z| <$70 cm to help insure the tracks origin comes from the best-instrumented part of the detector to help insure a quality track used in the timing measurement.

- d_0 **Corrected Impact Parameter:**

  This is a measurement of the tracks impact parameter (distance of closest approach to the beam line) corrected for the spatial location of the beam position.

Small values of this parameter ($d_0 < 0.2$) indicate whether the charged particle comes directly from the beam line as opposed to being from the secondary decays of a long-lived particle or was a track created from the interactions with detector material.

- $nCOTHits$ **Number of COT Hits:**

  This variable considers the trajectory of the track and, using the known geometry of the tracking chamber, compares the observed number of hits along the trajectory to the expected number of hits. We use this variable to ensure that the track has activated a sufficient amount of COT hits to ensure we have a real track.

- $COTAxialHits$ **Number of COT Axial Hits:**

  Since the P_T of the track is primary determined by it's curvature in the phi direction, we simply counts the total number of axial segment hits associated with a track to help insure the track has a well measured P_T.

B.2 Photons

As described in Section 2.4.3, the CDF detector has been used to accurately identify and measure high energy photons for over 25 years using well established identification requirements [61]. Photons at CDF are identified as an energy deposits in up to three calorimeter towers in η and one tower in ϕ where the seed tower exceeds 3 GeV. Additionally we require a matching cluster of energy in the CES in the same seed tower; this cluster provides a precision measurement of the position of the photon. Below is the definition of the various variables not previously described in the text used to identify photons at CDF discussed in Table 2.8 that are not described in more detail in the text itself.

- **Fiducial**

  In order for a photon candidate to be considered in the analysis, we require that it be deposited in the well instrumented ("fiducial") region of the detector where the calorimeter is likely to have made full measurement of the photon shower and has the highest quality measurements of the photon properties. Since we want a full shower in the CES, we define the fiducial region in terms of the CES detector and is set in order to avoid inactive regions of the detector. For this analysis we only consider photons found in the central part of the detector ($|\eta|$ <1.0). This is due to the fact that the central region is not only better instrumented, with the full set of tracking chambers, but the EMTiming system has been fully calibrated and validated in this region. This region is defined as near the center of each tower, within 21 cm of the tower center in $r-\phi$ ($|X_{CES}|$ <21 cm) and in z is 9< $|Z_{CES}|$ <230 cm and the fiducial variable is set such that a photon either is measured inside our outside the fiducial area.

- $\frac{\text{HAD(E)}}{\text{EM(E)}}$:

  Since most photons leave most of their energy in the electromagnetic portion of the calorimeter, the ratio of energy deposited in the hadronic part of calorimeter towers in the cluster to that in the electromagnetic part helps separate photons from jet backgrounds.

- **Energy Isolation**

  Since photons from the decays of $\pi^0 \rightarrow \gamma\gamma$ as parts of jets are a significant background to promptly produced photon, we help separate them by considering the amount of energy around the photon cluster. For this reason we use an isolation variable, defined as

$$Isolation = \frac{E_T^{cone} - E_T^{cluster}}{E_T^{cluster}} \tag{B.1}$$

where E_T^{cone} is the sum of the transverse energy in both the electromagnetic and hadronic calorimeters in the towers adjacent within a radius of $\Delta R = \sqrt{\Delta\phi^2 + \Delta\eta^2} = 0.4$ and $E_T^{cluster}$ is the transverse energy as measured in the EM calorimeter only.

- **Track Isolation**

  We also consider isolation in the tracking chamber as well as the calorimeter. To help separate photons from jets we create a tracking isolation variable to be the ΣP_T of all tracks within a cone of $\Delta R = \sqrt{\Delta\phi^2 + \Delta\eta^2} = 0.4$ around the photon tower.

- **N3D Track Rejection**

  In order to distinguish between electrons and photons, whose showers look almost identical in the calorimeter, we search for the presence 3D tracks that have an extrapolated position at the CEM calorimeter of certain quality but below a P_T threshold. To further clarify, a N3D track is any track that contains readout coming from both the SVX (if present) and COT tracking system with P_T >0.3 GeV/c. Our variable is to count the number of 3D tracks, N3D. Since we allow the presence of a single low P_T track, our variable considers the PT of the track found, if any.

- **2nd CES Cluster Energy**

  In order to reject photons that are due to $\pi^0 \rightarrow \gamma\gamma$ decay, we search the CES in the EM cluster for the presence of a second CES cluster. If one is found this variable is a measure of it's energy. Note that as the photon energy gets higher the probability that part of the shower creates a second, small CES cluster gets larger so it is useful to have requirements on this variable scale with the overall photon energy.

B.3 Electrons

As described in Section 2.4.4, at CDF electron candidates are identified by using mostly the same calorimeter information as is used in the identification of photons [62]. Thus, we use many of the same variables, albeit often with different selection requirements. Unlike the case of a photon, where we explicitly require there to be no track associated, if a calorimeter cluster can be matched to a track we call this an electron candidate. Below is the definition of the various variables not previously described in the text used to identify electrons at CDF discussed in Table 2.9 that are not described in more detail in the text itself.

- $|\Delta X|$ and $|\Delta Z|$

  By extrapolating the electron track to the cluster we can measure the separation between the extrapolated track position and the centroid of the CES cluster in the X and Z views, where $|\Delta X_{CES}|$ and $|\Delta Z_{CES}|$ are as defined as:

  $$|\Delta X| = X_{track} - X_{CES} \tag{B.2}$$

  $$|\Delta Z| = Z_{track} - Z_{CES}. \tag{B.3}$$

  If there is a track that extrapolates to the electromagnetic cluster, it is considered to be associated with the cluster.

- **E/P**

  The ratio of the energy to the momentum of the highest P_T track pointing to the full energy of the EM cluster is useful in separating out electrons from jets that deposit a good deal of neutral energy objects in the calorimeter that will not show up in the single track with large momentum.

- L_{shr}: **L-Share**

  The L-Share (Laterial Sharing) variable is a measure of the transverese profile of the electromagnetic shower shape and the comparison of the expected lateral sharing of energy in the calorimeter towers of the electron cluster [62]. The L_{shr} variable is defined as:

$$L_{shr} = 0.14 \sum_i \frac{E_i^{adj} - E_i^{prob}}{\sqrt{0.14^2 E + (\Delta E_i^{prob})^2}} \tag{B.4}$$

  where E_i^{adj} is the energy in the tower adjacent to the tower of the electron, E_i^{prob} is the expected energy in an adjacent tower calculated from text beam data, and $0.14^2 E$ is the error associated with the energy measurement.